Engineering of Spiky Hedgehog Particles

by

Douglas G. Montjoy

A dissertation submitted in partial fulfillment
of the requirements for the degree of
Doctor of Philosophy
(Chemical Engineering)
in The University of Michigan
2020

Doctoral Committee:

Professor Nicholas Kotov, Chair
Professor Jinsang Kim
Professor Suljo Linic
Professor Michael Solomon

Douglas G. Montjoy
montjoyd@umich.edu
ORCID iD: 0000-0003-3675-8596

© Douglas G. Montjoy 2020

ACKNOWLEDGEMENTS

I would like to first thank and acknowledge my mom and dad. Both have been supportive throughout my life and helped fund my undergraduate at The Ohio State University where I learned my love for research. Additionally, I would like to thank my fiancée Kathryn, who has been very supportive throughout the whole process.

A PhD advisor defines the dissertation journey. Professor Nicholas Kotov has helped me realize my own passion for science and it has been a very enriching PhD experience with him. It is inspiring to see the breadth of research that our lab involves, and the passion which is readily apparent. The ability to tackle many different problems of an interdisciplinary nature has been very engaging and a distinct and unique experience. I would also like to thank my committee members, Professors Linic, Solomon, and Kim. Each have given me helpful advice in their respective areas, and they have helped me be able to better understand different applications and fields.

Finally, I would like to thank my lab members. Doing a PhD requires some companionship in a large lab and the Kotov Lab has had a diverse set of knowledgeable undergraduate students, PhD students, postdocs, and visiting scholars. Joong Hwan Bahng has helped me throughout my PhD as my ‘Hedgehog’ mentor and now collaborator and I appreciate that help. In addition, my undergraduates, Aydin Eskafi, Junhui Zhang, Harrison Hou, Joseph Middleton, and Eileen Li have helped me accomplish a large set of work. Harrison in particular, has been a great collaborator on experiments and helped invest time in many of the projects. Other lab members have been very helpful and it has been enjoyable to meet many different scholars from various backgrounds.

The research in this project would not have been possible without the funding of a large number of sources including the National Science Foundation, the Department of Defense, and the Electric Power Research Institute. Additionally, the Michigan Center for Materials Characterization has been integral in the ability to examine morphology of my samples.

TABLE OF CONTENTS

LIST OF FIGURES

LIST OF TABLES

ABSTRACT

Hedgehog particles (HPs) represent a platform for engineering dispersion stability by marked reduction of van der Waals forces from nanoscale spikes. This dissertation utilizes the dispersion stability of HPs in a broad array of applications including sensing in biofluids, catalysis in high ionic strengths and nonpolar environments, and for the creation of stimuli-responsive materials. New chemistries of HPs including development of core materials, spike materials, and nanoparticle coatings have been utilized to achieve functional properties.

In chapter II, we introduced functional sensing nanoparticles and polyelectrolytes through the deposition of layer-by-layer nanoparticle films on HPs. Gold-modified HPs were used to overcome the problem of colloidal aggregation in surface enhanced Raman spectroscopy probes resulting in an order of magnitude enhancement in sensing capability directly in biofluids. In this study, we also explored the limits of engineering dispersible structures, demonstrating that nanostars did not exhibit strong enough surface corrugation and very thick branching nanoparticle and polymer layers could disrupt the dispersion stability on HPs.

HPs originally, consisted of commercial carboxylated polystyrene cores. For catalysis and other applications, the production of both more chemically resistant and lab made materials is required. In chapter III, we developed a method utilizing layer-by-layer assembly to engineer microscale lab-made SiO_2 cores with nanoscale ZnO spikes that can be dispersed in both high ionic strength and nonpolar environments. Electrolyte environments enable control of product selectivity and yield but see little use with dispersible heterogeneous catalysts due to poor catalyst stability. SiO_2 HPs in concentrated electrolytes allowed for control of product selectivity and greatly enhanced yield in the photooxidation of 2-phenoxy-1-phenylethanol. SiO_2 HPs can engineer different reaction pathways in a high ionic strength environment.

Chapter IV involved the development of active core materials with complementary

properties and multifunctional core and spike materials. Omnidispersible HPs carrying stiff ZnO nanospikes were prepared with Fe_2O_3 hematite microcubes, Fe_3O_4 magnetite microcubes, hollow Au microspheres, and hollow TiO_2 microcubes. Inorganic core HPs maintained dispersion in a wide array of nonpolar environments and exhibited enhanced thermal and chemical stability. In a water and cyclohexane emulsion system, hematite HP proceeded in a novel chemical pathway to produce cyclohexene oxide, a valuable intermediate.

In Chapter V, a tunable polymer-based shell was developed for control of stability based on environmental conditions. In order to create a flexible polymer-based HP or Tendril particle (TP), polyallylamine films were crosslinked with glutaraldehyde. Hollow, flexible polymer spikes with controlled zinc oxide content were formed which can be loaded with small molecules and nanoparticles. TPs consisted of a flexible shell but retained remarkable dispersion properties including in heptane and high ionic strength media. Through addition of Poly(N-isopropylacrylamide-co-acrylic acid) (PAA-NIPAM) and dopamine subunits, controlled aggregation was observed in response to high temperature and pH respectively.

In conclusion, this thesis centers on the development of omnidispersible colloids that can function in high ionic strength and nonpolar environments. We utilize these colloids to develop new chemical pathways in these complex fluid environments and demonstrate their ability to function in sensing in biofluids and as an environmentally responsive material.

Chapter 1

Introduction

1.1 Motivation: Dispersion Stability

While the molecular engineering of particles has greatly diversified to complex shapes and chemistries, the ways to stabilize them have remained largely the same. The engineering of dispersion stability traditionally utilizes chemical coatings, which can otherwise hinder catalytic activity, sensing capability, and functionality. Dispersion of functional materials in complex fluid environments is critical to many different applications in catalysis, biosensing, and stimuli-responsive materials. It has become even more important with the development of many new reactive nanomaterials that are not as stable in complex environments such as nonpolar or high ionic strength fluids.

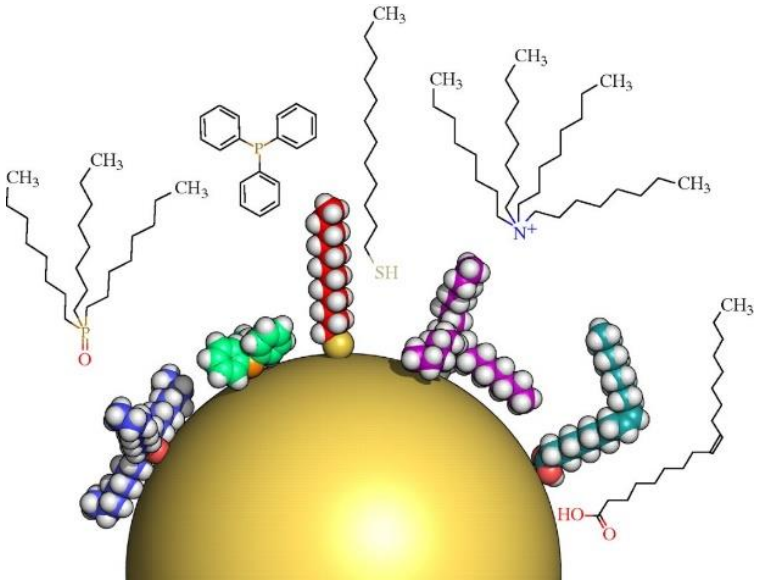

Figure 1.1: Gold Nanoparticle with different ligand molecules on the surface. Left to right: trioctylphosphine oxide (TOPO), triphenylphosphine (TPP), dodecanethiol (DDT), tetraoctylammonium bromide (TOAB) and oleic acid (OA). Obtained from Reference 1.[1]

Traditionally, surface coatings can involve a variety of different polar and nonpolar ligands used to stabilize nanoparticles (**Figure 1.1**).[1]. These coatings only allow for stability in certain chemical environments dependent on the polarity, and require phase transfer methods in order to disperse materials in the opposite polarity. [2,3] Additionally, surface coatings hinder the ability for particles to be applied broadly to applications which will require stability in a variety of fluids. Dispersion in apolar media traditionally requires hydrophobic ligands such as dodecanethiol. [3] Nanoparticle cores can also be stabilized by steric interactions between the ligands.[4] For many semiconductor nanoparticles (NPs), there are issues with desorption of these stabilizing ligands which can lead to aggregation.[5] An additional method to disperse particles in nonpolar solvents requires hydrophobic surface coatings such as thick silane coatings.[6,7] All of these dispersion methods are bound by the heuristic rule "like dissolves like" and require the addition of a nonpolar component to enhance dispersion. Functionality, in particular, for catalysts can be greatly reduced with these coatings and ligands.[8] Surfactants are unfavorable, in particular with thick hydrophobic coatings or large hydrophobic ligands since reactions take place on the catalyst surface.[9]

Dispersion in high ionic strength media is something that is also difficult. In particular, the ability for sensing probes to function in biofluids has a large dependence on their stability in high ionic strength environment. For gold nanoparticles used in clinical applications, aggregation occurs in physiological conditions due to reduction of electrostatic repulsion from screening of charge.[10,11] At 0.1 M NaCl, characteristic of biological conditions, gold nanoparticles rapidly aggregate to over 100 times the size, reducing active area and functionality.[10] Steric coatings can help stabilize nanoparticle sensors, but can lead to issues with substrate binding[12,13] and have a strong effect on adsorption[14] for catalytic applications.

Utilizing surface corrugation enables dispersion of materials in both nonpolar and high ionic strength environments. Nature has used spiky particles to control interparticle forces, for example, in pollen (**Figure 1.2**). Mimicking this ability in the laboratory such as with spiky colloids referred to as 'hedgehog particles'[15] has indicated their multifaceted technological utility.[16–19] The surface corrugation of HPs can be controlled as a strategy to improve both catalytic activity and dispersion stability. Stiff ZnO spikes (**Figure 1.2**) surrounding a solid core reduce van der Waals (vdW) forces by 10 times, which results in the ability of HPs to disperse in both organic

and aqueous solvents. [15]HPs were first synthesized utilizing a sonothermal method involving the growth of ZnO nanorods from nanoparticle seeds on a microparticle.

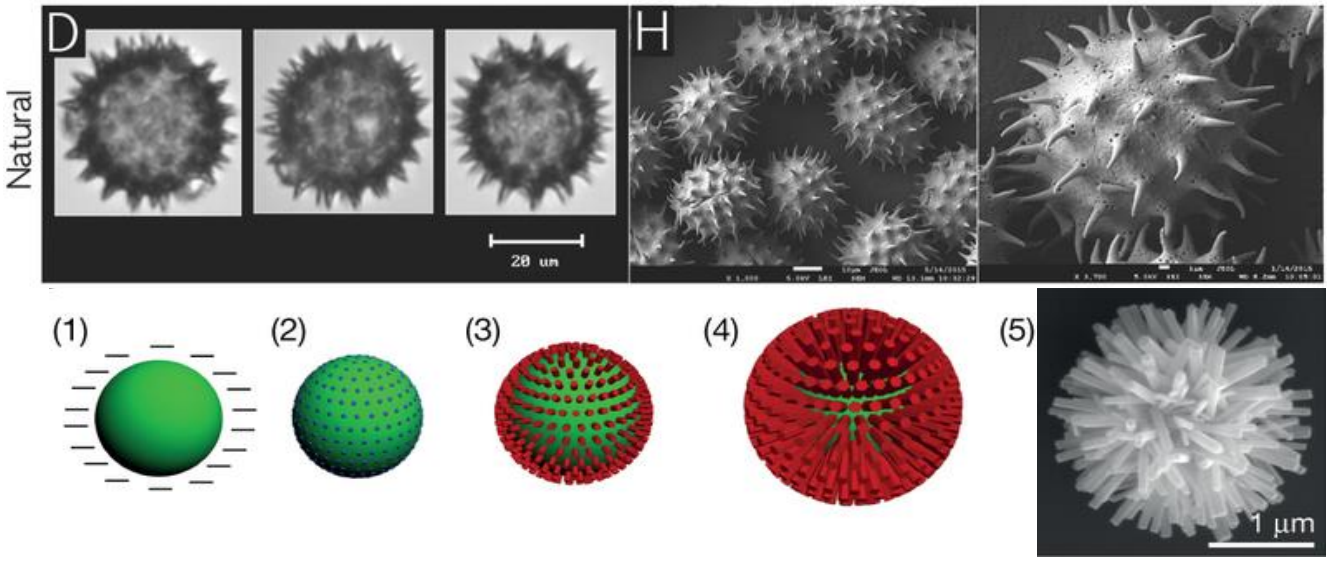

Figure 1.2: Above: Natural pollen grains captured in FlowCam at 20× magnification (D) and SEM (H), respectively, adapted from Reference 20.[20] Below: Schematic of Spiky Hedgehog Particle Synthesis. Adapted from Reference 15.[15]

HPs form stable dispersions in highly apolar organic solvents such as hexane, heptane, and toluene, as verified by confocal microscopy, while the individual components ZnO nanorods and polystyrene beads do not disperse (**Figure 1.3**). In order to quantitatively understand, the mechanism of dispersion of HPs in phobic solvents, DLVO theory was applied within additivity limits. The total energy of HP-HP interactions were evaluated as $V_{DLVO} = V_{vdW} + V_{DL.}$ $V_{DLVO,}$ where van der Waals (V_{vdW}) and electrical double layer (V_{DL}) interactions approximate the total potential (V_{DLVO}) between the interacting colloids. It was found that the presence of stiff nanoscale inorganic

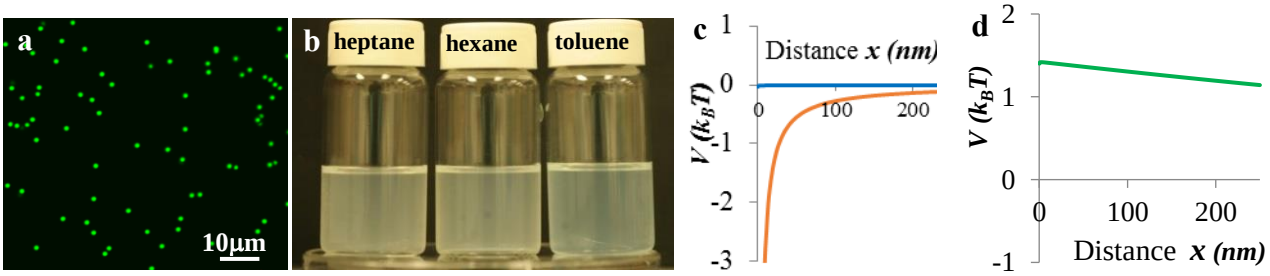

Figure 1.3: Dispersion of HPs in phobic solvents (**a**) Confocal microscopy of hydrophilic HPs dispersed in highly apolar heptane; (**b**) Photographs of dispersion of hydrophilic HPs in apolar solvents such as heptane, hexane and toluene; (**c**) van der Waals attraction, V_{vdW}, of hydrophilic HPs (blue) and polystyrene microsphere (orange) in heptane; (**d**) Total interaction potential, V_{DLVO}, of hydrophilic HPs in heptane.[15]

wires transforms the colloidal behavior of HPs. **Figure 1.3c** illustrates $V_{DLVO,\,HPs} = 1.4\ k_BT$ at the contour around the spike tips. The anomalous dispersion stability in a phobic solvent is achieved by a significant reduction in the attractive component, V_{vdW}, in HPs compared with smooth particles, **Figure 1.3d.**[15]

1.2 Layer-by-Layer Assembly

Various techniques exist to modify surfaces of colloidal particles. Polymer film formation at the surface has been achieved through the addition of monomers then subsequent polymerization[21,22]. Additionally, the formation of a polymer shell around the particle can be achieved through emulsion polymerization[23,24]. Layer-by-layer assembly (LbL) was first introduced by Iler in 1966 and then reintroduced by Decher and colleagues in 1991.[25–27] Originally, the LbL method consisted of alternatively deposited charged polymer layers on a flat substrate to form a multilayer film. LbL partners have been expanded to various types of nanoparticles as well as to different interactions including hydrogen bonding.[28,29] Multilayer composites with exceptional mechanical properties and optical properties have been achieved utilizing LbL.[30,31] LbL modification has been expanded to colloidal particles include the formation of multilayer capsules[32] and the formation of protein films[33]. This has led to numerous applications in use of LbL-modified films and particles as stimuli-responsive materials[34] and in drug delivery[35].

LbL on patterned surfaces has been explored including photolithography materials by Caruso and co-workers.[36,37] However, the vast majority of studies are limited to flat substrates. Recently, Caruso and co-workers demonstrated layer-by-layer assembly of polyelectrolytes using a patterned colloidal substrate (diatom) as a sacrificial template.[38] . LbL films have been used as successful supports for catalytic nanoparticles in numerous reactions.[39] LbL films result in increased nanoparticle loading, which has been used to create effective catalytic membranes[40,41] as well as dense coatings of plasmonic NPs for surface-enhanced Raman scattering(SERS) applications.[42,43] . Additionally, LbL films can be used to introduce selectivity into catalytic reactions.[44]

1.3 Semiconductor Photocatalysis

The nanoscale engineering of inorganic materials provides essential tools for the control of electronic properties and catalytic sites, thereby improving reaction reactivity and selectivity of catalysts [45–49]. These special properties of inorganic nanostructures have led to intense research in the fields of sustainable fuel conversion and pollutant mineralization [50–56] initiated by band gap photoexcitation followed by electron transfer reactions on different sites of catalytic nanoparticles (NPs, **Figure 1.4**). The use of photonic energy rather than thermal energy enables mild reaction conditions and reduction of carbon footprint. The favorable photocatalytic properties of nanoscale inorganic materials can be potentially taken advantage of in organic synthesis [57,58] The hydrophilic nature of uncoated inorganic NPs limits these processes, however, to mostly aqueous or polar media [59–62].

ZnO and titanium dioxide (TiO_2) represent two commonly used large band gap catalysts. [63] Extensive investigation has been done on TiO_2 photocatalysts[64,65] including degradation of environmental pollutants such as CO_2[66] and nitrate[67].The wide band gaps of TiO_2 and ZnO prevent absorption of visible light and only allow for photoactivation under UV irradiation (Figure 1.4). Many researchers have focused on narrowing the band gap of TiO_2[68–70] and ZnO[71] through doping so that the photocatalytic activity will be enhanced with exposure to visible light. The addition of metal co-catalysts such as platinum and palladium to TiO_2 helps prevent charge recombination. Additionally, coupling semiconductors such as CdS with TiO_2 can increase charge separation and the range for photoexcitation of the system.[64]

ZnO has been used to create many complex microstructures[72,73] and has also been used for environmental remediation.[74,75] One-dimensional ZnO nanostructures, such as nanorods, exhibit high crystallinity that reduces surface trapping states, and effectively delocalize charge carriers leading to efficient charge separation.[75,76] ZnO nanorod arrays

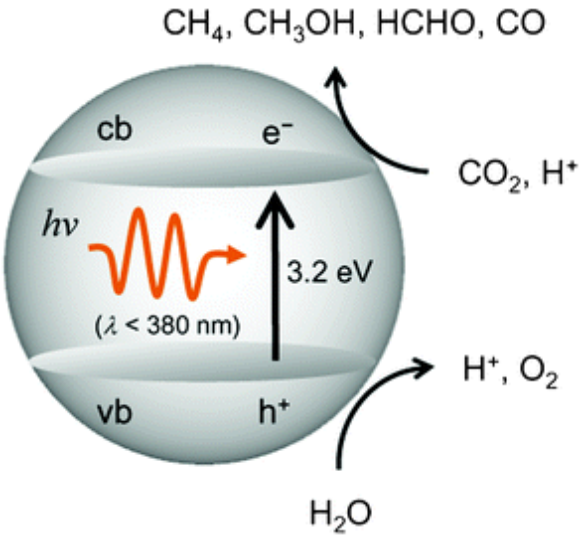

Figure 1.4: **Photocatalytic conversion of CO_2.** Reaction scheme for the photocatalytic reduction of CO_2 with H_2O on a wide band gap semiconductor.[332]

were demonstrated to have enhanced photocatalytic activity in degradation of Methyl orange over commercial ZnO particles.[77]

1.4 Thesis overview

In this thesis, surface corrugation was used as basis to achieve functional sensing, catalytic, as well as tunable optical and physical properties in complex fluid environments. HPs represent a novel way to disperse materials in high ionic strength and opposite polarity environments. Engineering of HPs was achieved through addition of sensing plasmonic nanoparticles, expansion to inorganic catalytic cores and spikes, and deposition of polyelectrolyte multilayers enabling responsive and tunable properties. By developing these new classes of HPs, new catalytic pathways were uncovered in high ionic strength environments in the oxidation of a lignin model compound and in the oxidation of nonpolar cyclohexane. Polyelectrolyte and nanoparticle multilayers enabled sensing capability directly in a biofluid environment utilizing vibrational spectroscopy traditionally plagued by poor reproducibility. Polyelectrolyte multilayers were used to give tunable properties and environmentally responsive behavior. HPs are broadly applicable—in the production of better biosensors, the creation of sustainable fuels and chemicals and engineering of responsive materials.

1.4.1 Sensing in Biofluids

Analysis of biofluids such as blood and urine using Raman spectroscopy allows for minimal invasive diagnostics, accessibility, and repeated samplings.[78,79]Plasmonic hotspots generated from aggregation of NPs have been shown to increase SERS intensity but can be unreliable and difficult to control (**Figure 1.5**).[80–82] Immobilization of nanoparticles on a support allows for close contact of NPs with greater control than aggregation of NPs in solution. Nanorod arrays are commonly used as a support since they allow close contact of NPs, and have a high surface area and aspect ratio for SERS (**Figure 1.5**).[83–85] Colloidal templates are also used since they increase dispersion stability, and can be used to add additional functionalities.[42,86] However, analysis in these fluids requires additional stability in a high ionic strength

environment that contains various biomolecules which easily induce aggregation in NP systems and can severely interfere with SERS spectra.[87,88]

Current bacterial culture techniques can take multiple days and many other techniques require extensive separation before detection. Sensitive, rapid multiplex detection is required to detect bacteria such as *Staphylococcus Aureus* and other pathogens in biofluids for many diseases including septicemia.[89–91] Therapeutic drug monitoring also requires precise quantification of drug molecules in biofluids.[88] However, analysis in these fluids requires additional stability in a high ionic strength environment that contains various biomolecules which easily induce aggregation in nanoparticle systems and can severely interfere with SERS spectra.[87,88] With the creation of HPs nanorod arrays can be used directly in a multifunctional omnidispersible SERS probe for analysis of biofluids.

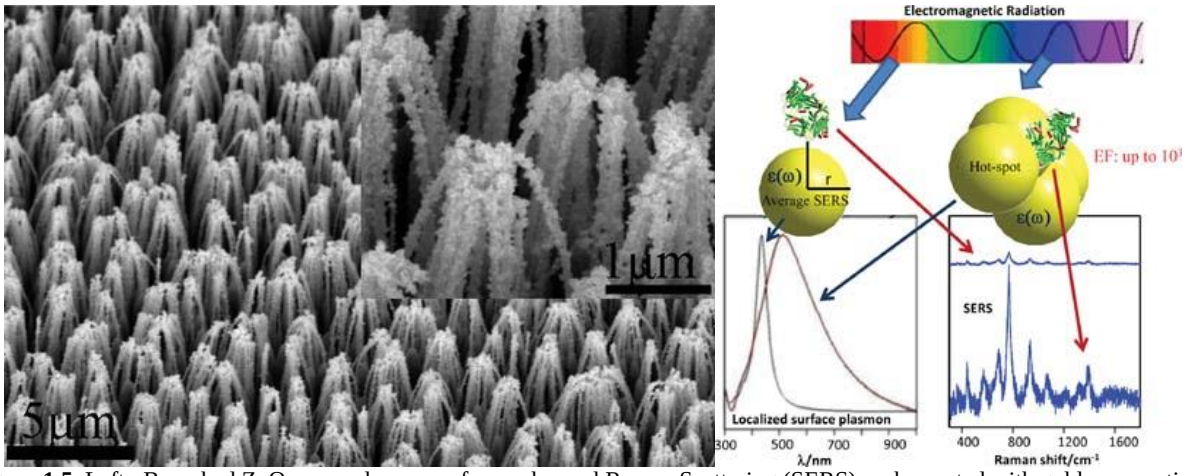

Figure 1.5. Left: Branched ZnO nanorod array surface-enhanced Raman Scattering (SERS) probe coated with gold nanoparticles from layer-by-layer assembly. Adapted from Reference 83. [83] Right: Schematic view of SERS on both non-interacting nanoparticles and aggregates. Coupling leads to the formation of hot spots, with large effects on the intensity of the SERS signal (additional enhancement factors up to 10^3), in this case for a protein from reference 92.[92]

1.4.2 Catalysis in Complex Fluids

There are a number of reactions with low yields due to the limited stability of catalysts in a nonpolar environment. Cyclohexane oxidation to KA oil, comprising cyclohexanol and cyclohexanone, is a multi-step conversion process. It is an important part of the, so called, CYCLOPOL process, a commonly used chemical industry sequence for the production of caprolactam and adipic acid, which are ultimately transformed to polyamide fibers and plastics (**Figure 1.6**). [93] The industrial process proceeds with a very low conversion of cyclohexane to KA

oil close to 4-10% to maintain 85-90% selectivity. The method consists of molecular oxidation with oxygen at high temperatures and pressures with cobalt salt and due to the apolar environment there is limited availability of other catalysts.[94] It is a challenging process as the products of interest are reactive intermediates such as cyclohexyl hydroperoxide or cyclohexene oxide.

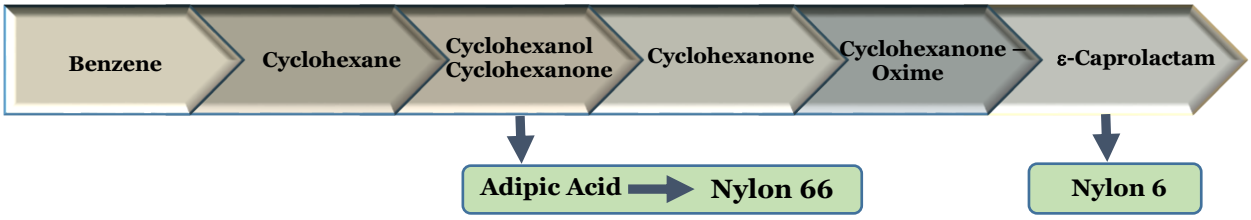

Figure 1.6. Different stages of conversion of benzene to cyclohexane and to Nylon™ polymers.

Converting carbon dioxide (CO_2) into liquid fuels and feedstocks has both economic and environmental value. Energy and economic analyses demonstrate, that photocatalytic conversion of CO_2 using solar energy is the most attractive route in the long run.[95–97] In its current form, however, the process has low efficiency, product selectivity, and catalyst stability.[98] The poor solubility of gaseous CO_2 in aqueous media is responsible for many of these problems.[99] The use of supercritical carbon dioxide ($ScCO_2$) overcomes this issue, but the non-polar nature of $ScCO_2$ results in poor catalyst dispersion stability and, therefore, activity.[100,101] The reduction of CO_2 into a valuable commodity such as methanol is a challenging but worthy goal because it simultaneously addresses global problems associated with the needs of the transportation and chemical feedstock industries, while reducing the amount of greenhouse gas.[102,103].

In addition to apolar media, there has been very limited use of photocatalysts in high ionic strength media. Electrolytes have been shown to have a large effect on selectivity in electrocatalysts. Ionic strength results in accelerated electron transfer from ascorbic acid to hexacyanoferrate by reducing electrostatic repulsion between them.[104] Additionally, high concentrations of electrolytes result in increased ethylene yield in CO_2 reduction[105] and increase the yield of C-C coupling on CuO_x electrodes.[106] These reactions indicate that high ionic strength environment has a distinct impact on the yield and selectivity catalytic processes. Importance of further exploration of high ionic strength conditions on catalysis is supported by their presence in many environmental processes, brine treatment and oil spill mitigation.[107] Dispersed particles,

however rapidly aggregate in high salinity conditions, which reduces active surface area and catalytic efficiency. [108,109]

The development of heterogeneous inorganic photocatalysts that can function in a nonpolar environment such as CO_2 or cyclohexane and concentrated electrolytes are critical for the sustainable production of feedstocks and fuels. Structurally predisposed for high colloidal and chemical stability as well as catalytic activity, HPs will establish a family of novel catalysts for apolar and high ionic strength environments.

1.4.3 Environmentally Responsive Colloids

The creation of colloids with tunable material shells and properties allow for a versatile set of optical and mechanical properties in different conditions. Through the controlled destabilization of nanoparticles the synthesis of many different nanostructures[110,111], composites[112], and crystalline materials[113] can be achieved and a variety of functions such as catalytic activity[114] can be tuned. The creation of particles that aggregate or respond to environmental conditions such as temperature[115–117], pH[118,119], light[120,121] have broad importance. Polymeric cross-linked colloids from LbL assembly are commonly used in drug-delivery and other applications requiring environmentally responsive behavior.[35] The stability of these particles in complex environments can be further improved with a stimuli-responsive spiky shell, which enables control of stabilization can be in a rapid manner.

The creation of responsive colloids also allows for the tunability of optical, mechanical, and catalytic properties.[114] Cross-linking can be used to improve colloidal mechanical properties as well as introduce environmentally responsive subunits.[122] Additionally, enzymes and a wide array of chemical/biological functionalities can be introduced through functional groups of the polymers.

Chapter 2

Omnidispersible Hedgehog Particles for Multiplexed Biosensing

Reproduced with minor modifications with permission from Montjoy, D. G.; Bahng, J. H.; Eskafi, A.; Hou, H.; Kotov, N. A. Omnidispersible Hedgehog Particles with Multilayer Coatings for Multiplexed Biosensing. *J. Am. Chem. Soc.* **2018**, *140* (25), 7835–7845. Copyright © 2018 American Chemical Society

2.1 Abstract

Hedgehog particles (HPs) replicating the spiky geometry of pollen grains revealed surprisingly high dispersion stability regardless of whether their hydrophobicity/hydrophilicity matches that of the media or not. This property designated as omnidispersibility is attributed to the drastic reduction of van der Waals interactions between particles coated with stiff nanoscale spikes as compared to particles of the same dimensions with smooth surfaces. One may hypothesize but it remains unknown, however, whether HPs modified with polymers or nanoparticles (NPs) would retain this property. Surface modifications of the spikes will expand the functionalities of HPs, making possible their utilization as omnidispersible carriers. Here, we show that HPs carrying dense conformal coatings made by layer-by-layer (LBL/LbL) assembly maintain dispersion stability in environments of extreme polarity and ionic strength. HPs, surface-modified by multilayers of polymers and gold NPs, are capable of surface-enhanced Raman scattering (SERS) and overcome the limited colloidal stability of other SERS probes. The agglomeration resilience of HPs leads to a greater than one order of magnitude increase of SERS intensity as compared to colloids with smooth surfaces and enables simultaneous detection of several targets in complex

media with high ionic strength. Omnidispersible optically active colloids open the door for rapid multiplexed SERS analysis in biological fluids and other applications.

2.2 Introduction

Dispersion stability is the essential property of colloids attained when particles have stronger interparticle repulsive forces (electrostatic, steric, etc.) than attractive ones (van der Waals, hydrogen bonding, etc.). Traditional methods of dispersing particles in solvents of opposite polarity typically involve coating particles with a layer of surface ligands following the similarity rule, "like dissolves like". [1,3,6] For instance, a dispersion of polar particles in apolar media requires chemical "camouflage" from a hydrophobic layer on the particle surface, such as silane. [6,7] Dispersions of apolar particles in polar solvents, such as water, require a layer of soft and flexible hydrophilic ligands. [123] In both cases, the coatings chemically passivate or otherwise often negatively impact the catalytic, optical, and sensing functionalities of the colloids. Spontaneous desorption of stabilizing ligands leading to particle aggregation presents a frequently encountered problem for dynamic coatings from surfactants. [2,3,5]

We are looking for an alternative strategy for dispersing particles in unfriendly solvents that avoids these problems. One such strategy is based on extreme surface corrugation. Recently, it was found that colloids carrying a layer of stiff inorganic spikes denoted as hedgehog particles (HPs) have unusually high dispersion stability in solvents of opposite polarity. The microscale HPs with outer diameters ranging from 1 to 3 microns were constructed by hydrothermal growth of nanoscale zinc oxide (ZnO) spikes onto a polystyrene core.[15] HP particles with analogous geometry but possessing smaller diameters of 200–300 nm were later constructed by the self-assembly of $FeSe_2$ nanoparticles (NPs).[124] Colloidal stability of HPs was attributed to marked reduction of van der Waals (London dispersion) forces for particles with rigid spikes. Mitigation of the non-specific attractive forces between particles enables them to disperse equally well in organic and aqueous solvents as well as in media with high ionic strength. These properties make HPs uniquely suitable for use in analysis,[79] catalysis,[8,125,126] and drug delivery.[127]

The similarity between the geometries of HPs and those of spiky pollen grains,[128–130] some cells,[131–133] and viruses[134–136] with highly corrugated surfaces should be noted. The congruence of their shapes is not accidental.[137] The rigid spikes of pollen particles have been designed by nature

to resist agglomeration under a variety of conditions while promoting their association with receptor-specific targets located on the spikes. Such design of the particles spanning Ångström, nanometer, and micrometer scales facilitates pollen dispersion, dissemination and, therefore, proliferation of the particular species.

Star-like particles with modest corrugation are known to have other remarkable properties that strongly differentiate them from particles with smooth surfaces.[16–19,86,138] These properties include concentration of the electrical field at their apexes,[139] lock-and-key assembly patterns,[140,141] catalytic activity related to topographic features,[142] as well as enhanced intracellular delivery.[143] These properties are expected to be retained in HPs and can be combined with omnidispersibility, enhancing the technological prospects of these engineered multiscale colloids.

The derivatization of HP surfaces with macromolecular components will greatly expand the functionalities of HPs. For instance, molecular engineering of the surface of ZnO nanorods with polymers and NPs will impart the HPs with desirable optical properties, reactive chemical groups, and biological specificity. However, surface modification of HPs by most techniques, for instance, by in-situ polymerization resulting in soft organic shells, is expected to compromise their omnidispersibility. Such surface modification will reduce nanoscale corrugation and result in increased van der Waals attraction.

Layer-by-layer assembly (LBL) permits molecular and nanoscale engineering of surfaces by sequential deposition of polyelectrolytes,[144–146] proteins,[33,147] NPs,[28,30,148,149] and many other functional compounds[34–37,150] involving different types of interactions.[29,151] Importantly, conformal deposition of nanoscale layers by LBL can be accomplished not only on flat surfaces but also on colloids[26,27,32,152,153] and surfaces with very complex geometries.[38,154–162] We hypothesized that the dense conformal LBL coatings will preserve omnidispersibility of HPs. Realization of LBL-coated HPs will answer a fundamental question of whether or not the dispersion properties observed for HPs are material dependent. Furthermore, LBL films are likely to expand the functionalities of HPs. For instance, layers of plasmonic NPs on HPs will make omnidispersible probes suitable for surface enhanced Raman spectroscopy (SERS).[42,43,163,164] Since enhancement factors and reproducibility of SERS are strongly dependent on the agglomeration state of the particles,[80–82] minimization of the dependence of the SERS intensity on particle agglomeration is critical for analysis of biofluids.[78,79,165] Additionally, dispersion stability is critical in media with high ionic strength and large amounts of various biomolecules, which

easily flocculates NPs and other SERS probes leading to a decrease of sensitivity and reliability of SERS-based biosensing.[87,88,163–165]

2.3 LBL Film of Polyelectrolytes on HPs

HPs constructed from PS cores and ZnO "needles" according to the previous study[15] were used as the model particles in this study due to the simplicity of their ZnO surface modification. For LBL deposition we chose sodium polystyrene sulfonate (PSS), and poly(diallyldimethylammonium chloride) (PDDA), as the primary multilayer system because they are known to form strong, dense coatings on substrates.[25,28] The $(PSS/PDDA)_n$ multilayers were deposited on HPs using the adsorption-centrifugation cycle described previously for microscale colloids with smooth surfaces.[152,166] Conformal films on HPs were also formed with weak polyelectrolytes, polyacrylic acid (PAA), and poly(allylamine hydrochloride) (PAH). These films show some interconnectivity of polymer coatings between the spikes for high values of *n* (**Figure 2.9**), which is undesirable in the context of this study. The density of the coatings can be tuned by varying ionic strength and pH of polyelectrolyte solutions.[167,168] In most cases, the LBL deposition was performed in the presence of 0.5 M NaCl to produce denser and thicker bilayers for each cycle unless otherwise noted.

Transmission (TEM) and scanning (SEM) electron microscopies indicated formation of compact conformal coatings (**Figure 2.1**) with uniform thicknesses around all of the spikes and cores of the HPs with no damage or alteration of the starting HP's geometry observed. The thicknesses of the $(PSS/PDDA)_2$, $(PSS/PDDA)_3PSS$, and $(PSS/PDDA)_5$ polymeric shells were 8.5 ± 2.0, 14.0 ± 3.4, and 17.6 ± 4.2 nm, respectively. In accord with previous observations of LBL films on flat surfaces, [26] LBL deposition without NaCl produced thinner films; for example, a $(PSS/PDDA)_5$ shell formed in the absence of NaCl had a thickness of only 6.3 ± 2.0 nm (**Figure 2.7).**

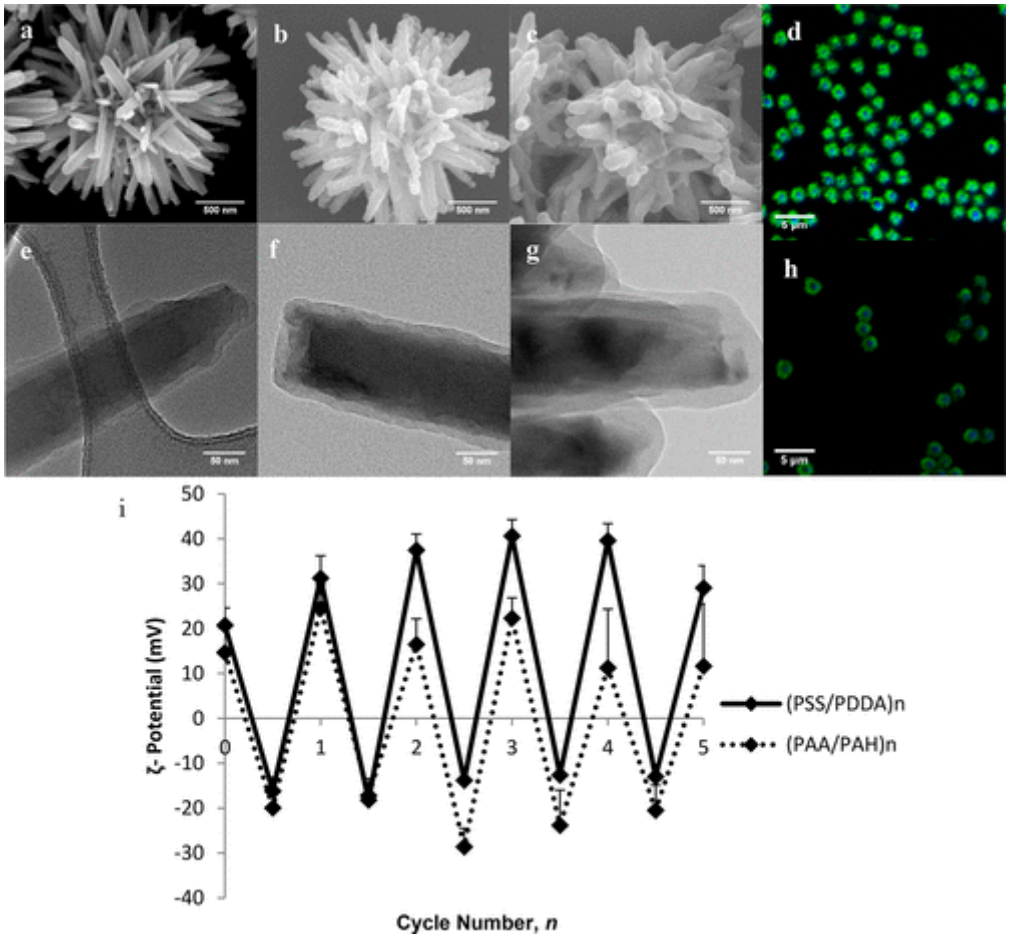

Figure 2.1. Deposition of Polyelectrolyte Films on HPs: SEM and TEM images of HPs modified using $(PSS/PDDA)_n$ multilayers deposited in the presence of 0.5 M NaCl for different deposition sequences: (**a,e**) $(PSS/PDDA)_2$, (**b,f**) $(PSS/PDDA)_3PSS$ (i.e., 3.5 bilayers), (**c,g**) $(PSS/PDDA)_5$, confocal microscopy of bright blue fluorescent core HPs modified with PSS/FITC-PAH (**d**) and PAA/FITC-PAH (**h**) films, (**i**) ζ-potential measurements as a function of bilayer number for HPs modified with PSS/PDDA (solid line) and PAA/PAH (dashed line).

We complemented TEM data with images obtained by confocal microscopy to gain a more detailed assessment of LBL coatings for the ensemble of particles. HPs were first coated by positively charged fluorescein-isothiocyanate-modified poly(allylamine hydrochloride) (FITC-PAH) serving as a contrast agent for confocal microscopy, then an LBL shell was sequentially assembled with negatively charged PSS or PAA. Both FITC-PAH coatings of HPs possessed bright green emission, while the carboxylate microspheres used as cores possessed bright blue emission (**Figure 2.1e,h**). Standard confocal (**Figure 2.1**) and super-resolution stimulation emission depletion (STED) microscopies (**Figure 2.8**) gave clear indications that uniform and conformal LBL films around the spikes for the HPs are formed. Electrodynamic ζ-potential

measurements further confirmed the deposition of alternately charged polymer layers on the HPs en masse (**Figure 2.1g**). The unmodified HPs have a ζ-potential of +14 mV. LBL-modified HPs revealed ζ-potentials of +40 and −20 mV for PDDA and PSS layers, respectively, and of +25 and −30 mV for PAH and PAA, respectively (**Figure 2.1i**).

2.4. LBL Film of Nanoparticles on HPs

Homogeneous conformal LBL films were also formed from negatively charged Au NPs (AuNP, **Figure 2.2, 2.10**) assembled with PDDA. [169] Without LBL modification, there was very limited adsorption of Au NP on HPs (**Figure 2.11**). A "base" layer of PSS was deposited prior to deposition of (PDDA/AuNP) multilayers to promote the uniformity of the coatings. [152] HPs were prepared with PSS(PDDA/AuNP) and PSS(PDDA/AuNP)$_2$ shells and will be referred to as AuHP and Au_2HP, respectively. Dispersions of AuHP and Au_2HP contained 12 and 27 picomoles of AuNPs per mg HP, respectively. PSS(PDDA/AuNP) films deposited in the presence of 0.5 M NaCl resulted in HPs that contained 43 picomoles of AuNP per mg HP and will be referred to herein as Au-SHP (**Figure 2.2**). Determining the amount of AuNP per mg HP (see methods) was essential for adequate comparison with particle functionalities, such as SERS intensity, dependent on the amount of plasmonic NPs. Typically, the NP-terminated coatings displayed ζ-potential between 0 and −10 mV, smaller than those made solely from polyelectrolytes (**Figure 2.1i**). For HPs with NP deposited in the presence of 0.5 M of NaCl, ζ-potential was ∼40 mV for PDDA-terminated layers and −20 mV for NP-terminated sequences, which was generally higher as compared to HPs without NaCl (**Figure 2.2g**). For coatings made in the presence of 0.5 M NaCl, an additional layer of PSS was adsorbed each cycle to create PSS/PDDA/AuNP to increase surface density of NPs (**Figure 2.13**).

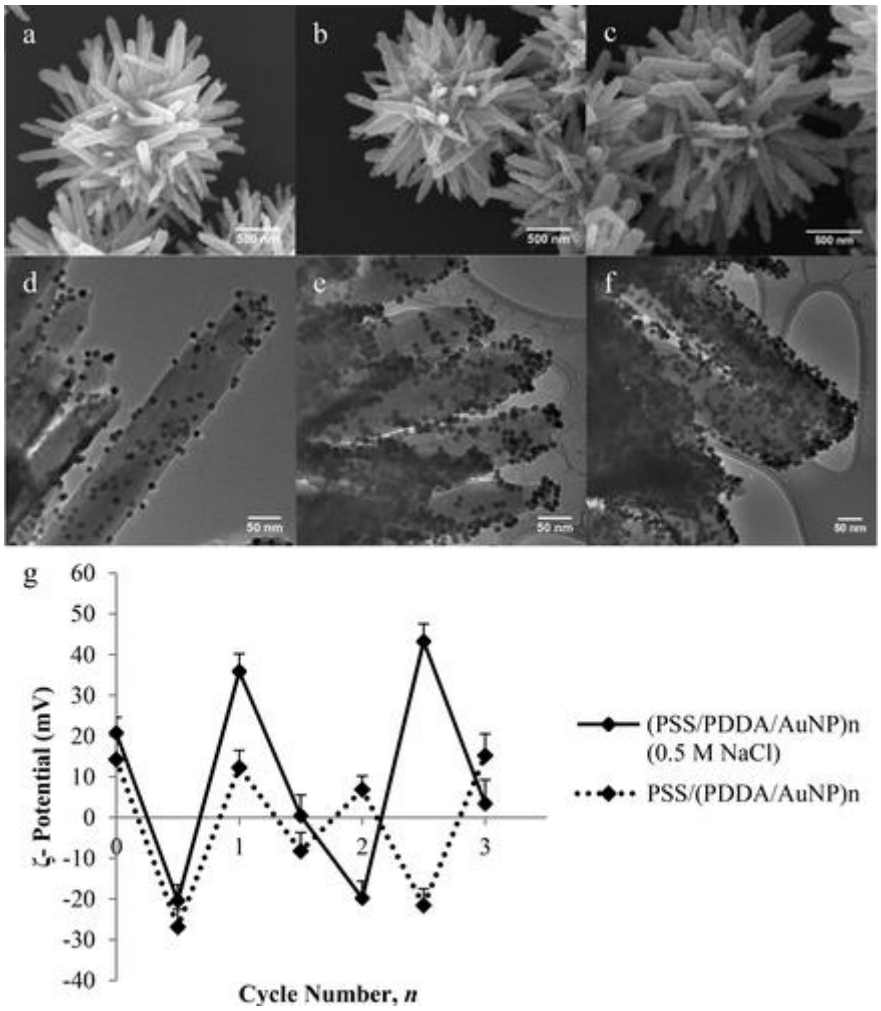

Figure 2.2. **Deposition of Nanoparticle films on HPs**: SEM and TEM images of HPs modified with Au NPs using different LBL layer sequence and deposition conditions: (**a,c**) PSS/PDDA/AuNP (AuHP), (**b,d**) PSS/(PDDA/AuNP)$_2$ (Au$_2$HP), (**c,f**) PSS/PDDA/AuNP deposited in the presence of 0.5 M NaCl (Au-SHP). (**g**) ζ-potential of HPs modified by (PSS/PDDA/AuNP)$_n$ deposited in the presence of 0.5 M NaCl (solid) and PSS/(PDDA/AuNP)$_n$ (dashed).

2.5. Dispersion Studies

HPs coated with (PSS/PDDA)$_2$ and (PSS/PDDA)$_3$PSS polymeric shells show little aggregation (**Figure 2.3**), which was confirmed with SEM (**Figure 2.3e–g**) and confocal images (**Figure 2.3b–d**). As the thickness of multilayers increases, for example, with five deposited bilayers, (PSS/PDDA)$_5$, significant aggregation is observed (**Figure 2.3**). While different surface charges are observed between layers, the magnitude of charge is still maintained at around +30 mV for the 5 bilayer film, which is greater than the −13 mV observed with the 3.5 bilayer film (**Figure 2.1i**). Instead, this change of dispersion behavior is associated with the partial loss of the

corrugation due to the merger of the PSS/PDDA layers between the spikes. This change of geometry of the colloids results in increased contact area between the spikes, stronger attraction forces, and greater aggregation (**Figure 2.1g**).

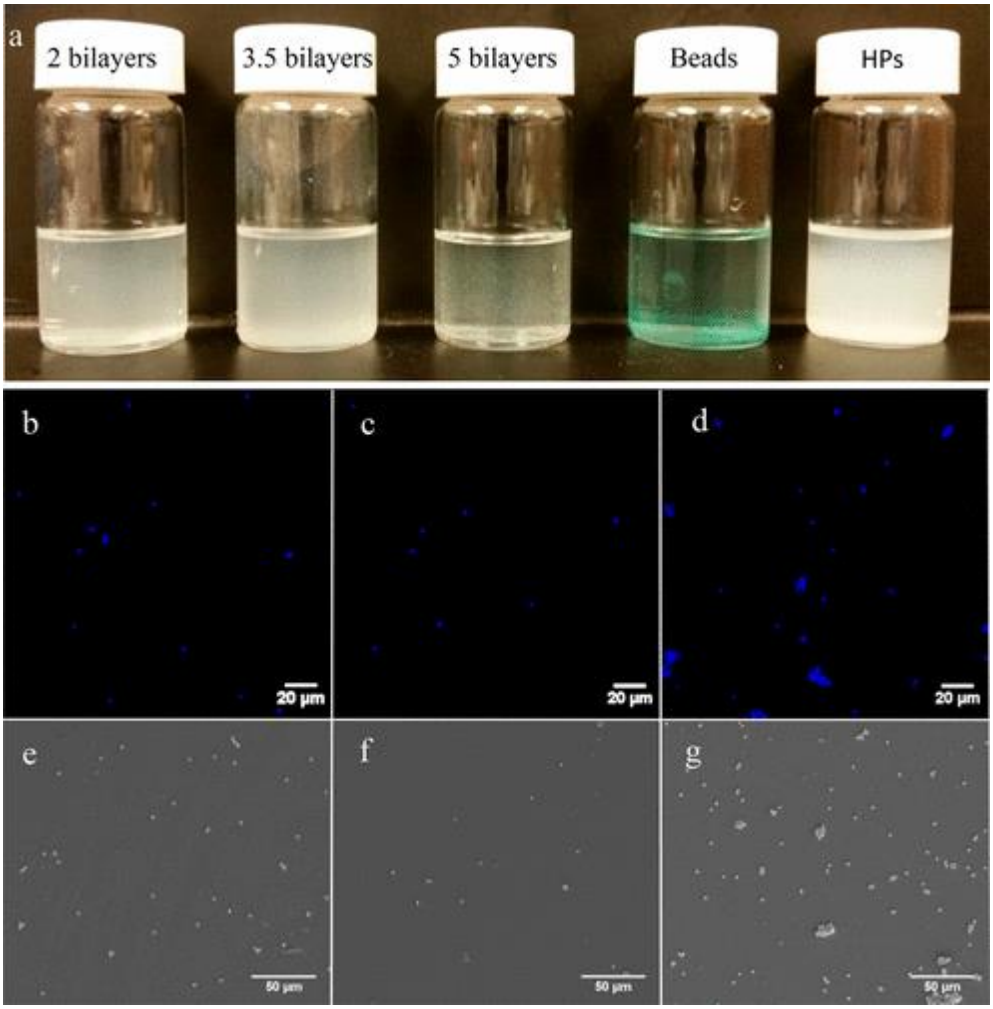

Figure 2.3: Dispersion of Polymer-modified HPs: (**a**) Photographs of heptane dispersions (0.25 mg/mL) of HPs modified with (PSS/PDDA)n in the presence of 0.5 M NaCl: $(PSS/PDDA)_2$ (2 bilayers), $(PSS/PDDA)_3PSS$ (3.5 bilayers), $(PSS/PDDA)_5$ (5 bilayers), PS beads (Beads), and unmodified HPs. Confocal microscopy (**b–d**) and SEM (**e–g**) images of heptane dispersions of HPs coated with (**b,e**) $(PSS/PDDA)_2$, (**c,f**) $(PSS/PDDA)_3PSS$, and (**d,g**) $(PSS/PDDA)_5$. HPs for confocal microscopy were prepared from PS beads with blue fluorescence.

As expected, HPs surface-modified with Au NPs (AuHP, Au_2HP, Au-SHP) disperse well in water (**Figure 2.16**). They also display stable dispersions in heptane for various thicknesses of NP films (**Figure 2.4, 2.17**), while smooth PS beads coated with (PDDA/AuNP) in 0.5 M NaCl, denoted here and further as Au-SBead (**Figure 2.14**), show visible agglomeration and precipitation (**Figure 2.4, 2.17**). SEM images in heptane illustrate that there is minimal aggregation for HPs, AuHP, Au_2HP, and Au-SHP samples, while significant aggregation is observed for Au-SBead

particles (**Figure 2.4, 2.17, 2.18**). These observations for particle ensembles were unequivocally confirmed by confocal microscopy images visualizing single particles (**Figure 2.5, 2.17, 2.18**). To further demonstrate the stability of Au-modified HPs in heptane, the concentration was increased from 0.25 to 1 mg/mL (**Figure 2.19, 2.20**); particles formed stable dispersions at all concentrations. AuNP-modified HPs with various thicknesses of LBL coatings also dispersed well in a high ionic strength environment, 1 M NaCl (**Figure 2.4, 2.21**). Importantly, AuBead-S particles and AuNPs by themselves severely aggregate (**Figure 2.4, 2.10**).

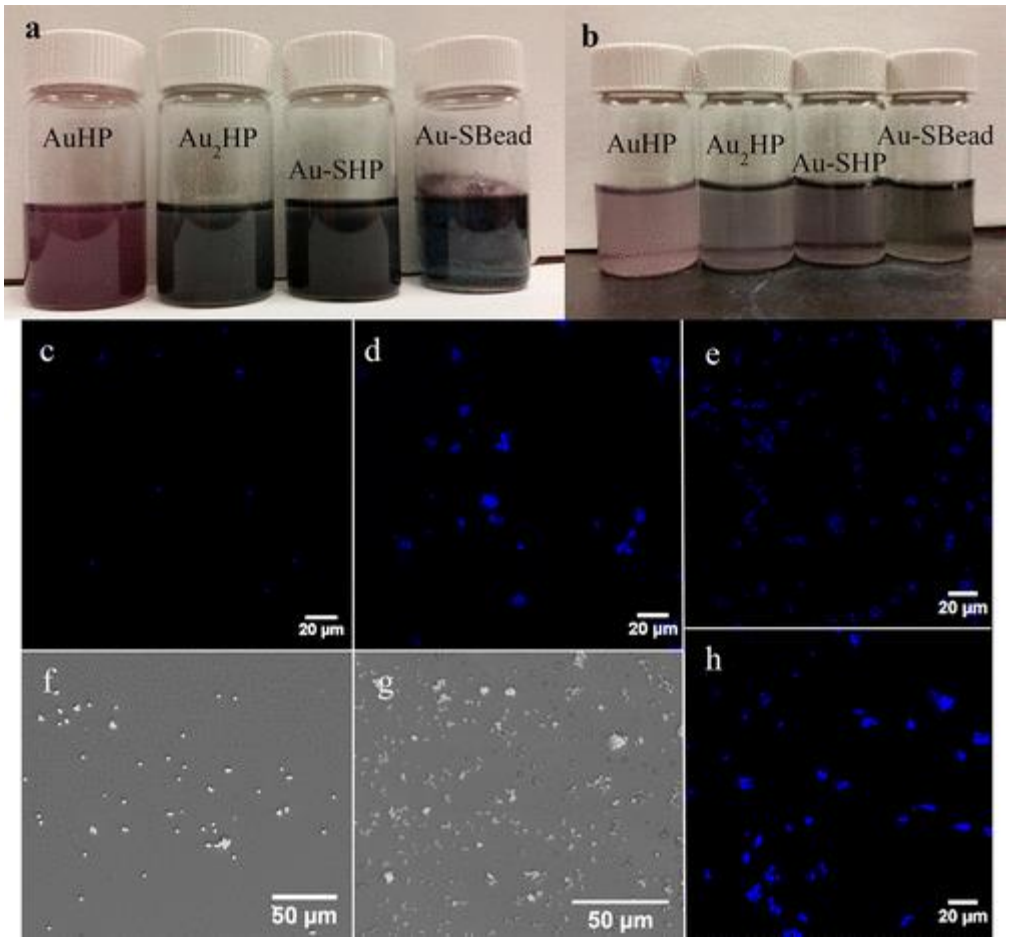

Figure 2.4. **Dispersion of Nanoparticle-modified HPs**. Photographs of dispersions of LBL-modified HPs (concentration 0.25 mg/mL) in (**a**) heptane and (**b**) 1 M NaCl. Confocal microscopy (**c,d,e,h**) and SEM (**f,g**) images of Au-SHP in (**c,f**) heptane and (**e**) 1 M NaCl as well as Au-SBead in (**d,g**) heptane and (**h**) 1 M NaCl. HPs for confocal microscopy were prepared from PS beads with blue fluorescence.

For a broader comparison, we also evaluated the dispersion stability of gold nanostars (AuNS), which display strong SERS enhancement[170–174] and were successfully used as SERS probes in the past.[175–179] Notably, they were reported to have improved dispersion stability as compared to smooth NPs. [180] However, AuNS in water and NaCl solution show distinct

agglomeration unlike HPs with similar surface ligands (**Figure 2.22a**). To confirm the attribution of the experimental observations to the surface corrugation effects, we also calculated pair potentials between AuNS using a classical version of the Derjaguin–Landau–Verwey–Overbeek (DLVO) theory.[181] Although AuNSs are within the size range that necessitates accounting for nonadditivity of particle interactions[182–185], the limitations of the theories accounting for the parametrization of the electrostatic, van der Waals, hydrophobic, and other forces between nanoscale objects do not allow at the moment for the adequate calculation of these interactions. The data reported for nanoshell assemblies[186] indicate that DLVO in case of realistic inorganic NPs underestimates the strength of attractive interactions. Thus, this theory can be used as a limiting case for agglomeration in different media. Our calculations presented in **Figure 2.22b** show an attractive pair potential for AuNS predicting their agglomeration under these conditions. The theoretical results match experimental observations for AuNS in aqueous media with increasing ionic strength. Similar calculations for heptane dispersions of AuNS carrying either 4-mercaptobenzoic acid (MBA) and thiol-polyethylene glycol-amine (PEG-SH) also match DLVO calculations (**Figure 2.23**). Analogous calculations for HPs with ZnO nanospikes with a partial account of nonadditivity were carried out in a previous publication.[15] The pair potential for HPs corresponds to predominantly repulsive interactions between particles due to extreme surface corrugation predicting their colloidal stability.

Omnidispersibility was also found for HPs carrying a stratified shell made from NPs of different diameters denoted as (PSS/PDDA/AuNP-small/PSS/PDDA/AuNP-large). This experiment is significant in the perspective of fine-tuning of the structure and composition of the multilayers designed for specific function, while retaining their limited colloidal stability. HPs were coated by a multilayer in the presence of 0.5 M NaCl, where the first NP layer consisted of NPs with an average diameter of 12 ± 1 nm and the second NP layer consisted of NPs with an average diameter of 39 ± 9 nm (complete multilayer denoted as Au_2-SHP) (**Figure 2.5b,c**). Au_2-SHP colloids disperse well in DI water and in aqueous solutions with high ionic strength environments such as 1 M NaCl (**Figure 2.24**). They also disperse in heptane, but show a greater propensity to aggregate than do other Au-modified HP samples (**Figure 2.19, 2.20, 2.24**). Large NPs between the ZnO nanospikes cause increased HP–HP attraction due to a partial loss of corrugation. These results indicate that the omnidispersibility of the LBL-modified HPs is maintained as long as the hedgehog-like corrugation of their surface is preserved.

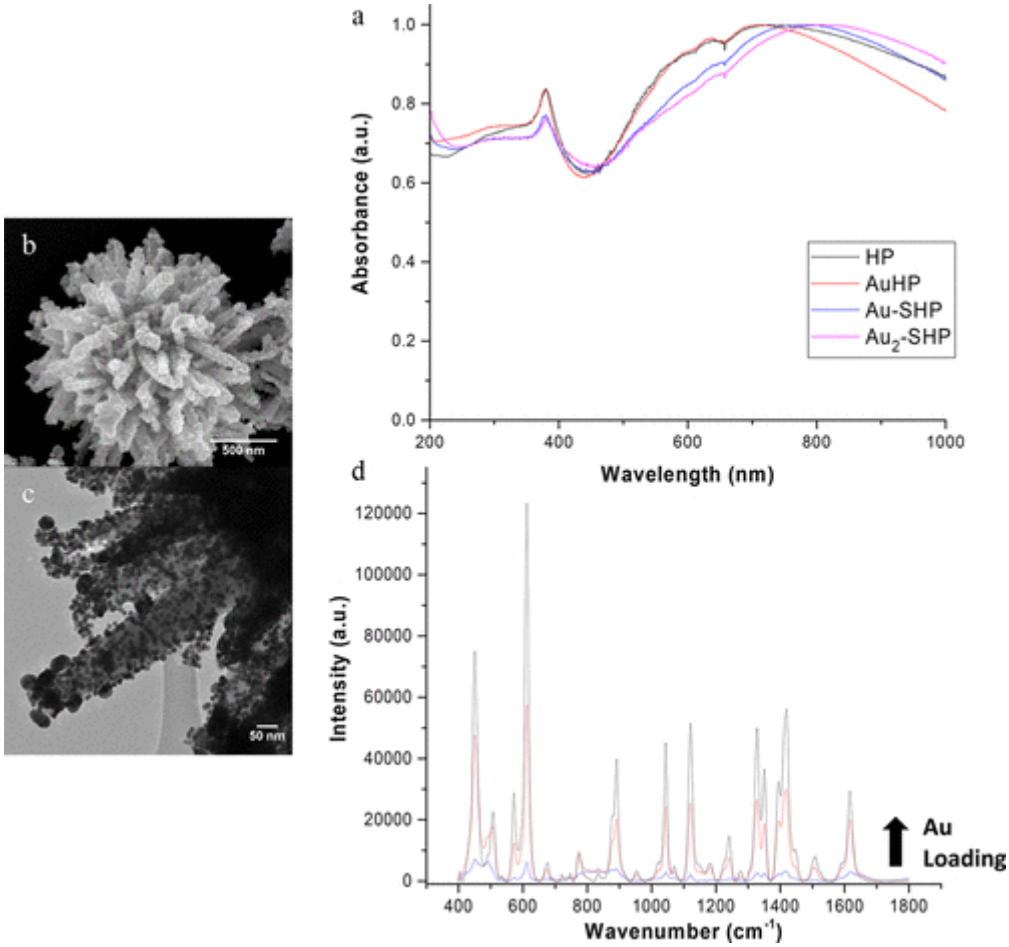

Figure 2.5. Optical Properties of AuNP-Modified HP: (**a**) Normalized extinction spectra of HPs as compared to AuHP, Au_1-SHP, and Au_2-SHP. (**b**) SEM and (**c**) TEM images of Au_2-S HPs, respectively. (**d**) background-corrected Raman scattering intensity of various AuNP-modified HPs for detection of 1 μM methylene blue with increasing loading of AuNPs; blue, AuHP: red, Au_1-SHP; black, Au_2-SHP.

2.6. Optical Characterization of AuNP-Modified HP and SERS Studies

The combination of plasmonic activity, high surface density of NPs, and dispersion stability in high ionic strength environment observed for Au_2-SHP particles makes them promising probes for analysis of biofluids using SERS (**Figure 2.5b,c**). Extinction spectra for Au_1-SHP and Au_2-SHP indicate that there is a strong plasmonic coupling in the NP multilayers exhibited by the red shift of the spectral maxima as the density of the NPs in the coating increases (**Figure 2.5a**). Different dispersions of Au-modified HPs with the same total amount of loaded AuNPs (7 picomole) were compared using a model SERS analyte, methylene blue (MB). The intensity of SERS bands for MB (1 μM) increases with progressively thicker coatings **(Figure 2.5d**). The

proximity of Au NPs results in the generation of so-called "hot spots" where SERS enhancement occurs[187,188] and can be observed for Au-SHP and Au_2-SHP. When bare HPs or free gold NPs are tested with the same concentrations, no MB peaks can be registered (**Figure 2.25**).

To investigate the effect of omnidispersibility on particle performance as Raman scattering probes in complex fluids, we compared SERS spectra obtained for Au_2-SHP and PS beads with smooth surfaces coated with the identical sequence of LBL layers (PSS/PDDA/AuNP-small/PSS/PDDA/AuNP-large) with the same total amount of loaded small AuNP denoted as Au_2-SBead particles (**Figure 2.14**). AuNS stabilized with PEG-SH, commonly used as SERS probes, were also tested (**Figure 2.15**). Characteristic peaks for MB are observed at 445, 1382, and 1422 cm^{-1} (C–N–C skeletal bending) and at 1494 and 1618 cm^{-1} (C–C ring stretching) (**Figure 2.6**). We found that Au_2-SHPs show strong SERS bands even under ionic strengths as high as 3 M NaCl (**Figure 2.26**). Also important is that the SERS band enhancements observed for Au_2-SHPs are greater than those of many reported ZnO nanostructures in water.[189] The high SERS intensity enables MB detection after incubation as quickly as one minute (**Figure 2.27**) for analysis of a clinically relevant 3.5 mL volume sample, which is more than one order of magnitude faster than other large volume analysis methods.[89]

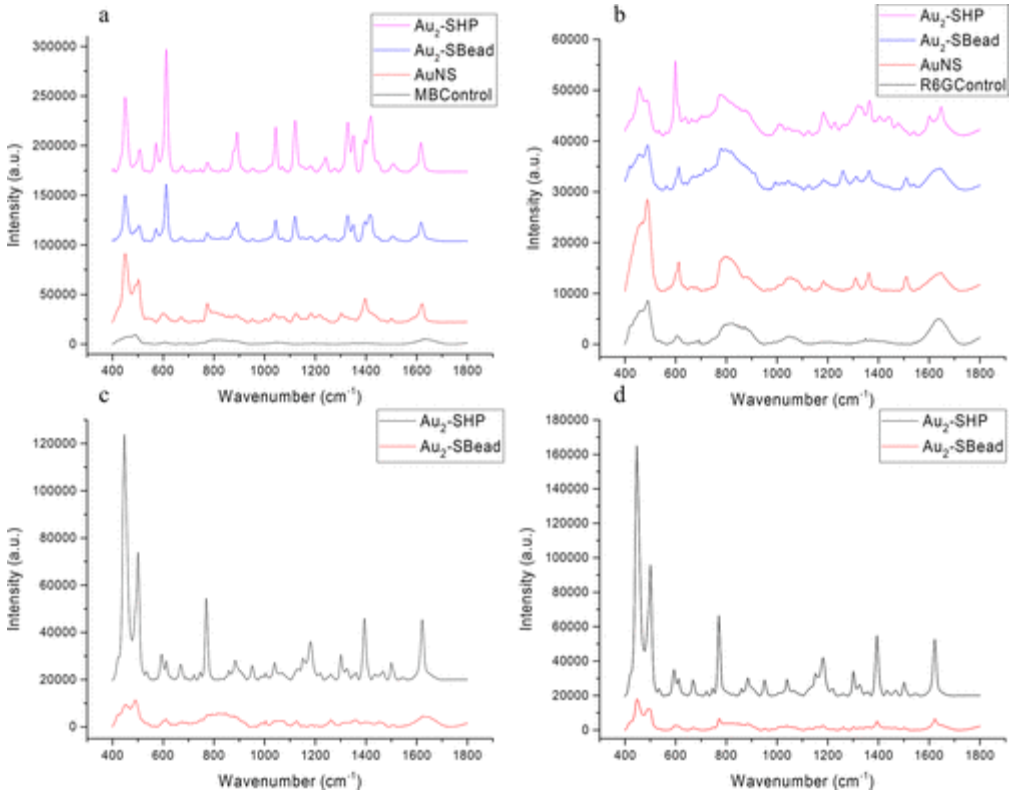

Figure 2.6. SERS Performance in Biofluids: Raman scattering spectra obtained with different SERS probes given in the graphs: (**a**) 1 μM MB in water, (**b**) 1 μM R6G in water, (**c**) 1 μM MB and 1 μM R6G in TSB, and (**d**) 1 μM MB and 1 μM R6G in DMEM. Without dye, there are minimal peaks observed in Au_2-SHP, Au_2-SBead, and AuNS samples (see also **Figure 2.22**).

Au_2-SHPs also allow SERS detection of Rhodamine 6G (R6G) whose 1 μM solution in water shows characteristic peaks at 1183 (C–H in-plane bending), 1311, and 1364 cm^{-1} (aromatic C–C stretching) (**Figure 2.6**). Multiplexed SERS detection was performed for aqueous solutions containing 1 μM R6G and 1 μM MB simultaneously comparing Au_2-SHPs and Au_2-SBead samples. Greatly diminished sensitivity to and limit of detection of MB are observed with no detection of R6G for Au_2-SBeads, while the dispersions of Au_2-SHPs show distinct peaks of MB and R6G (**Figure 2.28**)

To further increase the complexity of the media and therefore the analytical challenge, we tested the SERS performance of Au_2-SHPs, Au_2-SBead, and AuNS in Dulbecco's modified eagle medium (DMEM) with 5% fetal bovine serum and 1% penicillin/streptavidin and tryptic soy broth (TSB) with addition of 1% glucose, commonly used in blood culture and as bacteria growth mediums, respectively. Simultaneous detection of both MB and R6G in both TSB and DMEM is possible for Au_2-SHP but not possible for Au_2-SBead samples. In the case of Au_2-SHPs, SERS signals show characteristic peaks for both dyes and maintain the enhancement observed in water (**Figure 2.29, 2.30**). Au_2-SBeads do not show distinct peaks for R6G in either fluid, and do not show distinct MB peaks in TSB (**Figure 2.6c,d, 2.31**). In addition, AuNS are unable to detect R6G and show greatly diminished detection of MB in both types of media (Figure 2.32, 2.33). The differences between SERS probes, Au_2-SHP, Au_2-SBead, and AuNS were quantified by analytical enhancement factors given in (**Table 2.1**)

Table 2.1: MB Analytical Enhancement Factors

	Water	**DMEM**	**TSB**	**DMEM2**	**TSB2**
Au_2-SHP	159	202	140	382	110
Au_2-SBead	40	41	23	28	7

Au_2-SHPs show greater than one order of magnitude enhancement over the beads and AuNS for multiplexed biosensing (**Table 2.1**) and can detect R6G in the presence of MB in both types of complex biological media, while the Au_2-SBeads and AuNS cannot (**Table 2.2**).

Table 2.2: R6G Analytical Enhancement Factors

	Water	DMEM	TSB	DMEM2	TSB2
Au_2-SHP	515	551	456	217	170
Au_2-SBead	208	148	198	ND*	ND*

*No distinct peak was observed at 1365 nm.

Note that the functions of corrugated morphology in AuNS and HPs are different. The nanoscale spikes on AuNS help increase the SERS intensity by concentration of the electrical field in their ends, whereas the spikes on HPs help reduce agglomeration. It is potentially possible to combine both structural designs in one particle for the maximum enhancement factors. Conformal and molecularly "tight" LBL shells can help accomplish this task by depositing AuNS on HPs. Realization of particle design based on hierarchical corrugation when stiff spikes ~100 nm in diameter are decorated with thinner but similarly stiff spikes ~10–30 nm in diameter may also increase dispersibility.

2.7 Conclusions

We demonstrated that polymer- and NP-modified HPs exhibit colloidal stability in archetypal hydrophobic and hydrophilic media as well as in aqueous solutions with high ionic strength and high protein content. The particles retain omnidispersibility as long as high surface corrugation is maintained from the compact and conformal shells made by LBL. The combination of plasmonic activity, dense NP packing, and omnidispersibility makes HPs with NP multilayers efficient SERS probes for the rapid multiplexed biosensing of biofluids. Besides biological analysis, LBL-modified HPs with such combinations of properties can provide unique capabilities for catalysts, aerosol drug carriers, and extraction processes where dispersion stability in media of a wide range of polarity is critical.

2.8 Methods

All materials were purchased from commercial sources: poly(diallyldimethylammonium chloride) (PDDA), sodium polystyrenesulfonate (PSS), polacrylic acid (PAA), poly(allylamine hydrochloride) (PAH), heptane, zinc nitrate hexahydrate ($Zn(NO_3)_2 \cdot 6H_2O$, ≥99% purum),

hexamethylene tetraamine ($C_6H_{12}N_4$, ≥99.5% puriss) trisodium citrate, thiol-polyethylene glycol (5K)-amine, and zinc oxide NPs (50 wt % solution) were purchased from Sigma-Aldrich (St. Louis, MO); grids with ultrathin carbon film on holey carbon film support for transmission electron microscope (TEM) measurements and silicon wafers for scanning electron microscope (SEM) measurements from Ted Pella (Redding, CA) and green dyed and fluorescent carboxylated polystyrene (PS) beads were ordered from Polysciences, Inc. (Warrington, PA).

2.8.1 Synthesis of Hedgehog Particles

All HPs were synthesized using a sonothermal method as described by Bahng et al. [15] Briefly, a ZnO NP solution (0.025 wt %) was incubated with carboxylated PS cores (125 μL, 2.7 wt %) to deposit seed particles on the beads. After this solution was filtered, the NP-decorated beads were combined with equimolar solutions of zinc nitrate hexahydrate (25 mM) and hexamethylenetetramine (25 mM) and then subjected to probe sonication with a Cole Palmer 500 W ultrasonic homogenizer with a CV33 Vibracell Sonicator probe for 90 min to grow out nanorods. [15,190]

2.8.2 Synthesis of Gold Nanostars

AuNS were synthesized via a surfactant-free method according to Yuan et al. [191] Briefly, 500 μL of gold seed nanoparticles synthesized via modified Turkevich method[169] was added to 200 mL of 0.25 mm Au(III) chloride solution with 200 μL of 1 M hydrochloric acid in a 250 mL Erlenmeyer flask. Quickly after, 2 mL of 3 mM silver nitrate and 1 mL of ascorbic acid (100 mM) were added simultaneously. Twenty milliliters of PEG-SH (110 μM) or MBA (110 μM) was added to produce a final concentration of 10 μM under moderate stirring for 30 min. AuNS were then centrifuged at 5000*g* for 15 min and washed three times with water before use.

2.8.3 Deposition of Layer-by-Layer Assembled Films

In a normal procedure, 5 mL of polyelectrolyte was added to 1 mL of HPs. Particles were incubated for 20 min and then placed in a centrifuge at 1000 rpm for 10 min and then washed for three cycles. For incubation with gold, the supernatant was collected after incubation to determine the quantity of NPs deposited based on the absorbance spectra of the supernatant according to Haiss et al. (**Figure 2.12**).[192] NP size was estimated using a minimum of 100 TEM images.

Because the thickness of weak polyelectrolyte films, such as PAA and PAH, is strongly dependent on the pH, a pH of 8 was used for PAA and PAH films to prevent degradation of the zinc oxide nanorods and to ensure the desired thickness of the film. [167] For confocal studies, FITC was conjugated to PAH according to a literature procedure. [193] Briefly, 4.5 mg of FITC was dissolved in 1 mL of dimethyl sulfoxide (DMSO), which was then combined with 500 mg of PAH dissolved in 6 mL of water. The pH of the solution was adjusted to 8.4 with NaOH, and then the solution was stirred for 2 days. Dialysis was then performed using a D-tube Dialyzer for 24 h to remove excess FITC. [193] For ζ-potential measurements, a 100 μL aliquot of HPs was set aside after deposition of each layer, and 900 μL of water was added before each ζ-potential measurement was taken. The ζ-potentials were measured using a Malvern Zetasizer Nanoinstrument Nano ZS. Each value was averaged from three parallel measurements.

2.8.4 Confocal Microscopy

Bright blue PS HPs were dispersed in Lab-Tek Chambered #1.5 coverglass (155379 2 chamber) and imaged using a Nikon A1 confocal microscope with a 400 nm laser excitation wavelength. For imaging FITC-Labeled films, particles were immobilized on a glass coverslide using prolong Diamond and then imaged using a 488 nm wavelength. STED microscopy images were taken using a super resolution Leica SP8MP confocal STED microscope. For dispersion confocal images, particles were at a concentration of 0.05 mg/mL.

2.8.5 Electron Microscopy

Twenty microliters of sample was dispersed on a silicon wafer and then evaporated. Afterward, samples were sputter coated with gold using a SPI-Module carbon/sputter coater. Particles were imaged using a FEI Nova 200 Nanolab SEM and FEI Helios 650 Nanolab SEM/FIB. NPs and coating were imaged using a JEOL 3011 high-resolution electron microscope. For dispersion SEM images, particles were at a concentration of 0.05 mg/mL.

2.8.6 DLVO Calculations

DLVO pair potentials of AuNS were calculated using a core–shell model to estimate van der Waals and electrostatic repulsion forces. Full details of the calculation are included in the Supplementary information.

2.8.7 SERS Measurements

All Raman measurements were done using a Raman microprobe from Kaiser optical systems, Inc. A 785 nm laser was used (400 mW) with a total exposure time of 100 s. Samples were incubated on a shaker for approximately 20 h prior to measuring Raman spectra unless otherwise noted. Raman measurements were done with the Raman probe facing the side of a 10 mm path length quartz cuvette with a solution volume of 3.5 mL. For media samples, 2.625 mL of media was mixed with 0.875 mL of dye solutions and hedgehog particles in water. All Au-modified HP and bead samples contained 7 pmol of small AuNP, and AuNS samples had a seed concentration of 7 pmol of AuNP for each Raman measurement. Au_2-S HPs contained 0.035 pmol of large AuNP, and Au_2-SBeads contained 0.042 pmol of large AuNP measurement for each Raman measurement. The quantity of adsorbed AuNP was measured using the UV–vis spectrum of the supernatant after incubation with HP/Bead to determine gold loading in samples according to Haiss et al. (**Figure 2.12**). [192] For all samples, two layers of PSS with 0.5 M NaCl were adsorbed as final layers to ensure a negative surface charge to promote dye adsorption. Background correction for all Raman spectra was done with Origin 2016 Graphing and Analysis and asymmetric least-squares smoothing with an asymmetric factor of 1×10^{-4}, threshold of 0.001, and smoothing factor of 6.

2.8.8 Enhancement Factor Calculations

SERS enhancement factors are commonly defined using $EF = \frac{I_{SERS}/N_{surf}}{I_{RS}/N_{vol}}$ (1)where N_{vol} is the average number of molecules in the scattering volume for the Raman (non-SERS) measurement and N_{surf} is the average number of adsorbed molecules in the scattering volume for the SERS experiment. [194–196] While this can be characteristic for a traditional SERS substrate, it can be very difficult to measure for nanostructures because of the inability to determine the number of adsorbed dye molecules and amplification of the flaws in the equation with complex morphology such as nanorods. [197] Because measurements were done in solution, an analytical enhancement factor was calculated on the basis of the concentration using the equation: $EF = \frac{I_{SERS}/c_{SERS}}{I_{RS}/C_{RS}}$ (2) Analytical enhancement factors were calculated using the intensity corresponding to peaks at 1626 cm^{-1} for MB (C–C ring stretching) and 1365 cm^{-1} for R6G (aromatic C–C stretching). Dye controls for the enhancement factor were done at higher concentrations (1 mM for R6G and 10

μM for MB), which showed distinct peaks (**Figure 2.34, 2.35**). To improve accuracy, particles were incubated with dye at 1 μM with concentrations identical to those of SERS samples and the supernatant was collected, which was used to determine the concentration of the dye adsorbed based on λ_{max} values of 664 and 524 nm for MB and R6G, respectively. The percentage of dye adsorbed was then multiplied to give a final analytical enhancement factor.

2.9 Supplementary Information

Abbreviations	
SEM	Scanning Electron Microscopy
TEM	Transmission Electron Microscopy
LBL	Layer-by-Layer
PSS	Polystyrene Sulfonate
PDDA	Poly (diallyldimethylammonium chloride)
PAH	Poly (allylamine hydrochloride)
PAA	Polyacrylic acid
FITC-PAH	Fluorescein isothiocyanate labeled Poly(allylamine hydrochloride)
NP	Nanoparticle
HP	Hedgehog particle
Au_1HP	Hedgehog particles modified with PSS(PDDA/Au_{NP})
Au_2HP	Hedgehog particles modified with PSS(PDDA/Au_{NP})$_2$
Au_1-SHP	Hedgehog particles modified with PSS/PDDA/Au_{NP}) (0.5 M NaCl)
Au_2-SHP	Hedgehog particles modified with PSS/PDDA/Au_{NP}-small/PSS/PDDA/Au_{NP}-large) (0.5 M NaCl)
Bead	Carboxylated Polystyrene Bead
Au-SBead	Beads modified with (PDDA/Au_{NP}) (0.5 M NaCl)
Au_2-SBead	Beads modified with (PDDA/Au_{NP}-small/PSS/PDDA/Au_{NP}-large) (0.5 M NaCl)
AuBead	Gold-modified polystyrene bead
MB	Methylene Blue
R6G	Rhodamine 6G
DMEM	Dulbecco's Modified Eagle Medium
TSB	Tryptic Soy Broth
AuNS	Gold Nanostar(s)
PEG-SH	Thiol-Polyethylene glycol-Amine
MBA	4-Mercaptobenzoic Acid

2.9.1 Supplementary Results

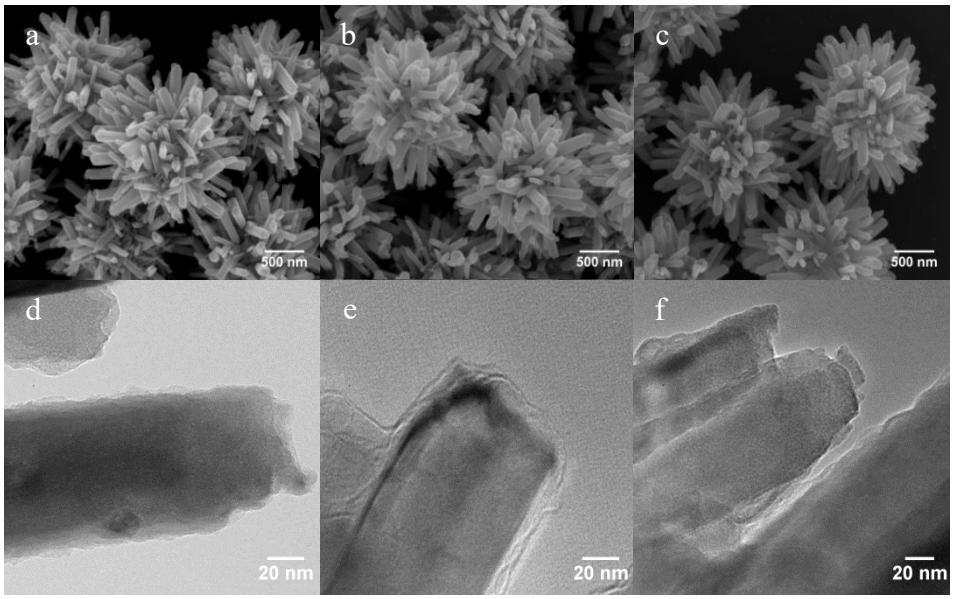

Figure 2.7: SEM and TEM images of HPs modified with $(PSS/PDDA)_n$ films: (**a,e**) $(PSS/PDDA)_2$, (**b,f**) $(PSS/PDDA)_3PSS$, (**c,g**) $(PSS/PDDA)_5$.

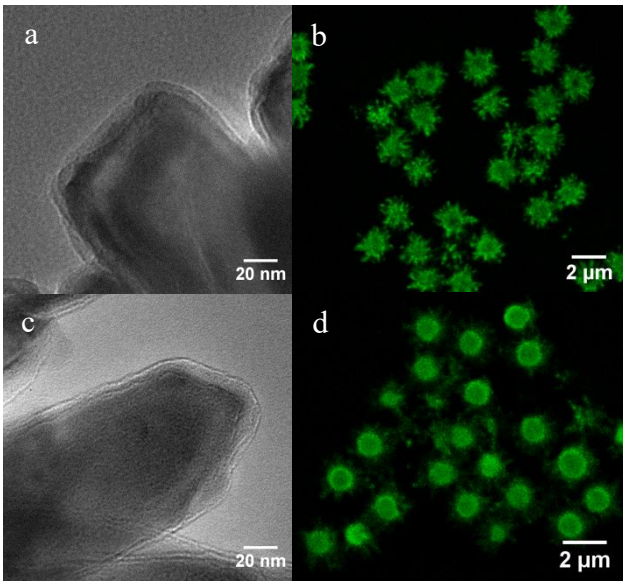

Figure 2.8: (**a,c**) TEM and (**b,d**) STED images of HPs modified with (**a,b**) $(PSS/FITC\text{-}PAH)_2$ and (**c,d**) $(PAA/FITC\text{-}PAH)_2$.

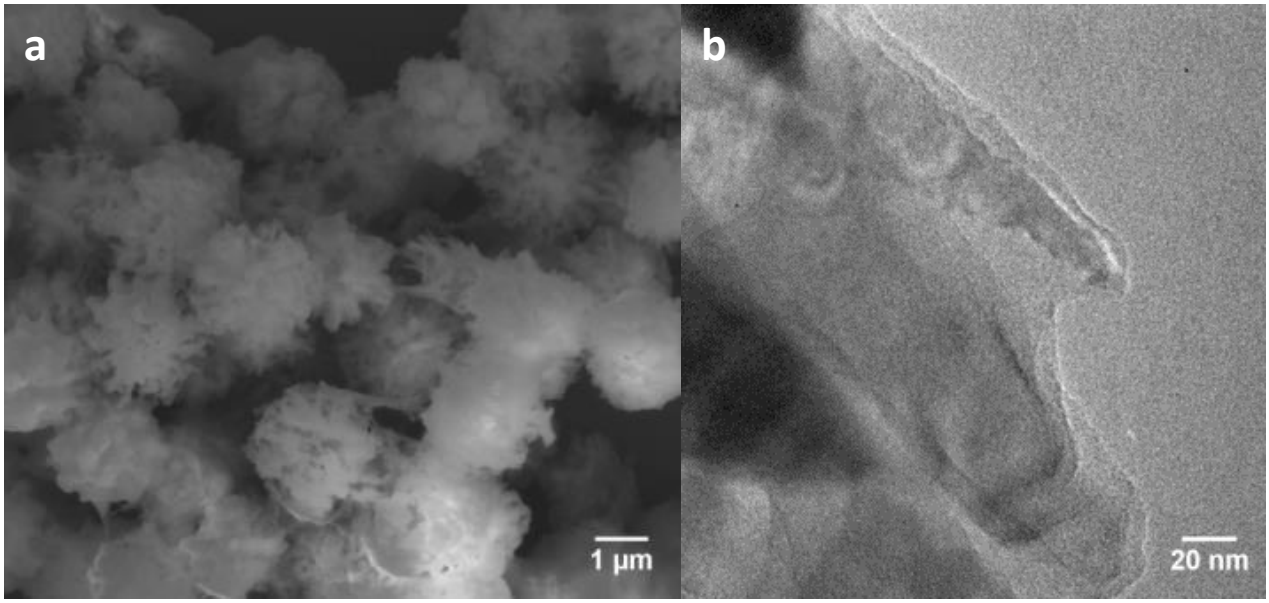

Figure 2.9: (**a**) SEM and (**b**) TEM images of HPs coated with $(PAA/PAH)_5$. Closing of the gaps between the spikes can be observed.

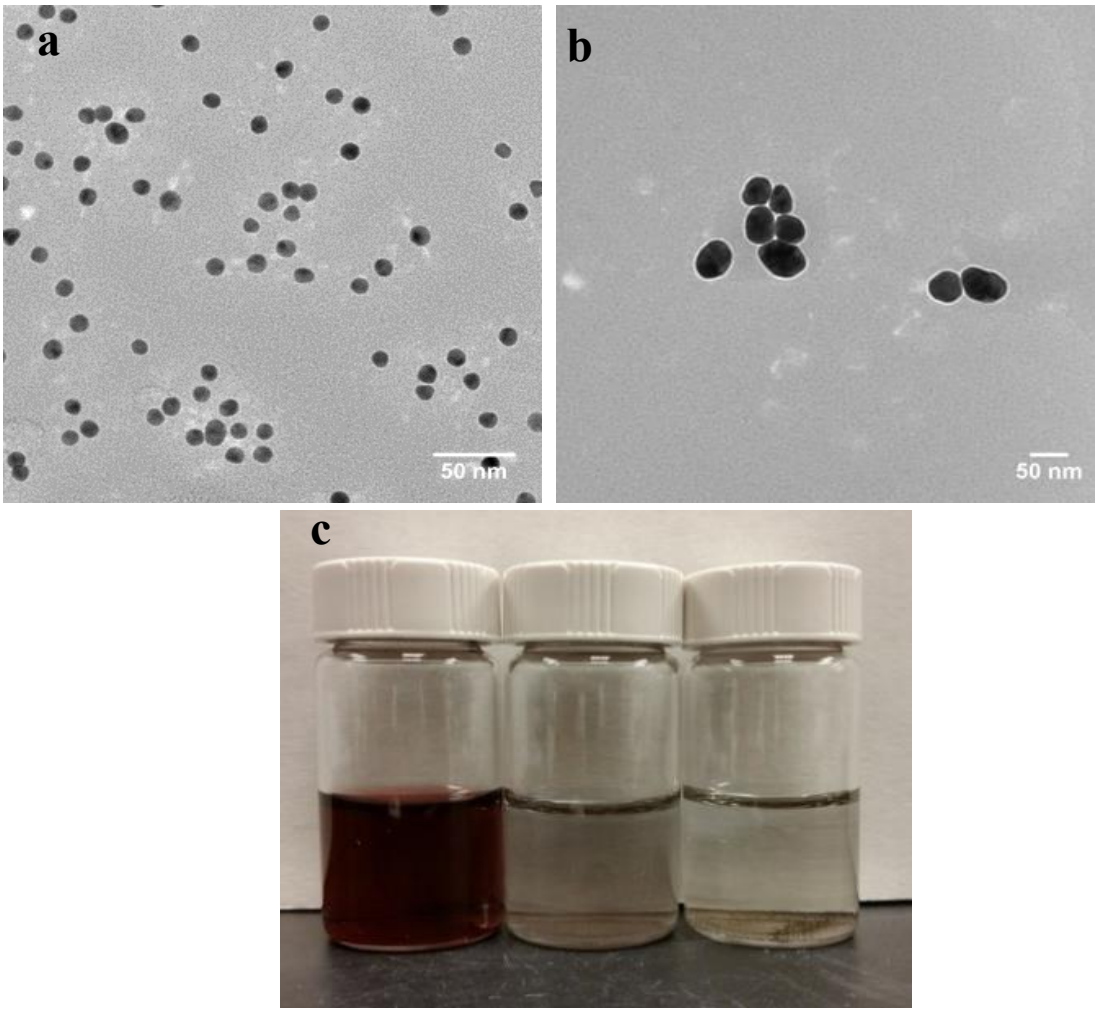

Figure 2.10: TEM images of (**a**) citrate-stabilized small Au NPs and (**b**) citrate-stabilized large Au NPs. (**c**) photographs of dispersion of Au NP with increasing NaCl concentration from left to right: 0 M, 0.1 M, and 1 M.

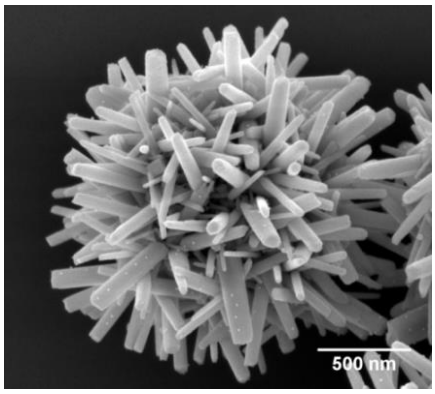

Figure 2.11: HPs after incubation with small Au NPs for 20 minutes without any polyelectrolyte LBL films to promote adhesion.

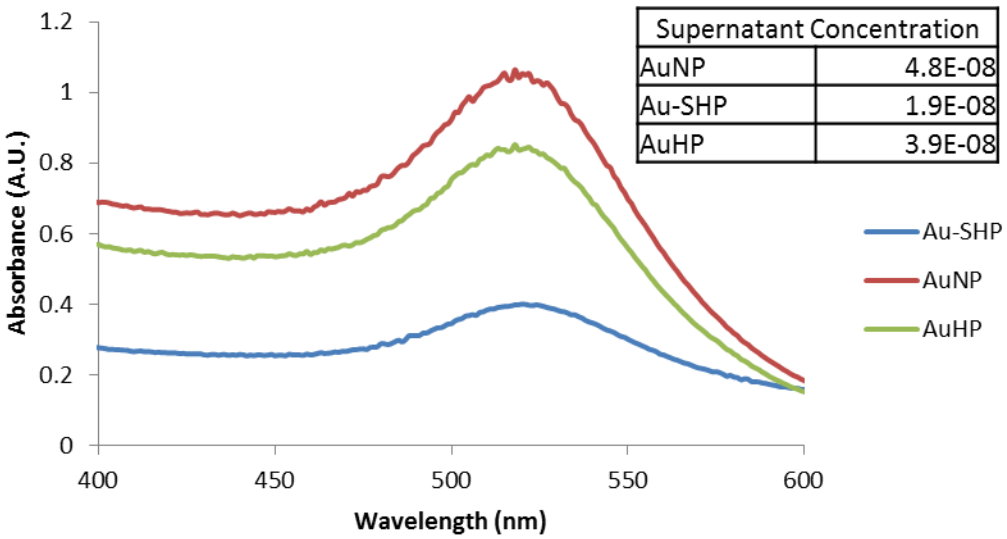

Figure 2.12: Au NPs (eightfold dilution) before and after incubation with HPs. Supernatant concentration was calculated using size and absorbance spectra.[192] AuHP, Au_2HP, and Au-SHP contained 12, 27, and 43 picomoles AuNP per mg HP, respectively. Au_2-SBeads contained 41 picomole AuNP per mg bead and 3.9 picomole large AuNP per mg bead. Au_2-SHP contained 2.7 picomole large AuNP per mg HP.

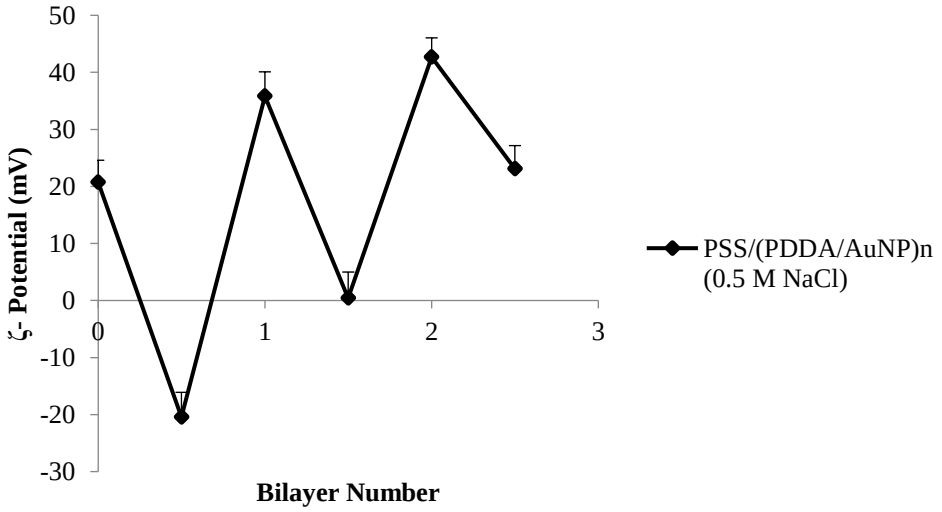

Figure 2.13: ζ-potential dependence on bilayer number for PSS $(PDDA/Au_{NP})_n$ (0.5 M NaCl) films on HPs. A much smaller drop in zeta potential is observed for adsorption of AuNPs on the second bilayer compared to $(PSS/PDDA/Au_{NP})_n$ (0.5 M NaCl) LBL films.

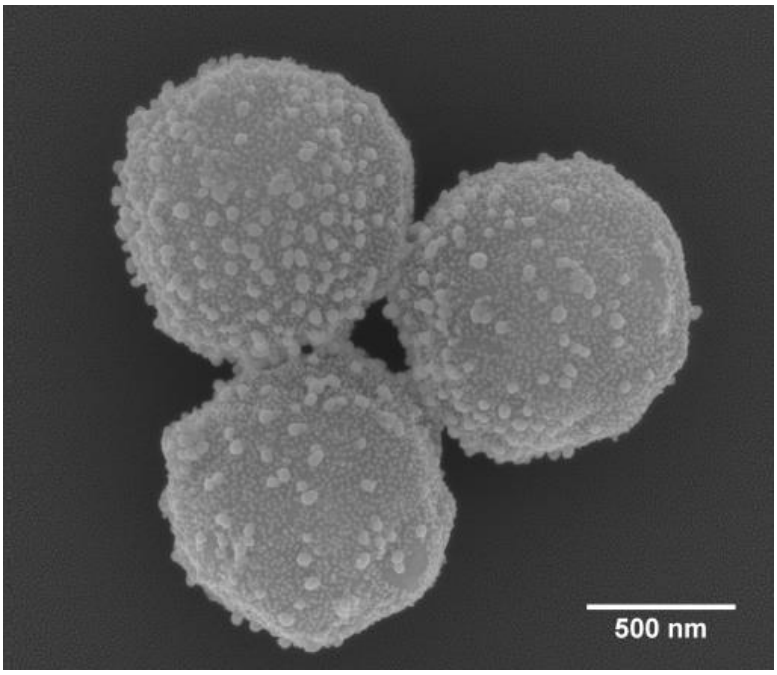

Figure 2.14: SEM image of Au_2-SBead**.**

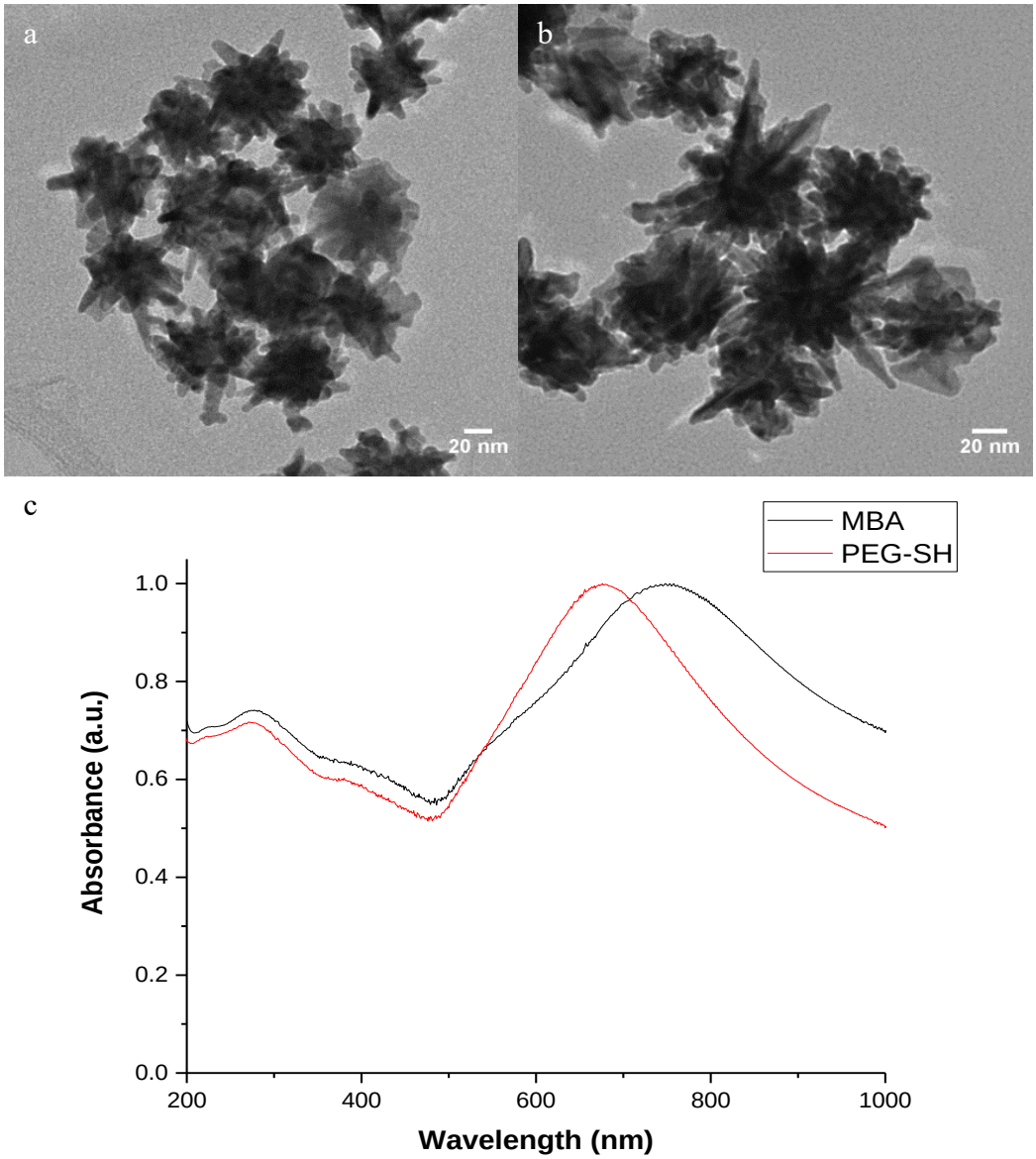

Figure 2.15: TEM Images of (**a**) AuNS capped with PEG-SH ligand and (**b**) AuNS capped with MBA ligand. (**c**) normalized absorbance spectra of AuNS with different ligands.

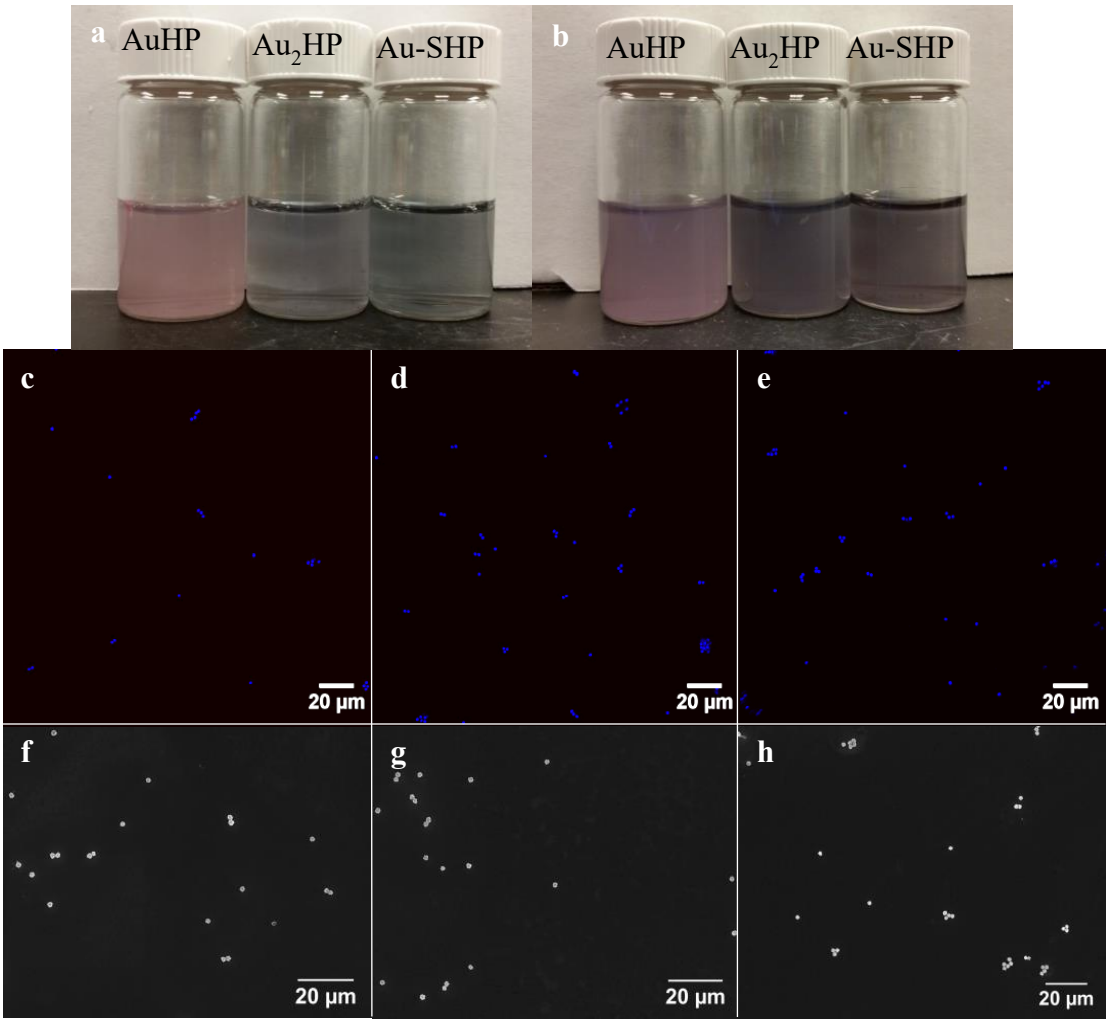

Figure 2.16: Photographs of dispersion of LBL-modified HPs (concentration 0.25 mg/mL) in (**a**) water and (**b**) 0.1 M NaCl from left to right: AuHP, Au_2HP, Au-SHP. Confocal with blue fluorescent core of dispersed (**c**) AuHP, (**d**) Au_2HP, (**e**) Au-SHP in water; SEM images of (**f**) AuHP, (**g**) Au_2HP, (**h**) AuHP-S in water.

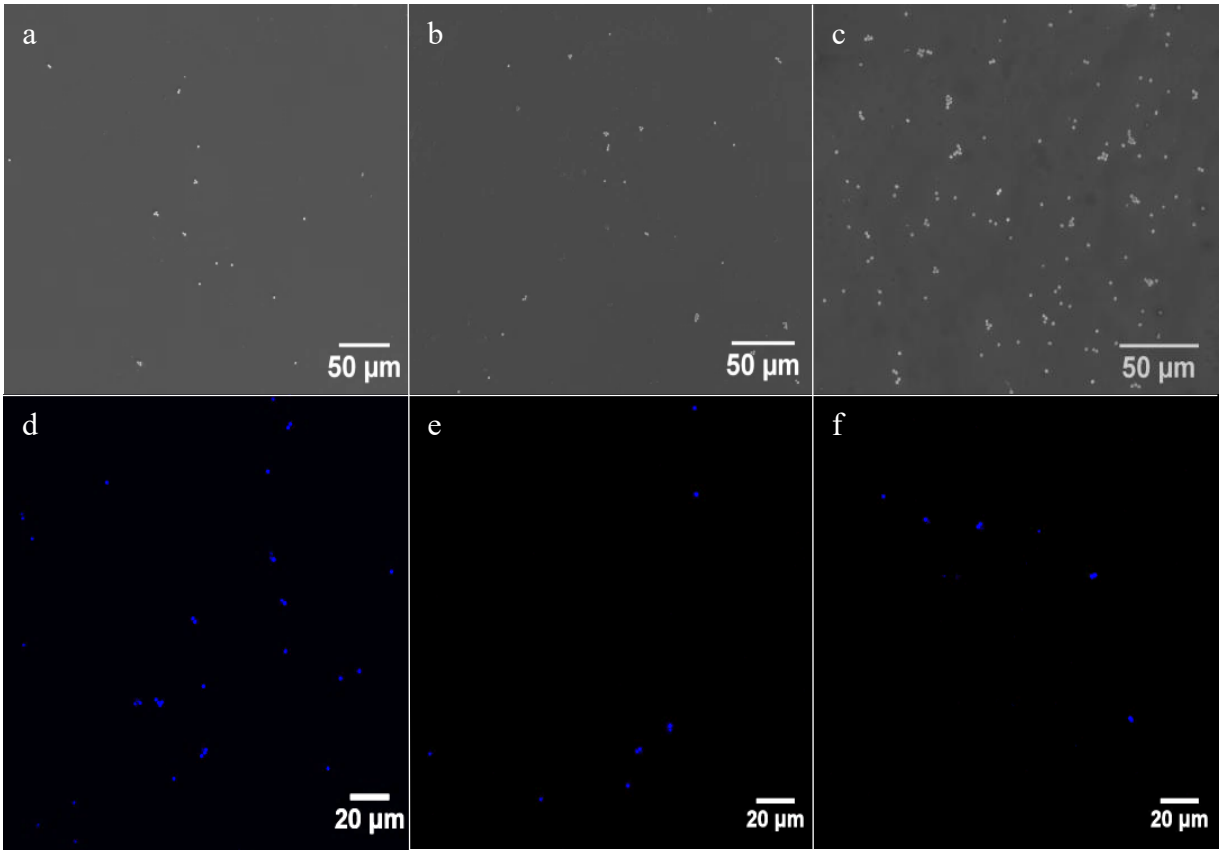

Figure 2.17: SEM and confocal microscopy with different blue fluorescent core HPs: (**a,d**) AuHP, (**b,e**) Au_2HP, (**c,f**) HP dispersed in heptane.

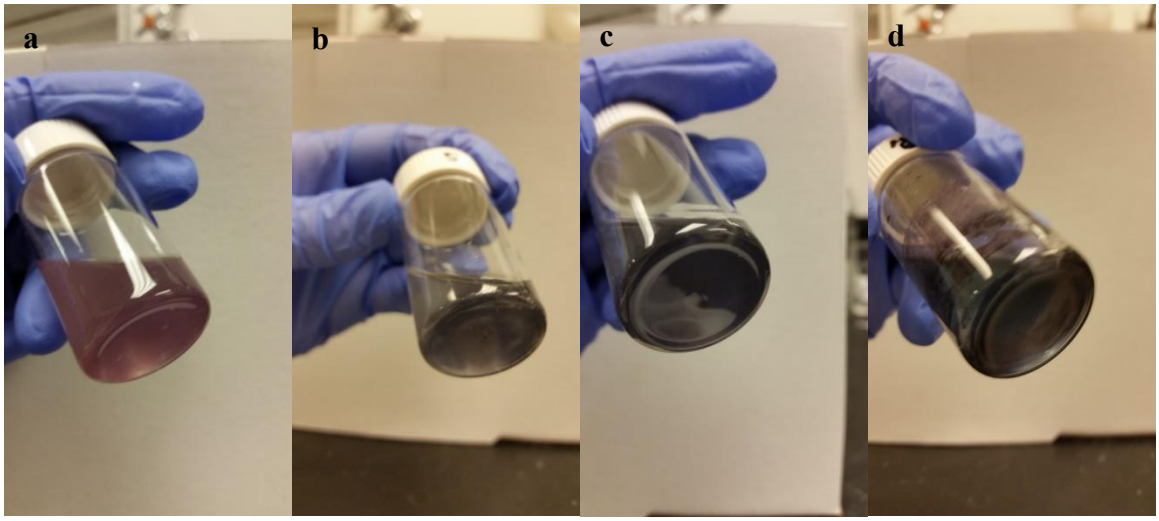

Figure 2.18: Photographs of dispersions of (**a**) AuHP, (**b**) Au_2HP, (**c**) Au-SHP, (**d**) Au-SBead in heptane (0.25 mg/mL)

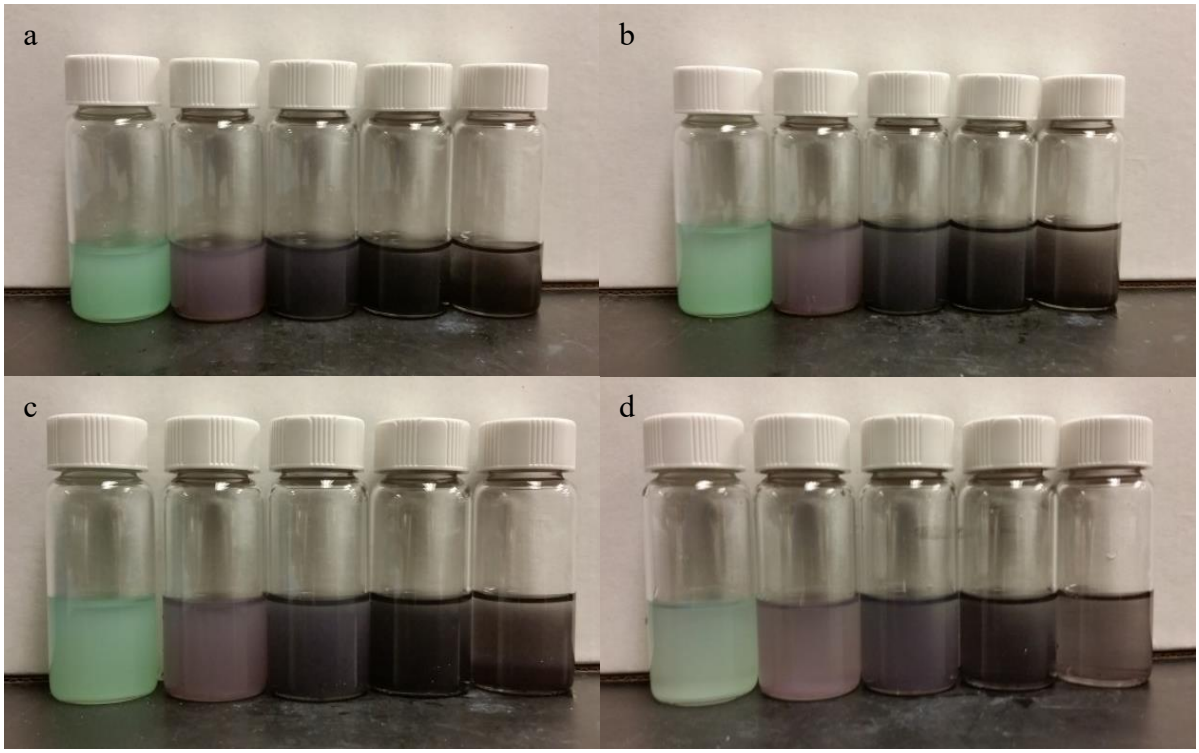

Figure 2.19: Photographs of dispersions of LBL-modified and non-modified HPs in heptane from left to right: HPs, AuHP, Au_2HP, Au-SHP, Au_2-SHP: 1 mg/mL (**a**) .75 mg/mL (**b**) .5 mg/mL (**c**) .25 mg/mL (**d**).

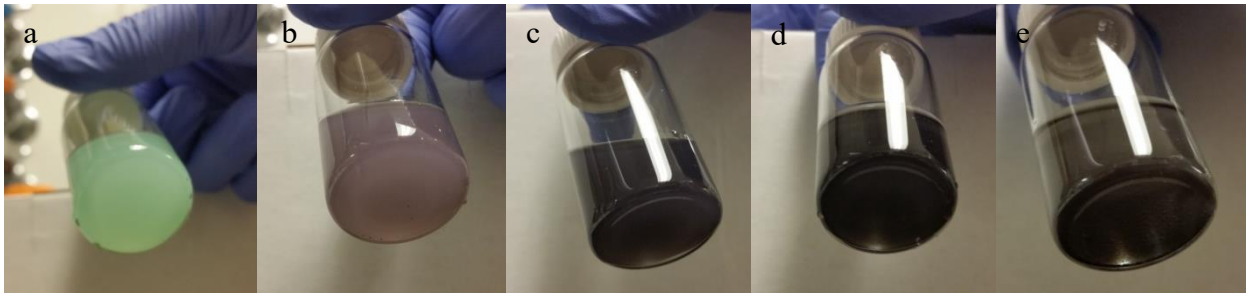

Figure 2.20: Photographs of dispersion of coated and non-coated HPs in heptane (0.75 mg/mL): HP (**a**) AuHP (**b**) Au_2HP, (**c**) Au-SHP, (**d**) Au_2-SHP (**e**).

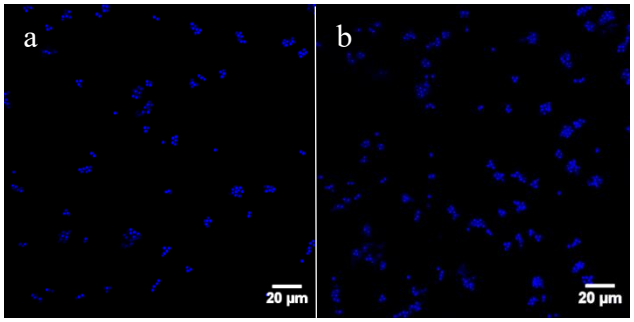

Figure 2.21: Confocal microscopy images of dispersed bright blue fluorescent core AuHPs (**a**) and Au_2HPs (**b**) in 1 M NaCl.

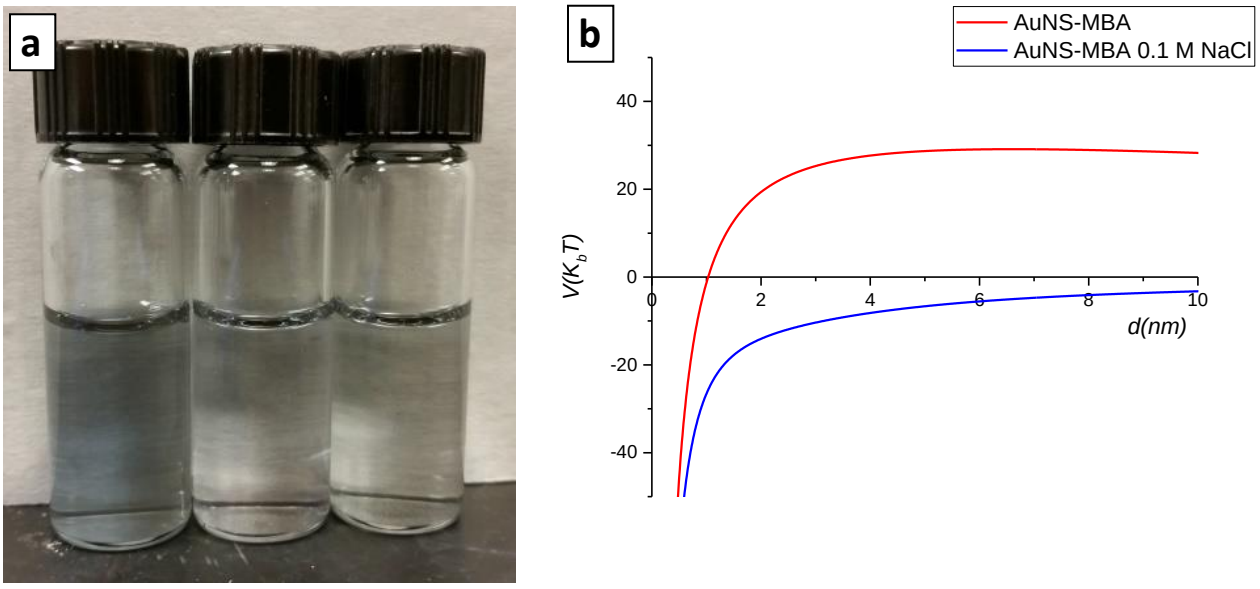

Figure 2.22: (**a**) AuNS capped with MBA dispersed in water at a concentration of 0.1 mg/mL: images from left to right: water, 0.1 M NaCl, 1 M NaCl. (**b**) DLVO pair potential of AuNS in water and 0.1 M NaCl.

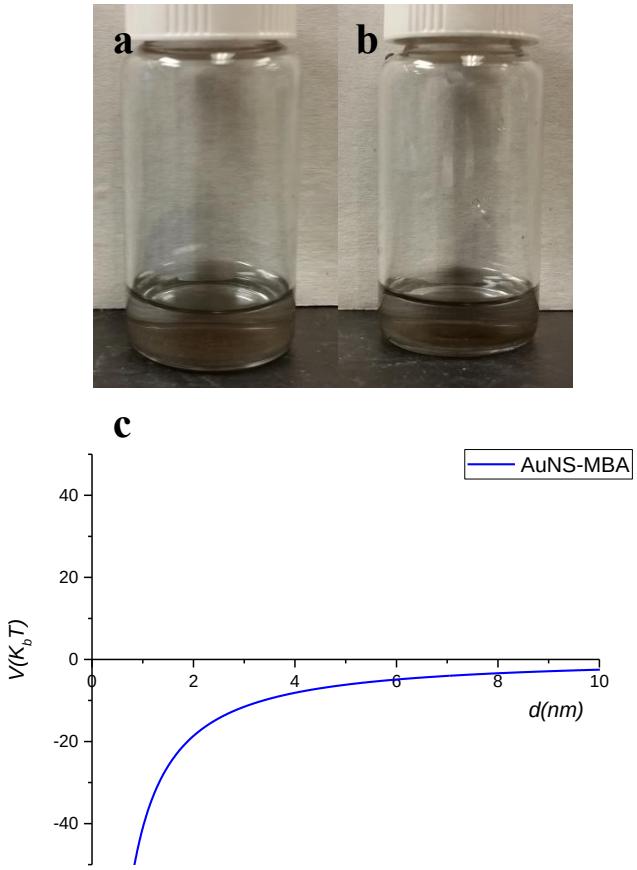

Figure 2.23: Images of AuNS capped with (**a**) PEG-SH and (**b**) MBA in heptane at a concentration of 0.2 mg/mL. (**c**) DLVO pair potential of AuNS dispersed in heptane**.**

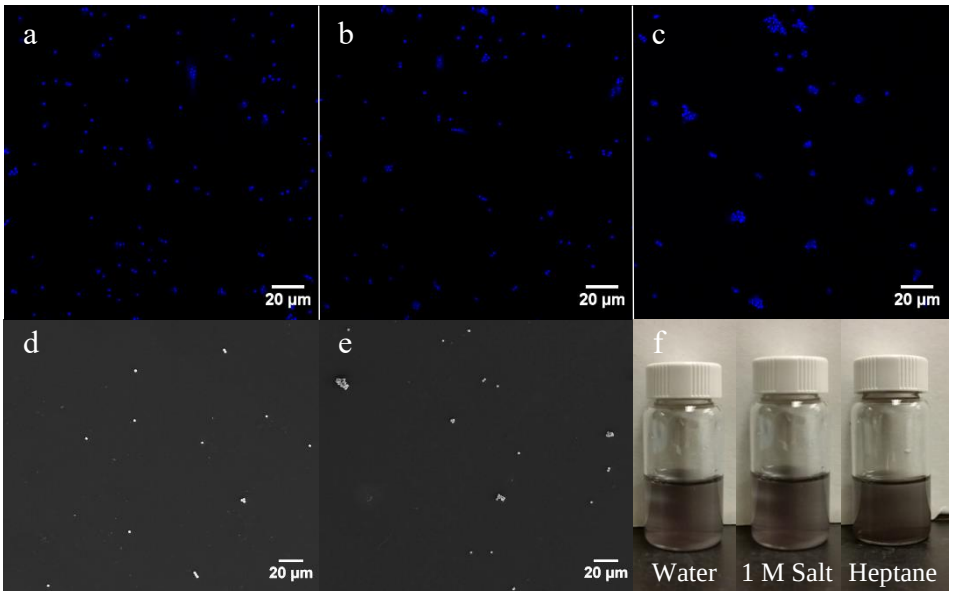

Figure 2.24: Confocal microscopy images of bright blue fluorescent core Au_2-SHP in (**a**) water, (**b**) 1 M NaCl, (**c**) heptane. SEM of Au_2-SHP in (**d**) water and (**e**) heptane; (**f**) image of dispersions (0.25 mg/mL) of Au_2-SHP from left to right: water, 1 M NaCl, and heptane

2.9.2 Additional Raman Scattering Results

All Raman experiments with coated HPs/Beads utilized a concentration of 2 nM of small AuNPs (12 ±1 nm). The concentration of larger AuNPs (39 ± 9 nm) with coated HPs/Beads was 0.01 nM for HPs and 0.0122 nM for Beads.

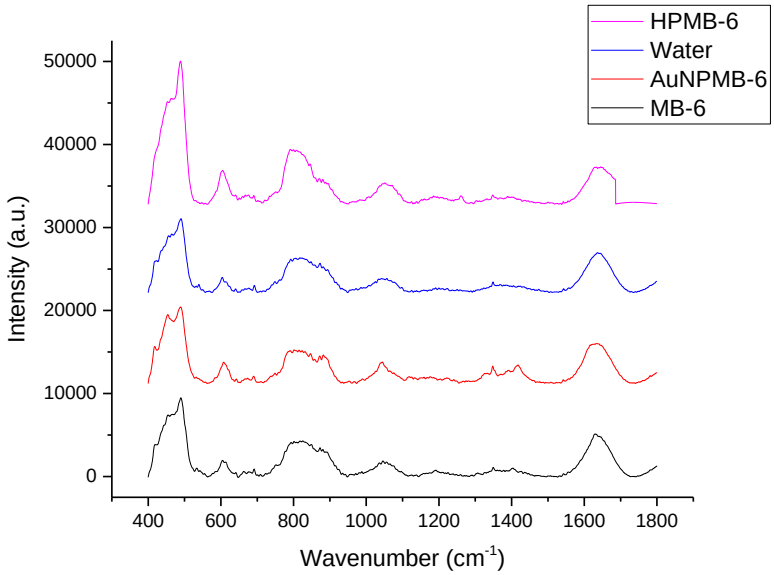

Figure 2.25: Background corrected control Raman scattering spectra with methylene blue (MB) concentration of 1 µM.

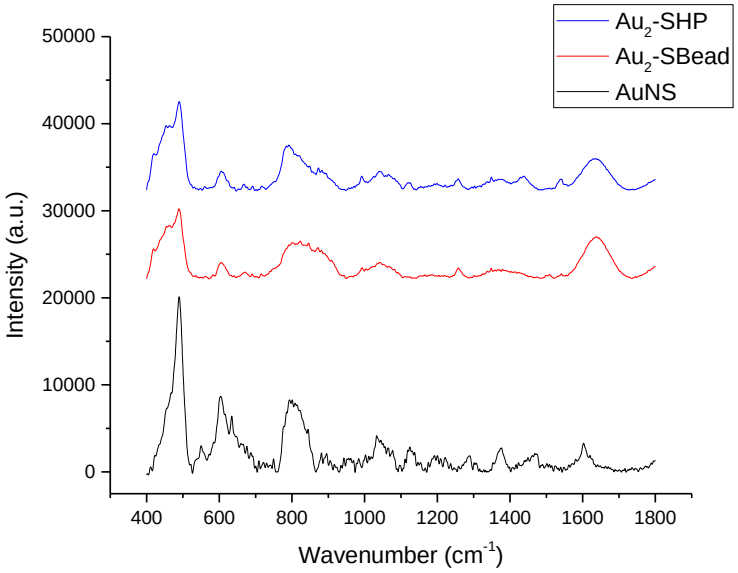

Figure 2.26: Background corrected control Raman spectra with no dyes.

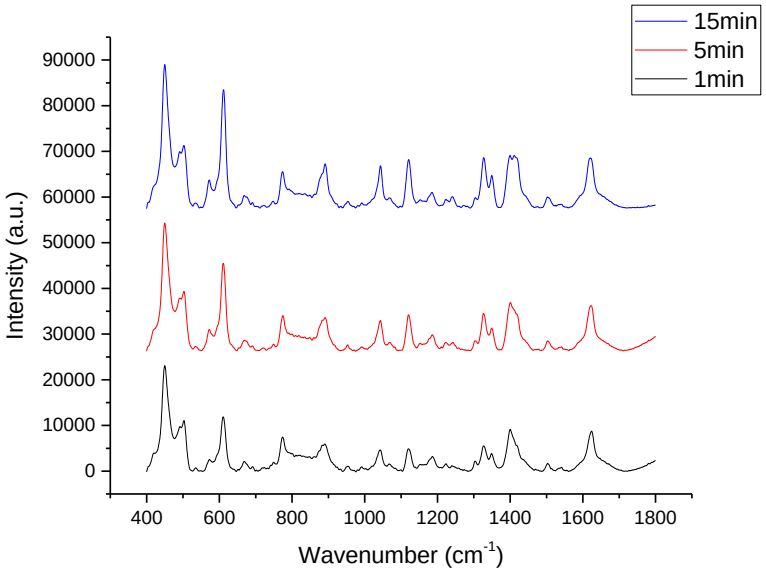

Figure 2.27: Background corrected Raman spectra of Au_2-SHP with MB concentration of 1 µM with various incubation times

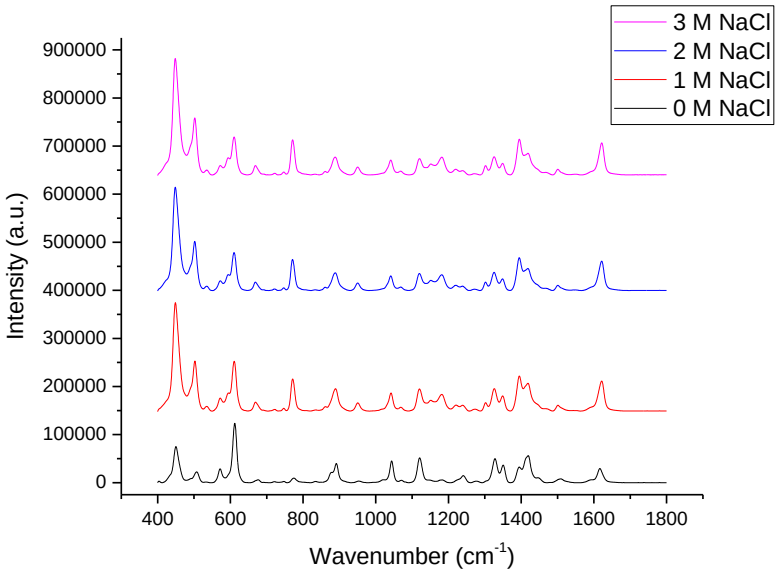

Figure 2.28: Background corrected Raman spectra of Au_2-SHP with MB concentration of 1 µM and various NaCl concentrations.

.

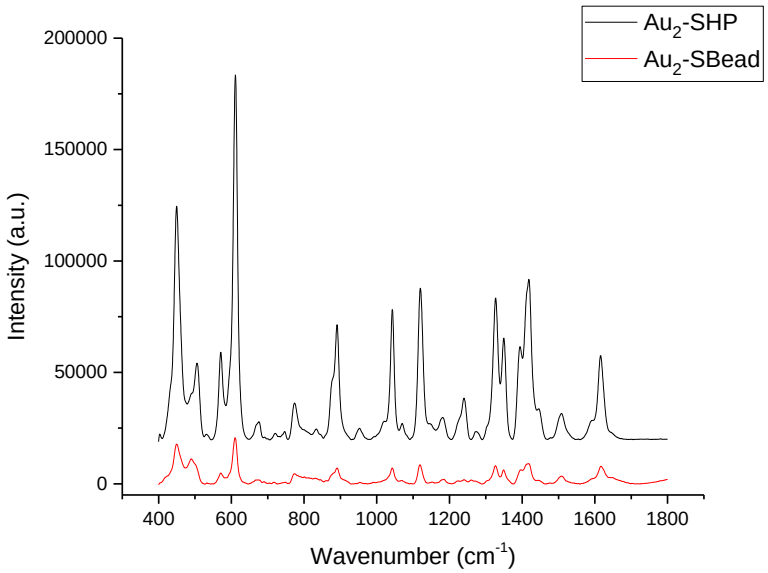

Figure 2.29: Background corrected Raman scattering spectra with MB and rhodamine 6G (R6G) concentration of 1 µM in water**.**

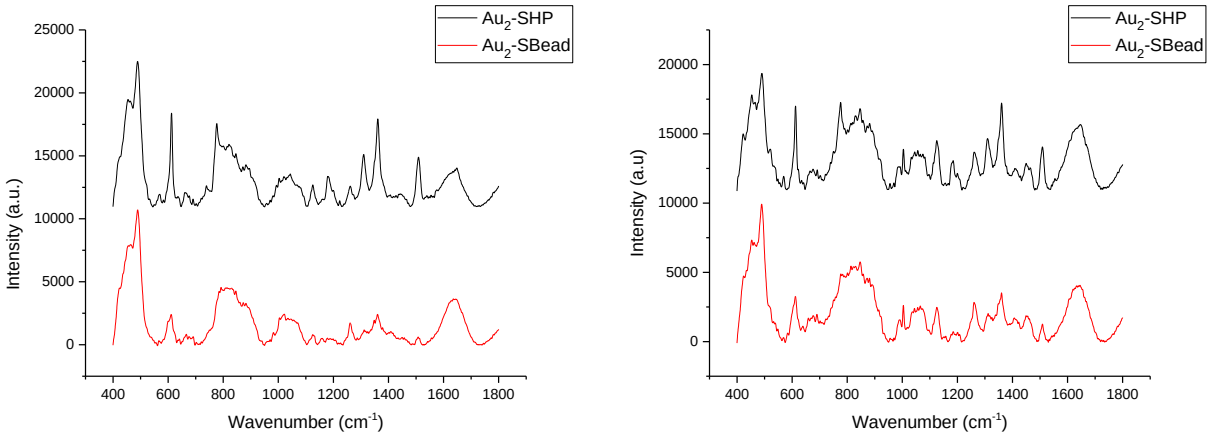

Figure 2.30: Background corrected Raman scattering spectra obtained with different SERS probes given in the graphs with MB concentration of 1 µM in DMEM (left) and TSB (right)

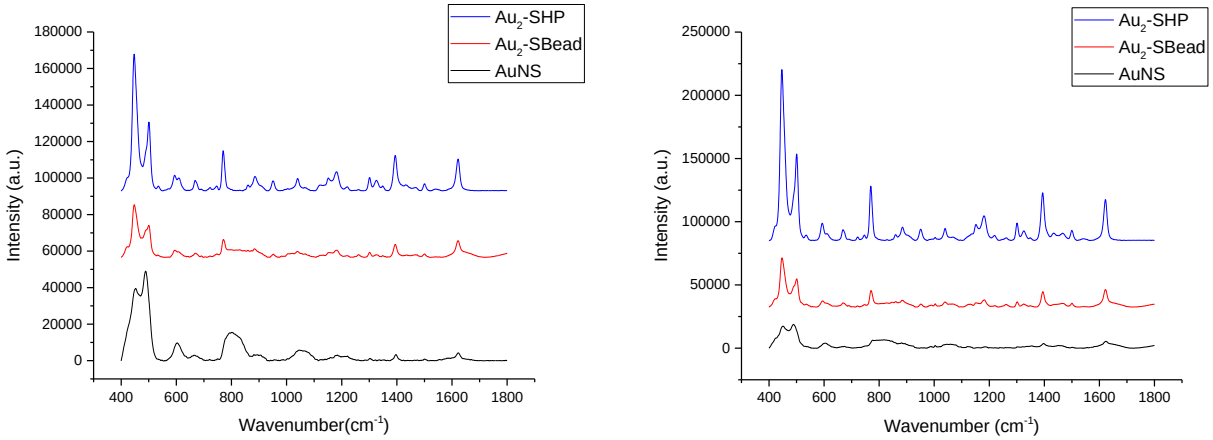

Figure 2.31: Background corrected Raman scattering spectra with R6G concentration of 1 µM in DMEM (left) and TSB (right)

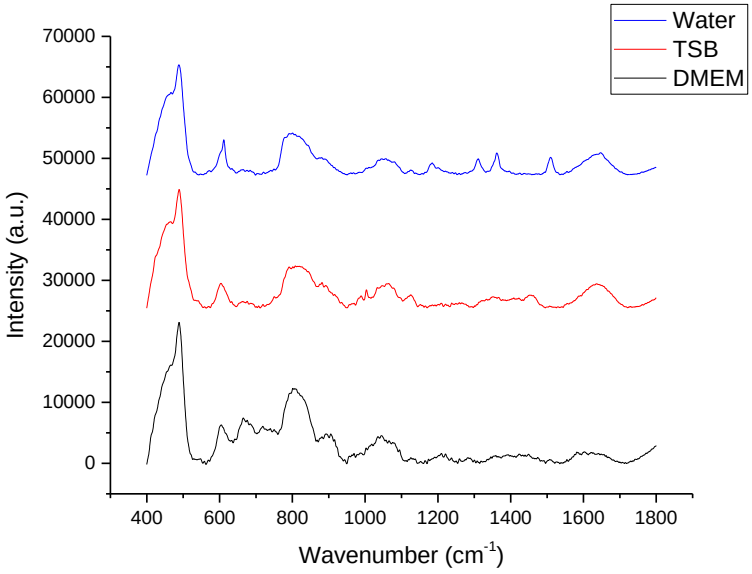

Figure 2.32: Background corrected Raman scattering spectra of AuNS stabilized with PEG-SH with R6G concentration of 1 µm in water, TSB, and DMEM

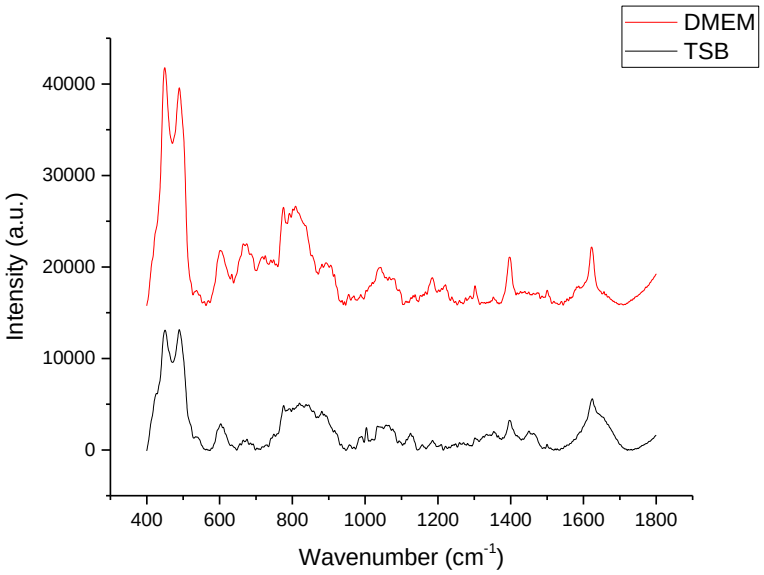

Figure 2.33: Background corrected Raman scattering spectra of AuNS stabilized with PEG-SH with R6G and MB concentration of 1 µm in DMEM and TSB**.**

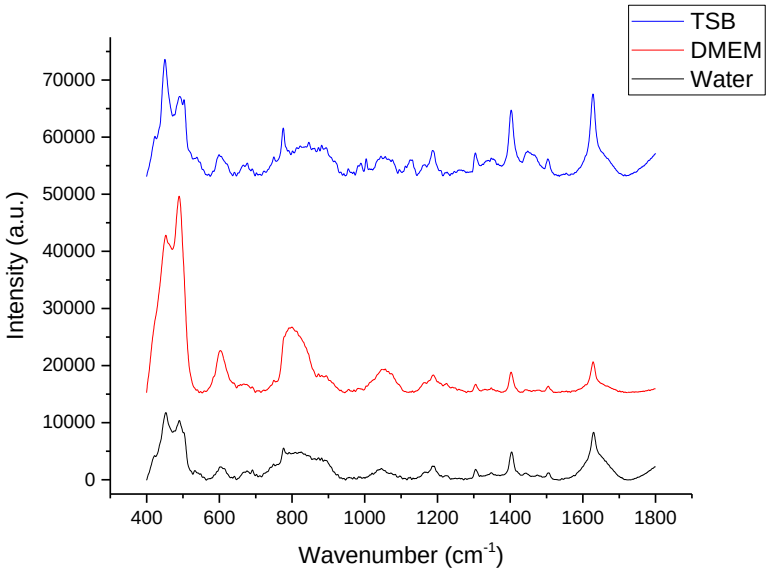

Figure 2.34: Background corrected Raman scattering spectra with MB concentration of 20 µM (TSB/DMEM) and 10 µM (water).

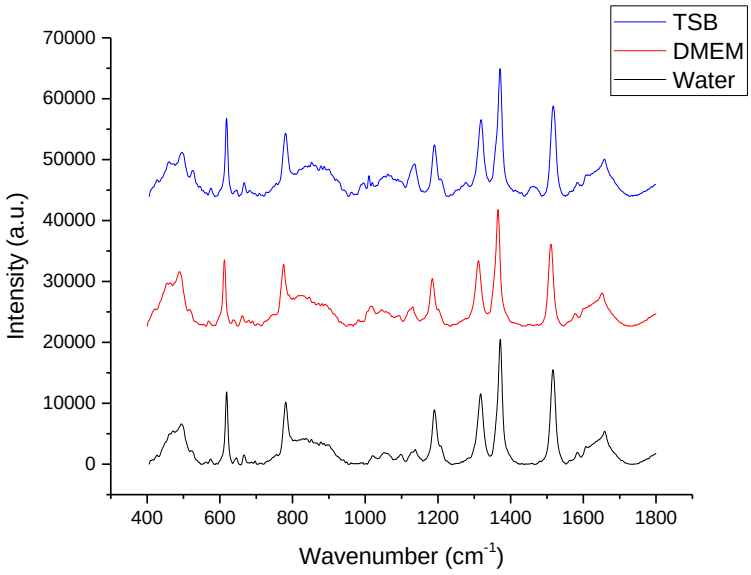

Figure 2.35: Background corrected Raman scattering spectra with R6G concentration of 1 mM.

2.9.3 Calculations of pair potentials for AuNS using DLVO Theory

The van der Waals attraction and electrostatic repulsion between the AuNS were analyzed using a core-shell approach. Nanostars were analyzed with a model AuNS with branches (N) with a branch base length (L_b), tip diameter (D_t), branch length (L_a), and sidewall length (L_s) and a gold core with diameter D_c according to Vo-Dinh et al.[198]

For the core-shell approach, a gold core equivalent to D_c and a shell with a homogeneous distribution of gold and solvent based on the number and dimensions of the branches was used.The van der Waals potential of the AuNS were approximated as additive contributions of London dispersion forces between a spherical gold core capped with a shell consisting of solvent/gold. The overall diameter and branch dimensions were used to determine the volume fraction of gold present φ_g. AuNS were analyzed as a frustum of a right circular cone with a spherical tip.

$$V_c = \frac{\pi}{12}\left({D_T}^2 + L_b D_t + {L_b}^2\right)\left(L_a - \frac{D_T}{2}\right)$$

$$\varphi_g = \frac{N\left(V_c + \frac{\pi {D_t}^3}{12}\right)}{\frac{\pi {D_s}^3}{6} - \frac{\pi {D_c}^3}{6}}$$

$$V_{VdW} = V_{VdW,shell} + V_{VdW,core} + V_{VdW,core-shell} + V_{VdW,shell-core}$$

Where V_c is the volume of the frustum of a right circular cone representing the volume of the branch of the AuNS and D_s refers to the overall spherical diameter encompassing the full nanostar (hydrodynamic size was used as an estimate for this diameter).

$$V_{VdW,shell} = -\frac{A_{232}H_{shell}(x,y)}{12} : x = \frac{d}{(D_c + 2L_a)}, y = 1$$

$$V_{VdW,core} = -\frac{A_{131}H_{core}(x,y)}{12} : x = \frac{d + 2L_a}{D_c}, y = 1$$

$$V_{VdW,core-shell} = -\frac{A_{132}H_{core-shell}(x,y)}{12} : x = \frac{d + L_a}{D_c}, y = \frac{D_c + 2L_a}{D_c}$$

$$V_{VdW,shell-core} = -\frac{A_{132}H_{shell-core}(x,y)}{12}\ x = \frac{d + L_a}{D_c + 2L_a}, y = \frac{D_c}{D_c + 2L_a}$$

The Hamaker function[199] of the core-shell is given by

$$H(x,y) = \frac{y}{(x^2+xy+x)} + \frac{y}{(x^2+xy+x+y)} + 2\ln\left[\frac{(x^2+xy+x)}{(x^2+xy+x+y)}\right]$$

L_a represents the thickness of the shell layer as it is the length of the nanostar branches.

$A_{131} = 3 \times 10^{-19}$ J (Hamaker constant for gold-water-gold interaction)[200].

$A_{33} = 3.72 \times 10^{-19}$ (Hamaker constant for water)[201]

$$A_{132} = A_{131}\varphi_g + (1 - \varphi_g)A_{33}$$

$$A_{232} = \sqrt{A_{131} \times A_{33}}$$

For heptane calculations

$A_{33} = 4.03 \times 10^{-19}$ (Hamaker constant for heptane)[202]

Electrostatic potential

The electrostatic interactions between the AuNS can be evaluated using the Poisson-Boltzmann formalism as follows[203]

$$V_{DL} = 4\pi\varepsilon_0\varepsilon_r {D_s}^2 \Gamma^2 (\frac{k_b T}{e})^2 \frac{\exp(-\kappa d)}{d + 2D_s}$$

$$\Gamma = \frac{8 \times \tanh(\frac{e\Psi_{Auns}}{4k_b T})}{1 + \sqrt{1 - \frac{2\kappa D_s + 1}{(\kappa D_s + 1)^2} \tanh \frac{e\Psi_{Auns}}{4k_b T}}}$$

Where ε_0 is the permittivity of vacuum, ε_r is the dielectric constant of water, e is electric charge (C) and Ψ_{Auns} is the zeta potential of AuNS coated with MBA in water (experimentally measured Ψ_{Auns} =-35 mV). κ represents the reciprocal double layer thickness and is given by

$$\kappa = \sqrt{\frac{1000 N_A e^2}{\varepsilon_0 \varepsilon_r k_b T} \Sigma_i M_i x {Z_i}^2}$$

where N_A is Avogadro's number, M_i and Z_i are the molar concentration and valency of ions. The practical Debye length of water was taken as κ^{-1}=100nm.[204] For heptane a Debye length of 960 nm was assumed based on that of pure water due to minimal presence of ions.[205]

Chapter 3

Photocatalytic Hedgehog Particles for High Ionic Strength Environments

Douglas Montjoy[1], Joong Hwan Bahng[1,2], Aydin Eskafi[1], Harrison Hou[1], Ruiyu Jiang[1], Nicholas A. Kotov[1-4]

[1]Department of Chemical Engineering, University of Michigan, Ann Arbor, Michigan 48109, USA;
[2]Department of Biomedical Engineering, University of Michigan, Ann Arbor, Michigan 48109, USA;
[3]Department of Materials Science, University of Michigan, Ann Arbor, Michigan 48109, USA;
[4]Biointerfaces Institute, University of Michigan, Ann Arbor, Michigan 48109, USA;
*E-mail: kotov@umich.edu

3.1 Abstract

High ionic strength environments can strongly influence catalytic reactions involving charged species. However, this method to control reaction selectivity and yield is rarely used for dispersible heterogeneous catalysts because high ionic strength leads to their coagulation. Here we show that hedgehog particles (HPs) made from microscale SiO_2 cores and ZnO nanorods forming radial spikes display colloidal stability in 0.25-2M solutions of monovalent and divalent salts in aqueous and nonaqueous media. While other nano/micro particles coagulate in these conditions, the photocatalytic activity of HPs is enhanced compared to ZnO nanorods. High salt media also increases the yield of benzaldehyde by six times from the photooxidation of 2-phenoxy-1-phenylethanol by HPs. Additionally by varying the salt concentration/composition, the yield of 2-phenoxyacetophenone is enhanced by 10 times. The increased stability of HPs in high ionic

strength environments can be used to engineer different reaction pathways in multitude of redox reactions catalyzed by inorganic colloids

3.2 Introduction

High ionic strength environments strongly alter electrostatic and other interactions of ions, charged molecules, particles, and polymers, which can be theoretically utilized to improve both selectivity and yield of many catalytic reactions.[206–208] Screening of electrostatic forces affords engineering the reaction pathways by varying repulsion and attraction or reactants and relative energy levels of the intermediate states. For instance, high ionic strength environment accelerates electron transfer from ascorbic acid to hexacyanoferrate by reducing electrostatic repulsion between reactants.[104] High concentrations of electrolytes are known to lower activation barriers and increases ethylene yield in CO_2 reduction[105] as well as other products.[209,210] Concentrated electrolytes based on alkali-metal cations were empirically found to increase the yield of C-C coupling on CuO_x electrodes.[106] While the mechanistic details in these reactions often remain uncertain, these examples indicate that high ionic strength environment make a big impact on catalytic processes essential for sustainable economic development. Importance of exploration of high salt conditions specifically for photocatalysis is punctuated by the need to design catalysts for many environmental processes, brine treatment, and oil spill mitigation.[107]

Ionic strength effects can be particularly strong for heterogeneous catalysts due to the high electrostatic fields (~10^9 V/m) produced in the double layers at solid-liquid interfaces.[211,212] However, switching between different reaction pathways by ionic strength is seldom possible for heterogeneous catalysts because dispersed particles rapidly aggregate under high salinity conditions.[108] Furthermore, agglomeration reduces accessibility of their surface drastically reducing their catalytic activity and efficiency.[109,114] In order to achieve dispersion stability, particles may be coated by organic ligands that reduces clumping.[1,4,213] However, the chemical "camouflage" with surfactants, organic tethers, or adsorbed polymers required for dispersion of particles in high salinity media,[1,6,10] passivates their surface and greatly diminishes substrate's accessibility to catalytic sites.[8,126,214]

A few years ago, it was found that the addition of stiff nanoscale spikes to microscale particles leads to marked reduction in van der Waals (vdW)forces between them.[15] This finding

made possible designing particles with the ability to disperse in the different types of media where smooth particles cannot. For example, the spiky hydrophilic particles were able to disperse in hydrophobic media. The same was true for particles carrying hydrophobic spikes in water. Reduction of the vdW forces also extended the range of colloidal stability of spiky colloids in high ionic strength conditions such as 1 M NaCl when spherical colloids agglomerate.[15,215] These spiky colloids, referred to as 'hedgehog' particles (HPs), consisted of a micron-sized polystyrene core surrounded by stiff nanoscale zinc oxide (ZnO) spikes. While HPs can be made from different semiconductors,[216,217] having the spikes made from metal oxide is important in the context of catalysis. ZnO is a potent photocatalyst with the direct bandgap of 3.0-3.3 eV, which makes light adsorption in the near-UV segment of the solar spectrum efficient.[218–220] The high crystallinity of ZnO nanorods (NRs) forming the spikes also reduces the density of trap states[75,77] detrimental for electron-hole separation. These colloidal, optical, and electronic properties of ZnO-based HPs make them promising heterogeneous catalysts for both hydrophobic and hydrophilic substrates in both organic and inorganic media.[221,222] High ionic strength environments open a theoretical possibility to avoid the total photoxidation of organic substrates to CO_2 [74,75,223] , that is typically dominant for ZnO and TiO_2 nanoscale catalysts, and can 'tune' the reaction pathway toward high value products.

One of the most challenging catalytic reactions is the oxidative valorization of lignin for the sustainable production of chemical feedstocks in the future.[224–226] Lignin constitutes ~20% of lignocellulosic biomass and represents the most abundant renewable source of aromatic compounds.[227] Cleavage of β-O-4 bonds is of particular importance as it comprises 50–60% of all the C–O linkages in lignin.[224] In this study, we show that HPs display phocatalytic activity of higher than individual ZnO NRs in both aqueous and organic media. Investigating the HP-mediated photooxidation of a lignin model compound with a β-O-4 bond, we demonstrate that high ionic strength drastically increases the yield of benzaldehyde and 2-phenoxyacetophenone depending on the chosen electrolytic environment.

3.3 Synthesis and Characterization of HPs with SiO_2 cores

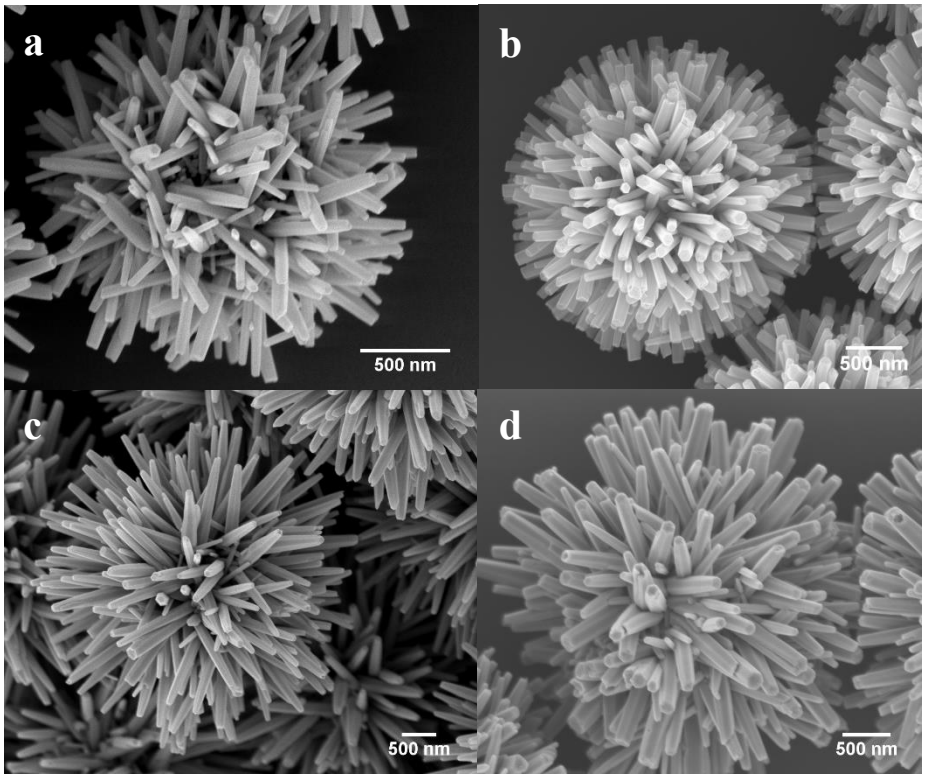

Figure 3.1: SEM images of shorter length SiO_2 HPs, (**a**) HP_{S1}, (**b**) HP_{S2} and longer length HPs: (**c**) HP_{L2}, (**d**) HP_{L1}. Synthesis conditions and measured spike parameters are listed in **Table 3.1** and a schematic of the synthesis in **Figure 3.7.**

In the past, HPs were synthesized based on organic poly(styrene) beads that were unstable in some organic solvents and under high temperature often needed for catalysis. To increase robustness of HPs, we made the spiky particles with SiO_2 cores (**Figure 3.6**)[228]. In brief, ZnO NPs were self-assembled onto SiO_2 microparticles with a diameter of 1.1 μm using layer-by-layer assembly (LbL).[26] Hydrothermal growth of ZnO nanorods in ultrasound field initiated by ZnO NPs (**Figure 3.7**) resulted in HPs with uniform spike density, shape, and size (**Figure 3.1**, **Figure 3.8, Figure 3.9**).

By altering the precursor concentration and sonication settings, the length and width of the nanospikes can be varied and adapted to reaction conditions of specific catalytic processes.[190] **Table 3.1** summarizes the different HP geometries that were synthesized. Among them, HPs with relatively short spike lengths of 482±63 nm and 758±56 nm combined with a relatively narrow spike widths of 58±14 and 72±17 will be denoted as HP_{S1} and HP_{S2}, respectively. HPs with relatively long spikes 1545±240 and 1864±122 combined with wider spikes with cross-sectional dimension of 166±27 and 146±25 nm, will be denoted as HP_{L1} and HP_{L2}, respectively **(Table 3.1**,

Figure 3.1). Free ZnO NRs (**Figure 3.10)** synthesized along the formation of HP_{s2} with a spike length 718 nm and a diameter of 95 nm were used as a benchmark for dispersion stability and catalytic activity. They displayed an electrokinetic zeta potential of 13.0±3.5 mV while HPs had a zeta potential of -11.6±4.1 mV.

3.4 Dispersion Stability and Optical Characterization

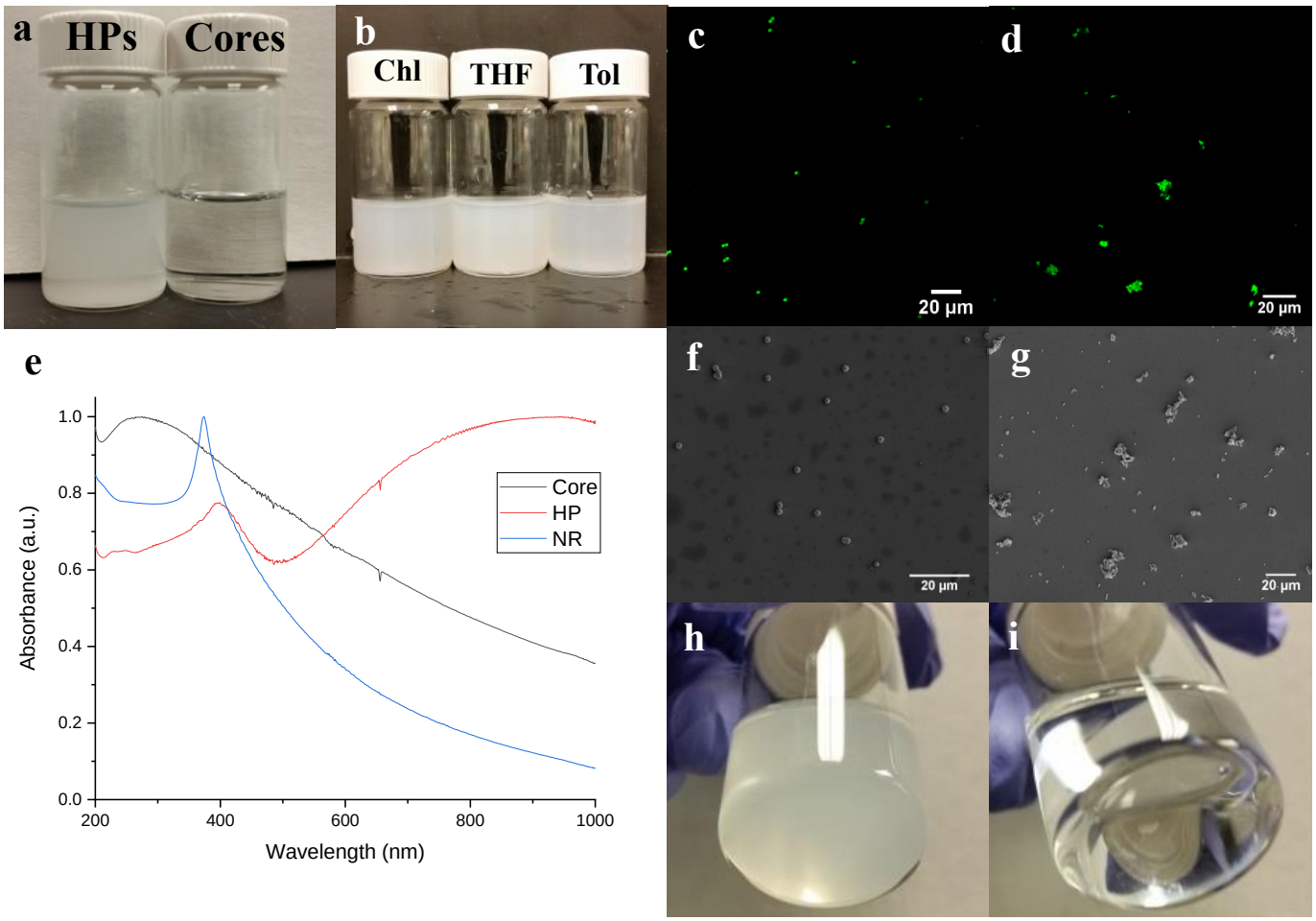

Figure 3.2: Photographs of dispersions of (**a**) SiO_2 HPs and SiO_2 cores in heptane and of SiO_2 HPs in chloroform (Chl), tetrahydrofuran (THF), and toluene (Tol) (**b**) (0.5 mg/mL). Confocal microscopy and SEM images of 0 dispersion respectively of SiO_2 HP (**c,f**) and SiO_2 cores (**d,g**) dispersed in heptane (0.1 mg/mL). Normalized UV-Vis absorbance spectrums of SiO_2 core (black), SiO_2 HPs (red), and NRs (blue) (**e**) Photograph of sediments of SiO_2 HP (**h**) and SiO_2 core in heptane (**i**) after 1 minute.

HPs with SiO_2 cores were expected to show similar dispersion stability as HPs made from poly(styrene) beads due to the presence of spikes.[15] Indeed, HP_{S2} form stable dispersions in heptane while the correspondent core materials do not disperse (**Figure 3.2**). This is confirmed with SEM images which show individual particles and no aggregation while core particles without

the spikes show visible aggregates (**Figure 3.2**). Confocal microscopy further supports the conclusion that SiO_2 HPs are well-dispersed in heptane while undecorated cores are not (**Figure 3.2**). Optical spectra of HPs featured a strong broadband scattering band between 700 and 1000 nm, which differentiates them from freely dispersed constituent ZnO NRs. On the other hand, the optical spectra in the UV range attributed primarily to the bandgap excitation of the semiconductor are similar for HPs and free NRs (**Figure 3.2e**). Absorbance spectra of HPs based on SiO_2 cores are nearly identical to those with polystyrene cores, indicating that the halo of the spikes in radial arrangement dictate the optical properties of HPs.

The advantages of the SiO_2 core include compatibility with a variety of organic solvents incompatible with polystyrene: toluene, chloroform, and tetrahydrofuran. Besides minimal aggregation in all three solvents, one may also find in SEM images of particles after this exposure that their geometry and morphology remains intact even after prolonged incubation (**Figure 3.2, 3.11**) when polystyrene dissolves. In addition, the SiO_2 HPs show no change in structure and morphology after calcining at 500°C (**Figure 3.12**). Thermogravimetric analysis further supports this observation with HPs retaining over 90% of their mass after heating to 600° C in air. For reactions in complex environments, calcining of the material would ensure that polymer stability does not restrict activity.

Unlike other nanoscale and microscale particles, HPs form stable dispersions in 1M NaCl solution in water, which was confirmed by confocal microscopy (**Figure 3.13**). While NRs appear to disperse in 1 M NaCl, aggregates are observed in confocal microscopy (**Figure 3.13**). A significant increase of NR aggregates in size and numbers was observed in aqueous media at 2 M NaCl media in particular at higher particle concentrations while HPs stay well-dispersed (**Figure 3.3, 3.14**) Increasing particle concentration results in visible sediments at higher concentrations with NRs while none are observed with HPs (**Figure 3.3**, **3.14**).

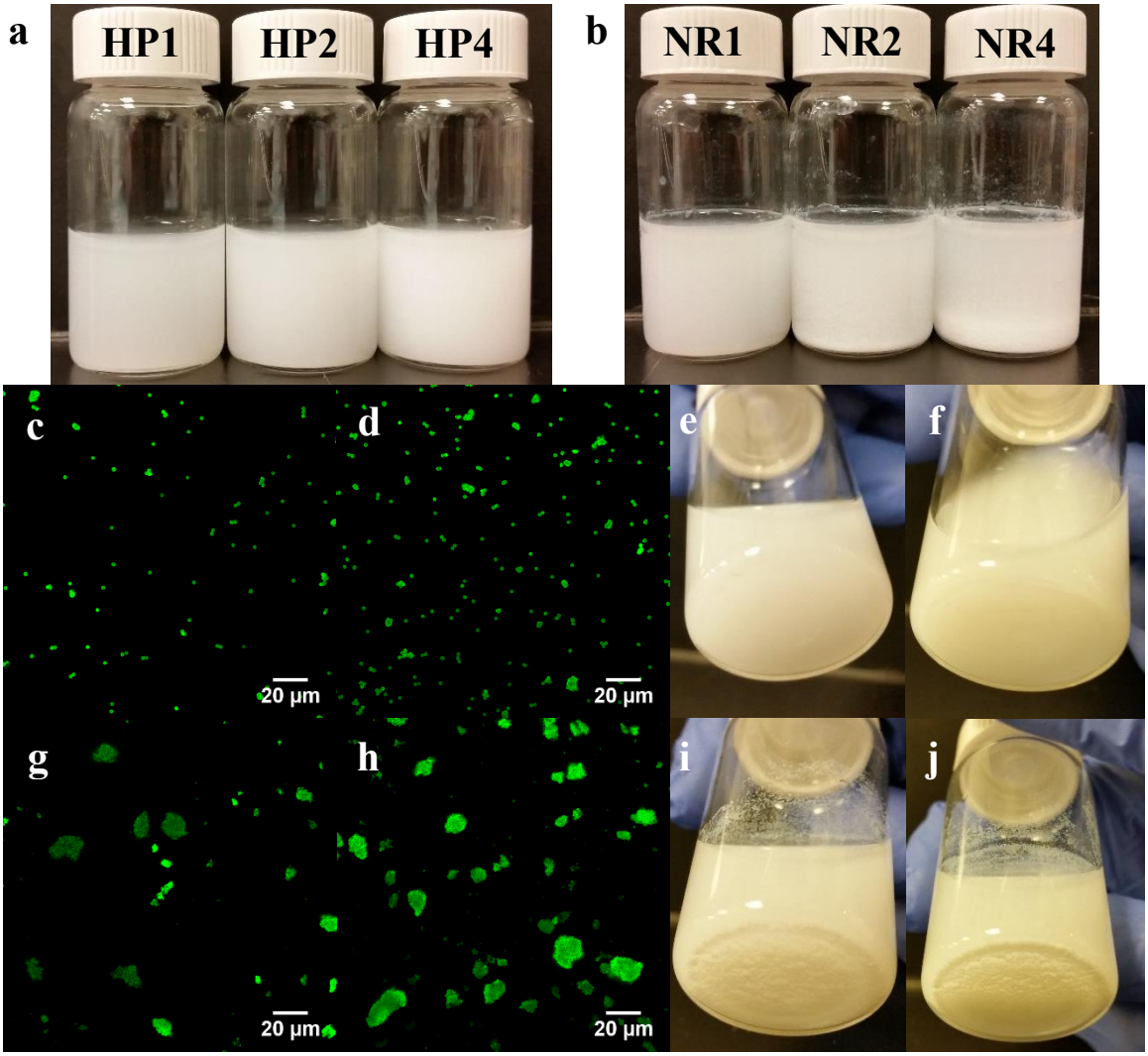

Figure 3.3: Photographs of dispersion of (**a**) HP_{S2} and (b) ZnO nanorods (NRs) in 2 M NaCl with increasing concentration from left to right (1 mg/mL, 2 mg/mL, and 4 mg/mL). Confocal microscopy respectively of HP_{S2} (**c,d**) and NRs (**g,h**) dispersed in heptane at 0.05 mg/mL (**c,g**) and 0.1 mg/ml (**d,h**). Photographs of sediment formed from HP_{S2} (**e,f**) and NRs (**i,j**) at 2 mg/mL (**e,i**) and 4 mg/mL (**f, j**) in 2 M NaCl after 1 minute.

3.5 Ionic Strength Effect in Aqueous Media

We used the photodegradation of methylene blue (MB) as a common model substrate to study the effects of high ionic strength environment and particle geometry on photocatalytic reactions. Monitoring of MB absorption peak at λ_{max} = 664 nm (**Figure 3.15**) allowed us to (a) compare photocatalytic activity of the HPs and NRs; (b) understand better the role of spiky particle geometry in photocatalysis, and (c) optimize HP geometry. Comparing MB degradation kinetics for HP_{S1}, HP_{S2}, HP_{L1}, HP_{L2}, we found that HP_{S2} with a spike diameter of 72 nm have the highest photocatalytic activity (**Table 3.1, Figure 3.16**). Even though HP_{S2} have smaller ZnO content and surface area than HP_{L1}, HP_{L2}, the electrostatic attraction between positively charged MB and

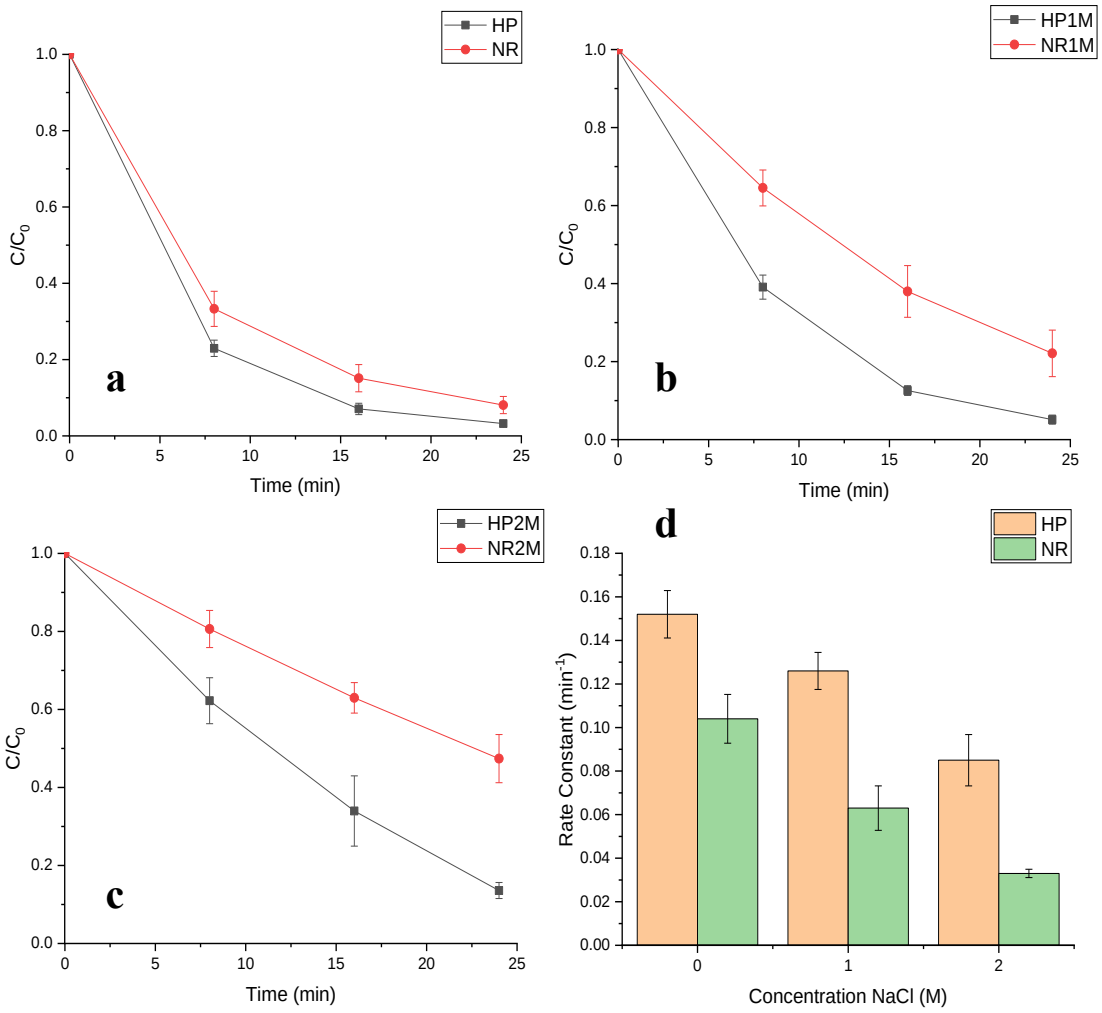

Figure 3.4: Degradation of MB with a starting concentration of $5*10^{-5}$ M in aqueous environments by ZnO NRs and HP_{S2} under a 302 nm light source: no salt added water (**a**) and 1 M NaCl (**b**) and 2M NaCl (**c**). Rate constants for MB degradation for HP_{S2} and NR catalyst as a function of salt concentration (**d**). Photodegradation kinetics of MB for different salt concentration without catalysts are displayed in **Figure 3.17** and **3.18**. The concentration of all catalysts was 2 mg/mL.

positively charged ZnO surface can vary in respect to spike length in a non-linear fashion due to ion-exclusion effects.[229,230]

Previous studies of the effect of inorganic salts covered only concentrations of NaCl up to 0.02 M; they showed inhibition of MB degradation due to catalyst agglomeration and Cl^- adsorption on the metal oxide surface.[231,232] We carried out photoinduced oxidation of positively charged MB with positively charged NRs (13.0±3.5 mV) and negatively charged (-11.6±4.1 mV) HPs. Expanding the NaCl concentration range to 2 M, we found that high salt conditions reduce the overall rate of MB degradation on HPs and NRs. This finding is attributed to the screening of electrostatic attraction between MB and the catalyst, which confirmed the regulatory role of ion strength in heterogeneous photocatalysis. Importantly, HPs displayed accelerated photooxidation

of MB compared to NRs (**Figure 3.4, 3.17**). To calibrate the catalytic activity in respect to the surface area, the Brunauer-Emmett-Teller surface area was measured for HPs and NRs (**Table 3.2**). HP_{S2} have a surface area of 8.65 m^2/g including the catalytically inactive SiO_2 core compared to 11.76 m^2/g for the NRs. The fact that HPs show catalytic activity higher than individual NRs despite reduced overall surface area highlights the importance of their higher dispersibility because otherwise ZnO in NRs and HPs is chemically identical. The rate of photocatalytic oxidation of MB observed for HPs exceed that of NR by 2.0 and 2.6 times in 1 M and 2 M NaCl, respectively (**Figure 3.4, Figure 3.17-3.18**). A broader evaluation of HPs as photocatalysts shows that their activity exceeds many other ZnO NPs and complex metal oxide with NP or NR geometries using even more intense light sources.[233,234] Degradation of MB in prior studies has shown rate constants of 0.012 min^{-1}, 0.077 min^{-1} and 0.090 min^{-1} for ZnO NPs, ZnO/ZnS and $ZnONiFe_2O_4$ NPs, respectively,[233,235] which are all lower than HPs with 0.153 min^{-1}.

3.6 Ionic Strength Effect in Organic Media

The possible impact of high ionic strength environment on feedstock sustainability can be demonstrated by photooxidation of the lignin model compound, 2-phenoxy-1-phenylethanol (PP-ol), which contains a dominant chemical linkage in lignin, the β-O-4 ether bond, known to be difficult to break in a single step.[236] Because PP-ol and lignin are poorly soluble in water, we had to expand the range of solvents and salts. PP-ol photooxidation was investigated in acetonitrile (ACN) as a co-solvent with ionic strength adjusted by metal chlorides and organic salts soluble in ACN and water-ACN mixtures (**Figure 3.5a**). HP_{L1}, revealed the highest activity in the PP-ol photooxidation (**Figure 3.19**). A distinct enhancement of the photocatalytic yield of benzaldehyde for high ionic strengths modulated by divalent metal chlorides, such as 1 M $MgCl_2$ was observed (**Figure 3.5b**). HPs enhance the yield of benzaldehyde by close to 50% over NRs likely due to enhanced dispersability of the spiky particles, particularly in the. HPs in 1M $MgCl_2$/ACN (2:1 ratio) produce over six times more benzaldehyde then a water/ACN and over two times more than pure ACN and 1 M NaCl/ACN (2:1 ratio) media (**Figure 3.5b**). The strength of electrical field in the double electric layer on ZnO HPs (with measured zeta potential) can be estimated to be 8.5 x 10^7 V/m, 5.1 x 10^7 V/m, 1.7 x 10^4 V/m, and 2.4 x10^4 V/m for 1 M $MgCl_2$/ACN, 1 M NaCl/ACN media, water/ACN, and ACN, respectively using DLVO theory and the Poisson-Boltzmann equation (**Figure 3.5c,** Supplementary Methods). The increase of benzaldehyde production is

consistent with the increase of the electrical field at the ZnO-solvent interface. Based on these experimental results and prior computational data[212], the enhanced yield of benzaldehyde can be related to large electric fields developing at solid-liquid interface.

$CaCl_2$ also enhances HP-mediated photooxidation of PP-ol but to a smaller degree than $MgCl_2$ (**Figure 3.20**), indicating that additional interactions beyond classical DLVO theory become important at high concentrations of electrolytes.[182] One of them is ion-ion correlations,[237,238] that are strongly dependent on coordination of metal in with the solvent. These and other collective interactions around the nanostructures[182] become particularly important at high ionic strengths and with multivalent metal ions as seen from other manifestations in colloidal science[239–241] and additional stabilization of 1M $MgCl_2$/ACN dispersion as reaction proceeds (**Figure 3.21**).

The possibility of drastically changing reaction pathways using salt as the only chemical control parameter can be demonstrated by varying the concentration and composition of organic salt in ACN. The yield of 2-phenoxyacetophenone (PP-one) increases as a function of tetrabutylammonium hexafluorophosphate concentration ($TBAPF_6$) with an increase by multiple orders of magnitude utilizing HPs and 1 M $TBAPF_6$. Again, yield of PP-one and benzaldehyde for HPs is higher than for NRs (**Figure 3.5d**) at all concentrations of $TBAPF_6$ (**Figure 3.22**). 'Tuning' of the reaction selectivity in high ionic strength environments was accomplished by varying the diameter of cations (**Table 3.3, Figure 3.5e**). We see a sharp reduction in the amount of PP-one, while the benzaldehyde production remains the same (**Figure 3.23**) as the diameter of the cation becomes smaller (~0.1 nm). The cation size (**Table S3**) can strongly alter the strength of the electrical field[239] at the ZnO interface and influences oxidation of the alcohol in a greater degree than breaking of the β-O-4 bond because the former process involves multiple charged species.[242,243]. Previous research has shown differing effects of oxidative atmosphere on hydrogenolysis of the β-O-4 bond to form aromatic products such as benzaldehyde and the oxidative dehydrogenation to form PP-one, with oxidative atmosphere having a much larger beneficial effect on dehydrogenation.[244] We believe that the electric field in an analogous manner is resulting in a localized oxidative atmosphere, which promotes dehydrogenation but has little effect on hydrogenolysis. Steric hindrance and hydrophobicity of the tetraalkylammonium ion may also be significant in for these reactions, which can also be varied, parametrized, and utilized in the control of reaction pathways by changing electrolytes.

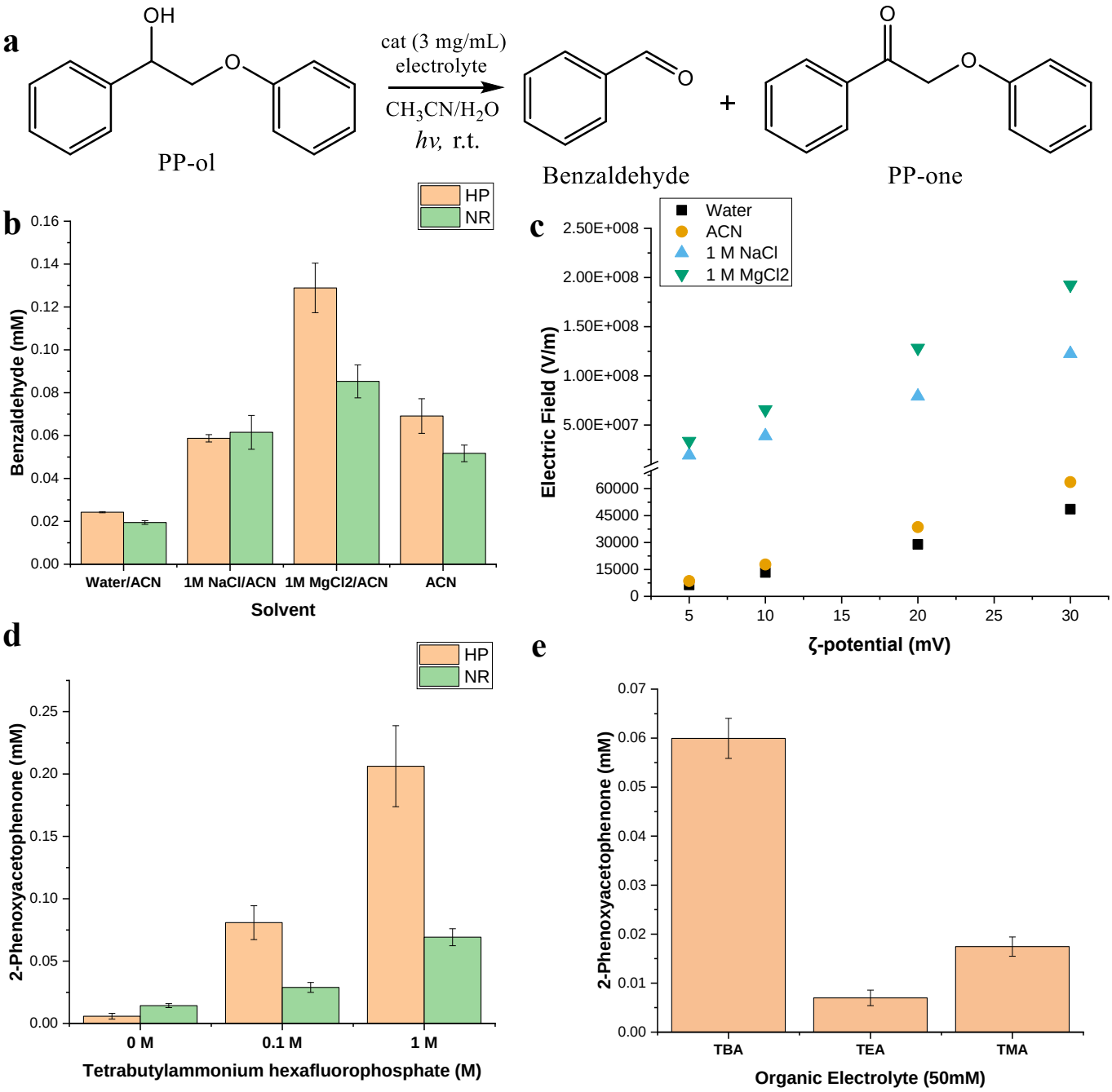

Figure 3.5: (**a**) Reaction schematic for oxidation of 2-Phenoxy-1-phenylethanol (PP-ol) to Benzaldehyde and 2-phenoxyacetophenone (PP-one) (**b**) Production of benzaldehyde in different media catalyzed by HP_{L1} and NRs; all aqueous and ACN mixtures were prepared with a ratio of 2:1. (**c**) Electric field strength calculated utilizing DLVO theory and the Poisson-Boltzmann equation for a spherical particle in aqueous and salt mixtures with ACN (2:1) and pure ACN as a function of ζ (see Supplementary Information). Note the difference in the electrical field strength axis for particles in and out of high salt environment. (**d**) Production of PP-one as a function of $TBAPF_6$ concentration in ACN with HP_{L1} and NR as catalysts (3 mg/mL) from photooxidation of PP-ol (5 mM) for 2 hours. (**e**) Production of PP-one for $TBAPF_6$, $TEAPF_6$, and $TMAPF_6$ in ACN (50 mM) using HP_{L1}. All experiments carried out with 302 nm light source. $TBAPF_6$ with light only (no catalyst) produces minimal amount of PP-one.

3.7 Conclusions

The dispersion-passivation conundrum associated with catalytic processes on metal oxide particles in unfriendly environments promoting their agglomeration can be resolved by engineering of microscale colloidal particles with nanoscale catalytic spikes that display enhanced catalytic activity compared to individual NRs in aqueous, mixed, and organic media. They enable the use of the salt concentration and composition as reaction parameters to increase reaction yield and modulate process selectivity. Detailed understanding of the chemical mechanisms associated with variations of electrical fields at the solid-liquid interface in high-salt environment could lead to unique (photo)catalytic processes and energy-efficient production of aromatic chemicals from complex and robust natural products, such as lignin. Since the rate-limiting stages of many photoinduced reactions involve charged species, inorganic HPs may serve as a general platform for photochemical synthesis. Future studies should also involve exploration of HPs for remediation needs in high salinity conditions in nature where traditional particle-based catalysts aggregate.

3.8 Supplementary Information

3.8.1 Methods

All chemicals were ordered from Sigma-Aldrich unless noted otherwise. Carboxylated SiO_2 was ordered from Polysciences, Inc. Polycarbonate track-etched membranes (0.8 micron, 90 mm) were ordered from Sterlitech.

Layer-by-Layer Coating of Core Particles

Limited adsorption of ZnO NPs was observed without layer-by-layer (LbL) coatings on both types of SiO_2 cores leading to irregular spike morphology and poor colloidal stability (**Figure 3.24**). To mitigate this problem, we deposited several LbL assembled polyelectrolyte bilayer to promote NP adhesion to the SiO_2 cores.[28,148,152,215] Strong polyelectrolytes, namely poly(diallyldimethyl ammonium chloride) and poly(styrene sulfonate), and weak polyelectrolytes, namely polyacrylic acid and poly(allylamine hydrochloride, were used in the preparation of the

adhesion-promoting bilayersSilica cores were coated with polyacrylic acid and poly (allylamine hydrochloride) in a layer-by-layer process. Briefly, 5 mL core was mixed with 25 mL polyelectrolyte solution (1 mg/ mL, 1 M NaCl) and incubated for 20 minutes. Cores were then centrifuged for 4000 RPM for 10 minutes and washed with .1 M NaCl pH 8 water 2 times and water 2 times before repeating the process with the next layer. A change in surface charge is observed with deposition . of each LbL layer for the silica core materials (**Figure 3.25**). The conformal nature of the LbL film producing a uniform charged surface for NP adsorption is more critical for HP formation then a negatively charged surface.

Synthesis of Hedgehog Particles with SiO_2 cores and ZnO NRs:

Inorganic core HPs were synthesized using a scaled sonothermal synthesis based on that of Bahng et al. 1.25 mL of coated core solutions (2.5 wt%) was mixed with 40 mL ZnO seed solution (0.025 wt%) and incubated for 1 hour.[15] Particles were then filtered using a track etch membrane and combined with equimolar (37.5 mM) solutions of zinc nitrate hexahydrate (ZnH) and hexamethylenetetraamine (HMT) in water. Concentrations of the precursors were varied to tune the width of the spikes, the default concentration was 37.5 mM. The solution was then filled to a final volume of 1.6 L and sonicated using a Hielscher 1000UIP HdT sonicator for 1 hour and 30 minutes. Samples were purified by removing excess zinc oxide nanorods after sedimentation of HPs. Longer HPs were created by doing an additional sonication with ZnH and HMT precursor solutions after purification. ZnO nanorods used for catalysis were obtained from the supernatant after sedimentation of HPs.

Zeta Potential Measurements

For ζ-potential measurements, a 100 μL aliquot of core particles was set aside after deposition of each layer, and 900 μL of water was added before each zeta potential measurement was taken. The ζ-potentials were measured using a Malvern Zetasizer Nanoinstrument Nano ZS. Each value was averaged from three parallel measurements.

Confocal Microscopy Imaging:

For confocal studies, FITC was conjugated to PAH according to a literature procedure.[193,215] Briefly, 4.5 mg FITC was dissolved in 1 mL dimethylsulfoxide (DMSO) and

combined with 500 mg PAH dissolved in 6 mL water. The pH of the solution was adjusted to 8.4 with NaOH and then the solution was stirred for 2 days. Dialysis was then performed using a D-tube™ Dialyzer for 24 h to remove excess FITC.[193] PAA/FITC-PAH films were deposited on HPs using LbL assembly with the same procedure described previously.[215]

Electron Microscopy Imaging

20 µL of sample was dispersed on a silicon wafer and then evaporated. Afterwards, samples were sputter coated with gold using a SPI-Module carbon/sputter coater. Particles were imaged using a FEI Nova 200 Nanolab SEM and FEI Helios 650 Nanolab SEM/FIB. NPs and coating were imaged using a JEOL 3011 high resolution electron microscope. For dispersion SEM images, particles were imaged at a concentration of 0.1 mg/mL.

Surface Area and Dimension Measurements

The surface areas of different catalysts were determined using N_2 physisorption based on the BET Method with a Micromeritics ASAP 2010 analyzer. Particle size dimensions were determined from SEM images by measuring over a minimum of 100 nanorods or HPs. The spike width was calculated utilizing the overall diameter and diameter of SiO_2 core microparticles.

Thermogravimetric Analysis

Thermogravimetric Analysis was done using a Discovery TGA Q5000IR (TA Instruments inc., Delaware, USA). 1-3 mg of sample was heated from ambient to 600°C at a heating rate of 10°C/min with a nitrogen flow rate of 30 mL/min.

Photocatalysis Experiments

A Hellma® 4.5 mL Quartz cuvette was used for all photocatalytic experiments. Samples were exposed to a 302 nm UV lamp (3UV™, 8 watt) under agitation with aliquots every eight minutes. All samples were centrifuged at 4000 RPM for 10 minutes and then the supernatant was tested using an Agilent Cary 8454 UV-Vis spectrophotometer. Degradation of methylene blue was determined from optical absorption spectra utilizing the optical density at λ_{max} = 664 nm. For 2-phenoxy-1-phenyl ethanol tests, catalysts were dispersed at 3 mg/mL and illuminated with the same 302 nm UV lamp. Supernatant samples were analyzed using an Agilent 1260 Infinity II

HPLC with an attached UV detector mixture of methanol and 1 mM trifluoroacetic acid aqueous solution (55:45 volumetric ratio) mobile solution at a flow rate of 0.4 mL/min.

DLVO Calculation of Electric Field

DLVO Calculation of electric field was done utilizing an analytical expression for the Poisson-Boltzmann equations for spherical particles in electrolyte.[245,246] Details are given in the supplementary text.

3.8.2 DLVO Calculation of Electric Field

The spherical Poisson-Boltzmann equation for the electric potential around a spherical particle in in a electrolyte solution[245,246] was computed to estimate the electric field. A particle with a constant surface charge density σ independent of the electrolyte concentration was assumed.[246] The equation for a 1:1 electrolyte is displayed below.[246]

$$\sigma = \frac{2\pi\varepsilon_0\varepsilon_r k_b \kappa T}{ze}\sinh\left(\frac{ze\Psi_{ZnO}}{2k_bT}\right)\sqrt{1+\frac{1}{\kappa a}\frac{2}{cosh^2\left(\frac{ze\Psi_{ZnO}}{4k_bT}+1\right)^2}+\frac{1}{\kappa a^2}\tanh\frac{8\ln[\cosh\left(\frac{ze\Psi_{ZnO}}{4k_bT}\right)]}{\sinh^2\left(\frac{ze\Psi_{HP}}{2k_bT}\right)}}$$

Where ε_0 is the permittivity of vacuum, ε_r is the dielectric constant of the media, e is electric charge (C) a is the particle radius and Ψ_{ZnO} is the zeta potential of ZnO in water (experimentally measured Ψ_{HP} =13.0 mV). Solutions were also computed as a function of zeta potential. κ represents the reciprocal double layer thickness and is given by

$$\kappa = \sqrt{\frac{1000 N_A e^2}{\varepsilon_0\varepsilon_r k_b T}\Sigma_i M_i x {Z_i}^2}$$

where N_A is Avogadro's number, M_i and Z_i are the molar concentration and valency of ions. [204] For computation of the debye length of the water/acetonitrile (ACN) mixture, the concentration of ions was assumed to be extremely dilute (10^{-7} M) with an estimate of the adjusted dielectric constant (64.7) based on the 2:1 mixture which is very close to literature values.[247] An extremely dilute concentration of ions (10-7 M) was also assumed for calculation of debye length of pure ACN. For the 1 M NaCl/ACN (56.8) and 1 M $MgCl_2$/ACN (53.3), literature values were used for the dielectric constant of the salt solutions[248,249], and then adjusted and estimated for the 2:1 mixture with acetonitrile. HPs were analyzed as a sphere with diameter equivalent to the total

core + shell diameter. In this case, shifting the size of the HP has little effect on the overall electric field.

For 1 M $MgCl_2$, the electric potential around a spherical particle was estimated using an analytical expression derived by Oshima et al for 2:1 electrolytes.[245]

$$p = 1 - exp(-\frac{e\Psi_{ZnO}}{k_b T})$$

$$q = (\frac{2}{3} exp\left(\frac{e\Psi_{ZnO}}{k_b T}\right) + \frac{1}{3})^{1/2}$$

$$\sigma = \frac{\varepsilon_r \varepsilon_0 k_b \kappa T}{e} (pq + \frac{2[(3-p)q-3]}{\kappa apq})$$

Where ε_0 is the permittivity of vacuum, ε_r is the dielectric constant of the media, e is electric charge (C) and Ψ_{HP} is the zeta potential of ZnO in water (experimentally measured Ψ_{HP} =13mV). Solutions were also computed as a function of zeta potential. The surface charge densities were converted to electric fields outside the particle by the equation below. For **Figure 4.5c**, the electric field was calculated 1 Å from the ZnO surface for a charged dielectric sphere by applying Gauss's Law for dielectrics.

$$E(r) = \frac{\sigma}{\varepsilon_0 \varepsilon_r} * \frac{R}{r}$$

Where R=HP Radius and ε_r is the dielectric constant of the reaction solvent.

3.8.3 Supplementary Results

Table 3.1: Spike width, length and total diameter of HPs synthesized using different chemical concentrations and sonication times.

HP	Spike Width (nm)	Spike Length (nm)	Total Diameter (nm)	Precusor Chemical Concentration (mM)	Number of Sonications in the synthetic process
HP_{S1}	58±14	482±63	2091±127	25	1
HP_{S2}	72±17	758±56	2643 ±113	37.5	1
HP_{L1}	166±27	1545±240	4216±480	37.5	2
HP_{L2}	146±25	1864±122	4855±244	25	2

Table 3.2: BET surface area measurements of HP_S and ZnO NR catalysts.

Catalysts	Surface Area (m^2/g)
ZnO NR	11.76±0.007
HP_{S2}	8.65±0.037
HP_{L1}	5.20 ± 0.015
HP_{L2}	8.20 ± 0.017

Table 3.3: Organic Ion Stokes Radii in Acetonitrile

Ions	**R_s (nm)**
Me_4N^+	0.2516[a]
Et_4N^+	0.2831[a]
Bu_4N^+	0.3866[a]
PF_6^-	0.228[b]

[a] Harknees et al.[250] [b] Tsierkezos et al.[251]

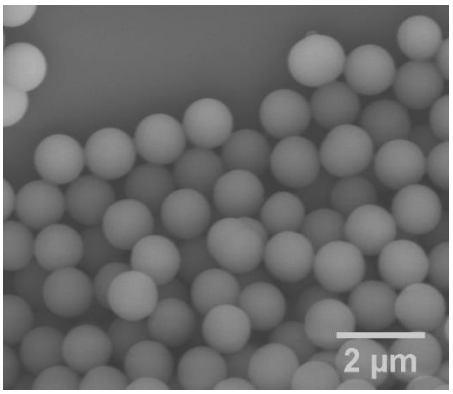

Figure 3.6: SEM image of SiO_2 particles serving as the core particles for HPs synthesized as described in Experimental using the Stöber process.[228,252]

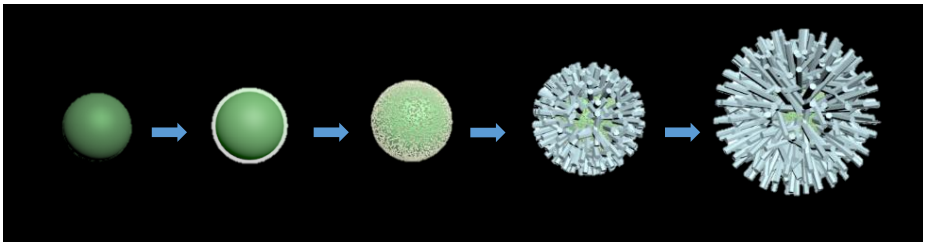

Figure 3.7: Schematic showing coating of SiO_2 Bead with LbL-film and then deposition of ZnO nanoparticles which are hydrothermally grown into spikes to form HPs.

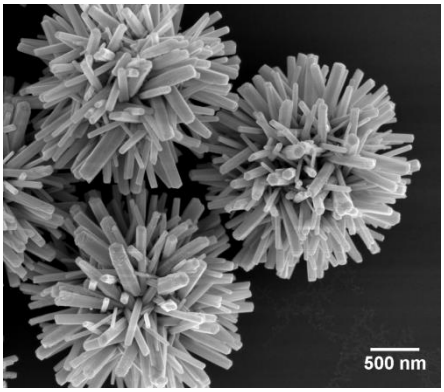

Figure 3.8: HP made using carboxylated SiO_2 core microparticles coated with LbL films.

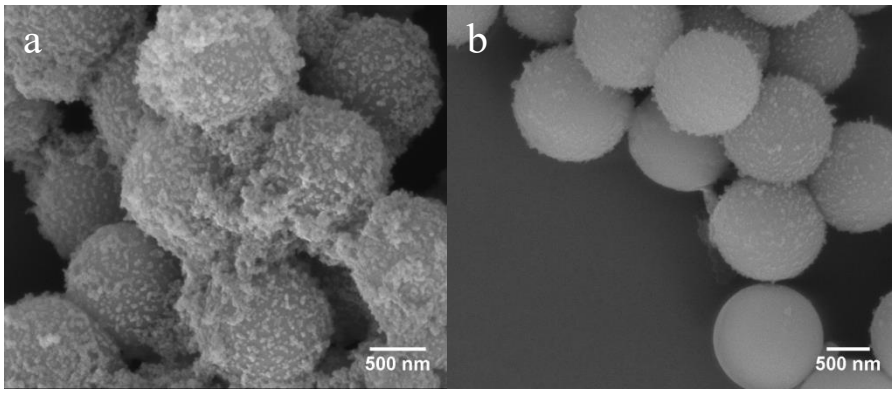

Figure 3.9: Stöber SiO_2 beads coated with PAA/PAH (**a**) and without PAA/PAH (**b**) coatings after incubation with ZnO NP for 1 hour.

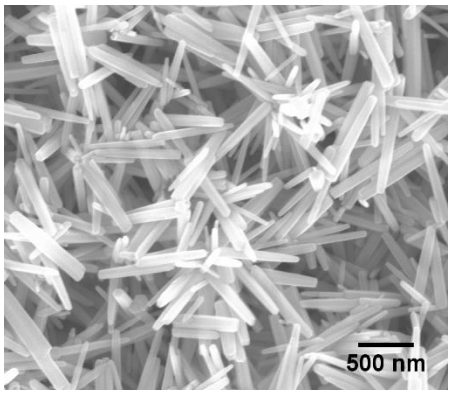

Figure 3.10: ZnO NR catalyst sample collected during purification from the supernatant of HP_{S2}

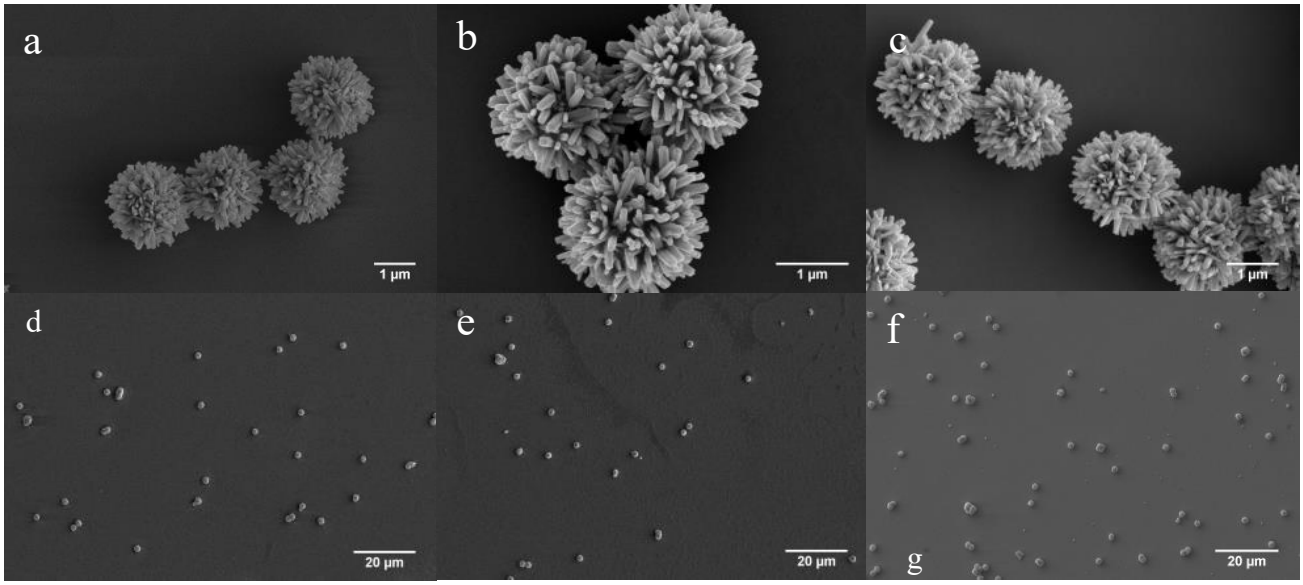

Figure 3.11 : SEM images of SiO_2 HPs in chloroform (**b**,**e**), tetrahydrofuran (**c**,**f**) and toluene (**d**,**g**) after 1 week (0.1 mg/mL).

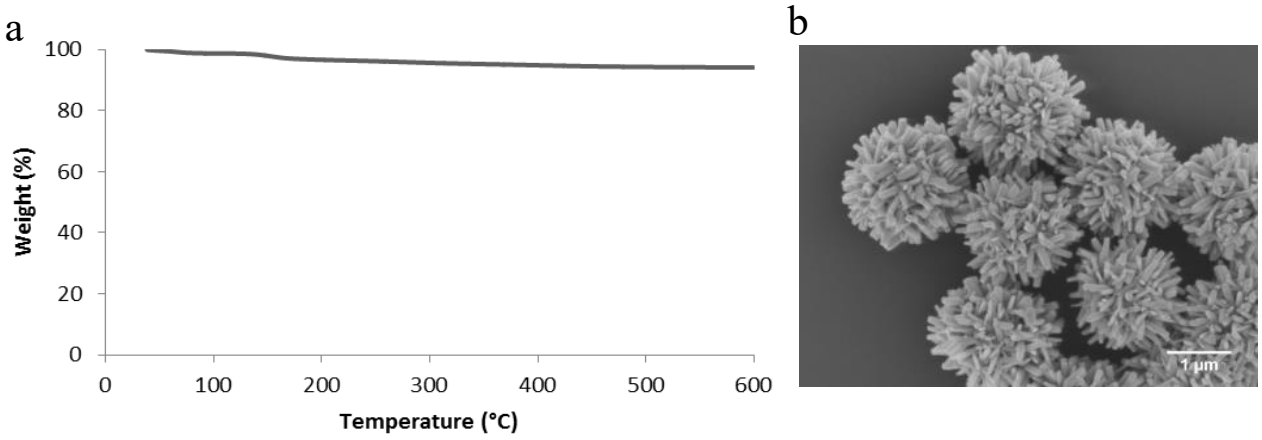

Figure 3.12: (**a**) Thermogravimetric analysis of SiO_2 HPs (**b**) SEM of SiO_2 HPs after treatment at 500ºC for 24 hours

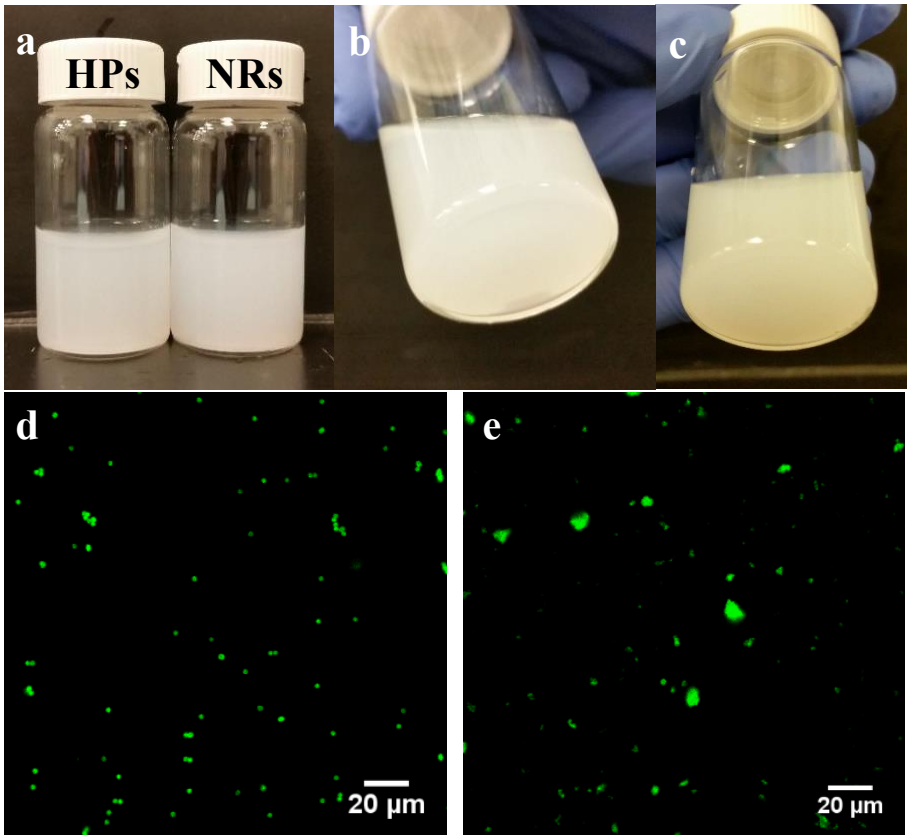

Figure 3.13: Images of dispersion of (**a**) SiO_2 HPs and ZnO NRs (NRs) in 1 M NaCl (0.5 mg/mL). Images of sediment of SiO_2 HPs (**b**) and NRs (**c**) in 1 M NaCl (0.5 mg/mL) after 1 minute. Confocal microscopy images of SiO_2 HP (**d**) and ZnO NRs (**e**) dispersed in 1 M NaCl (0.1 mg/mL).

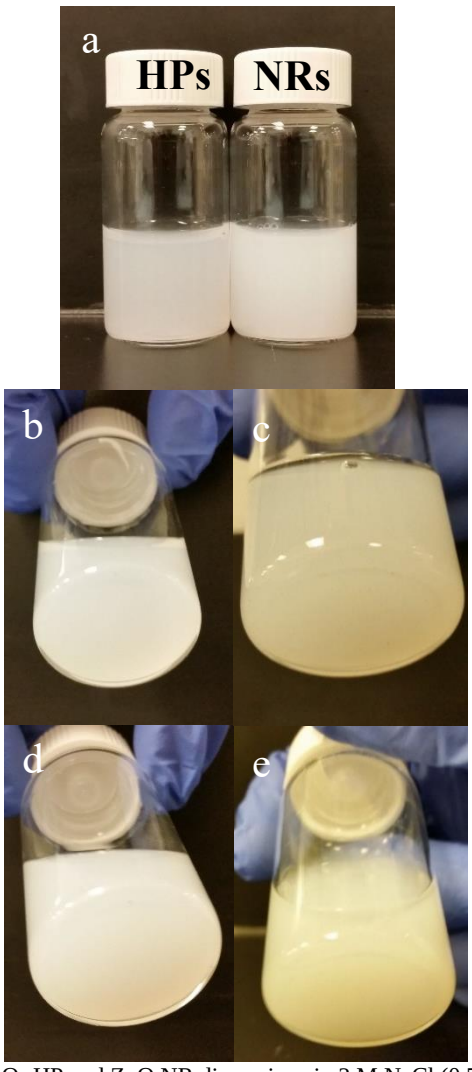

Figure 3.14: Photographs of (**a**) SiO_2 HP and ZnO NR dispersions in 2 M NaCl (0.5 mg/mL). Images of sediment of SiO_2 HPs (**b,c**) and NRs (**b,d**) at 0.5 mg/mL (**c,e**) and 1 mg/mL in 2 M NaCl after 1 minute.

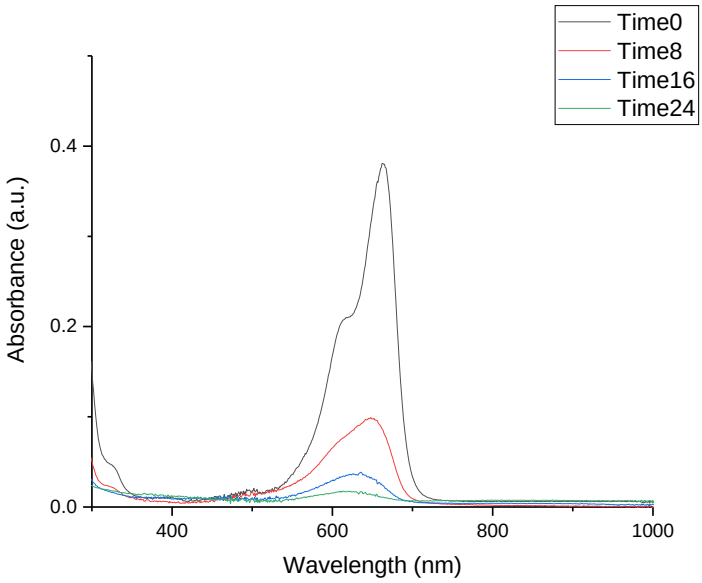

Figure 3.15: Spectral changes of MB solution (5×10^{-5} M) upon photo-degradation catalyzed by HP_{S2} (2 mg/mL) utilizing a 302 nm light source.

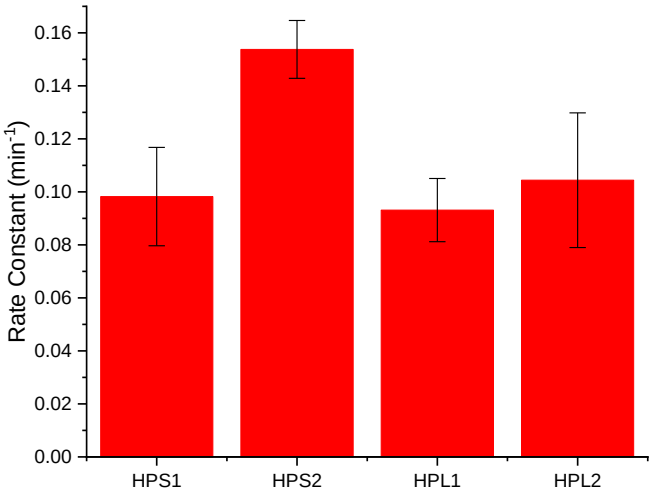

Figure 3.16: Rate constants in MB photooxidation for different HPs with different spike lengths and widths; geometrical parameters are given in **Table 3.1**. Total concentration of HPs was 2 mg/mL for all the experimental sets here.

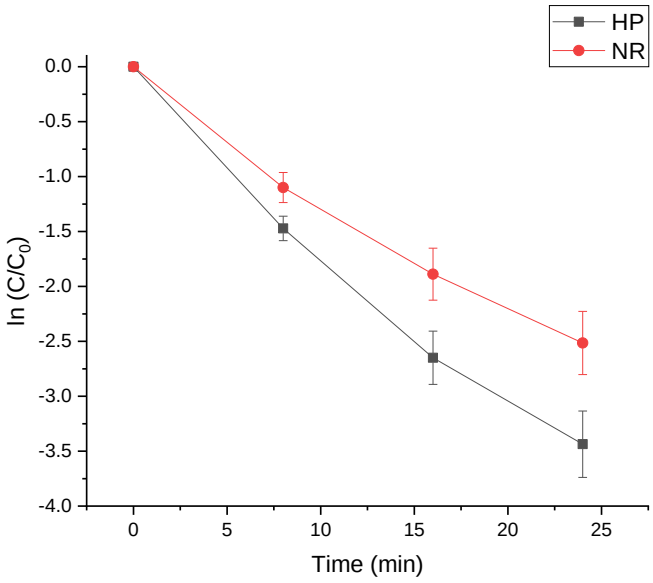

Figure 3.17: Photodegradation kinetics of MB with HPs and NRs in water (2 mg/mL) under a 302 nm light.

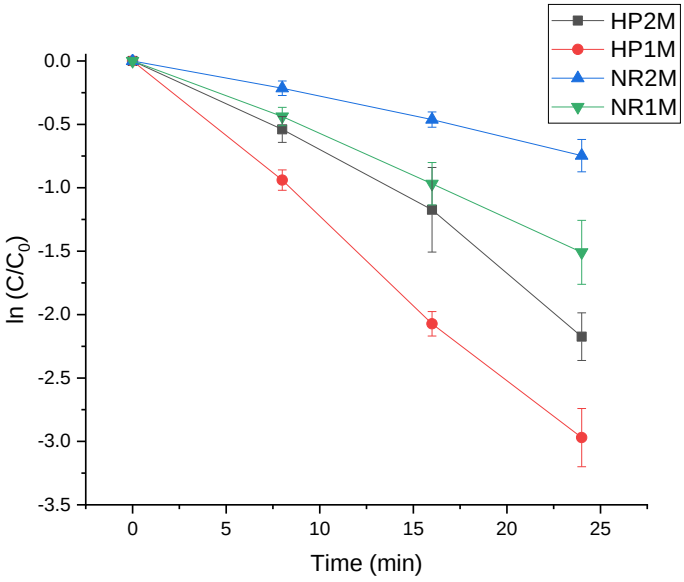

Figure 3.18: Photodegradation kinetics of MB with HPs and NRs in 1 M NaCl and 2 M NaCl.

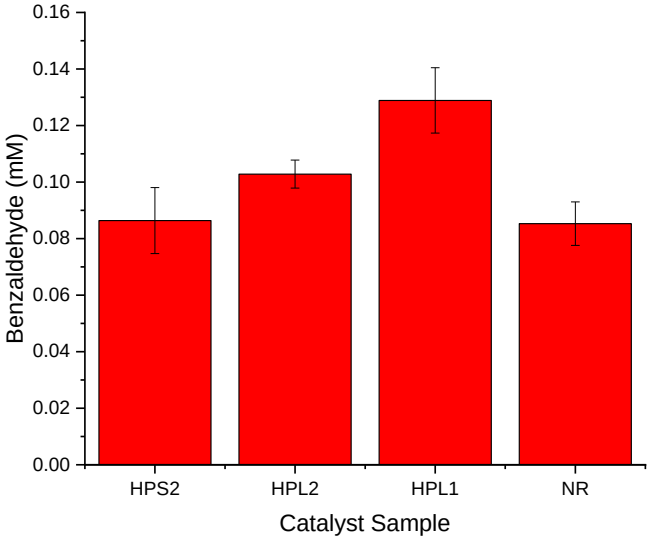

Figure 3.19: Production of benzaldehyde from photooxidation of 2-phenoxy-1-phenylethanol for 2 hours with different heterogeneous catalysts added in the amount of 3 mg/mL in 1 M $MgCl_2$/acetonitrile (2:1). A 302 nm light source (8W) was used.

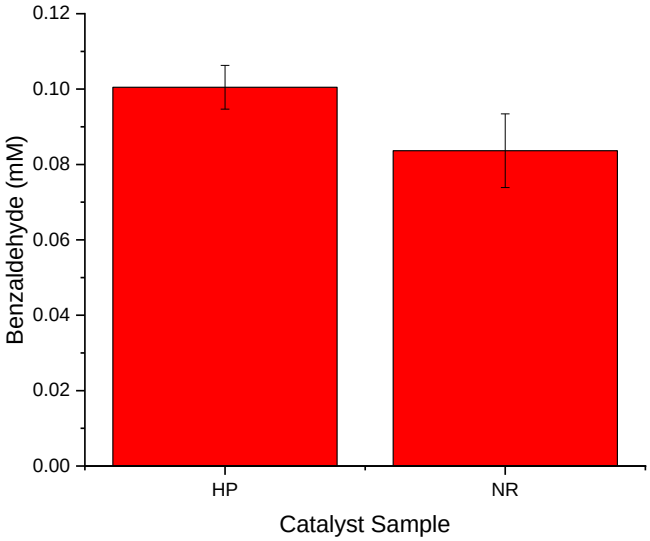

Figure 3.20 Production of benzaldehyde from photooxidation of 2-phenoxy-1-phenylethanol for 2 hours with HP_{L1} and NRs added in the amount of 3 mg/mL in 1 M $CaCl_2$/acetonitrile (2:1). A 302 nm light source (8W) was used.

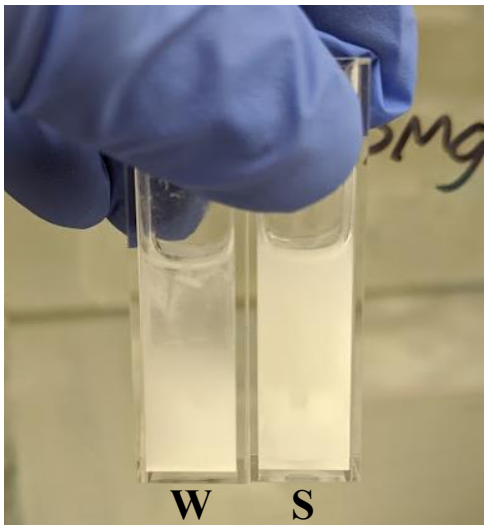

Figure 3.21: Photograph of cuvettes after 2hr photocatalytic (302 nm light source) reaction with HPs (3 mg/mL) in Water/ACN (W) and 1 M $MgCL_2$/ACN (S) (both 2:1 by volume).

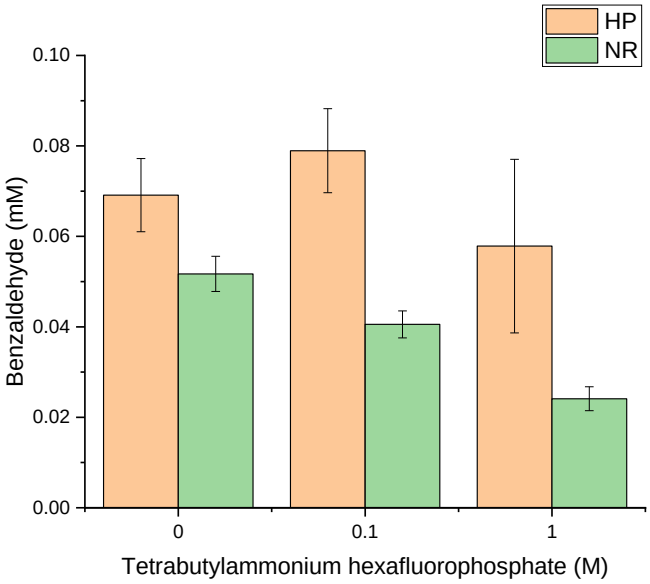

Figure 3.22: Production of benzaldehyde from photooxidation of 2-phenoxy-1-phenylethanol for 2 hours with 302 nm light source as a function of tetrabutyl ammonium hexafluorophosphate concentration in acetonitrile with HP_{L1} and NR catalyst samples.

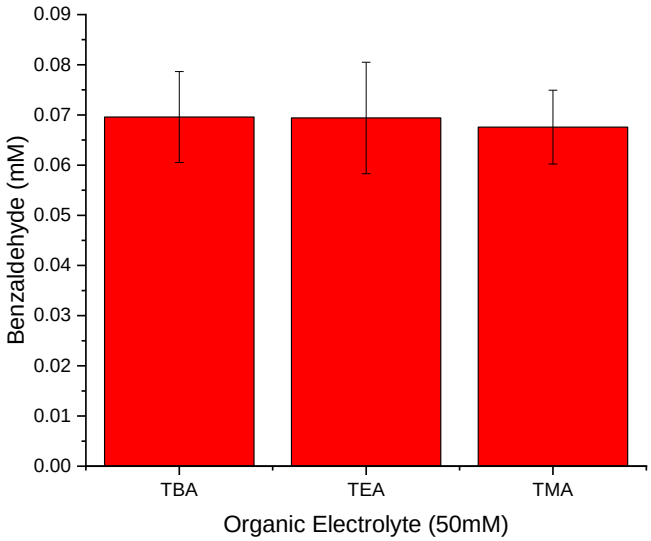

Figure 3.23: Production of benzaldehyde from photooxidation of 2-phenoxy-1-phenylethanol for 2 hours with 302 nm light source for different organic electrolytes in acetonitrile with HP_{L1} catalyst (3mg/mL) Organic electrolytes are hexafluorophosphate salts of tetrabutylammonium (TBA), tetraethylammonium (TEA), and tetramethylammonium (TMA).

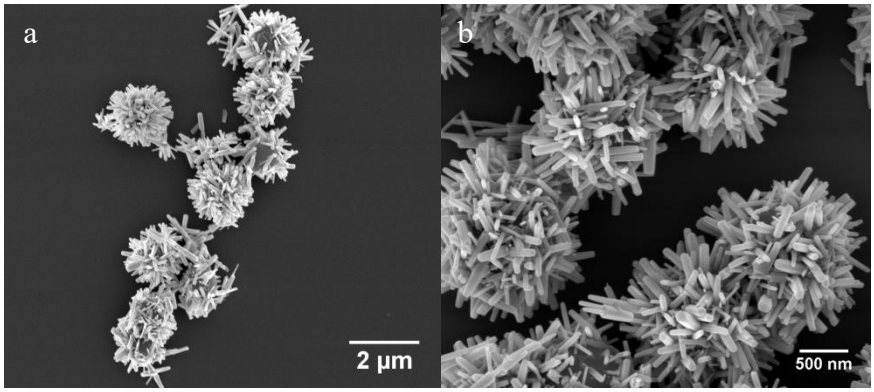

Figure 3.24: HPs without LbL coating made from (**a**) carboxylated SiO_2 and (**b**) SiO_2 synthesized using the Stöber process**.**

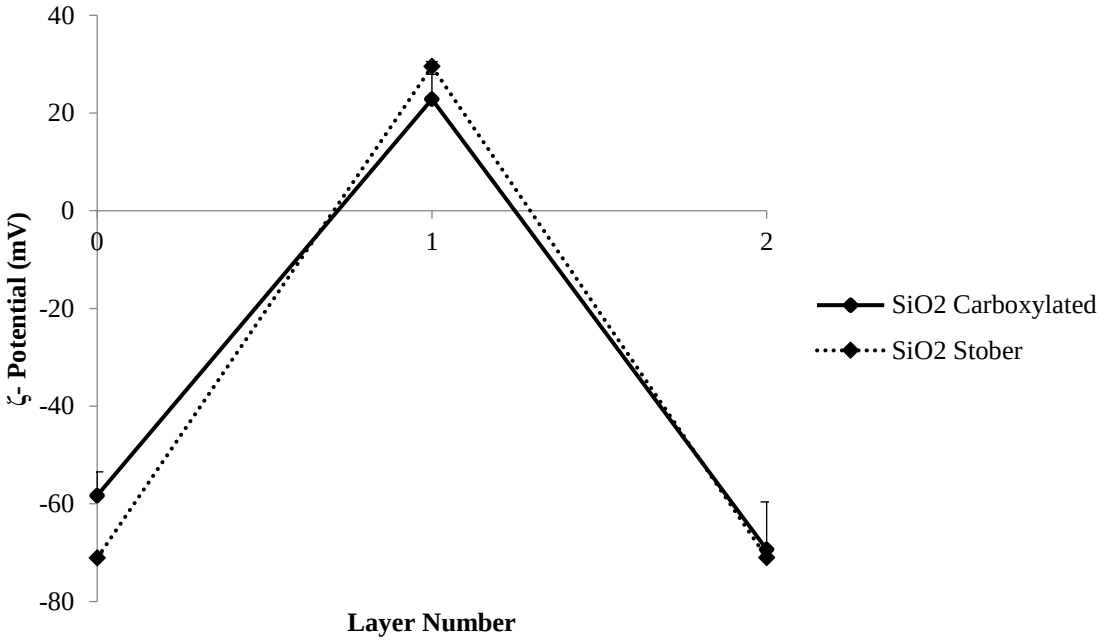

Figure 3.25: Zeta potential of commercial carboxylated SiO_2 and Stöber SiO_2 microparticles as a function of layer number.

Chapter 4

Hedgehog Particles with Inorganic Cores

Douglas Montjoy[1], Harrison Hou[1], Joong Hwan Bahng[2], Elizabeth Wilson[1], Aydin Eskafi[1],

Nicholas A. Kotov[1,3,4,5]

[1]Department of Chemical Engineering, University of Michigan, Ann Arbor, Michigan 48109, USA;
[2]Department of Electrical Engineering, California Institute of Technology, Pasadena, California 91125, USA;
[3]Department of Biomedical Engineering, University of Michigan, Ann Arbor, Michigan 48109, USA;
[4]Department of Materials Science, University of Michigan, Ann Arbor, Michigan 48109, USA;
[5]Biointerfaces Institute, University of Michigan, Ann Arbor, Michigan 48109, USA;
*E-mail: kotov@umich.edu

4.1 Abstract

Dispersion of inorganic particles in polar and apolar media represents one of the perpetual challenges in chemistry, physics, biology and various technological areas. A new dispersion strategy taking advantage of surface corrugation is exemplified by hedgehog particles (HPs) with high aspect ratio stiff spikes that markedly reduce attractive dispersive interactions and enable dispersion of particles in both polar and nonpolar solvents. However, the majority of HPs developed in the past are based on organic poly(styrene) cores. While proving the concept of dispersibility, these HPs with polymeric cores limit temperature and solvent stability of the particles as well as their catalytic activity. In this study, we show that a versatile array of HPs with inorganic cores following a similar design strategy as those with organic ones and with a variety of materials properties can be prepared. The omnidispersable HPs carrying stiff ZnO nanospikes were prepared with Fe_2O_3 hematite microcubes, Fe_3O_4 magnetite microcubes, hollow Au

microspheres, and hollow TiO_2 microcubes. Additionally, HPs with TiO_2 spikes are created using liquid state deposition. Inorganic core HPs maintain dispersion in a wide array of nonpolar environments and exhibit enhanced thermal and chemical stability. We expect this family offunctional dispersible HPs to excel in environments where traditional catalysts aggregate such as hydrophobic and high ionic strength environments.

4.2 Introduction

Dispersions of inorganic particles in both polar and apolar environments are critical to many technologies. This is particularly significant for new catalysts because particle aggregation greatly reduces catalytic activity.[109,114] Dispersion stability of nano-, meso-, and microscale particles is typically achieved through coatings of layers of polymers, surfactants, and organic tethers that increase the electrostatic and steric repulsion between particles.[1,4,6,7] While suitable for some applications, the chemical "camouflage" added to semiconductor and metallic nanoparticles results in greatly reduced catalytic activity.[8,126,214] Development of novel heterogeneous catalysts for apolar media is particularly affected because thick hydrophobic coatings block the surface of inorganic particles where catalytic reactions take place. [3,8,9] Additional issues with this strategy of particle stabilization emerge when stabilizing surface ligands have a measurable tendency to desorb. The changes in sorption equilibrium due to variations in particle concentration, pH, or polarity of the media inevitably result in particle aggregation.[5] Recently, spiky colloids referred to as 'hedgehog' particles (HPs) were introduced which utilize surface corrugation as a dispersion strategy.[15] The original design of HPs was based on a micron-sized polystyrene (PS) core surrounded by nanoscale zinc oxide (ZnO) spikes. The surface corrugation from the spikes leads to a marked reduction in van der Waals forces, resulting in the ability to disperse in both organic and aqueous solvents.[15] Subsequent studies confirmed that the reduction of omnipresent attractive interaction, rather than an increase of repulsive forces, is responsible for their omnidispersibility.[215]

The addition of different functionalities and probing potentially complementary properties of core and spikes is possible with a diverse set of core materials. In particular, the creation of thermally and chemically stable HPs with functional cores rather than fairly inert and temperature-sensitive PS microparticles noticeably expands their functionality and design space. Both chemical

and physical properties of inorganic cores are of interest. As such, hematite (Fe_2O_3) represents an earth abundant metal oxide semiconductor that can be used as a thermal or photo-catalyst that could greatly benefit from the ability to disperse in apolar medium. Fenton reactions catalyzed by hematite in apolar media can be particularly useful in many green chemical processes.[253,254] Similarly, titania (TiO_2) is a low cost metal oxide semiconductor that is one of the most prevalent photocatalysts in aqueous (polar) media, but has difficulties as a heterogeneous catalyst in organic media due to poor dispersability.[255,256] The rapidly developing area of plasmonic catalysis[257,258] takes advantage of hot electrons and holes that are estimated to react with substrates within 22 and 47 nm from the surface of plasmonic particles respectively with very short lifetimes of ~30 fs.[259] Removal of the organic ligand layer with much shorter carrier lifetimes[260] around plasmonic particles such as gold could significantly improve yield and selectivity of plasmonic catalysts dispersed in hydrophobic media and allow for direct charge excitation at the adsorbate/metal interface.[261,262]

There are a number of reactions with low yields due to the limited stability of catalysts in a nonpolar environment. The current state-of-the art in polymer precursor synthesis is represented by reactions conducted in polar organic solvents.[263–265] However, studies have shown that the selectivity of, for instance, the photooxidation of cyclohexane to cyclohexanone and cyclohexanol (a mixture known as KA oil), is strongly dependent on the polarity of the solvent, regardless of the type of catalyst used.[266–268] The need for an organic media in this reaction is evidenced by the fact that the presence of water leads to marked reduction in both reactivity and selectivity.[269] Additionally, while the photocatalytic conversion of CO_2 using solar energy is one of the most attractive routes to mitigate global warming,[95–97] currently the process has low efficiency, product selectivity, and catalyst stability.[98] The poor solubility of gaseous nonpolar CO_2 in aqueous media is a cause of several of these issues. The development of heterogeneous inorganic photocatalysts that can function in a nonpolar environment such as cyclohexane or CO_2 is critical for sustainable production of feedstocks and fuels.

In this study, we have developed inorganic microparticles with plasmonic, magnetic, and catalytic properties with a shell of photocatalytic spikes consisting of ZnO or TiO_2. The spiky architecture enables robust dispersion of the particles in nonpolar environments. The dispersion and enhanced thermal stability in concert with functional properties allow application of inorganic core hedgehogs to a wide array of catalytic reactions in complex liquid media.

4.3 Inorganic Core Synthesis and Characterization

HPs are traditionally synthesized via a hydrothermal process which involves the deposition of ZnO microparticles on carboxylated PS beads. Many studies have shown layer-by-layer (LbL) films to promote NP adhesion on microparticles including on HPs.[28,148,152,215] In a concurrent paper, we describe how polyelectrolyte coatings including weak and strong polyelectrolytes help form uniform and tunable SiO_2 HPs. SiO_2, however, is an inert core, and does not serve any additional function for catalysis and other applications. Based on this method, we looked at expanding the use of layer-by-layer assembly to create a family of functional HPs.

Iron oxide materials such as hematite are used both as a catalyst and to enhance visible light absorption in conjunction with ZnO nanorods.[270,271] The hematite cube cores were synthesized via a literature hydrothermal process (**Figure 4.11**).[272] Deposition of a negative polyelectrolyte using LbL to create a negatively-charged surface is necessary for positively-charged ZnO adsorption (**Table 4.1, Figure 4.12**). Heating hematite cubes in a hydrogen atmosphere at 400°C results in magnetite cubes allowing for the creation of magnetic HPs (**Figure 4.1, 4.11**). [273,274]

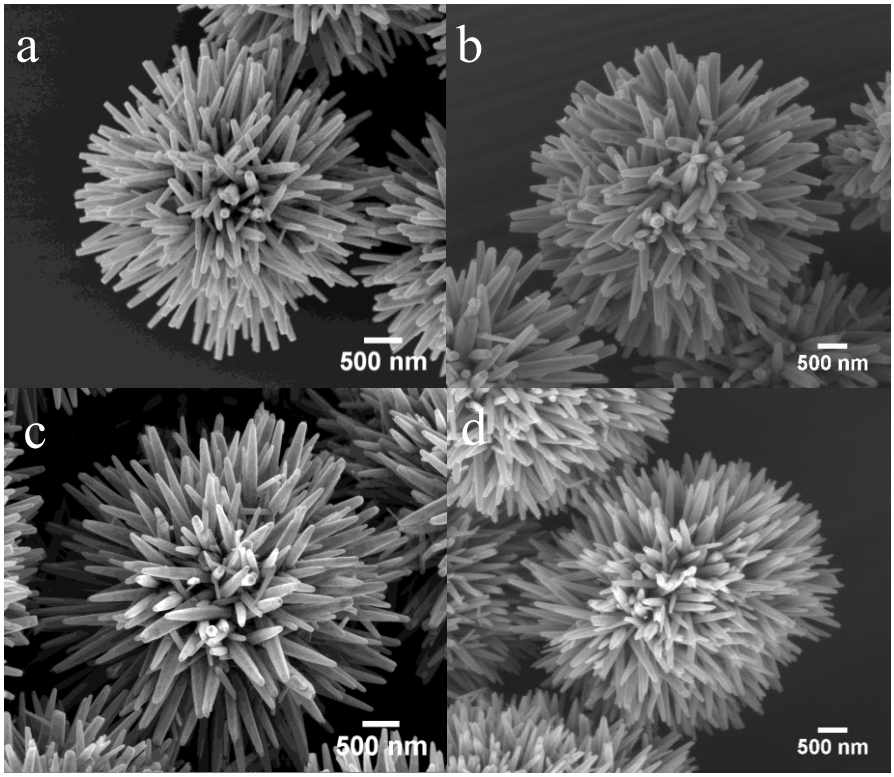

Figure 4.1: SEM images of different inorganic core HPs with ZnO spikes: (**a**) Fe_2O_3 microcube, (**b**) Fe_3O_4 microcube, (**c**) hollow Au microsphere (**d**) hollow TiO_2 microcube with ZnO spikes.

Magnetite HPs enable greatly accelerated purification (one day compared to a week) and easy separation from reaction mixtures for different applications, including catalysis (**Figure 4.13**).

Next, templating of silica and hematite cores was explored to create a variety of hollow catalytic cores to maximize active surface area and light absorption.[275,276] The first material considered was gold, as it can assist with light absorption and help prevent electron hole recombination in semiconductors. 2 nm gold particles capped with tetrakis-(hydroxymethyl)-phosphonium chloride (THPC) were deposited using LbL on SiO_2 cores using methods from our previous work.[215] After a dense coating of gold nanoparticles was obtained on the silica spheres, formaldehyde was used as a reducing agent to create a complete gold shell.[257,277] Hydrofluoric acid was used to dissolve the silica core, leaving behind hollow gold microspheres (**Figure 4.11, 4.14**). With the addition of a PSS LbL layer, ZnO seed was subsequently deposited and hollow AuHPs were synthesized (**Figure 4.1**).

Hollow TiO_2 microparticles have shown excellent photocatalytic activity and been used as an anode material for lithium-ion batteries.[278,279] In this case, titanium dioxide coatings were achieved using liquid-phase TiO_2 deposition using ammonium hexafluorotitanate based on a literature method.[280,281] The hematite core was removed using HCl incubation for a prolonged time so that uniform hollow cubes were produced (**Figure 4.1, 4.11, 4.14**). It was found that a certain thickness of the TiO_2 coating was required for stability; a liquid state deposition of 16 hours, showed uniform hollow cubes, while there was some degradation observed with deposition for only 4 hours (**Figure 4.15**).

4.4 Inorganic core HPs with TiO_2 Spikes

The liquid state deposition process was extended to create hollow TiO_2 spikes as a new photocatalytically-active spike and potential support material. TiO_2 has enhanced chemical stability compared to ZnO while retaining similar high photocatalytic activity.[46,282] Both fully templated structures and core-shell structures can be produced depending on the amount of boric acid used (**Figure 4.2**). The length of incubation and concentration of ammonium hexafluorotitanate can tune the thickness of the TiO_2 coating.[281,283,284] Calcination of the coating

produces crystalline TiO_2 particles with anatase phase (**Figure 4.16**). Additionally, prolonged deposition enables the creation of single component, fully hollow TiO_2 HPs from Fe_2O_3 HP after dissolution of the hematite core with HCL.

4.5 Optical and Thermal Characterization of Inorganic Core HPs

UV-Vis Spectroscopy shows that in particular, spikes with long lengths result in enhanced broadband scattering with all cores as previously observed with HPs.[15,285] (**Figure 4.3**). Even with very different core particle materials, similar extinction is observed, indicating that the spiky array dictates the optical behavior. The base hematite cubes display much greater absorbance in the visible and NIR region. For hematite HPs, a distinct increase in absorbance and defined peak is observed close to 400 nm, corresponding to the ZnO nanorod array[286], as well as a red shift of the hematite peaks. With a gold plasmonic core and shorter length spikes, the absorption extends into the near infrared region (**Figure 4.17**). This indicates potential for synergistic systems with gold and semiconductor spikes for photocatalysis. TiO_2 HPs were also investigated, and a distinct change in absorption is observed as a function of calcination (**Figure 4.18**). A calcination temperature of 600°C appears to produce the most absorption in the UV-region, which likely corresponds to the crystalline anatase

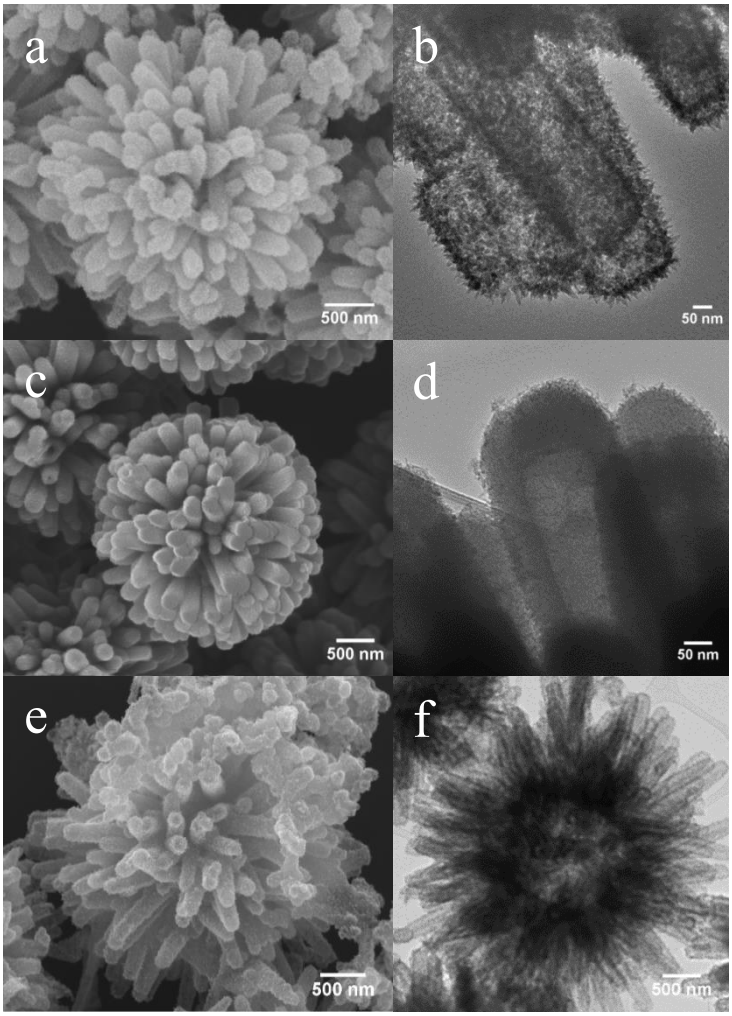

Figure 4.2: TiO_2 HPs created by liquid state deposition of ammonium hexafluorotitanate ($(NH_4)_2TiF_6$). SEM (**a,c,e**) and TEM (**b,d,f**) of (**a,b**) 75mm (**c,d**) 37.5 mM ($(NH_4)_2TiF_6$) on SiO_2 HP (**e,f**) 37.5 mM ($(NH_4)_2TiF_6$) on Fe_2O_3 HPs after treatment with HCL at 100°C for 72 hrs and calcination at 600°C.

phase produced. We expect TiO_2 HPs to show enhanced photocatalytic activity in high ionic strength environments as seen with SiO2 HPs as well as in nonpolar environments.

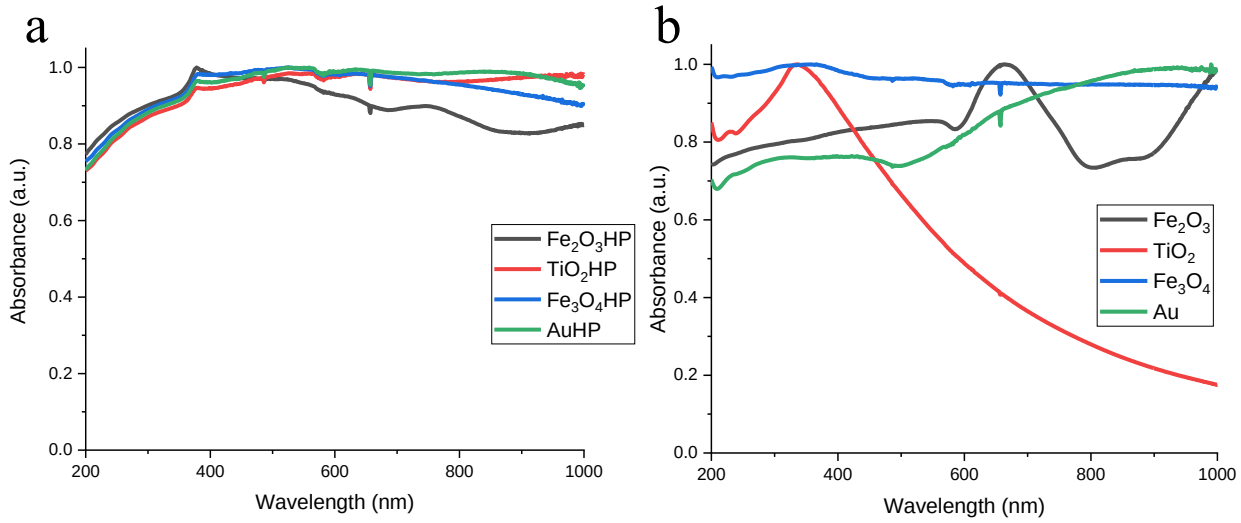

Figure 4.3: Absorbance spectrum of (**a**) HPs with different inorganic cores and (**b**) inorganic microparticle cores without ZnO spikes (SEM images of HPs and core particles and in **Figure 4.1**, and **4.11** respectively).

Thermogravimetric analysis was used to analyze particle stability at the high temperatures used for many catalytic processes. Polystyrene cores, used in the original HPs, are not stable at high temperatures. TGA results confirm the lack of thermal stability as the melting of the cores reduces accessible surface area for catalysis. With inorganic HPs, the morphology is maintained and very little weight loss (corresponding to loss of LbL film) is observed compared to the PS (**Figure 4.4**).

4.6 Apolar Dispersion Stability

HPs with different, inorganic cores were expected to show similar dispersion stability as the original HPs. Hematite, magnetite, hollow gold, and hollow TiO_2 core HPs form stable dispersions in heptane while the corresponding core materials without spikes do not disperse (**Figure 4.5**, **4.19-4.21**). This is confirmed with SEM results that show individual particles and no aggregation while core materials show aggregates (**Figure 4.5**, **4.19**). Confocal microscopy shows well dispersed inorganic HPs modified with a layer of fluorescein-isothiocyanate labeled-PAH in heptane (**Figure 5**, **4.19**). Additionally, the dispersion of core-shell and fully template

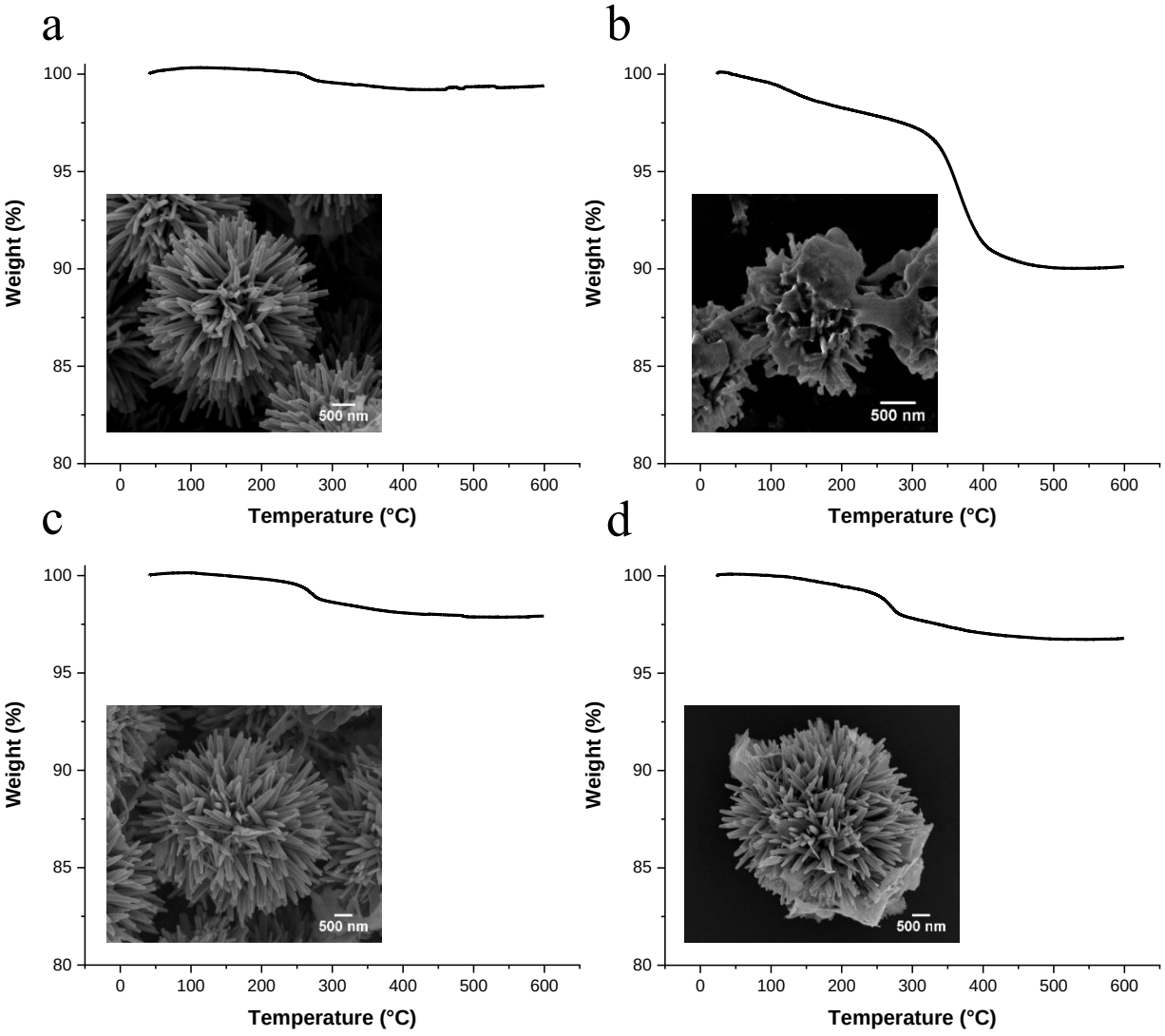

Figure 4.4: Thermogravimetric analysis of inorganic core HPs (Inset: SEM image after calcination at 600°c for 1 hr): (**a**) Fe_2O_3 HP , (**b**) PS HP, (**c**) Au HP, (**d**) TiO_2 HP.

TiO_2 spike HPs were compared to commercial Aeroxide® P25 TiO_2 nanoparticles. The TiO_2 spike HPs stay well dispersed in heptane and chloroform while the P25 nanoparticles form large aggregates (**Figure 4.6**, **4.22-4.23**) as seen in SEM and dispersion images.

In conclusion, HPs with inorganic cores represent a new class of omnidispersible material with functional catalytic, magnetic, and plasmonic properties. Future studies will investigate the use of active hematite cores in Haber-Weiss reactions for accelerated degradation of peroxide-based oxidants. Peroxide-based oxidants are used in many industrial organic processes, and the use of HPs to facilitate expansion to a wide array of chemical environments has the potential to help increase efficiency in numerous reactions.[94]

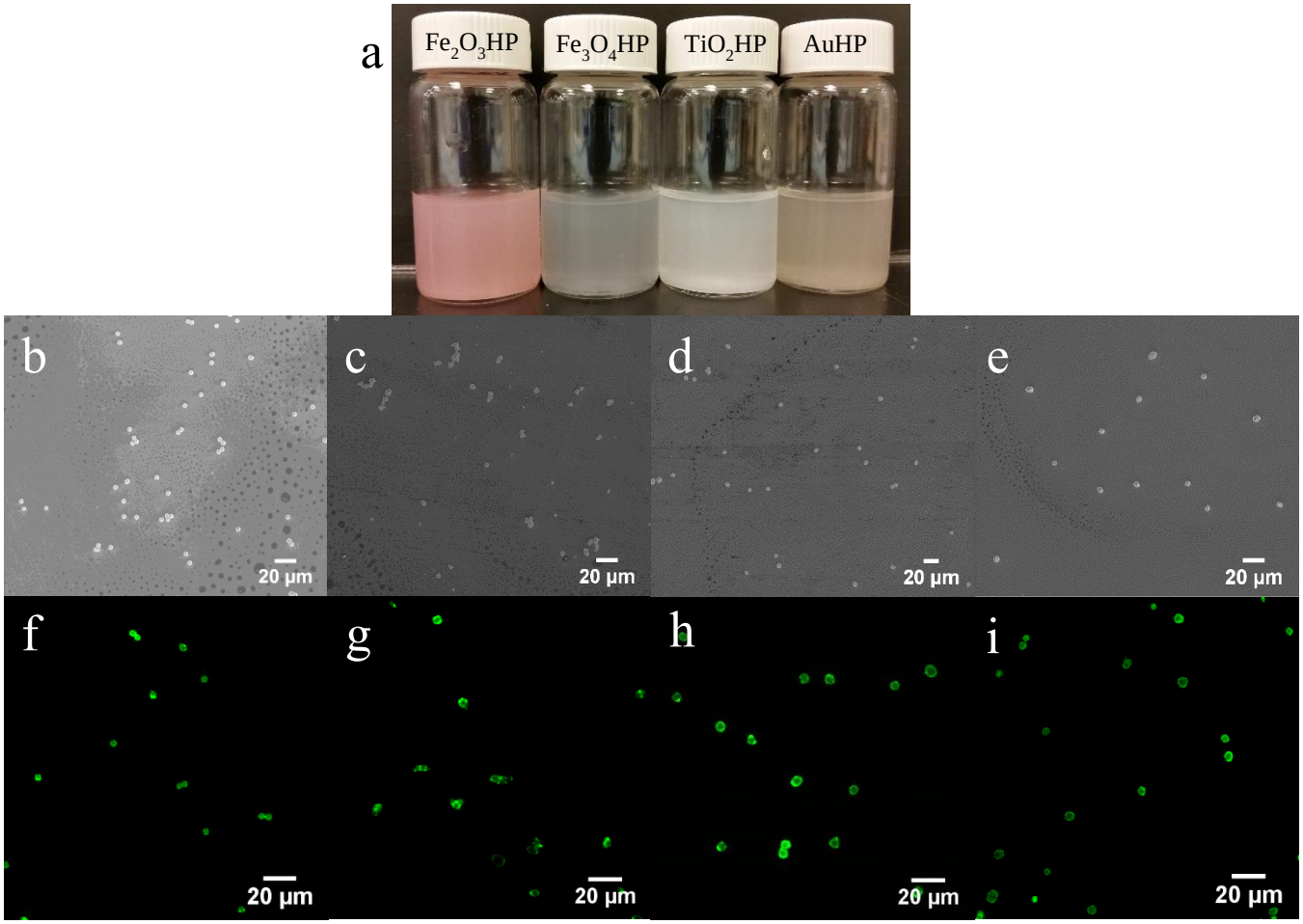

Figure 4.5: (**a**) Image of dispersions of inorganic ZnO HPs (0.5 mg/mL) in heptane (0.5 mg/mL). SEM (**b-e**) and Confocal (**f-i**) images of Dispersions of **(b,f)** Fe_2O_3HP, (**c,g**) Fe_3O_4HP, (**d,h**) TiO_2HP, and (**e,i**) AuHP. Confocal Microscopy was done using FITC-PAH coated core microparticles. All particles were dispersed at 0.05 mg/mL.

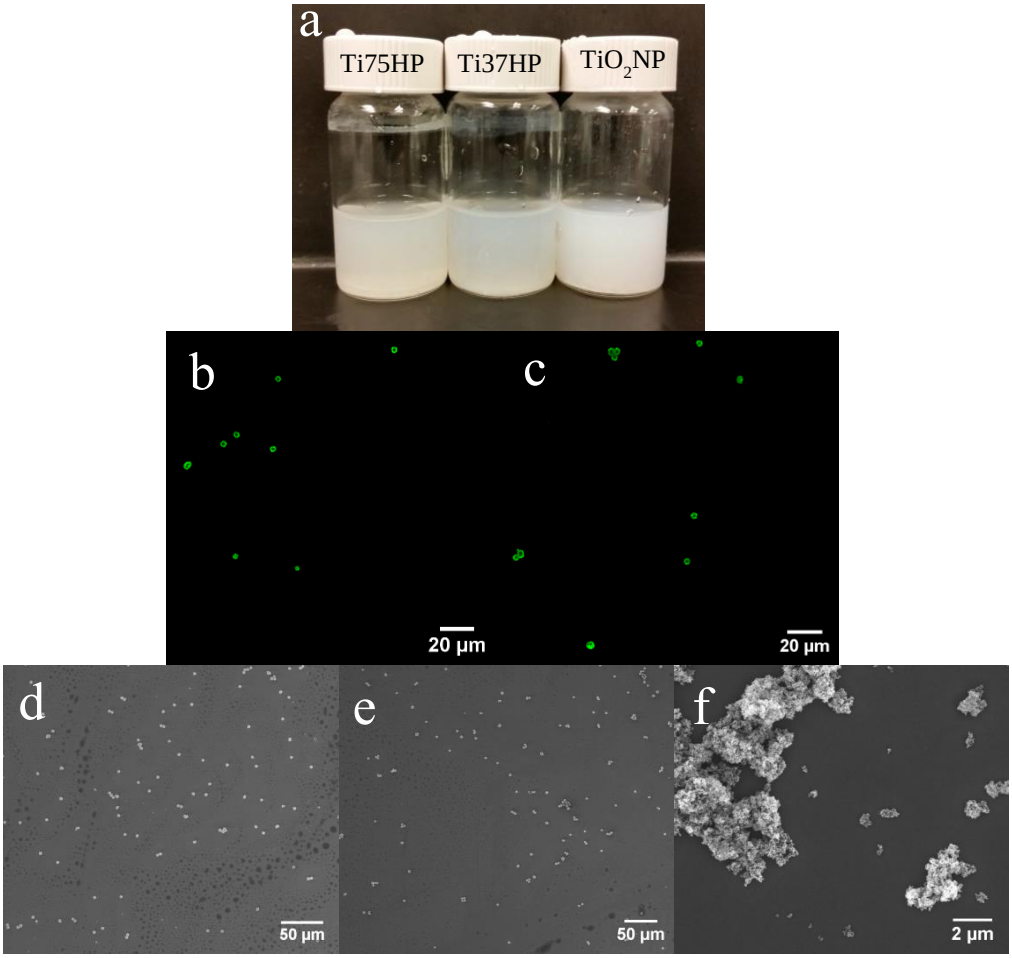

Figure 4.6: (**a**) Image of dispersions of 37.5 mM and 75 mM TiO_2 spike SiO_2 HP and TiO_2 NP in heptane (0.5 mg/mL). Confocal microscopy of SiO_2 HP with (**b**) 75 mM (**c**) 37.5 mM TiO_2 spikes. SEM images of SiO_2 HPs with (**d**) 75 mM (**e**) 37.5 mM TiO_2 spikes, and (**f**) TiO_2 NPs in heptane.

4.7 Cyclohexane Oxidation and Epoxidation with Photocatalytic HPs

The photo-oxidation of alkanes has wide spread applications in organic synthesis. The synthesis of KA-oil consisting of cyclohexanone and cyclohexanol from the oxidation of cyclohexane involves over 8000 kilotons produced annually primarily for the industrial production of Nylon 6 and Nylon 6,6.[287] Traditionally, industrial production of KA-oil involves oxidation with molecular O_2 at high pressure and high temperatures with good selectivity (85-90%) at the expense of low conversion (4-15%).[288] This has led to the exploration of a wide array of alternative methods for producing nylon precursors including oxidants such as hydrogen peroxide[289] or t-butyl hydroperoxide[290,291] with cyclohexane. Photocatalytic oxidation of

cyclohexane has primarily been investigated with semiconductors such as titanium dioxide.[268,292] Traditionally cyclohexanone is observed as a dominant product with selectivity dependent on light source and water content.[293]

An alternative pathway to nylon precursors is through cyclohexene oxidation. Cyclohexene oxidation to adipic acid was demonstrated by Sato et al. in 1998 utilizing Na_2WO_4 catalyst and an acidic phase-transfer reagent $[CH_3(n\text{-}C_8H_{17})_3N]HSO_4$ but requiring a very high consumption of H_2O_2 for each mol of adipic acid.[294] Cyclohexene is produced by partial hydrogenation of benzene which requires higher temperatures with moderate selectivity.[94] Many other studies have followed involving polyoxometalates and other materials for the process including with molecular oxygen and other oxidants.[295,296]

Cyclohexene oxide is a valuable industrial intermediate which is used in a wide array of products including pesticides, stabilizers for halogenated hydrocarbons, and pharmaceuticals.[297,298] Cyclohexene oxide is primarily formed through the epoxidation of cyclohexene. Synthesizing cyclohexene oxide directly from cyclohexane which is more stable and widely produced is desirable. Epoxidation of olefins is also valuable for the production of many different epoxy and rubber-based products.

There has been limited exploration of photocatalysts and dispersible nanocatalysts due to poor dispersion stability. One method for catalyst activation in nonpolar systems involves the use of emulsions and interfacial catalysts such as oxides. [226,299] A new dispersion strategy based on surface corrugation utilizing 'Hedgehog' particles (HPs) was recently introduced.[15] These HPs were expanded with different films[215], as well as utilization of new inorganic core materials. HPs show a marked reduction of van der Waals forces allowing for dispersion in both polar and non-polar environments.

Here we report the use of a photocatalytic HP in combination with a green oxidant functioning in a Haber-weiss mechanism for accelerated degradation of hydrogen peroxide. Through utilization of active HPs in a water/cyclohexane emulsion, we see the production of cyclohexene oxide directly from cyclohexane in one-step utilizing Fe_2O_3 HPs with ZnO spikes. In this case, by using an active Fe_2O_3 catalyst core with ZnO and TiO_2 spikes, a new direct one-step pathway to cyclohexene oxide is developed, and reaction selectivity is engineered utilizing HP composition.

4.7.1 Synthesis of HP Catalysts

Hematite cores were synthesized using a literature hydrothermal method.[272] ZnO HPs were synthesized using a method described in a previous publication. Layer-by-layer films were used to conformally deposit ZnO seeds onto hematite cores and then sonothermal growth of ZnO spikes was used to create HPs with diameters close to 4 μm (**Figure 4.7a**). Liquid state deposition of ammonium hexafluorotitanate with boric acid was used to create a TiO_2 HPs as described previous study. In this case, the incubation was for 4 hours to produce a thin coating that was still stable after heating. Samples were calcined at 500° C to create crystalline anatase TiO_2 (**Figure 4.7b-e**). A uniform coating is observed including on the core particle with crystalline spikes.

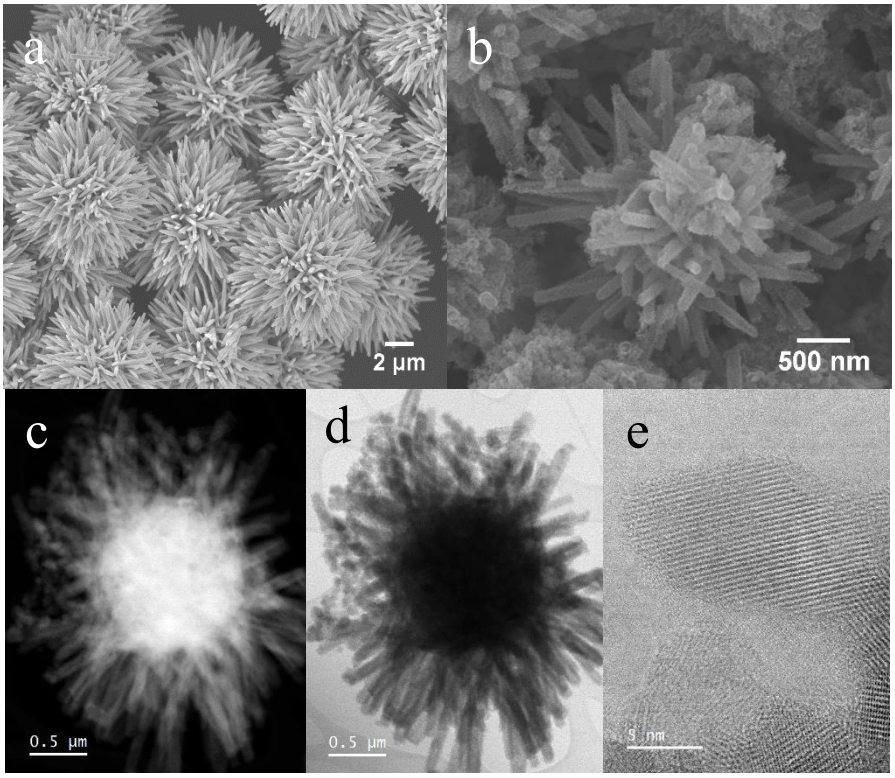

Figure 4.7: SEM image of ZnO HP with Fe_2O_3 core (**a**) and TiO_2 hp with Fe_2O_3 core (**b**) annular dark-field (**c**), and bright-field (**d**) and high resolution TEM images (**e**) of TiO2 HP with Fe_2O_3 core.

4.7.2 Oxidation of Cyclohexane with ZnO HPs

An emulsion system with cyclohexane and water was chosen so that hydrogen peroxide could be used with the expectation that HPs would help stabilize the emulsion. The presence of

water has been shown to increase the concentration of hydroxyl radicals on the surface and in solution which can react to form cyclohexanone and cyclohexanol. It also can promote desorption of cyclohexanone and cyclohexanol.[268] The reaction is shown below in **Scheme 4.1**. While the first 3 products are well established in the oxidation of cyclohexane, the production of cyclohexene epoxide has not been reported in literature.

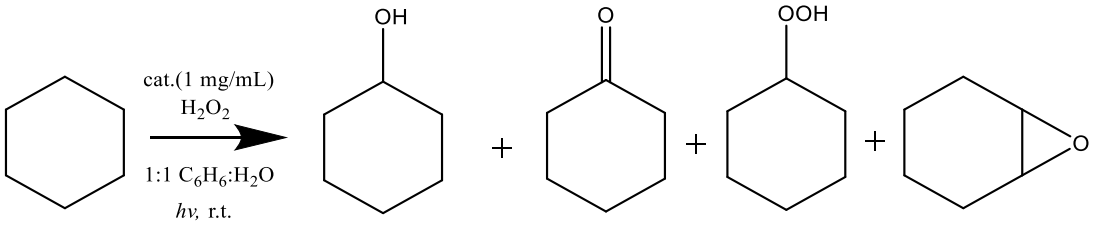

Scheme 4.1: Oxidation of Cyclohexane

A Fenton-like mechanism with hydrogen peroxide is expected to occur with the hematite core of the HP.[300] This is consistent with the increased amount of cyclohexyl hydroperoxide, and its decomposition products, cyclohexanol, and cyclohexanone observed with all hematite samples. First a low concentration of H_2O_2 (12 mM) consistent with studies of fenton-based mechanisms was tested (**Figure 4.8a**). HPs result in an enhancement in the production of cyclohexyl hydroperoxide and cyclohexanone over cubes, which is expected due to OH· radicals produced by ZnO. Next, a higher concentration of H_2O_2 (1 M) was tested to further promote production of alkyl hydroperoxide. The higher concentration of H_2O_2 has a drastic effect on the product distribution. Cyclohexene epoxide is seen as a major product with HPs but not with cubes or the control (**Figure 4.8b**). As expected, there is also an increase in cyclohexyl hydroperoxide and cyclohexanone production with both cubes and HPs. The formation of the epoxide in a one-step process from cyclohexane has not been reported in literature.

Kinetic results show that the epoxide yield still increases to over 1 mM for reaction times for 64 hrs (**Figure 4.8c**) albeit at a slower rate. The epoxide traditionally is produced in the oxidation of cyclohexene which can be formed from the dehydration of cyclohexanol or cyclohexane.[301] The epoxide stability is likely due to non-acidic conditions that were employed in the synthesis, otherwise hydrolytic ring cleavage would be expected.[294,302] The dehydration of cyclohexanol to cyclohexene is dependent on the acidic sites on the catalytic surface. ZnO has been shown to be selective in the production of cyclohexene from cyclohexanol, so we suspect that this is how cyclohexene is produced.[303] With the lack of additional alkenyl species such as cyclohexen-2-one (negligible amounts were detected), it is clear that the hydroperoxidation of the allylic

carbon atom via an H-abstraction by a HO• radical is not favored, while epoxidation is. This selectivity could be beneficial other reactive alkenes in addition to cyclohexene which have multiple oxidation sites.

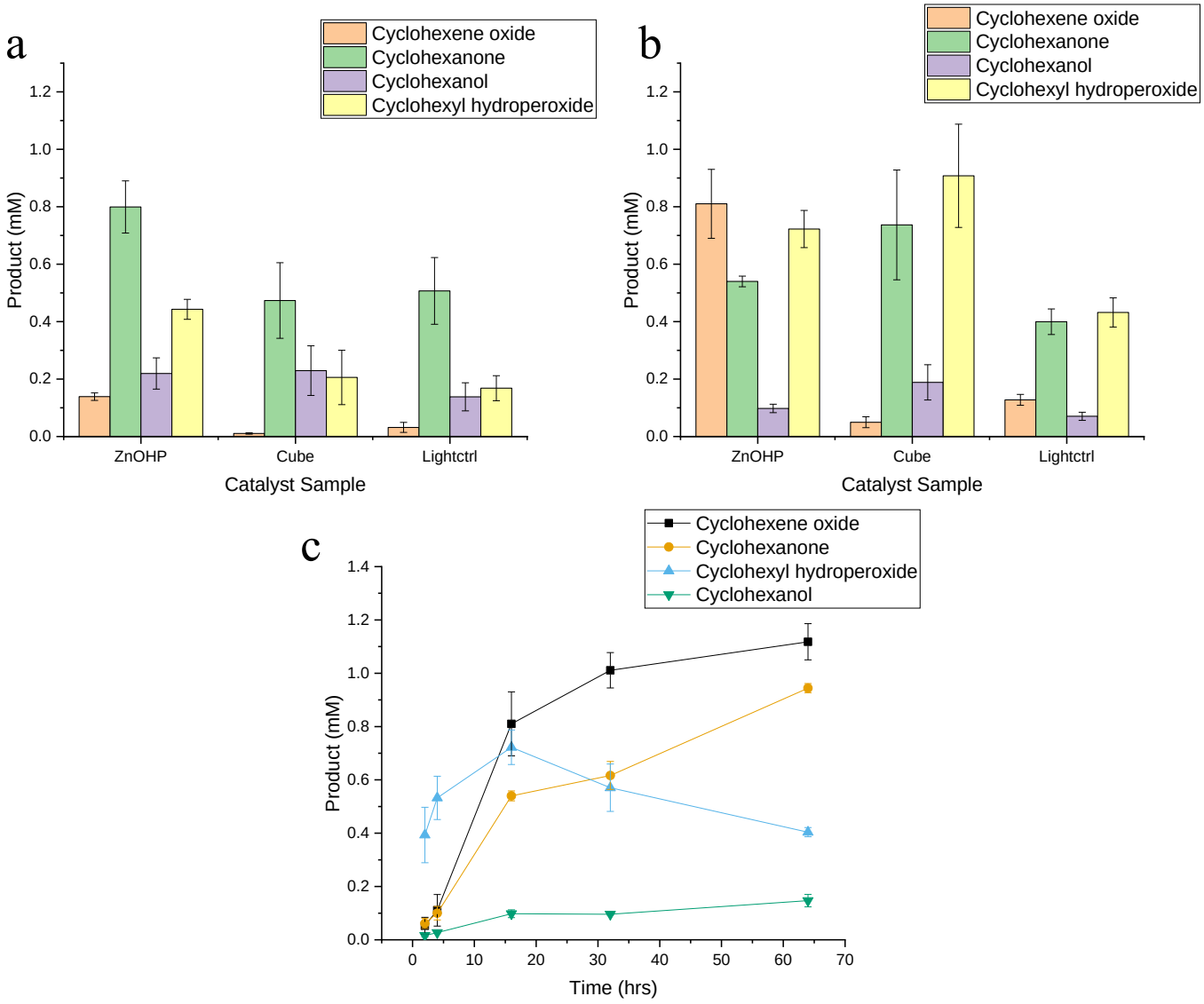

Figure 4.8: Product distribution from the oxidation of cyclohexane in a 1:1 cyclohexane/aqueous H_2O_2 emulsion emulsion (1:1) with 1mg/mL catalyst. 12mM H_2O_2 (a) 1 M H_2O_2 (b). Product distribution as a function of time for oxidation of cyclohexane with ZnO/Fe_2O_3 HP.

For the process, we expect, that likely the cyclohexane is oxidized to cyclohexene (step A) and then through epoxidation converted to cyclohexene oxide (Step B) (**Figure 4.9a**). Step A is expected to consist of oxidation to cyclohexanol and then dehydration to cyclohexene by zinc

oxide as mentioned earlier. Corresponding with the reduction in rate of epoxide production, there is a significant decrease in the concentration of cyclohexyl hydroperoxide from 16 to 64 hours, indicating that it is a probable intermediate. Cyclohexanone yield increases by a factor of close to two times, likely from decomposition of the hydroperoxide (**Figure 4.9b**). The suspected pathway to cyclohexene oxide, is through the oxidation to cyclohexene from dehydration of cyclohexanol, and the epoxidation reaction to form cyclohexene oxide, which is greatly enhanced at high concentrations of hydroperoxide (**Figure 4.9c**).[304,305] The light source accelerates degradation of H_2O_2 and generates OH radicals for oxidation through ZnO and Fe_2O_3.

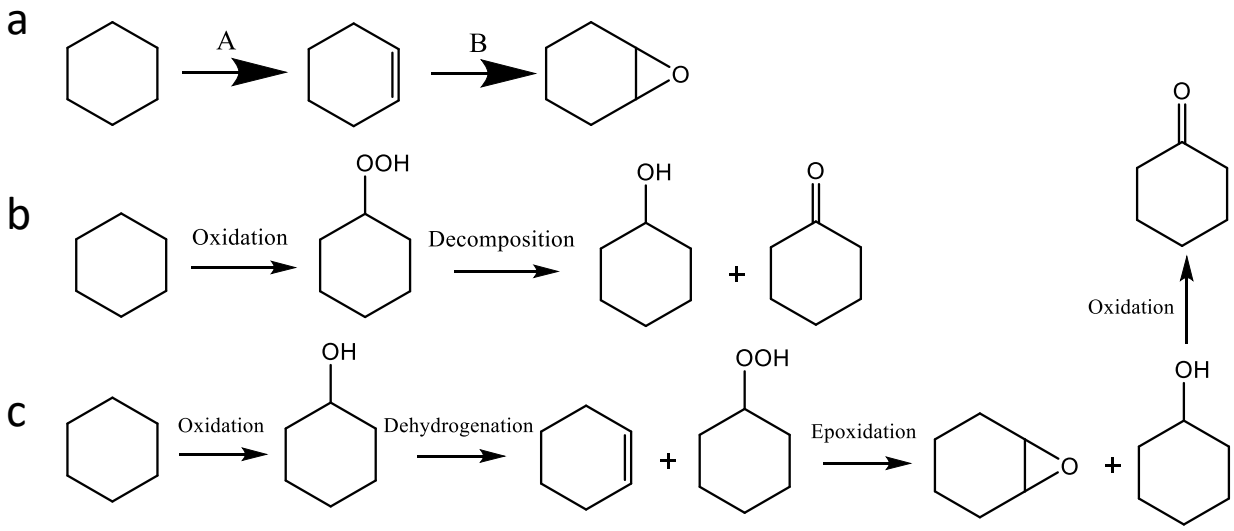

Figure 4.9: Different schematics of cyclohexane oxidation with HPs. (**a**) The major proposed pathway of oxidation of cyclohexane to cyclohexene (A) and then epoxidation of cyclohexene to cyclohexene oxide (B). (**b**) Pathway for oxidation of cyclohexane to cyclohexyl hydroperoxide with decomposition to cyclohexanone and cyclohexanol. (**c**) Proposed pathway for cyclohexane oxidation to products involving cyclohexene and cyclohexyl hydroperoxide (formed in B) resulting in production of cyclohexene oxide and cyclohexanone. This does not include oxidation to CO_2 which is likely to happen to some of the cyclohexanol and cyclohexene produced.

To further explore the roles of ZnO and Fe_2O_3, ZnO nanorods were tested, which show limited production of cyclohexene oxide. A decrease in the cyclohexyl hydroperoxide is observed without the Fe_2O_3 core which is needed at a higher concentration to produce cyclohexene oxide (**Figure 4.10a**). Potential intermediates were also added at the beginning of the reaction, to see how they influenced product distribution. 1 mM cyclohexene inhibits the reaction, in particular, the production of cyclohexyl hydroperoxide and cyclohexene oxide significantly. This is surprising, as it is the most logical intermediate. We believe, that the cyclohexene must function with cyclohexyl hydroperoxide for the epoxidation reaction to occur

(**Figure 4.9c**) and without the hydroperoxide at the beginning, it follows an oxidative pathway to CO_2 which also reduces formation of cyclohexyl hydroperoxide. The lower amount of cyclohexyl hydroperoxide and less favored dehydrogenation reaction, we believe then leads to minimal cyclohexene oxide production. We also added 1 mM cyclohexanol which does not appear to have a large effect on the reaction, except that this cyclohexanol is clearly consumed, which we believe would be through oxidation to CO_2 which is well-documented.[290,293] With 2 M H_2O_2 we see a decrease in the production of cyclohexanone with similar amounts of the cyclohexene oxide, which we believe is due to reduced light absorption in ZnO for oxidation to cyclohexanone (**Figure 4.24**). Based on these results, we believe ZnO plays a pivotal role in the dehydrogenation of cyclohexanol to form cyclohexene intermediate which then interacts with the cyclohexyl hydroperoxide in an epoxidation reaction which is accelerated by the hematite core. The high interfacial area and stability of HPs seen in the reaction, also promote oxidation at the interface (**Figure 4.25**). We hypothesize that this allows for the dehydrogenation and epoxidation to occur in one step to produce cyclohexene oxide with further investigation planned.

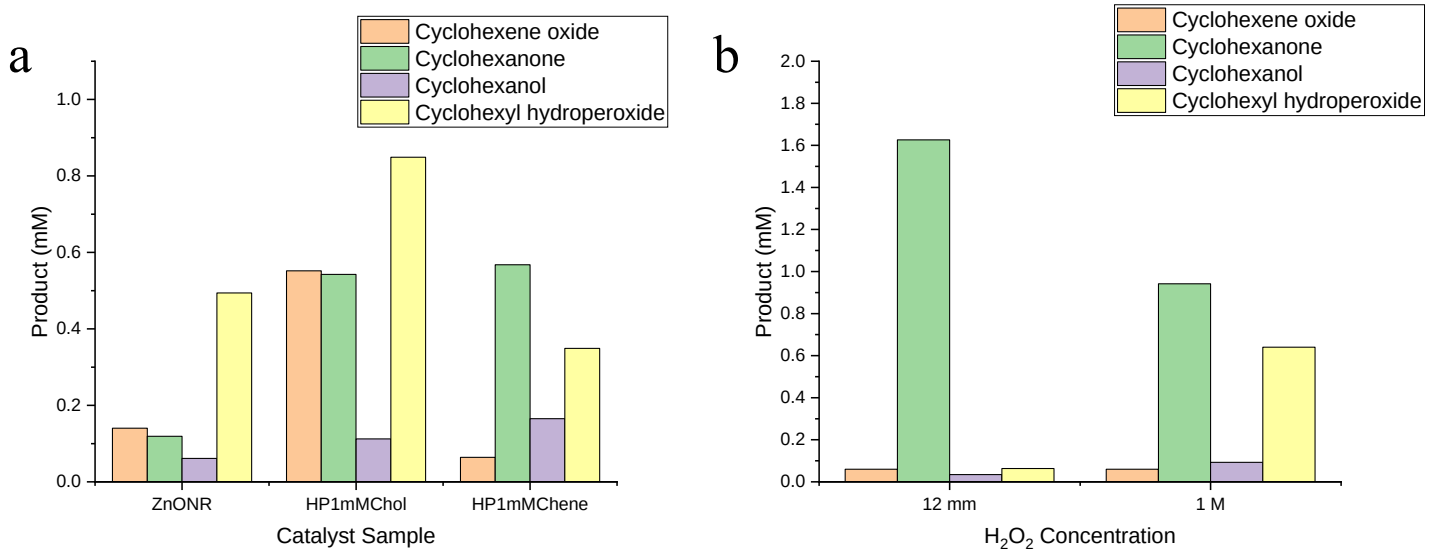

Figure 4.10: Preliminary results from oxidation of cyclohexane: (**a**) oxidation of cyclohexane using different ZnO catalyst samples and additives with 1 M H_2O_2 ; (**b**) oxidation of cyclohexane utilizing 12mm and 1 M H_2O_2 with TiO_2 HPs with Fe_2O_3 cores. All experiments were conducted with X-cite® 120 light source for 16 hrs.

4.7.3 Oxidation of Cyclohexane with TiO_2 HPs

To investigate and better understand production of cyclohexene oxide, TiO_2 HPs were also investigated. Preliminary Results indicate that TiO_2 HPs show a much greater selectivity to cyclohexanone, with over two times the product of ZnO HPs with 12 mM H_2O_2(**Figure 4.10b**). Minimal cyclohexyl hydroperoxide is observed, indicating that the deperoxidation happens quickly. However, TiO_2 HPs at high H_2O_2 concentrations do not show production of the cyclohexene oxide. A distinct difference between the ZnO and TiO_2 HPs, is that the TiO_2 coating, completely covers the hematite core, likely dominating the reactivity. This is consistent with the increase in production of cyclohexanone with lower concentrations of H_2O_2. OH radicals on the surface are expected to result in oxidation to cyclohexanone. With higher concentrations of H_2O_2, ultraviolet light is absorbed by the H_2O_2 which is not as efficient in the oxidation of cyclohexane as the TiO_2 HPs. The limited effect of H_2O_2 indicates that the Fe_2O_3 core is having a very limited effect, and due to the thickness of the TiO_2 coating, might be absorbing limited light. As a catalyst without additional oxidant, the TiO_2 HPs outperform ZnO HP.

The oxidation with TiO_2 catalysts is well-documented in literature with oxidation to cyclohexyl hydroperoxide from cyclohexyl radical and then decomposition into cyclohexanone and cyclohexanol (**Figure 4.9b**). Cyclohexanol can be easily converted into cyclohexanone through an additional oxidation, which we expect is happening. The cyclohexanol product is also more likely to be oxidized directly into CO_2. Additionally, cyclohexyl hydroperoxide can be oxidized into cyclohexanone and water.

4.7.4 Conclusions

HPs in an emulsion system with a green oxidant and light source have enabled conversion of cyclohexane directly into cyclohexene oxide for the first time. The selectivity is dependent both on the hydrogen peroxide oxidant concentration, and HP composition. This could have large implications in other organic synthesis reactions, as it is a new pathway that has not been seen in literature. The exploration of HPs as a catalyst for olefin synthesis and epoxidation

and in other epoxidation reactions could lead to use of this pathway and discovery of other new pathways for synthesis of other important chemicals and chemical intermediates.

4.8 Methods

All chemicals were ordered from Sigma-Aldrich unless noted otherwise. grids with ultrathin carbon film on holey carbon film support for transmission electron microscope (TEM) measurements and silicon wafers for scanning electron microscope (SEM) measurements were purchased from Ted Pella (Redding, CA). Polycarbonate track-etched membranes (0.8 micron, 90 mm) were ordered from Sterlitech.

4.8.1 Synthesis of Core particles

Hematite cube particles were synthesized based on a literature hydrothermal method.[272] Briefly, in a typical procedure, $FeCl_3 \cdot 6H_2O$ and NaOH were added to an autoclave at a fixed molar ratio (3:5) which was then heated at 160° C for 24 hours. The synthesized cubes were then washed two times in ethanol and water to remove excess reactants. Magnetite cores were produced from heating hematite cores in a calcination oven at 400°C for 24 hrs in H_2 atmosphere.[273] TiO_2 cores were obtained from the liquid-state deposition of TiO_2 on hematite using 75 mM ammonium hexafluorotitanate $(NH_4)_2TiF_6$ and 0.2 M boric acid (H_3BO_3) for 16 hours (as described in Section 4.3).[280] 0.5 M HCl incubation at 100° C for 96 hours was used to remove hematite to create hollow cores.

For Au cores, 2 nm gold nanoparticles (AuNPs) were synthesized using Tetrakis(hydroxymethyl)phosphonium chloride (THPC) in a literature method.[277,306] Briefly, 0.5 mL of 1 M NaOH and 1 mL of THPC solution (12 µL of 80% THPC in 1 mL nanopure water) were added to 45 mL of nanopure water. The reaction mixture was stirred for 5 min, followed by the rapid addition of 10mL of 5 mM $HAuCl_4 \cdot 3H_2O$ to the stirred solution. The AuNPs were utilized in the layer-by-layer coatings of SiO_2 microparticles (described below in 4.2). The coated SiO_2 particles were then used for gold shell formation as described in the literature.[257] The gold hydroxide used for shell formation was synthesized by adding 0.25 g K_2CO_3 to 925 mL of nanopure water. After stirring 10 minutes, 75 mL of 5 mM $HAuCl_4 \cdot 3H_2O$ was added quickly. After stirring 1 hour, the solution was aged in the dark for 24 hours before use. Briefly, 1-5 mL of gold nanoparticle-coated SiO_2 particles dispersed in nanopure water were added to 75-150 mL

of $Au(OH)_3$. In five minute increments, 5-15 mL of 37% formaldehyde was added to the solution, followed by 2-10 mL of 29% ammonium hydroxide. The particle slurry was then poured into centrifuge tubes and the Au-modified SiO_2 particles were centrifuged/washed three times with water. The particles were then incubated in 2% hydrofluoric acid for 24 hours to dissolve SiO_2 and centrifuged/washed six times to remove any remaining acid.

4.8.2 Layer-by-Layer Coating of Core Particles

Positively-charged inorganic cores were coated with polystyrene sulfonate (PSS, 0.5 M NaCl) in a layer-by-layer process to enhance ZnO seed adsorption and will be described in detail in another concurrent study. Negatively-charged cores were coated with poly(dimethylammonium chloride) (0.5 M NaCl) and then PSS (0.5 M NaCl). To make Au-modified cores, SiO_2 was coated with $(PSS/PDDA/AuNP)_2$ utilizing AuNP described above. Briefly, 5 mL core was mixed with 25 mL polyelectrolyte (1 mg/ mL, 0.5 M NaCl) or 25 mL nanoparticle solution and incubated for 20 minutes. Cores were then centrifuged at 4000 RPM and washed with water 3 times before repeating the process with the next layer.

4.8.3 Synthesis of Inorganic HPs

Inorganic HPs were synthesized using a scaled sonothermal synthesis based on that of Bahng et al.[15] 1.25 mL of coated core solutions (2.5 wt%) was mixed with 40 mL ZnO seed solution (0.025 wt%) and incubated for 1 hour. Particles were then filtered using a 0.8 micron track etch membrane and combined with equimolar (25 mM) solutions of zinc nitrate hexahydrate (ZNH) and hexamethylenetetraamine (HMT) in water. Concentrations of the precursors were varied to tune the width of the spikes, with a default concentration of 25 mM. The solution was then filled to a final volume of 1.6 L with nanopure water and sonicated using a Hielscher 1000UIP HdT sonicator for 1 hour and 30 minutes. HPs used in the study were purified by sedimentation over a week and then an additional sonication (25 mM additional precursors, 2.5 hours) was used to grow longer and more uniform spikes. For catalysis samples, 2 additional growths involving sonication with 37.5 Mm ZnH and HMT for 2.5 hours were done once HPs were fully purified to increase length and uniformity. Nanorods were collected from the supernatant in the first wash to use as a catalyst benchmark.

4.8.4 TiO_2 Templating of ZnO HP

Liquid-state deposition of TiO_2 on HP was achieved using ammonium hexafluorotitanate $(NH_4)_2TiF_6$ and boric acid (H_3BO_3).[280] 12 mL of HPs (~3 mg/mL) and 6 mL $(NH_4)_2TiF_6$ (112.5 mM or 225 mM) were combined and incubated on a shaker. After 5 minutes, 4.5 mL of $(NH_4)_2TiF_6$ solution and 9 mL of H_3BO_3 solution (0.5 M) were added. After an additional 5 minutes, another 4.5 mL of $(NH_4)_2TiF_6$ and 9 mL of H_3BO_3 were added of the same concentration bringing the final concentration to 0.2 M H_3BO_3 and 37.5 or 75 mM $(NH_4)_2TiF_6$ for core-shell or fully templated structures respectively. After centrifuging for 1000 RPM for 10 min, the solution was replaced with 35 mL with 0.5 M H_3BO_3 or 1 M H_3BO_3. For catalysis samples, 37.5 mM $(NH_4)_2TiF_6$ and 0.2 M H_3BO_3 was used for liquid state deposition for a total of 4 hrs

4.8.5 Zeta Potential

For ζ-potential measurements, a 100 μL aliquot of core particles was set aside after deposition of each layer, and 900 μL of water was added before each zeta potential measurement was taken. The ζ-potentials were measured using a Malvern Zetasizer Nanoinstrument Nano ZS. Each value was averaged from three parallel measurements.

4.8.6 Confocal Microscopy

For confocal studies, FITC was conjugated to PAH according to a literature procedure and mentioned in a previous publication.[193,215] Briefly, 4.5 mg FITC was dissolved in 1 mL dimethylsulfoxide (DMSO) and combined with 500 mg PAH dissolved in 6 mL water. The pH of the solution was adjusted to 8.4 with NaOH and then the solution was stirred for 2 days. Dialysis was then performed using a D-tube™ Dialyzer for 24 h to remove excess FITC.[193] PAA/FITC-PAH films were deposited on HPs and inorganic cores using LbL assembly with the same procedure described previously.[215]

4.8.7 Electron Microscopy

20 μL of sample was dispersed on a silicon wafer and then evaporated. Afterwards, samples were sputter coated with gold using a SPI-Module Carbon/Sputter Coater. Particles were imaged using a FEI Nova 200 Nanolab SEM and FEI Helios 650 Nanolab SEM/FIB. NPs and

coating were imaged using a JEOL 3011 High Resolution Electron Microscope. For Dispersion SEM images, particles were at a concentration of 0.1 mg/mL.

4.8.9 Thermogravimetric Analysis

Thermogravimetric Analysis was done using a Discovery TGA Q5000IR (TA Instruments inc., Delaware, USA). 1-3 mg of HP sample was heated from ambient to 600°C at a heating rate of 10°C/min with a nitrogen flow rate of 50 mL/min.

4.8.10 Photocatalysis Experiments

A metal halide lamp (X-Cite® 120) was used for all photocatalytic experiments at a specified distance (**Figure 4.25**) to minimize heating of the reaction solution. All experiments were done using 15 mL cyclohexane and 15 mL water with a specified amount of hydrogen peroxide. A quartz flask was used with a condenser attached to prevent evaporated.

4.8.11 Product analysis with GC

After reaction, the sample was transferred to a scintillation vial. After 10 minutes to allow the phases to separate, 2 1 mL aliquots from the cyclohexane phase was removed. To one aliquot, excess triphenylphosphine was added to convert all remaining cyclohexyl hydroperoxide to cyclohexanol based on a literature method.[307] After 15 minutes both of these were analyzed with a Gas Chromatograph (GC-2014A, Shimadzu) with a capillary flame ionization detector (FID) with a RTX-5 60m 0.5 µm column. An injector temperature of 270°C was used and temperature was ramped 10°C/min from 60C (hold for 1 minute) to 260°C (hold for 2 minutes For each product, controls were run to determine the concentration of each product in the sample. GC-MS was also used to verify products.

4.9 Supplementary Results

Table 4.1: Zeta potential of hematite microcubes as a function of layer number

Fe_2O_3 Cube	**Zeta Potential (mV)**
Layer0	35±4.28
Layer 1 PSS	-33±3.68

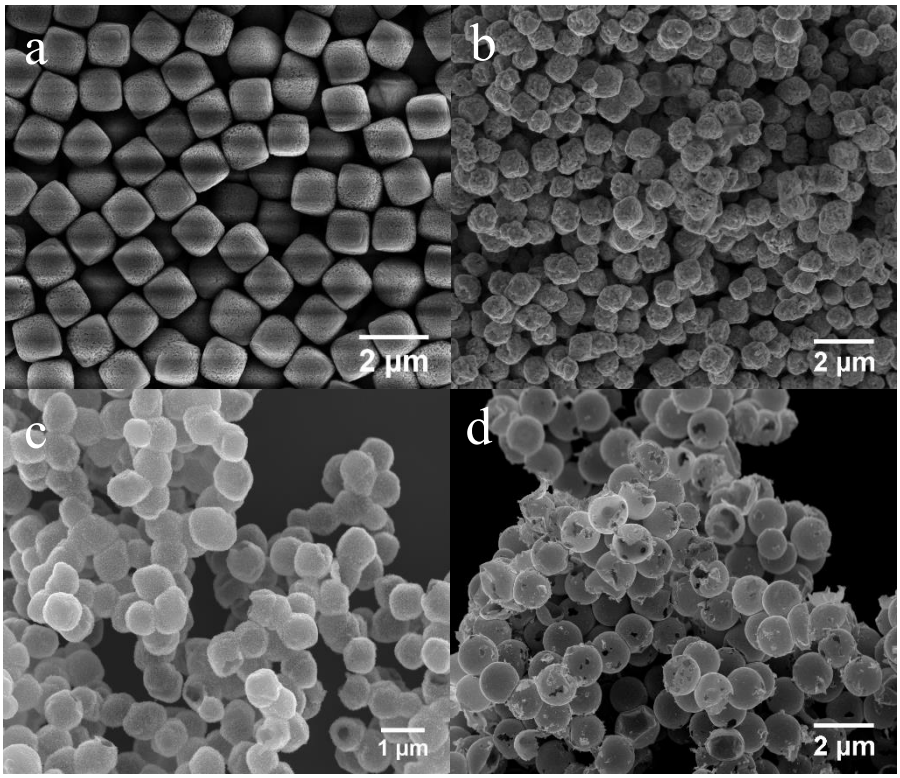

Figure 4.11: SEM images of (**a**) Fe_2O_3 cubes, (**b**) Fe_3O_4 cubes, (**c**) hollow TiO_2 cubes, and (**d**) hollow Au spheres that were utilized as inorganic cores for HPs.

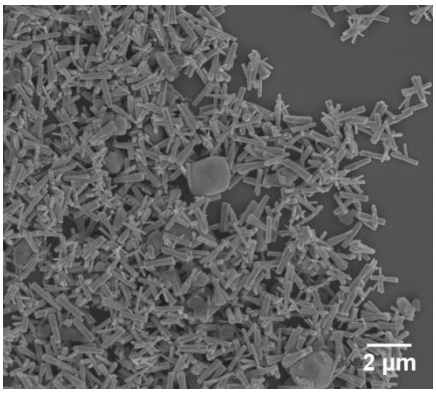

Figure 4.12: HPs formed without LbL coating using Fe_2O_3 Cubes

Figure 4.13: Magnetite HPs (0.5 mg/mL) after applying neodymium magnet for 1 minute.

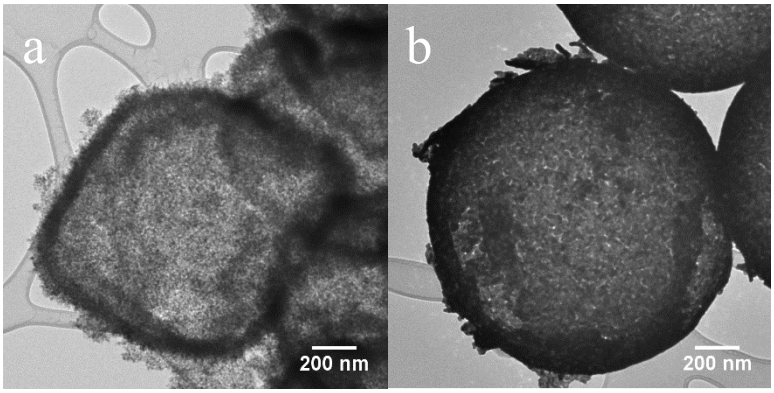

Figure 4.14: TEM images of (**a**) hollow TiO_2 cubes and (**b**) hollow Au spheres (SEM in Figure 4.11)

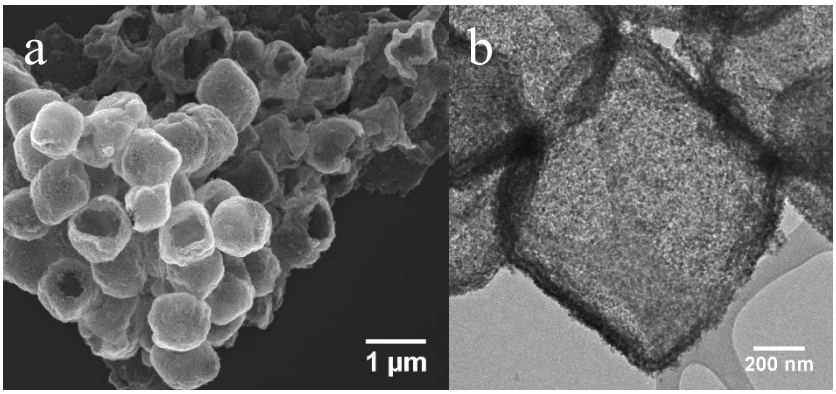

Figure 4.15: SEM (**a**) and TEM (**b**) of hollow TiO_2 cores created with 4 hr incubation with ammonium hexafluorotitanate.

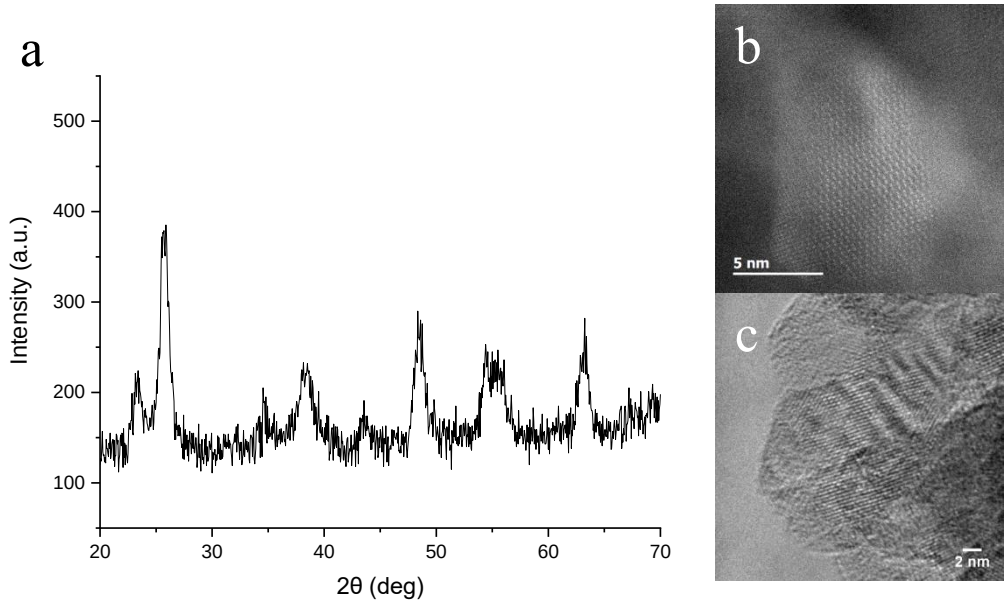

Figure 4.16: (**a**) XRD of TiO_2 HPs calcined at 600°C, (**b**) STEM and (**c**) HRTEM of TiO_2 HPs calcined at 600°C.

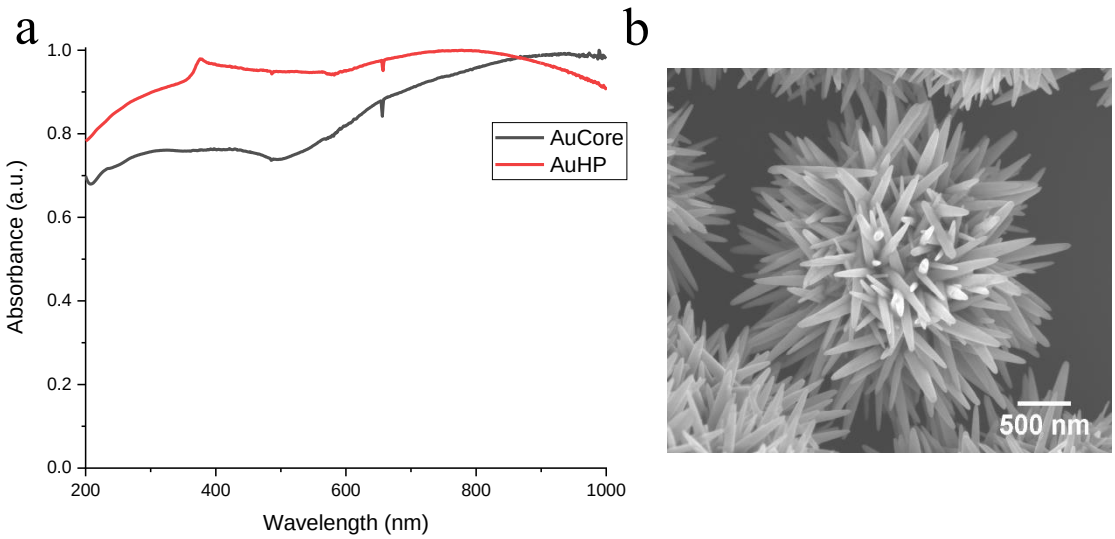

Figure 4.17: (**a**) UV-Vis absorbance spectrum for single growth Au HP, (**b**) SEM image of single growth Au HP

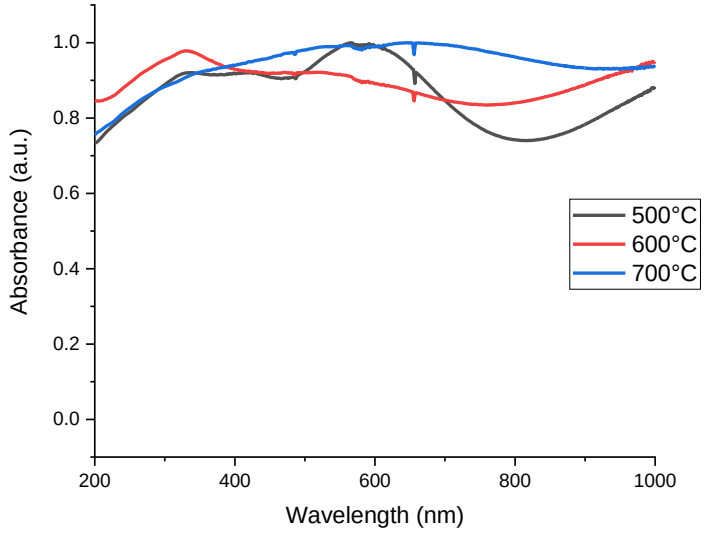

Figure 4.18: Absorbance spectrum of 75 mM TiO_2 HPs calcined at different temperatures for 1 hour.

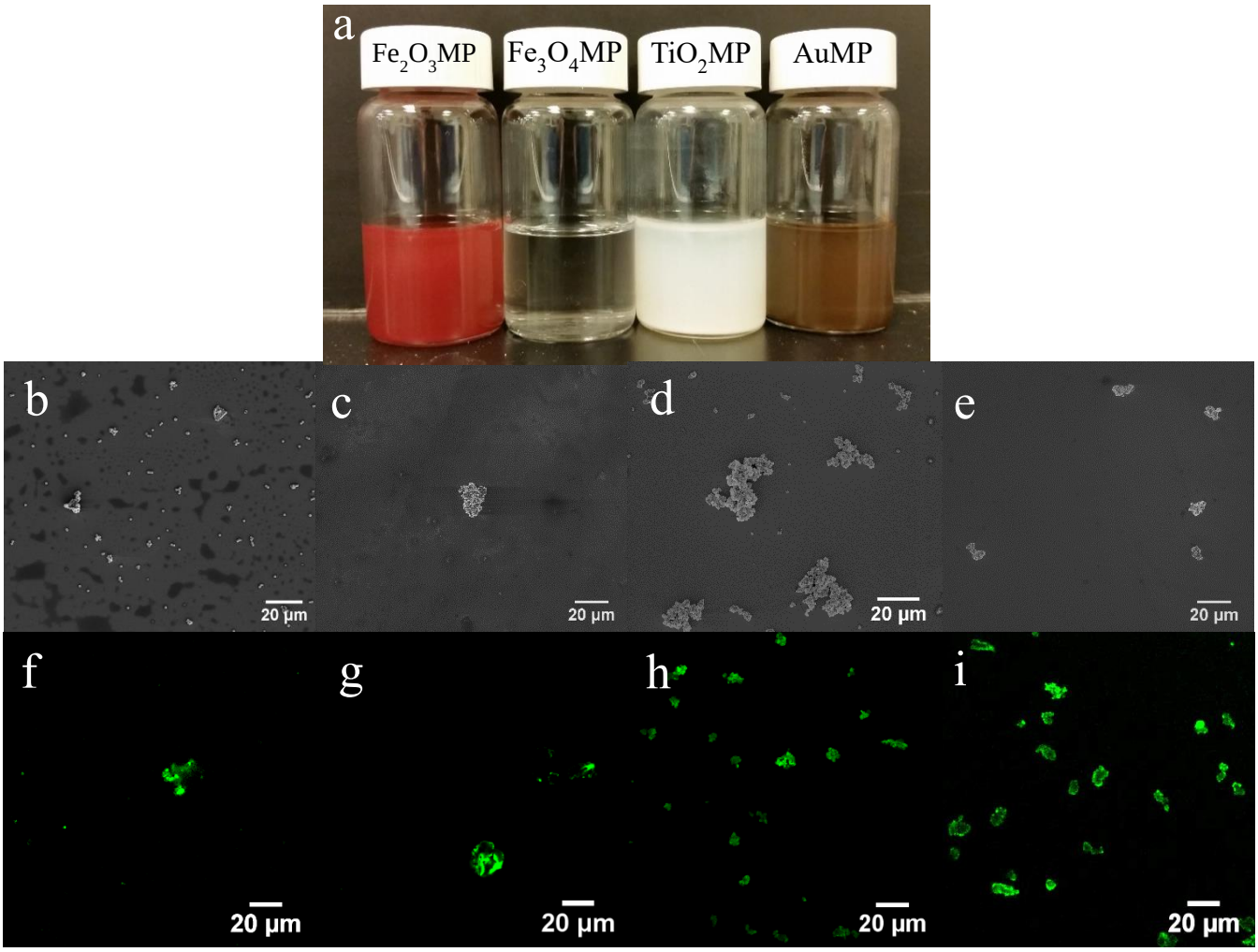

Figure 4.19: (**a**) Image of dispersions of core microparticles (MPs) in heptane (0.5 mg/mL). SEM (**b-e**) and confocal microscopy (**f-i**) images of dispersions of (**b,f**) Fe_2O_3MP (**c,g**) Fe_3O_4MP, (**d,h**) TiO_2MP, and (**e,i**) AuMP (0.1 mg/mL). Confocal Microscopy was done using FITC-PAH coated HPs.

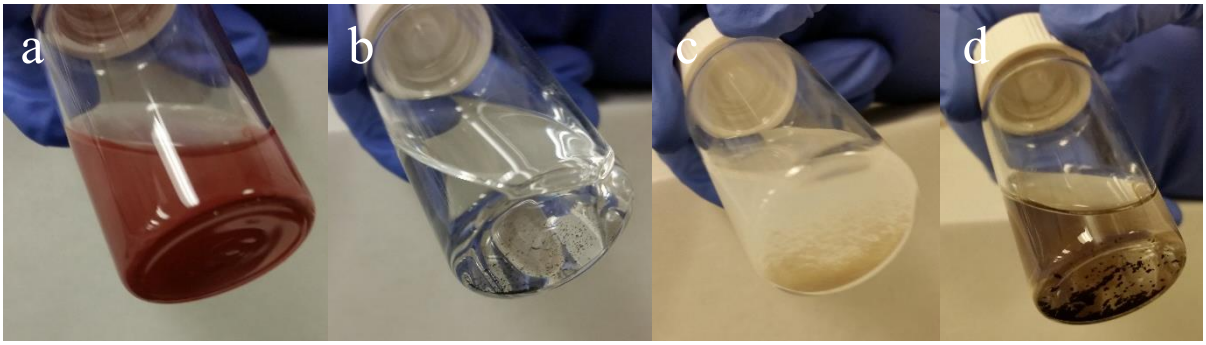

Figure 4.20: Sediments of inorganic microparticle cores respectively in heptane after 1 min. (**a,e**) Fe_2O_3 (**b,f**) Fe_3O_4 (**c,g**) TiO_2 (**d,h**) Au.

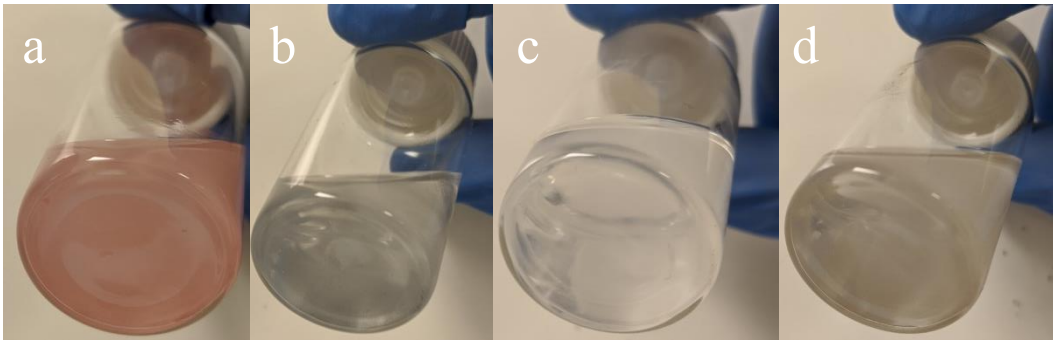

Figure 4.21: Dispersion of different composition HPs respectively in heptane (0.5 mg/mL) after 1 min. (**a**) Fe_2O_3 (**b**) Fe_3O_4 (**c**) TiO_2 (**d**) Au.

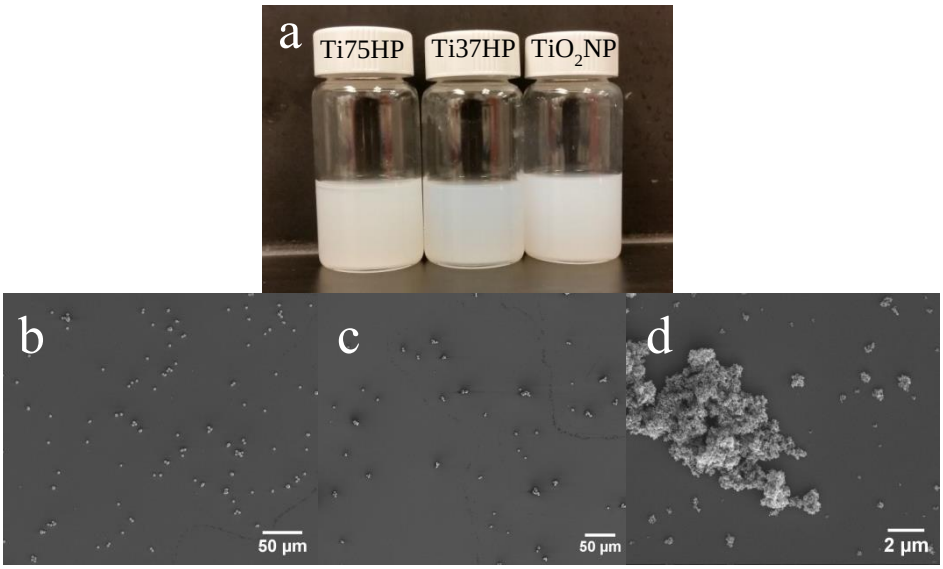

Figure 4.22: (**a**) Photograph of dispersions of TiO_2 spike HP and TiO_2 NP in chloroform. SEM images of SiO_2 HP with (**b**) 75 mM TiO_2 spikes and (**c**) 37.5 mM TiO_2 spikes and (**d**) TiO_2 NP dispersed in chloroform.

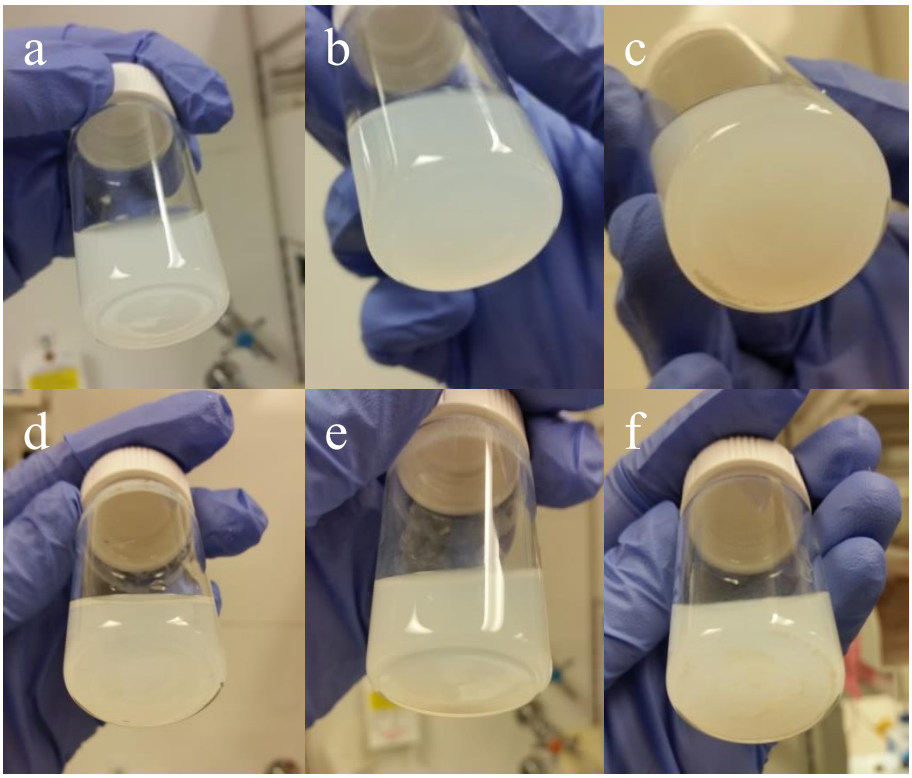

Figure 4.23: Dispersions of 37.5 mM TiO_2 HP; 75 mM TiO_2 HP, TiO_2 NP in chloroform (**a**,**b**,**c**) and heptane (**d**,**e**,**f**) respectively (0.5 mg/mL).

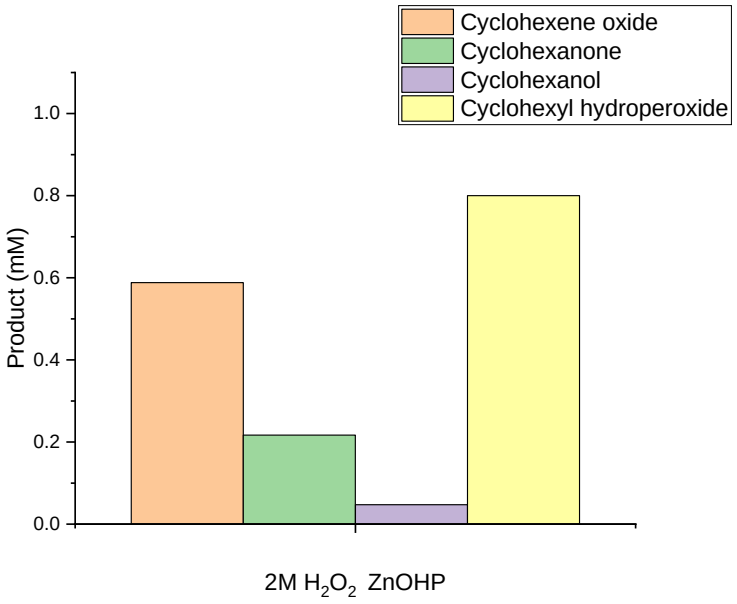

Figure 4.24: Product distribution from the photooxidation of cyclohexane in a 1:1 cyclohexane water emulsion with 2 M H_2O_2 in the aqueous phase and 1 mg/mL ZnO HP catalyst with X-Cite® 120 light source for 16 hours.

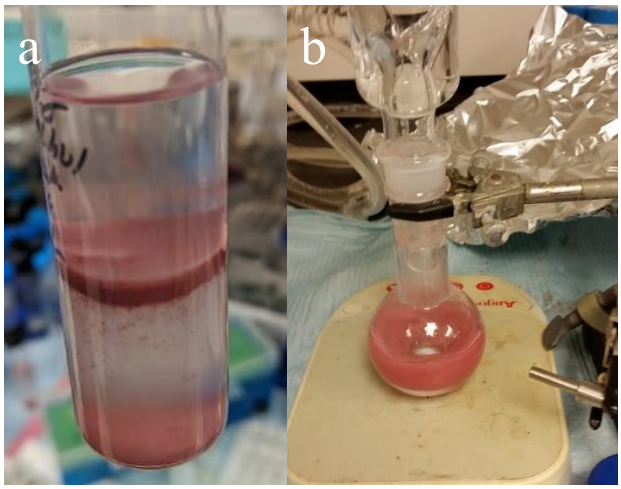

Figure 4.25: Hedgehog particles (HPs) at the interface after reaction from photocatalytic cyclohexane/water emulsion reaction flask with 1 M H_2O_2 for 16 hours (**a**). (**b**) Reaction set up with 15 mL cyclohexane and 15 mL 1 M H_2O_2 with 1 mg/mL HP and condenser and X-Cite® 120 light source.

Chapter 5

Tendril Particles: Microscale Colloids with Nanoscale Polymeric Spikes

Douglas Montjoy[1], Harrison Hou[1],Joong Hwan Bahng[2], Nicholas A. Kotov[1,3,4,5]

[1]Department of Chemical Engineering, University of Michigan, Ann Arbor, Michigan 48109, USA;
[2]Department of Electrical Engineering, California Institute of Technology, Pasadena, California 91125, USA;
[3]Department of Biomedical Engineering, University of Michigan, Ann Arbor, Michigan 48109, USA;
[4]Department of Materials Science, University of Michigan, Ann Arbor, Michigan 48109, USA;
[5]Biointerfaces Institute, University of Michigan, Ann Arbor, Michigan 48109, USA;
*E-mail: kotov@umich.edu

5.1 Abstract

Particle stability in a broad array of fluid environments is critical for colloids in catalysis, sensing, and composites. Hedgehog particles (HPs) inspired by the spiky geometry of pollen grains and viral capsids enable dispersion stability regardless of whether their polarity matches that of the solvent or not. Previous implementations of HPs were all based on rigid spikes from inorganic materials, whereas polymeric spikes offer a different and unique spectrum of optical, electrical, chemical, thermal, and mechanical properties including potential stimuli-responsive behavior. Microscale particles with nanoscale polymeric spikes that will be referred to as tendil particles (TPs), were made using layer-by-layer assembly (LBL) of polyallylamine films crosslinked with glutaraldehyde deposited onto the rigid ZnO templates. After removal of the template, the spikes on TPs can be described as semi-rigid sleeves. While being hydrophilic, they show dispersibility in nonpolar media such as heptane and high ionic strength aqueous media.

Polymer spikes are selectively permeable at low pH allowing for loading of cargo nanoparticles, molecules, and polymers. By adding poly(*N*-isopropylacrylamide-co-acrylic acid) subunits, controlled aggregation is observed in response to temperature. Additionally, crosslinking of dopamine into the structure allows for controlled aggregation in response to alkaline conditions. Environmentally responsive TPs have been engineered to respond to multiple stimuli at once and in both a reversible and irreversible manner.

5.2 Introduction

Surface corrugation with stiff spikes can be used as a universal strategy to reduce van der Waals forces between dispersed particles by more than an order of magnitude.[15] The drastic reduction of attractive forces leads to unexpected colloidal stability of particles with hydrophilic inorganic spikes in hydrophobic solvents and *vice versa*.[217] This effect also leads to increased stability of spiky colloids in a high ionic strength environment,[15,215] in contrast to the predictions of Derjaguin, Landau, Verwey and Overbeek (DLVO) theory about the colloidal stability of smooth spherical particles. The generality of this effect can be seen in many particles with spiky geometries that were tested for omnidispersibility, for instance, for the particles whose spikes were conformably coated with organic layers by layer-by-layer assembled (LBL) films[26,29,145,308–310] as a method to verify the role of particle geometry in the reduction of van der Waals forces.[215] There are also multiple other examples of spiky and flower-like particles from different inorganic materials[311–314], which were not tested for dispersibility in unfriendly solvents that are expected to display similar colloidal properties.

Rigid inorganic spikes impart HPs with a variety of unique properties, with a typical broad band extinction band in the near IR part of the spectrum[215–217,285] due to strong light scattering on the inorganic spikes.[217,285] Engineering of HPs with fully polymeric yet sufficiently rigid spikes would, in theory, allow one to impart these particles with additional functions available in predominantly for polymers and not for inorganic spikes. The functions of particular interest include (a) tunability of the characteristic extinction band; (b) engineering of compartments and their loading with molecules, nanoparticles or polymers; and (c) stimuli-responsive behavior. Note, however, that all of these functions originate in structural reconfigurability of the polymers,

and thus may impact or diminish omnidispersibility because the softness of nanoscale polymeric spikes will result in recovery of van der Waals and other interactions.

Polyelectrolyte systems allow encapsulation of different functional materials, including magnetic NPs[35,115] and enzymes[315,316]. Additionally polyelectrolyte systems exhibit pH-responsive, temperature-responsive, and light-responsive behaviors.[35,120,317] A key aspect of polymeric systems is the ability to crosslink to introduce new materials as well as enhance mechanical properties and stability.[122,318] Control of polyelectrolyte configuration can tune the optical properties including fluorescence or absorption.[319]

In this study, we demonstrate that HPs with polymeric sleeve-like spikes that will be referred to here as tendril particles (TPs) can be produced. In order to retain omnidispersibility, they must be, however be cross-linked. Nevertheless, molecular-level engineering of polymeric films makes possible to vary their optical properties and load them with functional cargo. We also observed the temperature, and pH-responsive loss of their dispersibility indicating fundamental validity of the proposed understanding of their omnidispersibility.

5.3 Engineering of Tendril Particles

Following the previous studies of making polyelectrolyte micro- and nanocapsules,[26,152,153,166] weak polyelectrolyte films were formed with polyacrylic acid (PAA) and poly(allylamine) hydrochloride (PAH) bilayers on HPs, building on previous work with LBL coatings of HPs[215] and allowing for multiple crosslinking sites. Young's modulus of PAA/PAH layers can range from to 250 MPA when uncrosslinked with an increase to 680 Mpa for crosslinked[122] in addition to high glass transition temperatures (128°C for PAA[320] and 223°C for PAH[320]) allowing for robust mechanical properties.

A thin polymer film is observed as expected after a two-bilayer film (**Figure 5.5**). By crosslinking this film with glutaraldehyde, TPs are observed (**Figure 5.1**). ZnO is only fully removed with additional acid washes which reduce the amount of Zinc from 43% Zn (43ZnTP) to 2.9%(2.9ZnTP) with 0.01 M HNO_3 and 0.57% (0.57ZnTP) with 0.1 M HNO_3 respectively resulting in hollow polymer spikes (**Table 5.1**).

STEM-EDS mapping shows that the hollow polymer spikes consist of primarily carbon, with oxygen, nitrogen, and a small amount of zinc present (**Figure 5.6**). The thickness of the

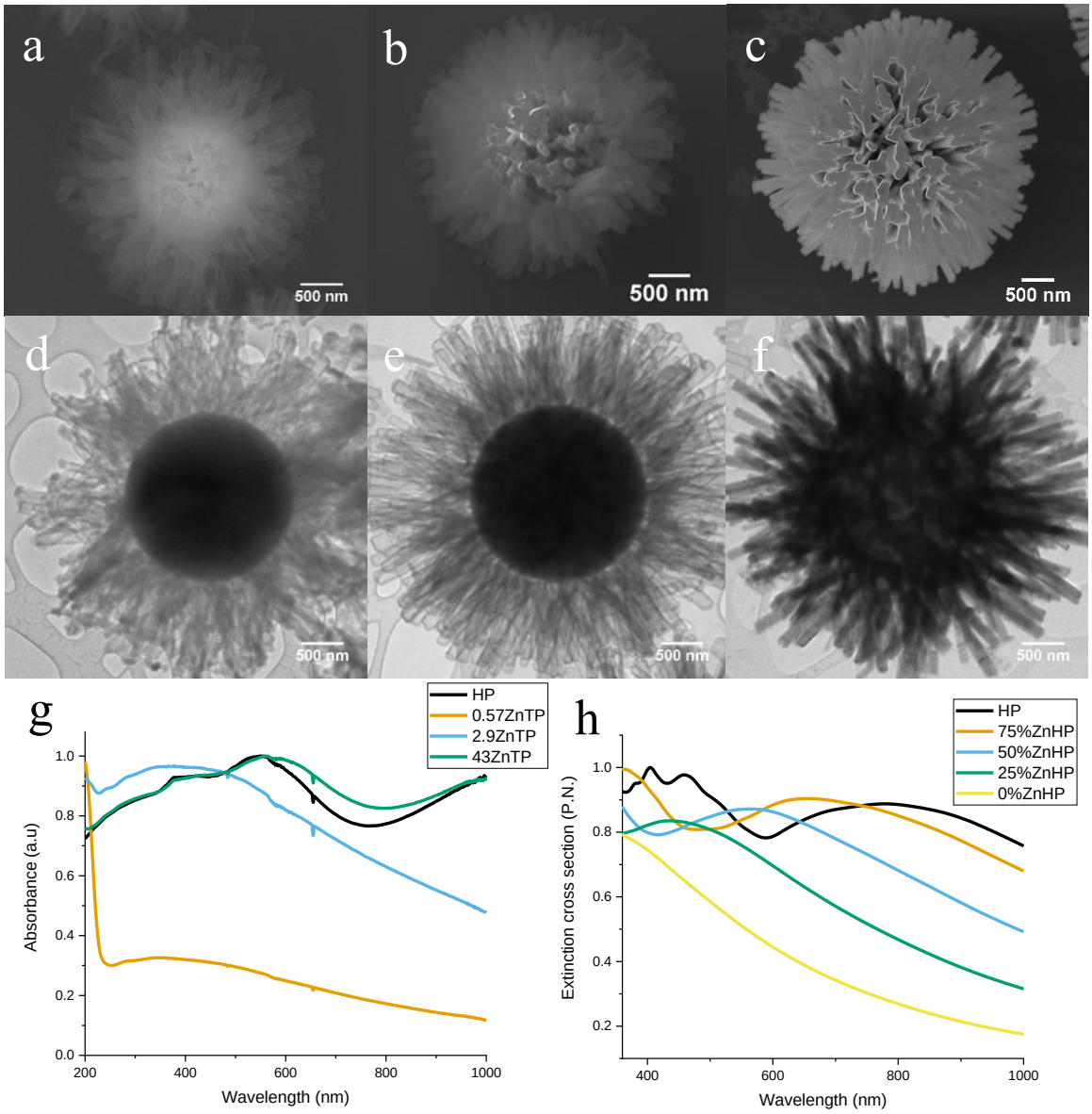

Figure 5.1: SEM (**a,b,c**) and TEM (**d,e,f**) of 2 bilayer tendril particles (TPs) crosslinked with glutaraldehyde with various Zn Content, 0.57ZnTP (**a,b**) (**b,e**) 2.9ZnTP (**c,f**) 43ZnTP. Extinction spectrum of HPs and TPs with different Zn contents (**g**) and calculated extinction spectra of HPs with various percentages of Zn (**h**; model HP parameters and scattering cross sections in **Figure 5.9**).

underlying polymer film is critical to maintaining the spiky morphology, as overly thick films form a polymer web over the spikes, mitigating its corrugation. Additionally, the underlying HP spikes require a certain thickness, as structural collapse is observed with thinner HP spikes (**Figure 5.7**). The core-shell structure is dependent on the morphology of the underlying HP allowing for polymer spikes with tunable lengths ranging from 500 nm to 1800 nm (**Figure 5.8**). The reduction in zinc content has a dramatic effect on the absorbance spectrum of the samples, showing a large reduction in broadband scattering (**Figure 5.1g**). An FDTD simulation of a model HP with

different ZnO content in the spikes was used to characterize the optical properties of TPs.[286] The simulation somewhat captures the scattering features. We see a reduction in scattering in the model representative of the reduction in ZnO corresponding to a decrease in the index of refraction. A broadband nature is observed for the low zinc content TPs and the simulation due to the low quality of the electromagnetic modes supported by the particle with its reduced refractive index (**Figure 5.1h**, **Figure 5.9**). HPs with polymer spikes can also be formed using ethylcarbodiimide (EDC) as a crosslinking agent, but are only stable with thicker 3.5 bilayer films and show a more rigid morphology (**Figure 5.10**). Hollow polymer spikes with controlled amounts of zinc oxide are also achieved with 1 M boric acid with partial dissolution of the spikes observed with shorter incubations in acid (**Figure 5.11**). Due to the presence of polyelectrolyte films, the spikes are not stable at lower pH without crosslinking, indicating as expected that the crosslinking stabilizes the spike (**Figure 5.12**). Glutaraldehyde also causes some degradation to HPs alone without polymer films, likely due to the lower pH. As expected, when treatment is at an elevated pH the zinc oxide spikes of HPs remain intact (**Figure 5.13**). Similar hollow shell structures are observed when solely ZnO nanorods are treated with glutaraldehyde at a lower pH (**Figure 5.14**).

5.4 Dispersion of Tendril Particles

HPs exhibit dispersion stability in a wide range of different polarities and ionic strengths. In a previous study, we determined that if surface corrugation is preserved with the addition of polymer and nanoparticles, omnidispersibility is maintained. With TPs, a softer interaction is expected, with a more flexible spike that is potentially deformable. We observed that the TPs maintain dispersibility in nonpolar environments and high ionic strength environments (**Figure 5.2, 5.15-5.16**), indicating that the crosslinked polymer enables reduction of van der Waals forces analogous with rigid zinc oxide. Confocal microscopy and SEM confirm well-dispersed particles in highly nonpolar heptane and in 1 M NaCl (**Figure 5.2, 5.16)**. It would be expected that the polymer would have a reduced attractive van der waals force, however, only with a reduction of contact area consistent with a rigid spike would dispersion be enabled in a nonpolar environment.[15] Based on these results, we believe that the crosslinked polymer is semi-rigid and does not completely deform upon contact, allowing for a marked reduction of van der Waals forces. TP

stability in high ionic strength environments as well as nonpolar environments has broad importance in biosensing, catalysis, and other fields.

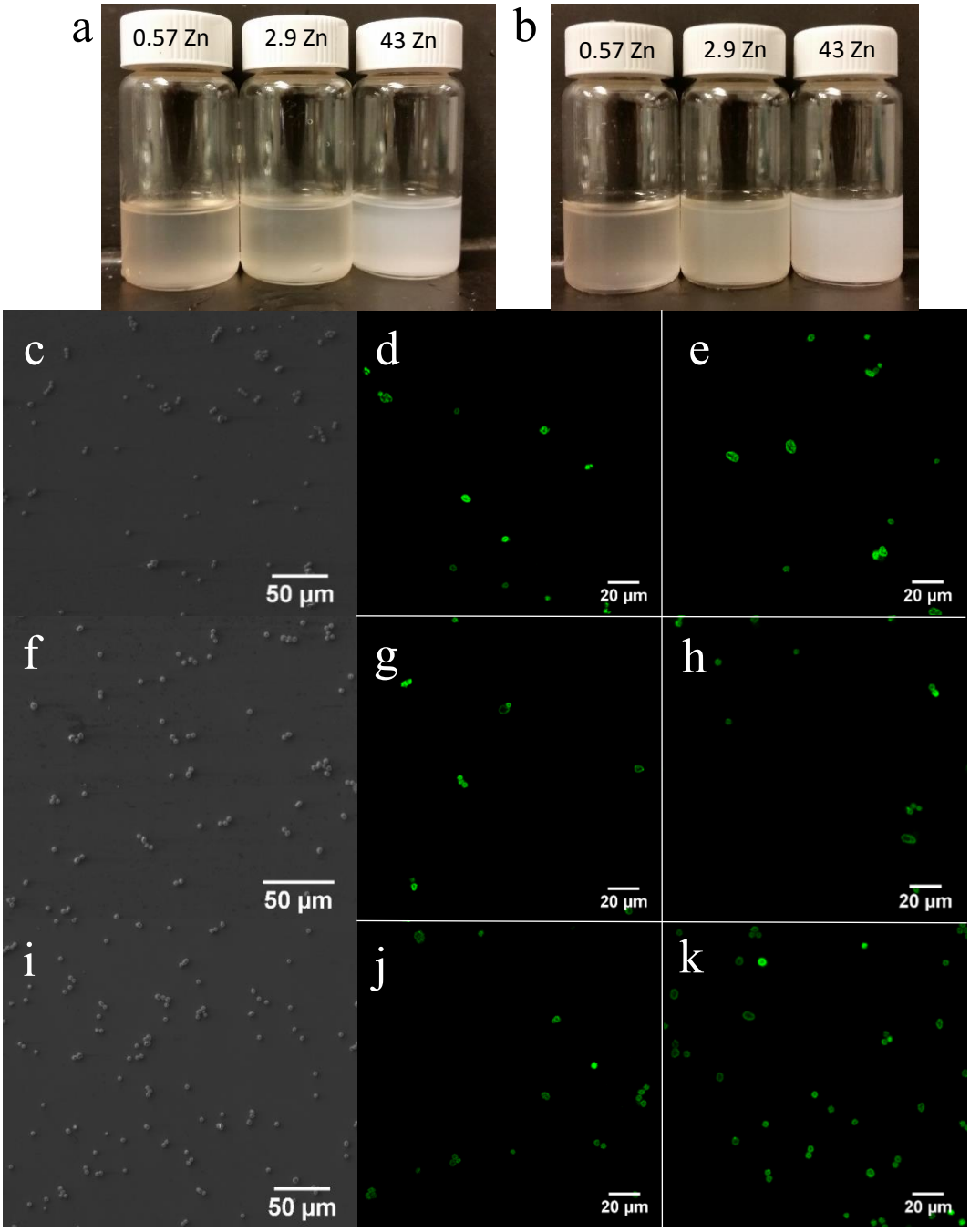

Figure 5.2: Photographs of TP dispersions (0.5 mg/mL) in heptane (**a**) and 1 M NaCl in water (**b**) with increasing zinc content from left to right. SEM (**c,f,i**) and confocal (**d,e,g,h,j,k**) of 0.57Zn TPs in heptane (**c,d**) and 1 M NaCl (**e**), 2.9Zn TPs in heptane (**f,g**) and 1 M NaCl (**h**), and 43Zn TPs in heptane (**i,j**) and 1 M NaCl (**k**). All SEM and confocal samples were prepared at 0.1 mg/mL.

5.5 Loading of Sleeve-like Compartments

To demonstrate the possibility of TP loading with functional cargo we first loaded plasmonic Au NPs inside TPs.[215] With the introduction of gold, we see a large broadening of the optical absorbance as a function of the density of the Au NP coating (**Figure 5.3a-d, 5.17**) The gold NPs will also provide electromagnetic hotspots due to surface plasmon resonance relevant to optical applications for the TPs. This demonstrates that the TPs have tunable optical properties and in this case electromagnetic hotspots are introduced for optical applications. We envision that TPs can achieve varied mechanical and electrical properties through nanoparticle loading.

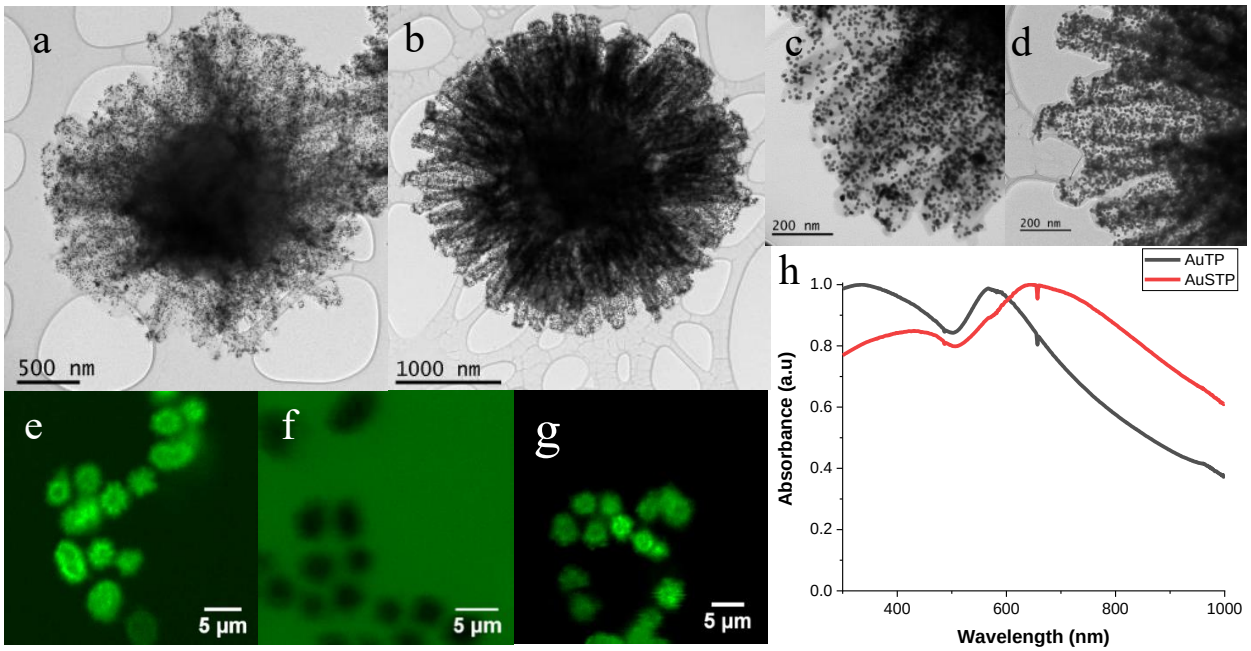

Figure 5.3: TEM of Tendril particles (TPs) with PSS/PDDA/AuNP (AuTP) (**a,c**) and with PSS/PDDA/AuNP (0.5 M NaCl; AuSTP) (**b,d**) layers encapsulated. Confocal microscopy images of TPs dispersed in FITC-Dextran (4000 MW; 1 mM) at pH3 (**e**) and pH 10 (**f**). Encapsulation of FITC-dextran by raising pH after treatment at pH 3 and washing off excess FITC-dextran(**g**) Normalized absorbance spectrum for AuTP and AuSTP (**h**).

Additionally, to demonstrate loading small molecules, we used FITC-dextran. In this case, we are able to make the polyelectrolyte film permeable at low pH (pH 3) while impermeable at high pH (pH 10) as seen in other studies.[32,33,321]This allows for encapsulation of the FITC-dextran into the hollow spikes by loading followed by raising the pH (**Figure 5.3f-h**). With the capability of selective loading and release, these TPs could be used for industrial coatings such as anti-corrosion coatings or for encapsulation of therapeutics.[322,323] Additionally, with creation of hollow

polyelectrolyte cores in addition to spikes, TPs would enable high loadings or selective loadings in each compartment.

5.6 Temperature and pH-based Agglomeration of Tendril Particles

The ability to modulate a polymer's reversible thermal response has been well-explored with polymers such as poly(N-isopropylacrylamide) (PNIPAM).[116,324,325] In addition, pH-responsive behavior has wide applications in biological systems and can be achieved with different polymeric subunits including dopamine.[326]

The introduction of thermoresponsive and pH-responsive polymers is expected to result in the loss of dispersion stability based on environmental conditions. To test thermoresponsive capability, we coated TPs with LBL films from poly(N-isopropylacrylamide-co-acrylic acid) (PNIPAM TPs) and evaluated particle stability at different temperatures. Particle stability was first evaluated at room temperature, 40°C, 60°C, and 80°C. PNIPAM TPs rapidly sediment within 5 minutes after being incubated at 60°C and 80°C while normal PAA TPs show limited sedimentation (**Figure 5.4a-d, 5.18, 5.19**). Some aggregation is observed at 40°C and with very little sedimentation at room temperature (**Figure 5.20, 5.21)**. Normal, non-modified TPs (PAA TPs) show some thermoresponsive behavior likely due to disruption of hydrogen bonding, but less aggregation than the PNIPAM TPs .We believe PNIPAM collapses at high temperature and covers the TP resulting in hydrophobic interactions and aggregation. The transformation of PNIPAM has been shown to be reversible[327], allowing for recovery and reuse of the TP.

Dopamine was conjugated to PAH using glutaraldehyde to create pH-responsive TPs (DOP TPs) (**Figure 5.22**). Limited aggregates are observed at pH 5.6 with confocal microscopy compared to large aggregates at pH 7.4. (**Figure 5.4e-f**). Additionally, absorbance was measured over 30 minutes for DOP TPs pH 5.6 and pH 7.4. in .01 M PBS to analyze sedimentation. There was a decrease in absorbance of almost 50 percent at pH 7.4 while only 20 percent at pH 5.6 over 30 minutes (**Figure 5.23**). When PAA TPs are tested, little difference is observed between the two pHs indicating that the dopamine group is responsible for the change (**Figure 5.24**). Dopamine contains catechol groups which when exposed to alkaline conditions oxidize to quinone or semiquinone forms which are reactive and result in covalent crosslinking.[328,329] In this case, the

reaction is irreversible unlike the NIPAM, which we observe when analyzing sedimentation of recovered DOP TPs after the pH is readjusted to 5.6 from 7.4 (**Figure 5.25**).

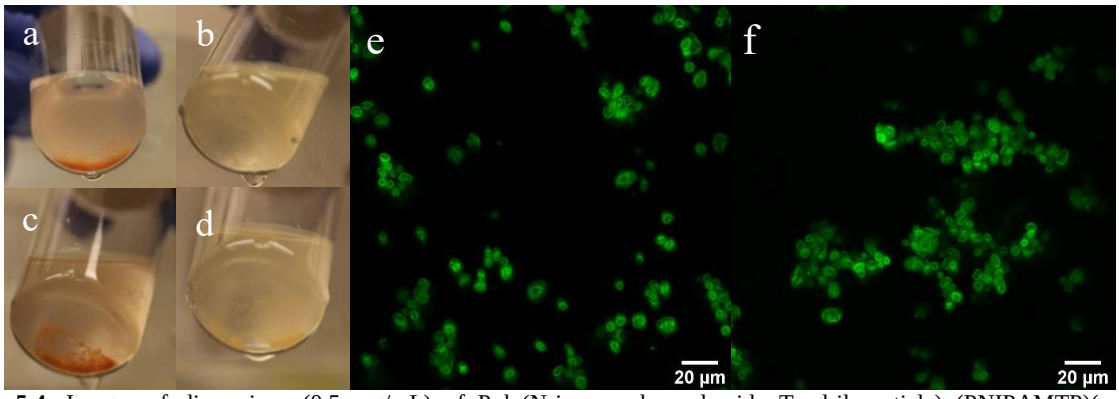

Figure 5.4: Images of dispersions (0.5 mg/mL) of Poly(N-isopropyl acrylamide Tendril particle) (PNIPAMTP)(**a,c**) and Zn2.9TP(**b,d**) after 5 minutes in water bath at (**a,b**) 60°C (**c,d**) 80°C. Confocal microscopy of dopamine-modified Tendril particle (DOPTP) (.1 mg/mL) at pH 5.6 (**e**) and pH 7.4 (**f**) in .01 M PBS.

5.7 Conclusions

TPs enable dispersion in a wide array of environments such as biofluids and nonpolar solvents and others making them ideal as a catalytic platform for enzymes which could be introduced via crosslinking[318,330] or sensing applications based on different nanoparticle cargo. Environmentally responsive TPs are ideal for applications requiring stimuli-responsive film formation. The tunable optical properties and mechanical properties from controlled crosslinking and introduction of nanoparticles, make TPs very appealing for viscoelastic composites. Composites are dependent on nanoparticle loading for mechanical properties, and TPs could represent a way to disperse unstable nanoparticles and ensure high loading. Additionally, they possess tunable deformability due to the crosslinked nature of the spike, which could lead to unique mechanical properties.

5.8 Methods

All materials were purchased from commercial sources: poly(diallyldimethylammonium chloride) (PDDA), sodium polystyrenesulfonate (PSS), polyacrylic acid (PAA), poly(allylamine hydrochloride) (PAH), zinc nitrate hexahydrate ($Zn(NO_3)_2 \cdot 6H_2O$, ≥99% purum), hexamethylene tetraamine ($C_6H_12N_4$, ≥99.5% puriss), boric acid, ammonium hydroxide (28 wt% solution), tetraethyl orthosilicate (TEOS), potassium chloride, glutaraldehyde (25 wt% solution), and zinc oxide NPs (50 wt % solution) were purchased from Sigma-Aldrich (St. Louis, MO); grids with ultrathin carbon film on holey carbon film support for transmission electron microscope (TEM) measurements and silicon wafers for scanning electron microscope (SEM) measurements from Ted Pella (Redding, CA) Carboxylated PS was ordered from Polysciences, Inc. Polycarbonate track-etched membranes (0.8 micron, 90 mm) were ordered from Sterlitech. All chemicals were ordered from Sigma-Aldrich unless noted otherwise.

5.8.1 Synthesis and Layer-by-Layer Coating of Core Particles

Silica microparticles were produced by a modified Stöber process.[228,252] Briefly, 0.017g of potassium chloride, 6.75 ml water, and 9 ml ammonium hydroxide were added to 65 ml ethanol. A solution of 34 ml ethanol and 2.2 ml of TEOS were added at a rate of 30 ml/hour via syringe pump under vigorous stirring. Silica cores were coated with poly(diallyldimethyl ammonium chloride) polystyrene sulfonate and in a layer-by-layer process as previously mentioned. Briefly, 5 mL core was mixed with 25 mL polyelectrolyte solution (1 mg/ mL, 1 M NaCl) and incubated for 20 minutes. Cores were then centrifuged for 4000 RPM for 10 minutes and washed with water 3 times before repeating the process with the next layer.

5.8.2 Synthesis of Hedgehog Particles

Polystyrene and SiO_2 core HPs were synthesized using a scaled sonothermal synthesis based on that of Bahng et al. 1.25 mL of coated core solutions (2.5 wt%) was mixed with 40 mL

ZnO seed solution (0.025 wt%) and incubated for 1 hour.[15] Particles were then filtered using a 0.8 micron track etch membrane and combined with equimolar (25mM) solutions of zinc nitrate hexahydrate (ZnH) and hexamethylenetetraamine (HMT) in water. Concentrations of the precursors were varied to tune the width of the spikes, the default concentration was 25 mM with 2 sonications. The solution was then filled to a final volume of 1.6 L and sonicated using a Hielscher 1000UIP HdT sonicator for 1 hour and 30 minutes. Samples were purified by removing excess zinc oxide nanorods after sedimentation of HPs. Longer HPs were created by doing additional sonications with ZnH and HMT solutions after purification.

5.8.3 Formation of Tendril particles

ZnO HPs were coated with 2 bilayers of polyacrylic acid (PAA) and poly(allyamine hydrochloride) (PAH) at pH 8 and 1 M NaCl. Each layer consisted of incubating HPs in polyelectrolyte for 20 minutes, and then centrifuging washing twice with a 0.1 M NaCl pH 8 buffer and twice with water. The polymer layers were then cross-linked using glutaraldehyde (2.5%). 4 mL of sample was incubated with 2 mL of glutaraldehyde (25%) and 32 mL of 1 M boric acid for 2 hours. This sample was then washed 3 times with water and then put into an additional acid wash (nitric acid or boric acid) to produce the desired amount of zinc. NIPAM modification was done in the same way, but the polymer was dissolved overnight in pH 8 solution. Crosslinking of 1-ethyl-3-(3-dimethylaminopropyl)carbodiimide (EDC) TPs was done with 10 mM EDC at pH 5.6 for 2 hours in 0.1 M PBS buffer. Dopamine-modified TPs were cross-linked with 0.05M dopamine and 2.5% glutaraldehyde in 0.1M PBS buffer.

5.8.4 Confocal Microscopy Imaging

For confocal studies, FITC was conjugated to PAH according to a literature procedure.[193,215] Briefly, 4.5 mg FITC was dissolved in 1 mL dimethylsulfoxide (DMSO) and combined with 500 mg PAH dissolved in 6 mL water. The pH of the solution was adjusted to 8.4 with NaOH and then the solution was stirred for 2 days. Dialysis was then performed using a D-tube™ Dialyzer for 24 h to remove excess FITC.[193] PAA/FITC-PAH films were deposited on HPs using LbL assembly with the same procedure described previously.[215]

5.8.5 Electron Microscopy Imaging

20 µL of sample was dispersed on a silicon wafer and then evaporated. Particles were imaged using a FEI Nova 200 Nanolab SEM and FEI Helios 650 Nanolab SEM/FIB. For dispersion SEM images, particles were imaged at a concentration of 0.1 mg/mL. STEM and TEM images were taken using a Talos F200X G2, JEOL 3011, and JEOL 2010. EDS was run on samples at a magnification of 65k a minimum of 3 times over spikes of TPs.

5.8.6 FDTD Simulation of Optical Properties

A model particle was constructed with a core SiO_2 sphere (diameter d=1µm) meta-shell containing a spherical array of 500 ZnO NRs (length l=1463 nm, thickness w=139 nm) to approximate the experimental construct in Lumerical FDTD. The length and thickness were measured from electron microscopy from a HP (minimum of 50 images) used for elaboration of TP model geometry. In the numerical calculation of the scattering cross-section, the refractive indices of the tendrils having various ZnO contents were calculated utilizing Maxwell-Garnet Medium approximations, where the quantity of ZnO contents are reflected in the volume fraction. As the spectral focus of our investigation lie in the visible wavelengths at which the materials

absorption for the TP components are negligible, extinction coefficients are not taken into consideration in the calculation and the following materials refractive indices are used in the approximation: 1.97 for ZnO, 1.56 for polymer, and 1.46 for SiO_2

5.8.7 Absorbance measurements

Absorbance measurements were done using a Cary 8454 spectrophotometer. Measurements were taken every 10 seconds for 30 minutes at a 275 nm wavelength in a 3 mL quartz cuvette with a particle concentration of 0.5 mg/mL. For pH-responsive testing, TPs were measured in a 0.1 M PBS buffer adjusted to pH 5.6 for acidic conditions and 7.4 for alkaline conditions. For thermal-responsive testing, TPs were heated using a commercial heat gun at approximately 1.5°C/ a min to 70°C in 30 minutes (Figure S14) and approximately 70°C in 10 minutes with it stabilizing at 81°C after 30 minutes (Figure S15).

5.8.8 Molecular loading with TPs

Loading of FITC-Dextran (4k MW) was done in pH3 solution. Encapsulation involved a pH3 TP solution with FITC-Dextran (1 mM) being washed at pH 10 repeatedly to ensure that there was no excess FITC in solution for confocal microscopy imaging.

5.9. Supplementary Results

Table 5.1: Zinc contents measured by energy dispersive spectroscopy (EDS) of TPs after different acid washes to remove change Zinc content after glutaraldehyde crosslinking.

Sample	Zinc Content (EDS)	Acid Wash
0.57ZnTP	0.57±0.12	0.1 M HNO_3
2.9ZnTP	2.9±0.21	0.01 M HNO_3
43ZnTP	43.0±3.3	No Acid Wash

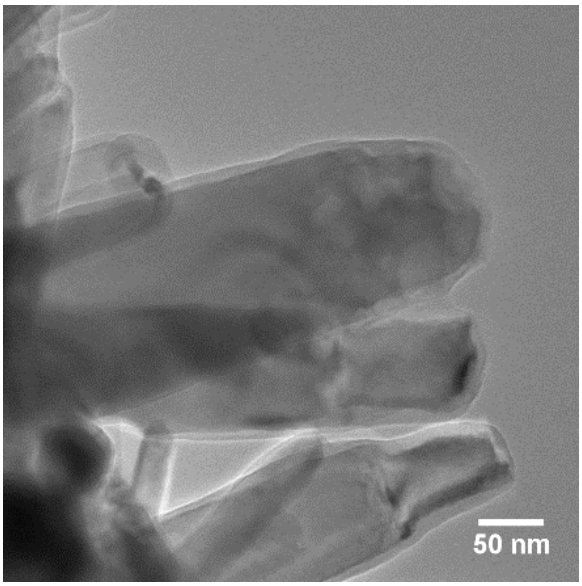

Figure 5.5: TEM Image of a conformal $(PAA/PAH)_2$ film on a HP.

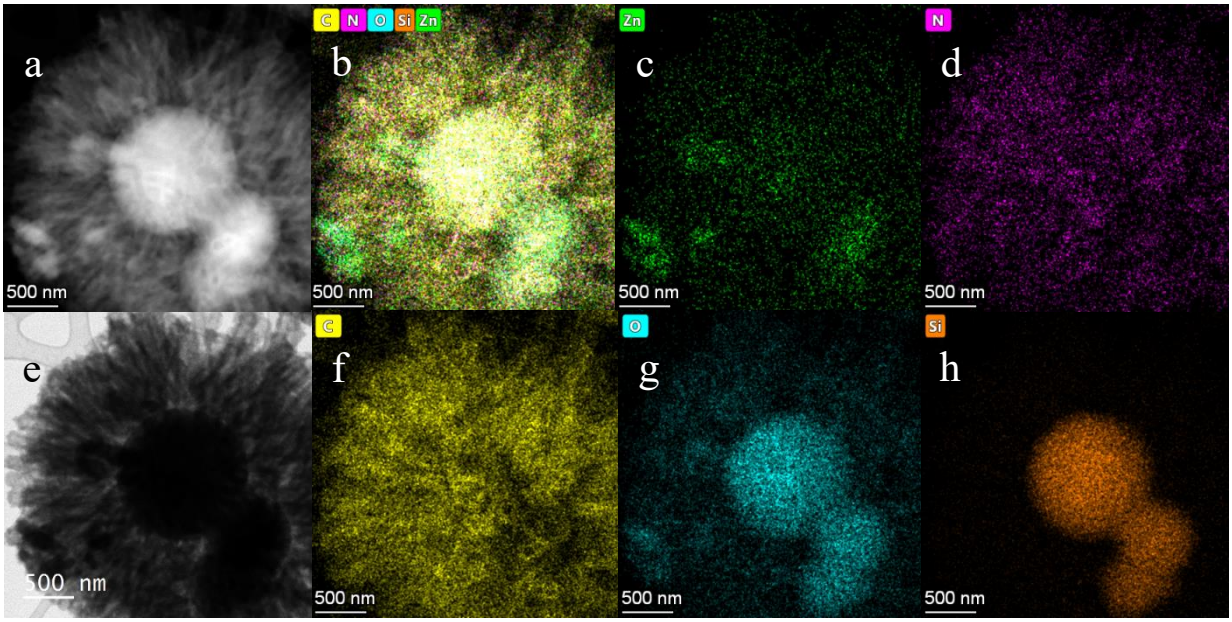

Figure 5.6: EDS map of TP washed with 1 M boric acid. (**a**) STEM HAADF image ; (**b**) composite EDS map; (**c**) zinc EDS map; (**d**) nitrogen EDS map; (**e**) bright-field STEM image; (**f**) Carbon EDS map; (**g**) oxygen map; (**h**) silicon map.

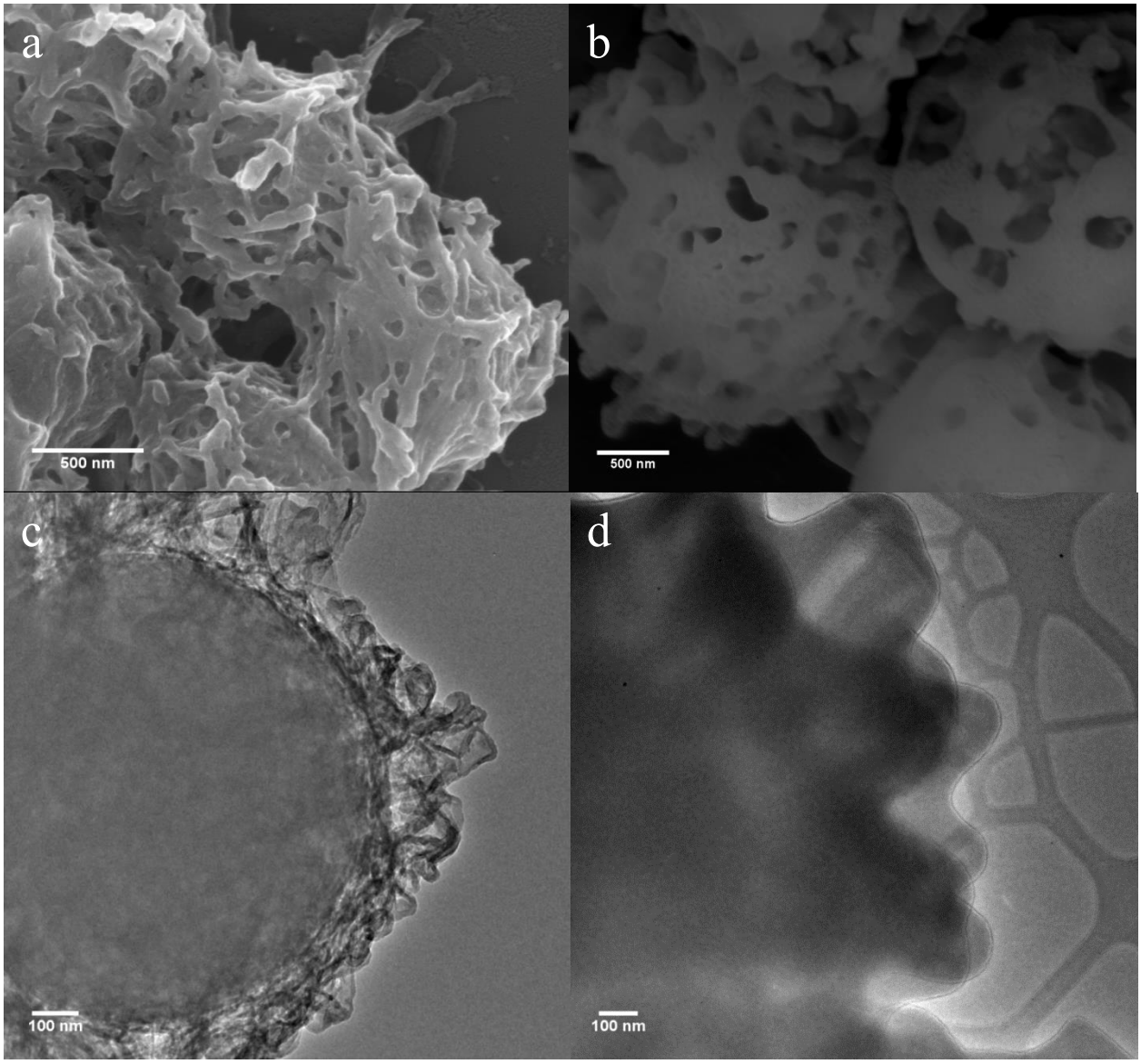

Figure 5.7: SEM (**a,b**) and TEM (**c,d**) images of a polystyrene PAA/PAH TP made from a HP with thin spikes (12.5 mM) TP 2 bilayer (**a,c**) and a cross-linked 5 bilayer polymer film (**c,d**).

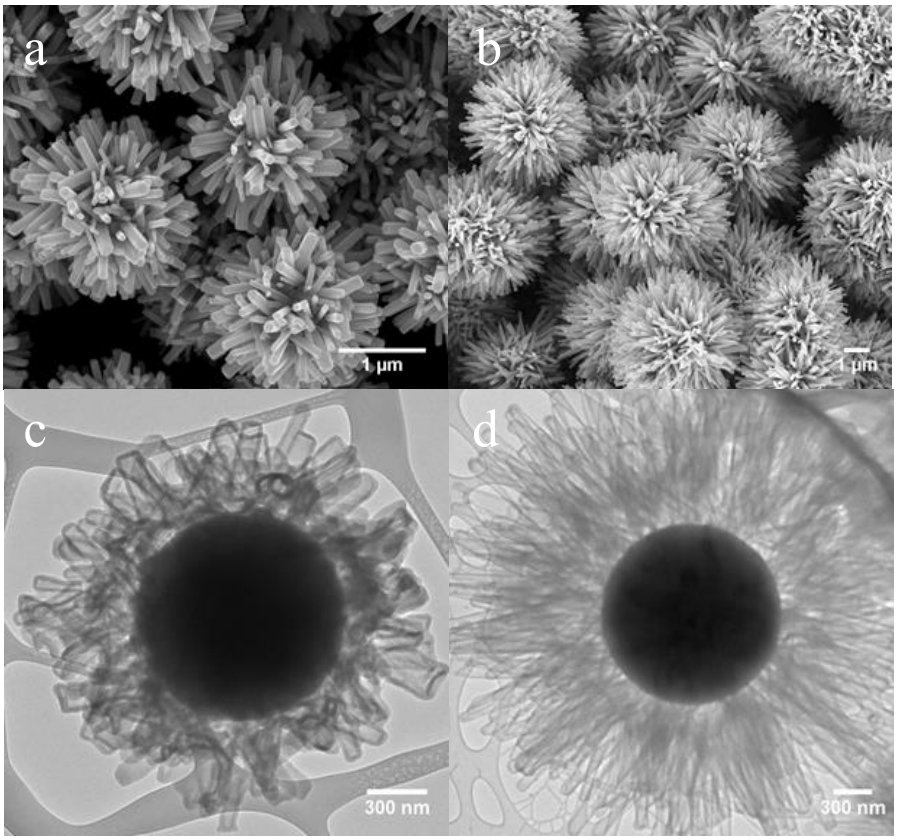

Figure 5.8: SEM (**a,b**) and TEM (**c,d**) images of short and long ZnO spike length HPs (**a,b**) and TPs prepared from those HPs (**c,d**)

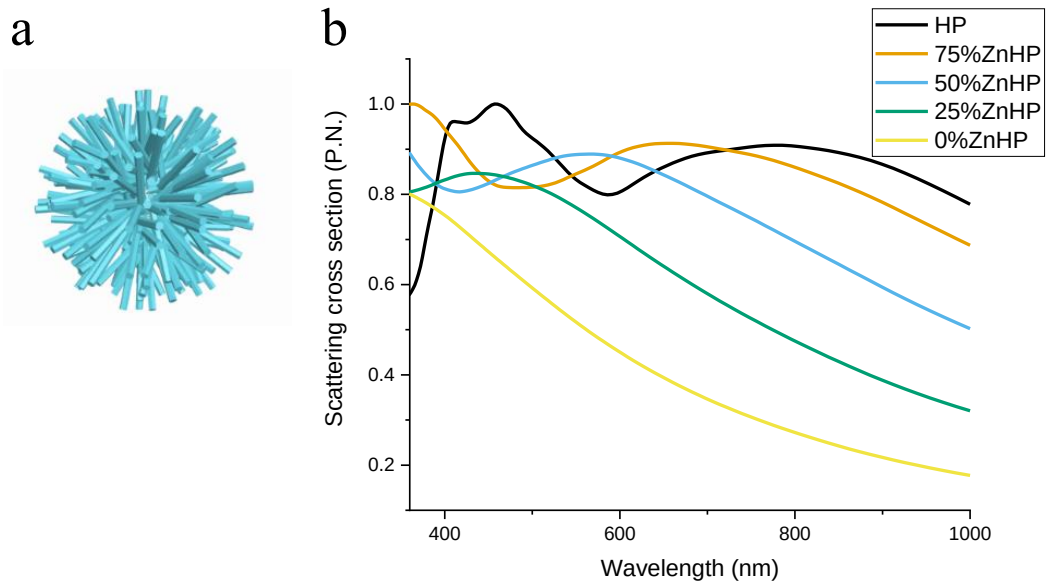

Figure 5.9: FDTD Model HP with spike length of 1463 nm, spike thickness of 163 nm, and 500 spikes (**a**). Normalized calculated scattering cross section of HPs with various percentages of Zn (**b**).

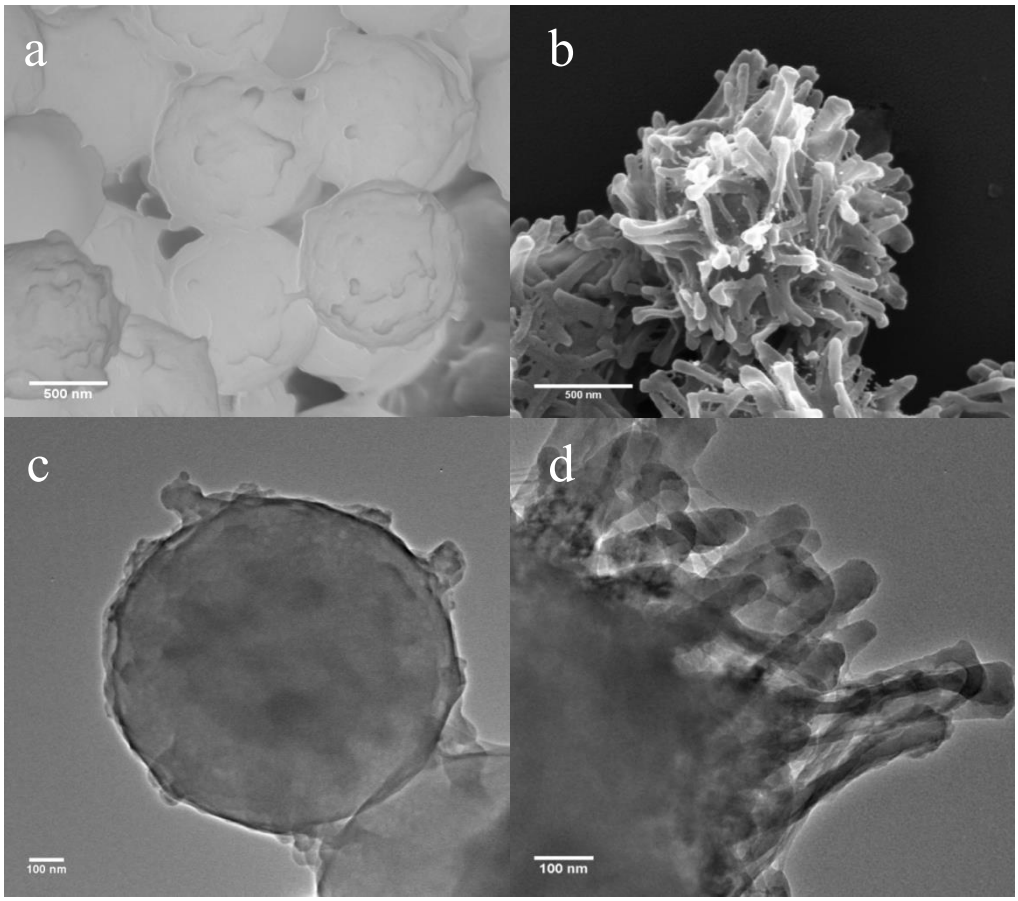

Figure 5.10: SEM (**a,b**) and TEM (**c,d**) of $(PAA/PAH)_2$ polystyrene tendrils (**a,c**) and $(PAA/PAH)_3PAA$ (**b,d**) cross-linked with EDC.

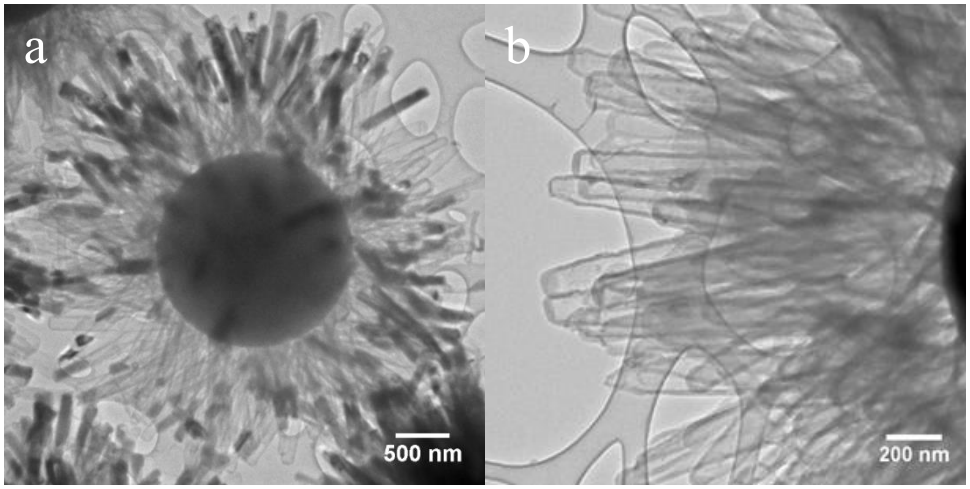

Figure 5.11: TEM Image of a TP produced after glutaraldehyde crosslinking at pH 4 and 2hr incubation with 1 M boric acid (**a**). TEM of TP spikes after glutaraldehyde crosslinking at pH 4 after 72hr incubation with 1 M boric acid (**b**).

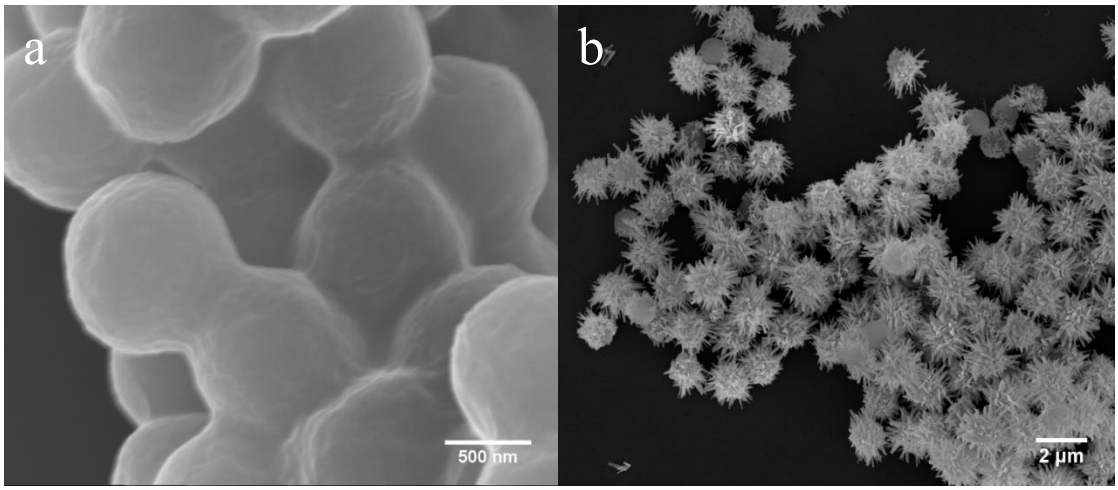

Figure 5.12: SEM of HPs modified with $(PAA/PAH)_2$ treated after pH 4 treatment for 2 hours (**a**) and a normal HP with no polymer film treated with glutaraldehyde (**b**).

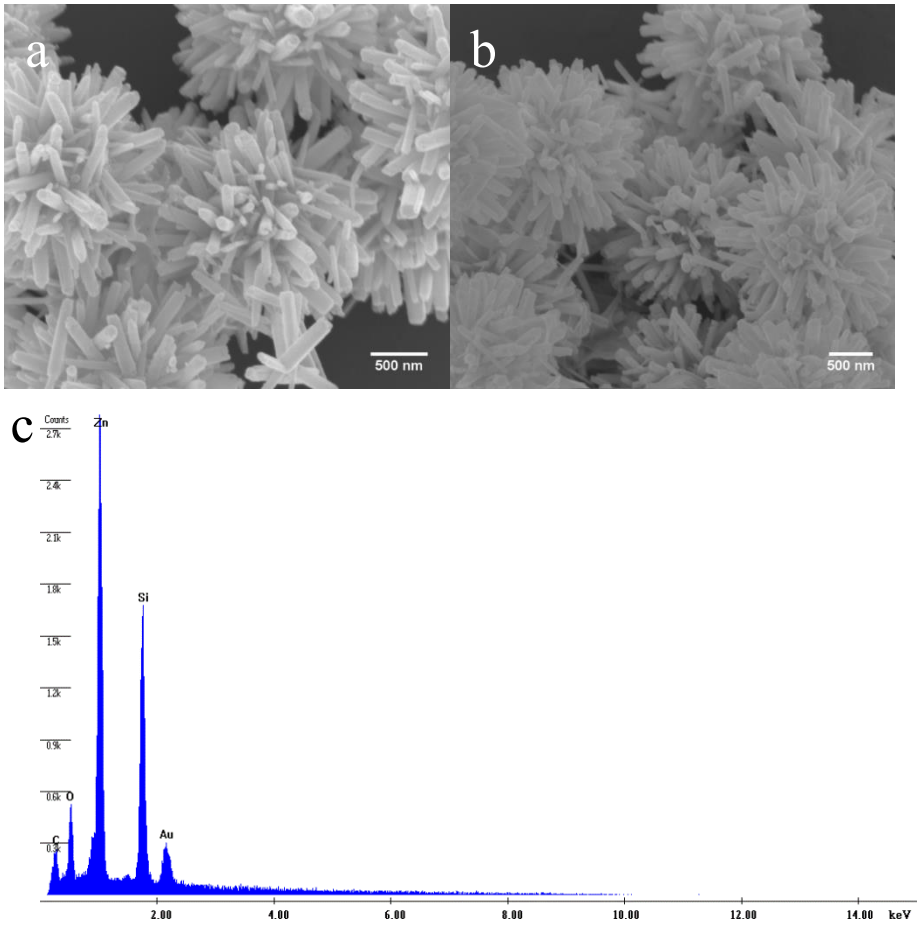

Figure 5.13: TPs formed with glutaraldehyde cross-linking at pH 10 (**a**) and pH 7 (**b**). Representative EDX spectra from glutaraldehyde at high pH (**c**).

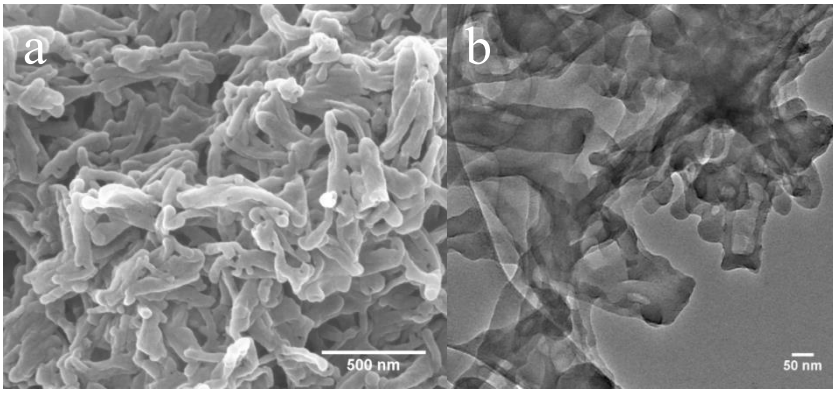

Figure 5.14: SEM (**a**) and TEM (**b**) of ZnO NRs coated with $(PAA/PAH)_2$ and cross-linked with glutaraldehyde at pH 4 analogous to process to create TPs.

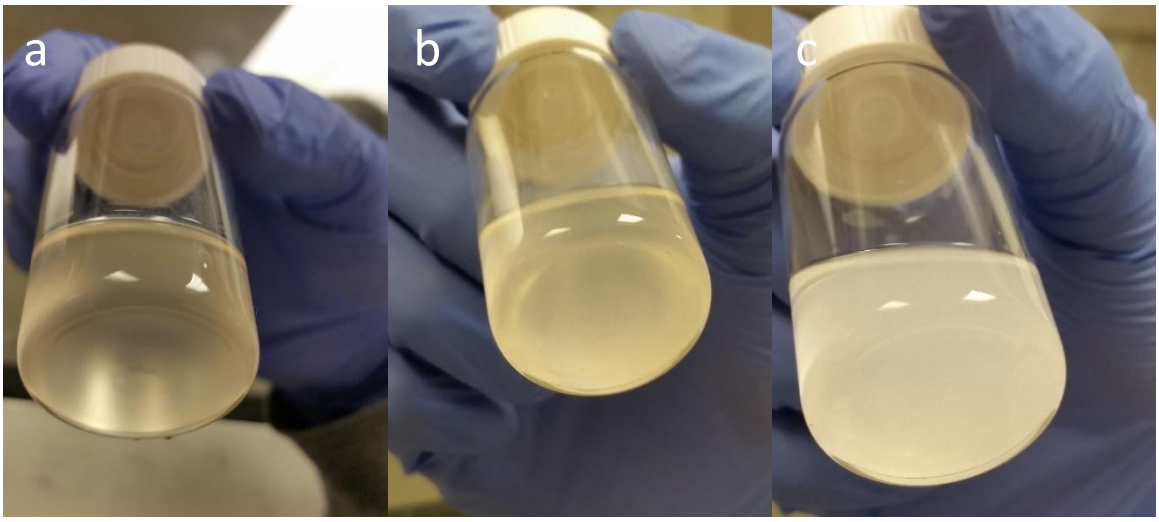

Figure 5.15: Photographs of dispersions of 0.57Zn (**a**), 2.9Zn (**b**), and 43Zn TPs (**c**) in heptane (0.5 mg/mL).

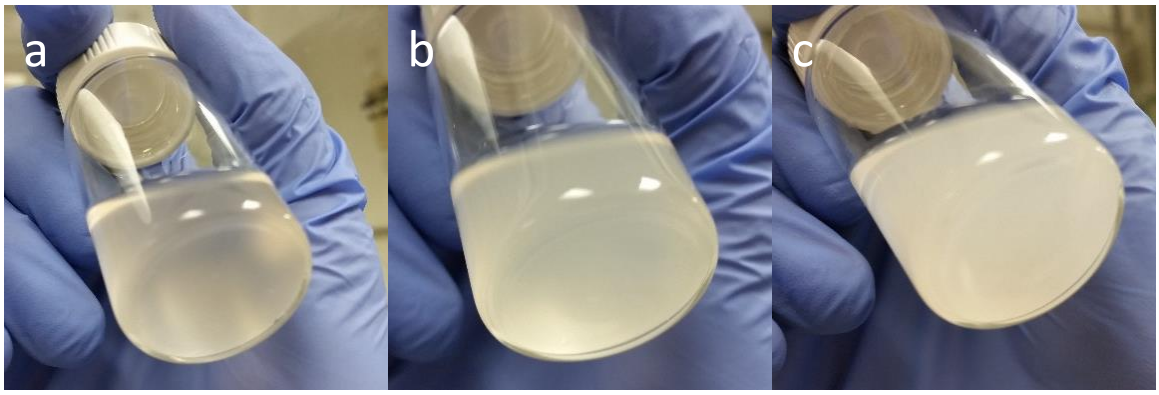

Figure 5.16: Photographs of dispersions of 0.57Zn (**a**), 2.9Zn (**b**), and 43Zn TPs (**c**) in 1 M NaCl (0.5 mg/mL)

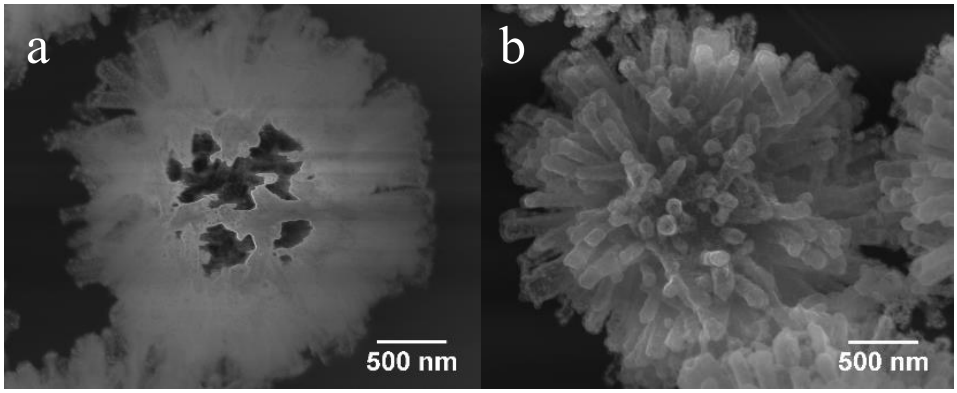

Figure 5.17: SEM of TPs with PSS/PDDA/Au NP (Au TP) (**a**) and with PSS/PDDA/Au NP (0.5 M NaCl; AuS_TP) layers encapsulated (**b**).

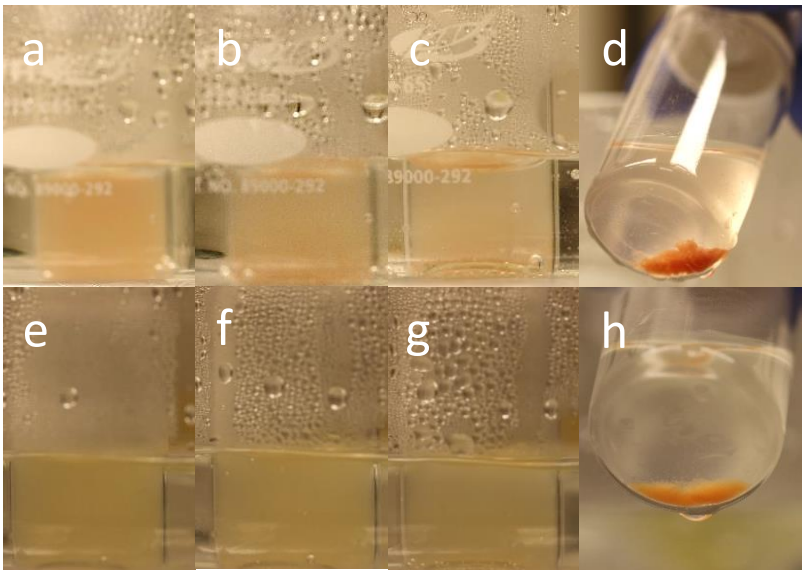

Figure 5.18: Photographs of dispersions of PNIPAM TPs (**a-d**) and PAA TPs (**e-h**) at 80°C dispersion (**a,e**) after 1 minute (**b,f**) after 5 minutes (**c,g**) after 10 minutes. Sediments after being incubated in a water bath for 10 minutes at 80°C (**d,h**).

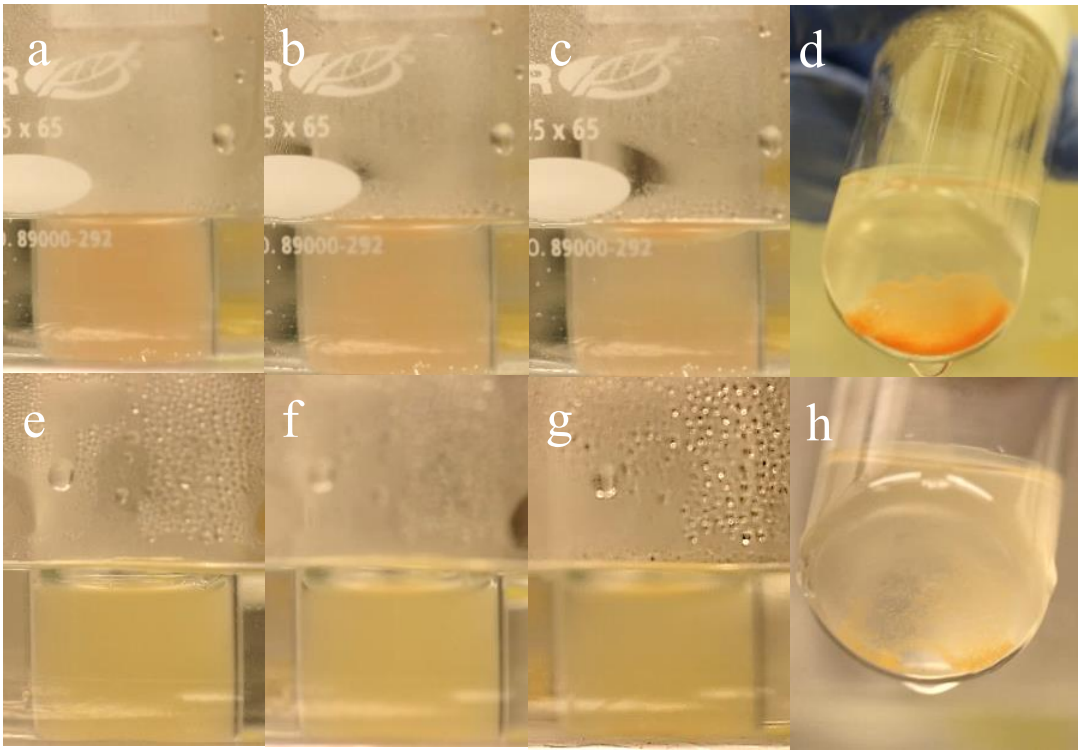

Figure 5.19: Photographs of dispersions of PNIPAM TPs (**a-e**) and PAA TPs (**f-j**) at 60°C dispersion (**a,f**) after 1 minute (**b,g**) after 5 minutes (**c,h**) after 10 minutes. Sediments after being incubated in a water bath for 10 minutes at 60°C (**e,i**).

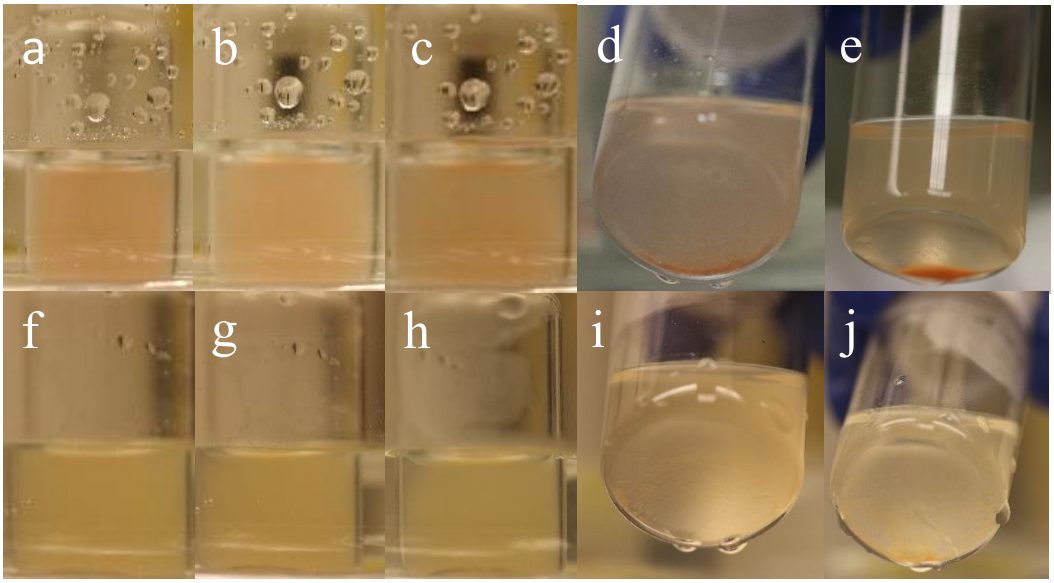

Figure 5.20: Photographs of dispersions of PNIPAM TPs (**a-e**) and PAA TPs (**f-j**) at 40°C dispersion (**a,f**) after 1 minutes (**b,g**) after 5 minutes (**c,h**) after 10 minutes. Sediments after being incubated in a water bath for 5 minutes (**d,i**) and 10 minutes (**e,j**) at 40°C.

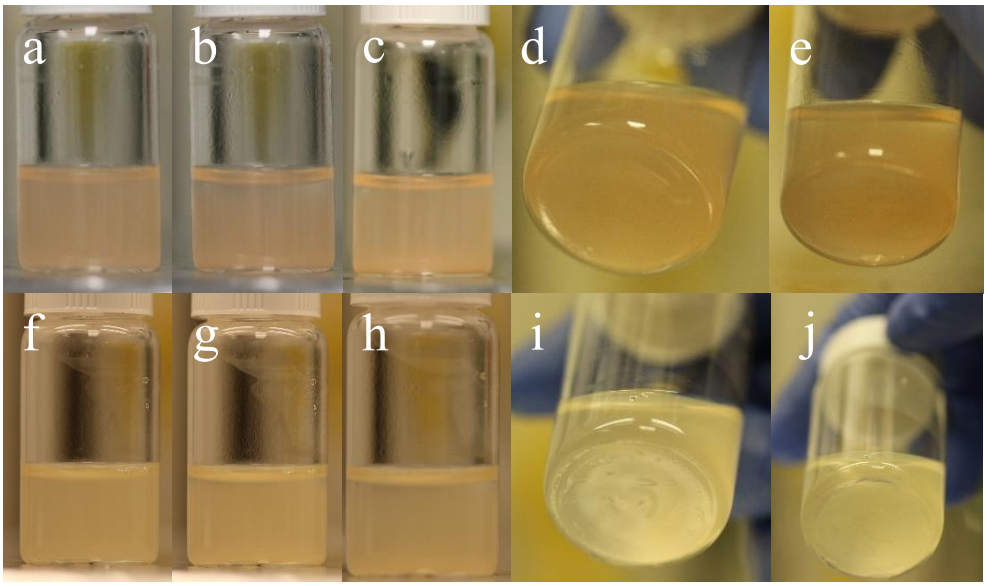

Figure 5.21: Photographs of dispersions of PNIPAM TPs (**a-e**) and PAA TPs (**f-j**) at room temperature (**a,f**) after 1 minutes (**b,g**) after 5 minutes (**c,h**) after 10 minutes. Sediments after 5 minutes (**d,i**) and 10 minutes (**e,j**) at room temperature.

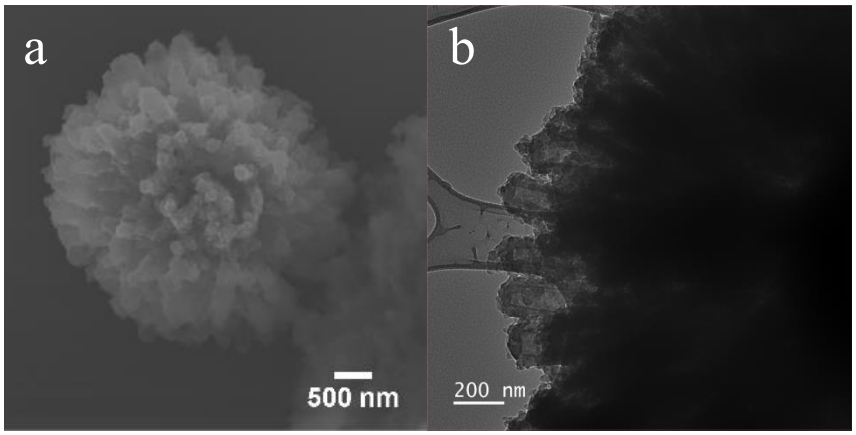

Figure 5.22: SEM (**a**) and TEM (**b**) of dopamine-modified TPs.

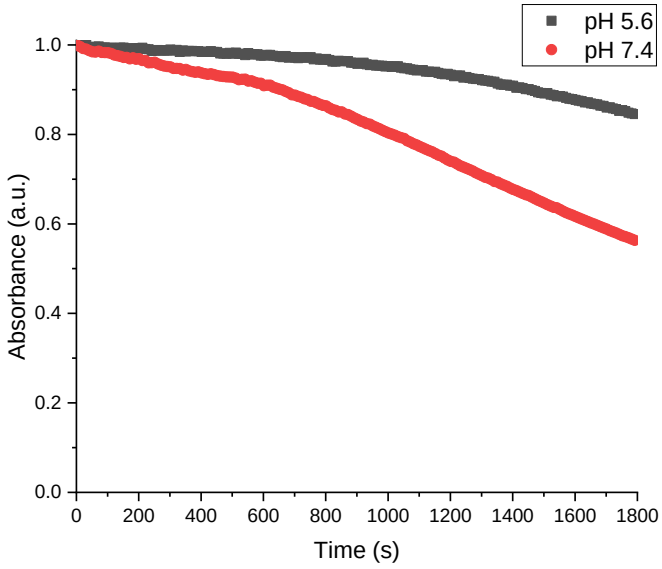

Figure 5.23: Absorbance measurements at 275 nm every 15s for 30 minutes of dopamine-modified TPs at pH 5.6 and pH 7.4 in .01 M PBS buffer.

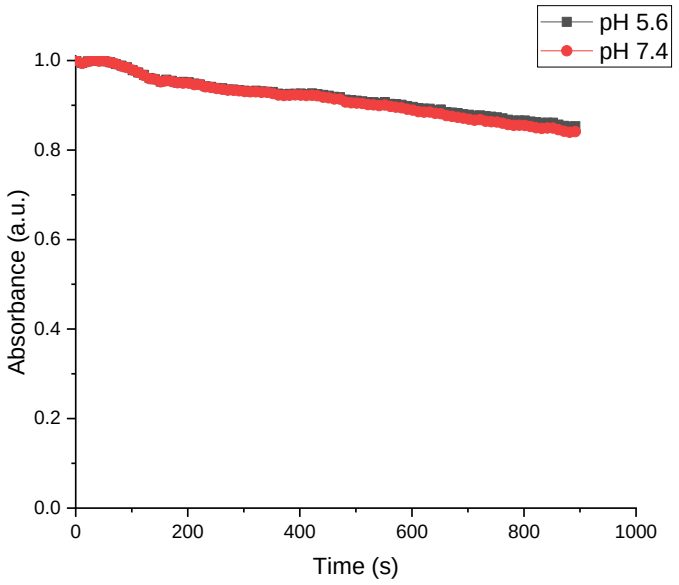

Figure 5.24: Absorbance measurements at 275 nm every 15s for 15 minutes of PAA TPs at pH 5.6 and pH 7.4 in .01 M PBS buffer**.**

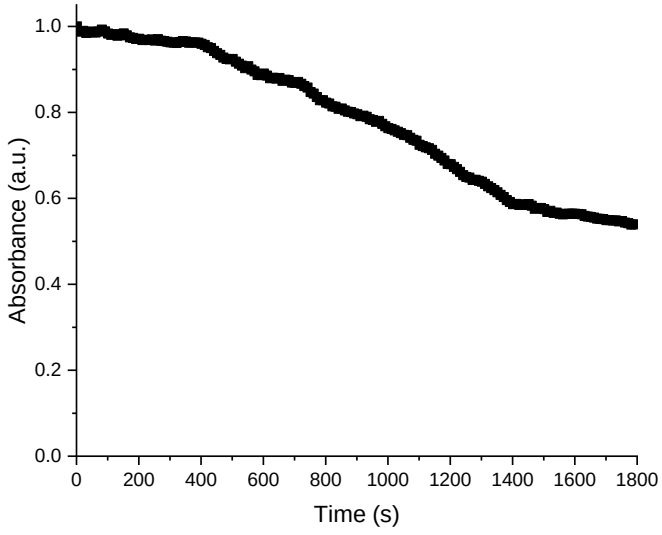

Figure 5.25: Absorbance measurements at 275 nm every 15s for 30 minutes of DOP TPs at pH 5.6.01 M PBS buffer after previously being adjusted to pH 7.4.01 M PBS buffer for 30 minutes.

Chapter 6

Conclusions and Future Directions

6.1 Conclusions

The wide expansion in different nanostructures and synthesis has led to a golden age of nanoscale chemistry. With this dissertation, a new method of stabilizing nanoparticles through surface corrugation utilizing Hedgehog particles (HPs), was applied to numerous applications including sustainable chemical production and sensing in biofluids. Utilizing this new class of colloid has great promise in addressing problems that stem from poor nanoparticle stability in difficult solvent environments.

In chapter II, we overcame the limited colloidal stability of SERS-based biosensors utilizing HPs. We demonstrated that HPs with multilayer coatings of polymer and nanoparticles are omnidispersible in high ionic strength and apolar media if the surface corrugation is maintained. HPs with thick gold layer-by-layer assembly (LbL) coatings enhance detection by over an order of magnitude comparing spiky HPs to smooth spheres. Additionally, HPs were able to detect multiple target molecules in a biofluid while beads were not. When compared to common SERS probe such as nanostars, it is seen that nanostars do not have enough defined surface corrugation to disperse, and result in reduced sensing capability in biofluids

In chapter III, we developed a LbL-coating method to synthesize inorganic SiO_2-based HPs which exhibit enhanced chemical stability. SiO_2 HPs form stable dispersions in heptane and importantly in high ionic strength environments where nanorods aggregate. When tested in a probe photocatalytic reaction, this is reflected, as HPs maintain over two times enhancement over NRs in NaCl. The oxidation of a lignin model compound, 2-phenoxy-1-phenyl ethanol was explored in high ionic strength environments. HPs in divalent salt and acetonitrile greatly enhance activity over water by six times , while organic salts result in multiple orders of magnitude increase in the

yield of 2-phenoxyacetophenone. HPs show that electrolytes in photocatalytic reactions can be used to tune reaction pathways and yields when used with a well-dispersed photocatalyst.

In chapter IV, We expand HPs to a wide array of different functional core materials including plasmonic gold, magnetic magnetite, catalytic hematite, and titanium dioxide. Hematite represent a scalable and cost-effective core material with wide applications. All of the inorganic HPs show stability in apolar environments. We show that by utilizing active hematite cores with ZnO spikes, we are able to develop a new photocatalytic pathway for the production of cyclohexene oxide from cyclohexane. These inorganic HPs have many applications in organic synthesis and reactions in nonpolar environments such as CO_2 where that has been little research due to poor inorganic catalyst stability.

In chapter V. polyelectrolyte films were used to tune the spiky shell of HPs. By introducing a deformable spike, we are able to create environmentally responsive polymer tendril particles (TPs). Both thermoresponsive and pH-responsive subunits were introduced, allowing for controlled aggregation and film formation. Additionally, hollow compartments can be formed which we demonstrate can be used to load nanoparticles for tunable optical properties or small molecules for drug delivery. These tendril particles represent a tunable HP, with promising ability to tune mechanical and optical properties in composites.

In summary, this dissertation has demonstrated the promise of HPs in a wide array of applications. It uncovers new chemical pathways in apolar and ionic strength environments, new sensing capability, and deepens fundamental understanding in corrugated colloids in complex environments. With this toolkit, further exploration could lead to the improvement of chemical processes, sensing, and materials.

6.2 Future Directions

In this dissertation, we developed many new HPs and showed their broad applicability. There are many new and compelling research ideas to investigate. One goal at the onset of this thesis was the development of catalysts in a nonpolar environment. CO_2 reduction is plagued by the poor solubility of CO_2 in water. There has been very limited exploration of catalysts in liquid or supercritical CO_2 because of poor dispersion stability in the environment. Current tests are being conducted with HPs as a catalyst for supercritical CO_2 reduction. Preliminary results

indicate that in particular TiO_2 HPs are stable in supercritical CO_2 (**Figure 6.1**), and further research is ongoing for their use as CO_2 reduction catalysts. The development of a large scale CO_2 reduction catalyst is paramount to addressing global warming and a way to create sustainable fuels.

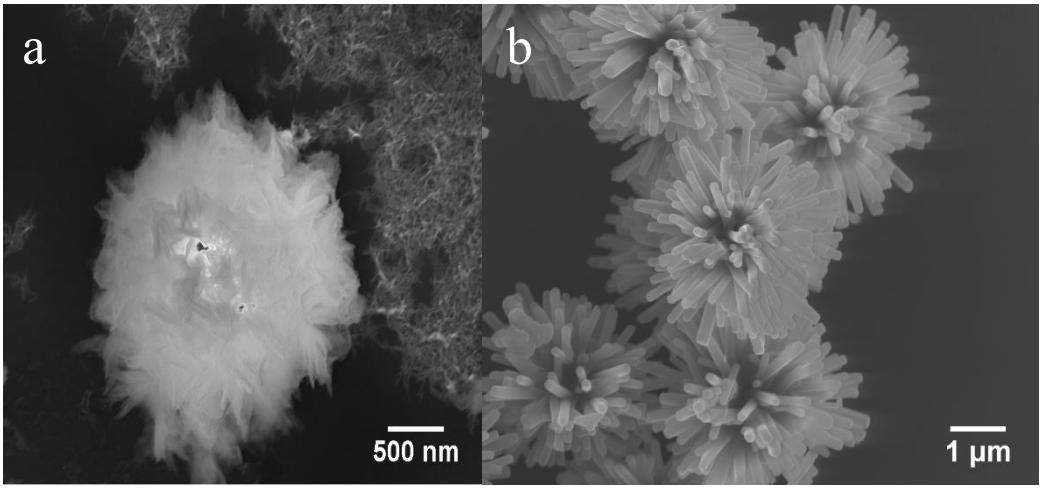

Figure 6.1: SEM images of (**a**) ZnO and (**b**) TiO_2 HPs after incubation in supercritical CO_2 at 40°C and 2000 psi.

Another ongoing project is in the oxidation of cyclohexane. The unique mechanism and selectivity seen in preliminary results indicate that by the use of interfacial HP catalysts, photocatalytic oxidation and in particular epoxidation can be greatly enhanced. Further investigation of this process, including with other olefins is planned, and could lead to many interesting discoveries of new mechanisms in apolar environments. Additionally, though only briefly discussed in this dissertation, HPs exhibit very strong unique broadband scattering. The ability to tune optical responses in the future with HPs and leveraging the optical properties for creation of photocatalysts is a part of future studies. Preliminary results show many interesting properties of these materials, show that these optical responses can be exploited for use in photocatalysis.

For sensing, the use of HP directly in a blood-based system for quick analysis is intriguing. Another very intriguing extension is the creation of conductive HPs. In composites, the addition of spiky nickel fillers has been shown to allow for responsive electronics, by forming a conductive pathway and then using a polymeric matrix to separate the spiky particles at high heat.[331] One particular material which is of interest is carbon nanotubes. Carbon nanotubes have long-standing problems of stability in different environments. However, they can

greatly enhance the mechanical and electric properties of many different composite materials. The creation of a HP consisting of a carbon nanotube array would be a very intriguing use of surface corrugation and have excellent mechanical properties and conductivity.

HPs have also been explored preliminary in coatings. HPs can be easily incorporated into into paints, plastics, and fabric coatings for enhancement of mechanical and flame-retardant properties (**Figure 6.2**).

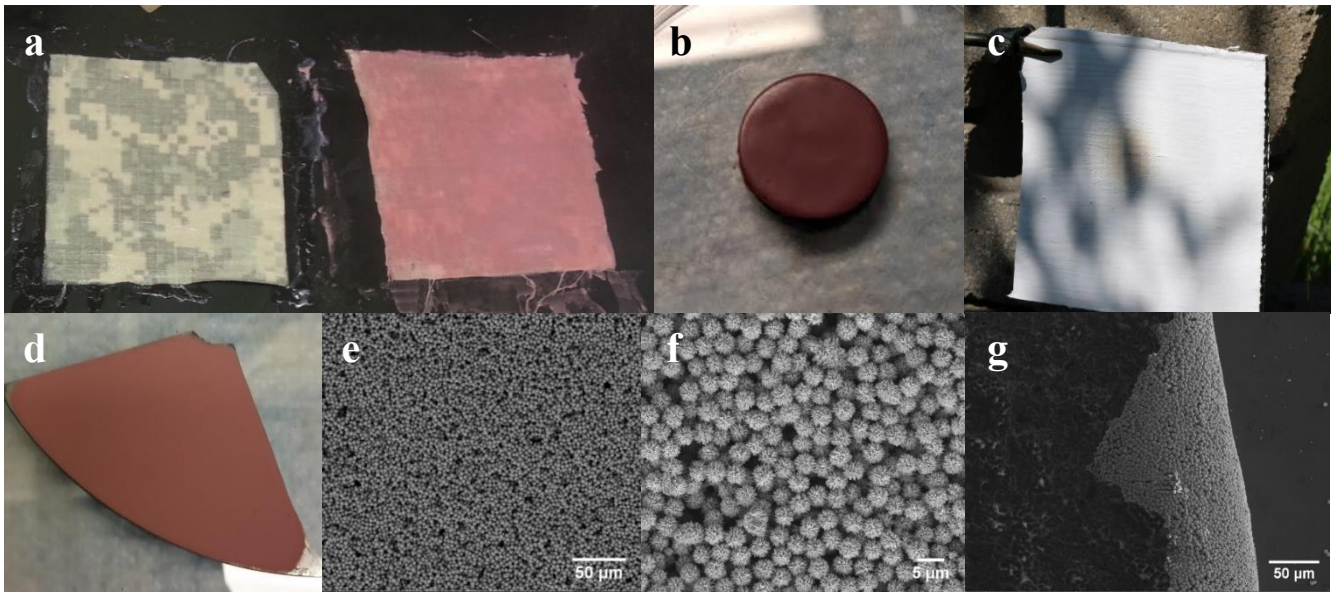

Figure 6.2. (**a**) Incorporation of HPs at low loading and high loading on uniform fabric utilizing commercial acrylate copolymer. (**b**) HP plastic polyurethane composite (**c**) Photograph after a 5 second horizontal flame test with a propane torch on cardboard coated with HPs dispersed in acrylic latex paint (**e**) HPs spin coated onto silicon wafer showing uniform film. SEM images showing distribution of HPs in coating (**e,f**) and (**g**) showing ability to remove film from wafer to create a stand-alone composite.

Composition needs to be tuned to further enhance these properties for a niche application. TPs represent a very intriguing material to test mechanically. With deformable spikes, some frequency-dependent viscoelastic properties are expected. With the ability to load nanoparticles in the spikes, a variety of different optical, mechanical, and electrical properties can be obtained. Overcoming poor material dispersion in composites is a very compelling and intriguing application.

In conclusion, the development of this new class of omnidispersible colloid will lead to exploration of more complex fluid environments for new efficient pathways for the synthesis of sustainable fuels and chemicals. In addition it can be used to further improve dispersion and the application of sensing probes in biofluids, and of nanoparticles in solid composites.

Bibliography

(1) Sperling, R. a; Parak, W. J. Surface Modification, Functionalization and Bioconjugation of Colloidal Inorganic Nanoparticles. *Philos. Trans. A. Math. Phys. Eng. Sci.* **2010**, *368* (1915), 1333–1383.

(2) Yang, J.; Lee, J. Y.; Deivaraj, T. C.; Too, H.-P. A Highly Efficient Phase Transfer Method for Preparing Alkylamine-Stabilized Ru, Pt, and Au Nanoparticles. *J. Colloid Interface Sci.* **2004**, *277*, 95–99.

(3) Brust, M.; Walker, M.; Bethell, D.; Schiffrin, D. J.; Whyman, R. Synthesis of Thiol-Derivatised Gold Nanoparticles In. *Chem. Commun.* **1994**, 801–802.

(4) Lin, S.-Y.; Tsai, Y.-T.; Chen, C.-C.; Lin, C.-M.; Chen, C. AuNP53-Two-Step Functionalization of Neutral and Positively Charged Thiols onto Citrate-Stabilized Au Nanoparticles. *J. Phys. Chem. B* **2004**, *108* (7), 2134–2139.

(5) Aldana, J.; Wang, Y. A.; Peng, X. Photochemical Instability of CdSe Nanocrystals Coated by Hydrophilic Thiols. *J. Am. Chem. Soc.* **2001**, *123* (36), 8844–8850.

(6) Rao, Y.; Antalek, B.; Minter, J.; Mourey, T.; Blanton, T.; Slater, G.; Slater, L.; Fornalik, J. Organic Solvent-Dispersed TiO2 Nanoparticle Characterization. *Langmuir* **2009**, *25* (21), 12713–12720.

(7) Kulkarni, S. A.; Ogale, S. B.; Vijayamohanan, K. P. Tuning the Hydrophobic Properties of Silica Particles by Surface Silanization Using Mixed Self-Assembled Monolayers. *J. Colloid Interface Sci.* **2008**, *318* (2), 372–379.

(8) Haider, P.; Urakawa, A.; Schmidt, E.; Baiker, A. Selective Blocking of Active Sites on Supported Gold Catalysts by Adsorbed Thiols and Its Effect on the Catalytic Behavior: A Combined Experimental and Theoretical Study. *J. Mol. Catal. A Chem.* **2009**, *305* (1–2), 161–169.

(9) Li, P. Z.; Aijaz, A.; Xu, Q. Highly Dispersed Surfactant-Free Nickel Nanoparticles and Their Remarkable Catalytic Activity in the Hydrolysis of Ammonia Borane for Hydrogen Generation. *Angew. Chemie - Int. Ed.* **2012**, *51* (27), 6753–6756.

(10) Pamies, R.; Cifre, J. G. H.; Espín, V. F.; Collado-González, M.; Baños, F. G. D.; De La Torre, J. G. Aggregation Behaviour of Gold Nanoparticles in Saline Aqueous Media. *J. Nanoparticle Res.* **2014**, *16* (4).

(11) Sakura, T.; Takahashi, T.; Kataoka, K.; Nagasaki, Y. One-Pot Preparation of Mono-Dispersed and Physiologically Stabilized Gold Colloid. *Colloid Polym. Sci.* **2005**, *284* (1), 97–101.

(12) Deckert, A. A.; Farrell, C.; Roos, J.; Waddell, R.; Stubna, A. Steric Considerations in the Covalent Binding of Myoglobin to Thin Films. *Langmuir* **1999**, *15* (17), 5578–5583.

(13) Bonanno, L. M.; DeLouise, L. A. Steric Crowding Effects on Target Detection in an Affinity Biosensor. *Langmuir* **2007**, *23* (10), 5817–5823. (14) Zhang, J.; Wang, L.; Shao, Y.; Wang, Y.; Gates, B. C.; Xiao, F. S. A Pd@Zeolite Catalyst for Nitroarene Hydrogenation with High Product Selectivity by Sterically Controlled Adsorption in the Zeolite Micropores. *Angew. Chemie - Int. Ed.* **2017**, *56* (33), 9747–9751.

(15) Bahng, J. H.; Yeom, B.; Wang, Y.; Tung, S. O.; Hoff, J. D.; Kotov, N. Anomalous Dispersions of 'Hedgehog' Particles. *Nature* **2014**, *517* (7536), 596–599.

(16) Brandon Goodwin, W.; Gomez, I. J.; Fang, Y.; Meredith, J. C.; Sandhage, K. H. Conversion of Pollen Particles into Three-Dimensional Ceramic Replicas Tailored for Multimodal Adhesion. *Chem. Mater.* **2013**, *25* (22), 4529–4536.

(17) Seo, J.; Wang, L.; Ng, W.; Cho, N.-J. Preparation of Highly Monodisperse Electroactive Pollen Biocomposites. *ChemNanoMat* **2016**, *2* (5), 414–418.

(18) Stassi, S.; Canavese, G. Spiky Nanostructured Metal Particles as Filler of Polymeric Composites Showing Tunable Electrical Conductivity. *J. Polym. Sci. Part B Polym. Phys.* **2012**, *50* (14), 984–992.

(19) Nguyen, T. Q. N.; Giam, H. L.; Wang, Y.; Pacławski, A.; Szlęk, J.; Mendyk, A.; Shao, Y.-H.; Lau, R. Surface Modification of Pollen-Shape Carriers for Dry Powder Inhalation through Surface Etching. *Ind. Eng. Chem. Res.* **2014**, *53* (51), 19943–19950.

(20) Mundargi, R. C.; Potroz, M. G.; Park, S.; Shirahama, H.; Lee, J. H.; Seo, J.; Cho, N. J. Natural Sunflower Pollen as a Drug Delivery Vehicle. *Small* **2016**, *12* (9), 1167–1173.

(21) Oyama, H. T.; Sprycha, R.; Xie, Y.; Partch, R. E.; Matijević, E. Coating of Uniform Inorganic Particles with Polymers, I. *Journal of Colloid and Interface Science*. 1993, pp 298–303.

(22) Huang, C.-L.; Matijevic, E. Coating of Uniform Inorganic Particles with Polymers: III. Polypyrrole on Different Metal Oxides. *J. Mater. Res.* **2011**, *10* (05), 1327–1336.

(23) Hergeth, W.; Steinau, U.; Bittrich, H.; Schmutzler, K.; Wartewig, S. Submicron Particles with Thin Polymer Shells. **1991**, *90*, 82–90.

(24) Quaroni, L.; Chumanov, G. Preparation of Polymer-Coated Functionalized Silver Nanoparticles [9]. *J. Am. Chem. Soc.* **1999**, *121* (45), 10642–10643.

(25) Decher, G.; Hong, J. D.; Schmitt, J. Buildup of Ultrathin Multilayer Films by a Self-Assembly Process: III. Consecutively Alternating Adsorption of Anionic and Cationic Polyelectrolytes on Charged Surfaces. *Thin Solid Films* **1992**, *210–211* (I), 831–835.

(26) Decher, G. Fuzzy Nanoassemblies: Toward Layered Polymeric Multicomposites. *Science (80-.).* **1997**, *277* (5330), 1232–1237.

(27) Iler, R. K. Multilayers of Colloidal Particles. *J. Colloid Interface Sci.* **1966**, *21*, 569–594.

(28) Kotov, N. a.; Dékány, I.; Fendler, J. H. Layer-by-Layer Self-Assembly of Polyelectrolyte-

Semiconductor Nanoparticle Composite Films. *J. Phys. Chem.* **1995**, *99* (35), 13065–13069.

(29) Stockton, W. B.; Rubner, M. F. Molecular-Level Processing of Conjugated Polymers. 4. Layer-by-Layer Manipulation of Polyaniline via Hydrogen-Bonding Interactions. *Macromolecules* **1997**, *30* (9), 2717–2725.

(30) Tang, Z.; Kotov, N. A.; Magonov, S.; Ozturk, B. Nanostructured Artificial Nacre. *Nat. Mater.* **2003**, *2* (6), 413–418.

(31) Podsiadlo, Paul, K. Ultrastrong and Stiff Layered Polymer Nanocomposites. *Science (80-.).* **2007**, *318* (5847), 80–84.

(32) Donath, E.; Sukhorukov, G. B.; Caruso, F.; Davis, S. A.; Möhwald, H. Novel Hollow Polymer Shells by Colloid-Templated Assembly of Polyelectrolytes. *Angew. Chemie - Int. Ed.* **1998**, No. 16, 2201–2205.

(33) Caruso, F.; Möhwald, H. Protein Multilayer Formation on Colloids through a Stepwise Self- Assembly Technique. *J. Am. Chem. Soc.* **1999**, *121* (25), 6039–6046.

(34) Stuart, M. a C.; Huck, W. T. S.; Genzer, J.; Müller, M.; Ober, C.; Stamm, M.; Sukhorukov, G. B.; Szleifer, I.; Tsukruk, V. V; Urban, M.; et al. Emerging Applications of Stimuli-Responsive Polymer Materials. *Nat. Mater.* **2010**, *9* (2), 101–113.

(35) Delcea, M.; Möhwald, H.; Skirtach, A. G. Stimuli-Responsive LbL Capsules and Nanoshells for Drug Delivery. *Adv. Drug Deliv. Rev.* **2011**, *63* (9), 730–747.

(36) Cho, J.; Jang, H.; Yeom, B.; Kim, H.; Kim, R.; Kim, S.; Char, K.; Caruso, F. Modulating the Pattern Quality of Micropatterned Multilayer Films Prepared by Layer-by-Layer Self-Assembly. *Langmuir* **2006**, *22* (3), 1356–1364.

(37) Park, J.; Kim, I.; Shin, H.; Lee, M. J.; Kim, Y. S.; Bang, J.; Caruso, F.; Cho, J. Integrated Catalytic Activity of Patterned Multilayer Films Based on PH-Induced Electrostatic Properties of Enzymes. *Adv. Mater.* **2008**, *20* (10), 1843–1848.

(38) Lang, Y.; Finn, D. P.; Caruso, F.; Pandit, A. Fabrication of Nanopatterned Polymeric Microparticles Using a Diatom as a Sacrificial Template. *RSC Adv.* **2014**, *4* (84), 44418–44422.

(39) Zhang, X.; Zana, X.; Su, Z. Polyelectrolyte Multilayer Supported Pt Nanoparticles as Catalysts for Methanol Oxidation. *J. Mater. Chem.* **2011**, *21*, 17783–17789.

(40) Dotzauer, D. M.; Dai, J.; Sun, L.; Bruening, M. L. Catalytic Membranes Prepared Using Layer-by-Layer Adsorption of Polyelectrolyte/Metal Nanoparticle Films in Porous Supports. *Nano Lett.* **2006**, *6* (10), 2268–2272.

(41) Dotzauer, D. M.; Bhattacharjee, S.; Wen, Y.; Bruening, M. L. Nanoparticle-Containing Membranes for the Catalytic Reduction of Nitroaromatic Compounds. *Langmuir* **2009**, *25* (3), 1865–1871.

(42) Mir-Simon, B.; Morla-Folch, J.; Gisbert-Quilis, P.; Pazos-Perez, N.; Xie, H.; Bastús, N. G.; Puntes, V.; Alvarez-Puebla, R. A.; Guerrini, L. SERS Efficiencies of Micrometric

Polystyrene Beads Coated with Gold and Silver Nanoparticles: The Effect of Nanoparticle Size. *J. Opt.* **2015**, *17* (11), 114012.

(43) Abalde-Cela, S.; Ho, S.; Rodríguez-González, B.; Correa-Duarte, M. A. M. A.; Álvarez-Puebla, R. A. R. A.; Liz-Marzán, L. M. L. M.; Kotov, N. A. N. A. Loading of Exponentially Grown LBL Films with Silver Nanoparticles and Their Application to Generalized SERS Detection. *Angew. Chemie - Int. Ed.* **2009**, *48* (29), 5326–5329.

(44) Kidambi, S.; Li, J.; Dai, J. H.; Bruening, M. L. Catalytic Pd Nanoparticles Embedded in Polyelectrolyte Multilayers. *Abstr. Pap. Am. Chem. S.* **2004**, *227* (Part 2), 201-PMSE.

(45) Bell, A. T. The Impact of Nanoscience on Heterogeneous Catalysis. *Science* **2003**, *299* (5613), 1688–1691.

(46) Hoffmann, M. R.; Hoffmann, M. R.; Martin, S. T.; Martin, S. T.; Choi, W.; Choi, W.; Bahnemannt, D. W.; Bahnemannt, D. W. Environmental Applications of Semiconductor Photocatalysis. *Chem. Rev.* **1995**, *95* (1), 69–96.

(47) Palmisano, G.; Augugliaro, V.; Pagliaro, M.; Palmisano, L. Photocatalysis: A Promising Route for 21st Century Organic Chemistry. *Chem. Commun. (Camb).* **2007**, No. 33, 3425–3437.

(48) Teoh, W. Y.; Scott, J. A.; Amal, R. Progress in Heterogeneous Photocatalysis: From Classical Radical Chemistry to Engineering Nanomaterials and Solar Reactors. *Journal of Physical Chemistry Letters*. 2012, pp 629–639.

(49) Tong, H.; Ouyang, S.; Bi, Y.; Umezawa, N.; Oshikiri, M.; Ye, J. Nano-Photocatalytic Materials: Possibilities and Challenges. *Adv. Mater.* **2012**, *24* (2), 229–251.

(50) Maeda, K. Photocatalytic Water Splitting Using Semiconductor Particles: History and Recent Developments. *Journal of Photochemistry and Photobiology C: Photochemistry Reviews*. 2011, pp 237–268.

(51) Moniz, S. J. a.; Shevlin, S. a.; Martin, D. J.; Guo, Z.-X.; Tang, J. Visible-Light Driven Heterojunction Photocatalysts for Water Splitting – a Critical Review. *Energy Environ. Sci.* **2015**, *8*, 731–759.

(52) Yuan, L.; Xu, Y.-J. Photocatalytic Conversion of CO2 into Value-Added and Renewable Fuels. *Appl. Surf. Sci.* **2015**, *342*, 154–167.

(53) Marszewski, M.; Cao, S.; Yu, J.; Jaroniec, M. Semiconductor-Based Photocatalytic CO 2 Conversion. *Mater. Horiz.* **2015**, *2*, 261–278.

(54) Tu, W.; Zhou, Y.; Zou, Z. Photocatalytic Conversion of CO2 into Renewable Hydrocarbon Fuels: State-of-the-Art Accomplishment, Challenges, and Prospects. *Adv. Mater.* **2014**, *26* (27), 4607–4626.

(55) Zangeneh, H.; Zinatizadeh, a. a. L.; Habibi, M.; Akia, M.; Hasnain Isa, M. Photocatalytic Oxidation of Organic Dyes and Pollutants in Wastewater Using Different Modified Titanium Dioxides: A Comparative Review. *J. Ind. Eng. Chem.* **2015**, *26*, 1–36.

(56) Chong, M. N.; Jin, B.; Chow, C. W. K.; Saint, C. Recent Developments in Photocatalytic

Water Treatment Technology: A Review. *Water Res.* **2010**, *44* (10), 2997–3027.

(57) Maldotti, A.; Molinari, A.; Amadelli, R. Photocatalysis with Organized Systems for the Oxofunctionalization of Hydrocarbons by O2. *Chem. Rev.* **2002**, *102* (10), 3811–3836.

(58) Fox, M. A.; Fox, M. A.; Dulay, M. T.; Dulay, M. T. Heterogeneous Photocatalysis. *Chem. Rev.* **1993**, *93* (1), 341–357.

(59) Cherevatskaya, M.; König, B. Heterogeneous Photocatalysts in Organic Synthesis. *Russ. Chem. Rev.* **2014**, *83* (3), 183–195.

(60) Munir, S.; Dionysiou, D. D.; Khan, S. B.; Shah, S. M.; Adhikari, B.; Shah, A. Development of Photocatalysts for Selective and Efficient Organic Transformations. *J. Photochem. Photobiol. B.* **2015**, *148*, 209–222.

(61) Zaera, F. Nanostructured Materials for Applications in Heterogeneous Catalysis. *Chem. Soc. Rev.* **2013**, *2*, 2746–2762.

(62) Zhang, H.; Shih, J.; Zhu, J.; Kotov, N. A. Layered Nanocomposites from Gold Nanoparticles for Neural Prosthetic Devices. *Nano Lett.* **2012**, *12* (7), 3391–3398.

(63) Hashimoto, K.; Irie, H.; Fujishima, A. Photocatalysis: A Historical Overview and Future Prospects. *Jpn. J. Appl. Phys.* **2005**, *44* (12), 8269–8285.

(64) Linsebigler, A. L.; Linsebigler, A. L.; Yates Jr, J. T.; Lu, G.; Lu, G.; Yates, J. T. Photocatalysis on TiO2 Surfaces: Principles, Mechanisms, and Selected Results. *Chem. Rev.* **1995**, *95* (3), 735–758.

(65) Schiavello, M.; Schiavello, M. Heterogeneous Photocatalysis. **1997**, No. v 3, 197 p.

(66) Anpo, M.; Yamashita, H.; Ichihashi, Y.; Fujii, Y.; Honda, M. Photocatalytic Reduction of CO 2 with H 2 O on Titanium Oxides Anchored within Micropores of Zeolites : Effects of the Structure of the Active Sites and the Addition of Pt. *J. Phys. Chem. B* **1997**, *5647* (96), 2632–2636.

(67) P, D. P.; Uv, H.; Doudrick, K.; Asce, M.; Monzón, O.; Mangonon, A.; Hristovski, K.; Ph, D.; Westerhoff, P. Nitrate Reduction in Water Using Commercial Titanium. **2012**, No. August, 852–861.

(68) Ohno, T.; Mitsui, T.; Matsumura, M. Photocatalytic Activity of S-Doped TiO2 Photocatalyst under Visible Light. *Chem. Lett.* **2003**, *32* (4), 364–365.

(69) Umebayashi, T.; Yamaki, T.; Tanaka, S.; Asai, K. Visible Light-Induced Degradation of Methylene Blue on S-Doped TiO2. *Chem. Lett.* **2003**, *32* (4), 330–331.

(70) Asahi, R.; Morikawa, T.; Ohwaki, T.; Aoki, K.; Taga, Y. Visible-Light Photocatalysis in Nitrogen-Doped Titanium Oxides. *Science (80-.).* **2001**, *293* (July), 2000–2002.

(71) Xiao, Q.; Ouyang, L. Photocatalytic Photodegradation of Xanthate over Zn1-XMnxO under Visible Light Irradiation. *J. Alloys Compd.* **2009**, *479* (1–2), 4–7.

(72) Tian, Z. R.; Voigt, J. a.; Liu, J.; Mckenzie, B.; Mcdermott, M. J.; Rodriguez, M. a.; Konishi, H.; Xu, H. Complex and Oriented ZnO Nanostructures. *Nat. Mater.* **2003**, *2* (12),

821–826.

(73) Kołodziejczak-Radzimska, A.; Jesionowski, T. Zinc Oxide—From Synthesis to Application: A Review. *Materials (Basel).* **2014**, *7* (4), 2833–2881.

(74) Amine, A.; Sehili, T.; Pilichowski, J.; Boule, P. Photocatalytic Degradation of 2-Phenylphenol on TiO 2 and ZnO in Aqueous Suspensions. *J. Photochem. Photobiol. A Chem.* **2001**, *141*, 231–239.

(75) Kumar, S. G.; Rao, K. S. R. K. Zinc Oxide Based Photocatalysis: Tailoring Surface-Bulk Structure and Related Interfacial Charge Carrier Dynamics for Better Environmental Applications. *RSC Adv.* **2015**, *5* (5), 3306–3351.

(76) Zou, X.; Fan, H.; Tian, Y.; Yan, S. Synthesis of Cu2O/ZnO Hetero-Nanorod Arrays with Enhanced Visible Light-Driven Photocatalytic Activity. *CrystEngComm* **2014**, *16* (6), 1149.

(77) Ma, S.; Li, R.; Lv, C.; Xu, W.; Gou, X. Facile Synthesis of ZnO Nanorod Arrays and Hierarchical Nanostructures for Photocatalysis and Gas Sensor Applications. *J. Hazard. Mater.* **2011**, *192* (2), 730–740.

(78) Good, D. M.; Thongboonkerd, V.; Novak, J.; Bascands, J. L.; Schanstra, J. P.; Coon, J. J.; Dominiczak, A.; Mischak, H. Body Fluid Proteomics for Biomarker Discovery: Lessons from the Past Hold the Key to Success in the Future. *J. Proteome Res.* **2007**, *6* (12), 4549–4555.

(79) Kong, K.; Kendall, C.; Stone, N.; Notingher, I. Raman Spectroscopy for Medical Diagnostics — From in-Vitro Bio Fl Uid Assays to in-Vivo Cancer Detection ☆. *Adv. Drug Deliv. Rev.* **2015**, *89*, 121–134.

(80) Sivapalan, S. T.; DeVetter, B. M.; Yang, T. K.; Schulmerich, M. V.; Bhargava, R.; Murphy, C. J. Surface-Enhanced Raman Spectroscopy of Polyelectrolyte-Wrapped Gold Nanoparticles in Colloidal Suspension. *J. Phys. Chem. C* **2013**, *117* (20), 10677–10682.

(81) Khan, M. A.; Hogan, T. P.; Shanker, B. Gold-Coated Zinc Oxide Nanowire-Based Substrate for Surface-Enhanced Raman Spectroscopy. *J. Raman Spectrosc.* **2009**, *40* (11), 1539–1545.

(82) Jiang, P.; Bertone, J. Single-Crystal Colloidal Multilayers of Controlled Thickness. *Chem. Mater.* **1999**, *11* (25), 2132–2140.

(83) Chen, L.; Luo, L.; Chen, Z.; Zhang, M.; Zapien, J. A.; Lee, C. S.; Lee, S. T. ZnO/Au Composite Nanoarrays as Substrates for Surface-Enhanced Raman Scattering Detection. *J. Phys. Chem. C* **2010**, *114* (1), 93–100.

(84) Ji, I. A.; Bang, J. H. Synthesis of Gold-Coated TiO2 Nanorod Array and Its Application as a Raman Substrate. *Mater. Lett.* **2013**, *97*, 158–161.

(85) Fan, J. G.; Zhao, Y. P. Gold-Coated Nanorod Arrays as Highly Sensitive Substrates for Surface-Enhanced Raman Spectroscopy. *Langmuir* **2008**, *24* (24), 14172–14175.

(86) Serrano-Montes, A. B.; Langer, J.; Henriksen-Lacey, M.; Jimenez de Aberasturi, D.;

Solís, D. M.; Taboada, J. M.; Obelleiro, F.; Sentosun, K.; Bals, S.; Bekdemir, A.; et al. Gold Nanostar-Coated Polystyrene Beads as Multifunctional Nanoprobes for SERS Bioimaging. *J. Phys. Chem. C* **2016**, acs.jpcc.6b02282.

(87) Pfeiffer, C.; Rehbock, C.; Huhn, D.; Carrillo-Carrion, C.; de Aberasturi, D. J.; Merk, V.; Barcikowski, S.; Parak, W. J.; Hühn, D.; Carrillo-Carrion, C.; et al. Interaction of Colloidal Nanoparticles with Their Local Environment: The (Ionic) Nanoenvironment around Nanoparticles Is Different from Bulk and Determines the Physico-Chemical Properties of the Nanoparticles. *J. R. Soc. Interface* **2014**, *11* (96), 20130931–20130931.

(88) Jaworska, A.; Fornasaro, S.; Sergo, V.; Bonifacio, A. Potential of Surface Enhanced Raman Spectroscopy (SERS) in Therapeutic Drug Monitoring (TDM). A Critical Review. *Biosensors* **2016**, *6* (3), 47.

(89) Pazos-Perez, N.; Pazos, E.; Catala, C.; Mir-Simon, B.; Gómez-de Pedro, S.; Sagales, J.; Villanueva, C.; Vila, J.; Soriano, A.; García de Abajo, F. J.; et al. Ultrasensitive Multiplex Optical Quantification of Bacteria in Large Samples of Biofluids. *Sci. Rep.* **2016**, *6* (July), 29014.

(90) Chang, Y.-C.; Yang, C.-Y.; Sun, R.-L.; Cheng, Y.-F.; Kao, W.-C.; Yang, P.-C. Rapid Single Cell Detection of Staphylococcus Aureus by Aptamer-Conjugated Gold Nanoparticles. *Sci. Rep.* **2013**, *3* (1), 1863.

(91) Catala, C.; Mir-Simon, B.; Feng, X.; Cardozo, C.; Pazos-Perez, N.; Pazos, E.; Gómez-de Pedro, S.; Guerrini, L.; Soriano, A.; Vila, J.; et al. Online SERS Quantification of *Staphylococcus Aureus* and the Application to Diagnostics in Human Fluids. *Adv. Mater. Technol.* **2016**, *1* (8), 1600163.

(92) Alvarez-Puebla, R. A.; Liz-Marzán, L. M. SERS-Based Diagnosis and Biodetection. *Small* **2010**, *6* (5), 604–610.

(93) Pohorecki, R.; Bałdyga, J.; Moniuk, W.; Podgórska, W.; Zdrójkowski, A.; Wierzchowski, P. T. Kinetic Model of Cyclohexane Oxidation. *Chem. Eng. Sci.* **2001**, *56* (4), 1285–1291.

(94) Schuchardt, U.; Cardoso, D.; Sercheli, R.; Pereira, R.; Da Cruz, R. S.; Guerreiro, M. C.; Mandelli, D.; Spinacé, E. V.; Pires, E. L. Cyclohexane Oxidation Continues to Be a Challenge. *Appl. Catal. A Gen.* **2001**, *211* (1), 1–17.

(95) Li, K.; An, X.; Park, K. H.; Khraisheh, M.; Tang, J. A Critical Review of CO2 Photoconversion: Catalysts and Reactors. *Catal. Today* **2014**, *224*, 3–12.

(96) Habisreutinger, S. N.; Schmidt-Mende, L.; Stolarczyk, J. K. Photocatalytic Reduction of CO2 on TiO2 and Other Semiconductors. *Angew. Chemie - Int. Ed.* **2013**, *52* (29), 7372–7408.

(97) Indrakanti, V. P.; Kubicki, J. D.; Schobert, H. H. Photoinduced Activation of CO2 on Ti-Based Heterogeneous Catalysts: Current State, Chemical Physics-Based Insights and Outlook. *Energy Environ. Sci.* **2009**, *2* (7), 745.

(98) Wang, W. N.; Soulis, J.; Jeffrey Yang, Y.; Biswas, P. Comparison of CO2 Photoreduction Systems: A Review. *Aerosol Air Qual. Res.* **2014**, *14* (2), 533–549.

(99) Kaneco, S.; Kurimoto, H.; Shimizu, Y.; Ohta, K.; Mizuno, T. Photocatalytic Reduction of CO2 Using TiO2 Powders in Supercritical Fluid CO2. *Energy* **1999**, *24* (1), 21–30.

(100) Pathak, P.; Meziani, M. J.; Li, Y.; Cureton, L. T.; Sun, Y.-P. Improving Photoreduction of CO2 with Homogeneously Dispersed Nanoscale TiO2 Catalysts. *Chem. Commun.* **2004**, No. 10, 1234.

(101) Pathak, P.; Meziani, M. J.; Castillo, L.; Sun, Y.-P. Metal-Coated Nanoscale TiO2 Catalysts for Enhanced CO2 Photoreduction. *Green Chem.* **2005**, *7* (9), 667.

(102) Arakawa, H.; Aresta, M.; Armor, J. N.; Barteau, M. A.; Beckman, E. J.; Bell, A. T.; Bercaw, J. E.; Creutz, C.; Dinjus, E.; Dixon, D. A.; et al. Catalysis Research of Relevance to Carbon Management: Progress, Challenges, and Opportunities. *Chem. Rev.* **2001**, *101* (4), 953–996.

(103) Benson, E. E.; Kubiak, C. P.; Sathrum, A. J.; Smieja, J. M. Electrocatalytic and Homogeneous Approaches to Conversion of CO2 to Liquid Fuels. *Chem. Soc. Rev.* **2009**, *38* (1), 89–99.

(104) Mehrotra, U. S.; Agrawal, M. C.; Mushran, S. P. Kinetics of the Reduction of Hexacyanoferrate(III) by Ascorbic Acid. *J. Phys. Chem.* **1969**, *73* (6), 1996–1999.

(105) Dinh, C.; Burdyny, T.; Kibria, G.; Seifitokaldani, A.; Gabardo, C. M.; Arquer, F. P. G. de; Kiani, A.; Edwards, J. P.; Luna, P. De; Bushuyev, O. S.; et al. Sustained High-Selectivity CO2 Electroreduction to Ethylene via Hydroxide-Mediated Catalysis at an Abrupt Reaction Interface. *Science (80-.).* **2018**, *787* (May), 783–787.

(106) Gao, D.; McCrum, I. T.; Deo, S.; Choi, Y. W.; Scholten, F.; Wan, W.; Chen, J. G.; Janik, M. J.; Roldan Cuenya, B. Activity and Selectivity Control in CO2 Electroreduction to Multicarbon Products over CuOx Catalysts via Electrolyte Design. *ACS Catal.* **2018**, *8* (11), 10012–10020.

(107) Azevedo, E. B.; Neto, F. R. D. A.; Dezotti, M. TiO 2-Photocatalyzed Degradation of Phenol in Saline Media: Lumped Kinetics, Intermediates, and Acute Toxicity. *Appl. Catal. B Environ.* **2004**, *54* (3), 165–173.

(108) Sunada, F.; Heller, A. Effects of Water, Salt Water, and Silicone Overcoating of the TiO2 Photocatalyst on the Rates and Products of Photocatalytic Oxidation of Liquid 3-Octanol and 3-Octanone. *Environ. Sci. Technol.* **1998**, *32* (2), 282–286.

(109) Zhao, M.; Sun, L.; Crooks, R. M. Preparation of Cu Nanoclusters within Dendrimer Templates. *J. Am. Chem. Soc.* **1998**, *120* (19), 4877–4878.

(110) Wang, Y.; Camargo, P. H. C.; Skrabalak, S. E.; Gu, H.; Xia, Y. A Facile, Water-Based Synthesis of Highly Branched Nanostructures of Silver. *Langmuir* **2008**, *24* (20), 12042–12046.

(111) Yang, M.; Sun, K.; Kotov, N. A. Formation and Assembly-Disassembly Processes of ZnO Hexagonal Pyramids Driven by Dipolar and Excluded Volume Interactions. *J. Am. Chem. Soc.* **2010**, *132* (6), 1860–1872.

(112) Luo, W.; Zhao, T.; Li, Y.; Wei, J.; Xu, P.; Li, X.; Wang, Y.; Zhang, W.; Elzatahry, A. A.;

Alghamdi, A.; et al. A Micelle Fusion-Aggregation Assembly Approach to Mesoporous Carbon Materials with Rich Active Sites for Ultrasensitive Ammonia Sensing. *J. Am. Chem. Soc.* **2016**, *138* (38), 12586–12595.

(113) Banfield, J. F.; Welch, S. A.; Zhang, H.; Ebert, T. T.; Penn, R. L. Aggregation-Based Crystal Growth and Microstructure Development in Natural Iron Oxyhydroxide Biomineralization Products. *Science (80-.).* **2000**, *289* (5480), 751–754.

(114) Wei, Y.; Han, S.; Kim, J.; Soh, S.; Grzybowski, B. A. Photoswitchable Catalysis Mediated by Dynamic Aggregation of Nanoparticles. *J. Am. Chem. Soc.* **2010**, *132* (32), 11018–11020.

(115) Erik, J.; Krishnakumar, A.; Mu, D. Layer-by-Layer Assembly of a Magnetic Nanoparticle Shell on a Thermoresponsive Microgel Core. **2007**, *311*, 219–223.

(116) Mueller, M.; Tebbe, M.; Andreeva, D. V.; Karg, M.; Alvarez Puebla, R. A.; Pazos Perez, N.; Fery, A. Large-Area Organization of PNIPAM-Coated Nanostars as SERS Platforms for Polycyclic Aromatic Hydrocarbons Sensing in Gas Phase. *Langmuir* **2012**, *28* (24), 9168–9173.

(117) Wang, H.; Li, B.; Yodh, A. G.; Zhang, Z. Stimuli-Responsive Shape Switching of Polymer Colloids by Temperature-Sensitive Absorption of Solvent. *Angew. Chemie - Int. Ed.* **2016**, *55* (34), 9952–9955.

(118) Bie, Y.; Yang, J.; Liu, X.; Wang, J.; Nuli, Y.; Lu, W. Polydopamine Wrapping Silicon Cross-Linked with Polyacrylic Acid as High-Performance Anode for Lithium-Ion Batteries. *ACS Appl. Mater. Interfaces* **2016**, acsami.5b10616.

(119) Shi, J.; Yang, C.; Zhang, S.; Wang, X.; Jiang, Z.; Zhang, W.; Song, X.; Ai, Q.; Tian, C. Polydopamine Microcapsules with Different Wall Structures Prepared by a Template-Mediated Method for Enzyme Immobilization. *ACS Appl. Mater. Interfaces* **2013**, *5* (20), 9991–9997.

(120) Borges, J.; Rodrigues, L. C.; Reis, R. L.; Mano, J. F. Layer-by-Layer Assembly of Light-Responsive Polymeric Multilayer Systems. *Adv. Funct. Mater.* **2014**, *24* (36), 5624–5648.

(121) Zhang, Q.; Schwartz, A. G.; Wang, L. V.; Chen, J.; Cobley, C. M.; Kim, C.; Xia, Y.; Song, K. H.; Xie, J.; Rycenga, M.; et al. Gold Nanocages Covered by Smart Polymers for Controlled Release with Near-Infrared Light. *Nat. Mater.* **2009**, *8* (12), 935–939.

(122) Tong, W.; Gao, C.; Möhwald, H. Manipulating the Properties of Polyelectrolyte Microcapsules by Glutaraldehyde Cross-Linking. *Chem. Mater.* **2005**, *17* (18), 4610–4616.

(123) Yu, W. W.; Chang, E.; Sayes, C. M.; Drezek, R.; Colvin, V. L. Aqueous Dispersion of Monodisperse Magnetic Iron Oxide Nanocrystals through Phase Transfer. *Nanotechnology* **2006**, *17* (17), 4483–4487.

(124) Deng, D.; Hao, C.; Sen, S.; Xu, C.; Král, P.; Kotov, N. A. Template-Free Hierarchical Self-Assembly of Iron Diselenide Nanoparticles into Mesoscale Hedgehogs. *J. Am. Chem. Soc.* **2017**, *139* (46).

(125) Ansar, S. M.; Gadogbe, M.; Siriwardana, K.; Howe, J. Y.; Dogel, S.; Hosseinkhannazer, H.; Collier, W. E.; Rodriguez, J.; Zou, S.; Zhang, D. Dispersion Stability, Ligand Structure and Conformation, and SERS Activities of 1-Alkanethiol Functionalized Gold and Silver Nanoparticles. *J. Phys. Chem. C* **2014**, *118* (43), 24925–24934.

(126) Lopez-Sanchez, J. a; Dimitratos, N.; Hammond, C.; Brett, G. L.; Kesavan, L.; White, S.; Miedziak, P.; Tiruvalam, R.; Jenkins, R. L.; Carley, A. F.; et al. Facile Removal of Stabilizer-Ligands from Supported Gold Nanoparticles. *Nat. Chem.* **2011**, *3* (7), 551–556.

(127) Hans, M. .; Lowman, A. . Biodegradable Nanoparticles for Drug Delivery and Targeting. *Curr. Opin. Solid State Mater. Sci.* **2002**, *6* (4), 319–327.

(128) Atlagic, J.; Marjanovic-Jeromela, A.; Marinkovic, R.; Terzic, S. Pollen Grain Traits of Oil Species from the Novi Sad Collection. *Genetika* **2009**, *41* (3), 263–270.

(129) Atlagić, J.; Terzić, S.; Marjanović-Jeromela, A. Staining and Fluorescent Microscopy Methods for Pollen Viability Determination in Sunflower and Other Plant Species. *Ind. Crops Prod.* **2012**, *35* (1), 88–91.

(130) Andresen, V.; Egner, a; Hell, S. W. Time-Multiplexed Multifocal Multiphoton Microscope. *Opt. Lett.* **2001**, *26* (2), 75–77.

(131) Siebrands, C.; Sanger, J. M.; Sanger, J. W. Myofibrillogenesis in Skeletal Muscle Cells in the Presence of Taxol. *Cell Motil. Cytoskeleton* **2004**, *58* (1), 39–52.

(132) Jacobs, G. H.; Rippey, J. J.; Altini, M. Prediction of Aggressive Behavior in Basal Cell Carcinoma. *Cancer* **1982**, *49* (3), 533–537.

(133) Fujii, T. Electron Microscopy of the Leucocytes of the Typhlosole in Ammocoetes, with Special Attention to the Antibody- Producing Cells. *J. Morphol.* **1982**, *173* (1), 87–100.

(134) Kogasaka, R.; Sakuma, Y.; Chiba, S.; Akihara, M.; Horino, K.; Nakao, T. Small Round Virus-like Particles Associated with Acute Gastroenteritis in Japanese Children. *J.Med.Virol.* **1980**, *5* (2), 151–160.

(135) Klose, T.; Reteno, D. G.; Benamar, S.; Hollerbach, A.; Colson, P.; La Scola, B.; Rossmann, M. G. Structure of Faustovirus, a Large DsDNA Virus. *Proc. Natl. Acad. Sci.* **2016**, *113* (22), 6206–6211.

(136) Perera, R.; Kuhn, R. J. Structural Proteomics of Dengue Virus. *Curr. Opin. Microbiol.* **2008**, *11* (4), 369–377.

(137) Kendall, K.; Kendall, M.; Rehfeldt, F. Background to Adhesion of Cells, Viruses, and Nanoparticles. In *Adhesion of Cells, Viruses, and Nanoparticles*; Springer Science & Business Media, 2011; p 3.

(138) Sanchez-Gaytan, B. L.; Park, S.-J. Spiky Gold Nanoshells. *Langmuir* **2010**, *26* (24), 19170–19174.

(139) Atta, S.; Tsoulos, T. V.; Fabris, L. Shaping Gold Nanostar Electric Fields for Surface-Enhanced Raman Spectroscopy Enhancement via Silica Coating and Selective Etching. *J. Phys. Chem. C* **2016**, *120* (37), 20749–20758.

(140) Sacanna, S.; Irvine, W. T. M.; Chaikin, P. M.; Pine, D. J. Lock and Key Colloids. *Nature* **2010**, *464* (7288), 575–578.

(141) Macfarlane, R. J.; Mirkin, C. A. Colloidal Assembly via Shape Complementarity. *ChemPhysChem* **2010**, *11* (15), 3215–3217.

(142) Liu, M.; Pang, Y.; Zhang, B.; De Luna, P.; Voznyy, O.; Xu, J.; Zheng, X.; Dinh, C. T.; Fan, F.; Cao, C.; et al. Enhanced Electrocatalytic CO2reduction via Field-Induced Reagent Concentration. *Nature* **2016**, *537* (7620), 382–386.

(143) Yuan, H.; Fales, A. M.; Vo-Dinh, T. TAT Peptide-Functionalized Gold Nanostars: Enhanced Intracellular Delivery and Efficient NIR Photothermal Therapy Using Ultralow Irradiance. *J. Am. Chem. Soc.* **2012**, *134* (28), 11358–11361.

(144) Decher, G.; Hong, J. -D. Buildup of Ultrathin Multilayer Films by a Self-assembly Process, 1 Consecutive Adsorption of Anionic and Cationic Bipolar Amphiphiles on Charged Surfaces. *Makromol. Chemie. Macromol. Symp.* **1991**, *46* (1), 321–327.

(145) Ariga, K.; Hill, J. P.; Ji, Q.; Niemeyer, C. M.; Pease, A. R.; Jeppesen, J. O.; Stoddart, J. F.; Luo, Y.; Collier, C. P.; Heath, J. R.; et al. Layer-by-Layer Assembly as a Versatile Bottom-up Nanofabrication Technique for Exploratory Research and Realistic Application. *Phys. Chem. Chem. Phys.* **2007**, *9* (19), 2319–2340.

(146) Schlenoff, J. B.; Dubas, S. T.; Farhat, T. Sprayed Polyelectrolyte Multilayers. *Langmuir* **2000**, *16* (26), 9968–9969.

(147) Hong, J. D.; Lowack, K.; Schmitt, J.; Decher, G. Layer-by-Layer Deposited Multilayer Assemblies of Polyelectrolytes and Proteins: From Ultrathin Films to Protein Arrays. In *Trends in Colloid and Interface Science VII*; Steinkopff: Darmstadt, 1993; pp 98–102.

(148) Caruso, R. A.; Susha, A.; Caruso, F. Multilayered Titania, Silica, and Laponite Nanoparticle Coatings on Polystyrene Colloidal Templates and Resulting Inorganic Hollow Spheres. *Chem. Mater.* **2001**, *13* (2), 400–409.

(149) Malikova, N.; Pastoriza-Santos, I.; Schierhorn, M.; Kotov, N. a.; Liz-Marzán, L. M. Layer-by-Layer Assembled Mixed Spherical and Planar Gold Nanoparticles: Control of Interparticle Interactions. *Langmuir* **2002**, *18* (9), 3694–3697.

(150) Ariga, K.; Hill, J. P.; Ji, Q. Layer-by-Layer Assembly as a Versatile Bottom-up Nanofabrication Technique for Exploratory Research and Realistic Application. *Phys. Chem. Chem. Phys.* **2007**, *9* (19), 2319–2340.

(151) Kotov, N. A. Layer-by-Layer Self-Assembly: The Contribution of Hydrophobic Interactions. *Nanostructured Mater.* **1999**, *12* (5).

(152) Caruso, F.; Caruso; R.; Moehwald, H. Nanoengineering of Inorganic and Hybrid Hollow Spheres by Colloidal Templating. *Science (80-.).* **1998**, *282* (5391), 1111–1114.

(153) Schneider, G.; Decher, G.; Nerambourg, N.; Praho, R.; Werts, M. H. V; Blanchard-Desce, M. Distance-Dependent Fluorescence Quenching on Gold Nanoparticles Ensheathed with Layer-by-Layer Assembled Polyelectrolytes. *Nano Lett.* **2006**, *6* (3), 530–536.

(154) Crisp, M. T.; Kotov, N. A. Preparation of Nanoparticle Coatings on Surfaces of Complex Geometry. *Nano Lett.* **2003**, *3* (2), 173–177.

(155) Azzaroni, O.; Lau, K. H. A. Layer-by-Layer Assemblies in Nanoporous Templates: Nano-Organized Design and Applications of Soft Nanotechnology. *Soft Matter* **2011**, *7* (19), 8709–8724.

(156) Yetisen, A. K.; Qu, H.; Manbachi, A.; Butt, H.; Dokmeci, M. R.; Hinestroza, J. P.; Skorobogatiy, M.; Khademhosseini, A.; Yun, S. H. Nanotechnology in Textiles. *ACS Nano* **2016**, *10* (3), 3042–3068.

(157) Lee, K. G.; Choi, B. G.; Kim, B. I.; Shyu, T.; Oh, M. S.; Im, S. G.; Chang, S.-J.; Lee, T. J.; Kotov, N. A.; Lee, S. J. Scalable Nanopillar Arrays with Layer-by-Layer Patterned Overt and Covert Images. *Adv. Mater.* **2014**, *26* (35).

(158) Fakhrullin, R. F.; Lvov, Y. M. "Face-Lifting" and "Make-up" for Microorganisms: Layer-by-Layer Polyelectrolyte Nanocoating. *ACS Nano*. American Chemical Society June 2012, pp 4557–4564.

(159) Zhang, L.; Li, Y.; Sun, J.; Shen, J. Mechanically Stable Antireflection and Antifogging Coatings Fabricated by the Layer-by-Layer Deposition Process and Postcalcination. *Langmuir* **2008**, *24* (19), 10851–10857.

(160) Jiang, C.; Tsukruk, V. V. Freestanding Nanostructures via Layer-by-Layer Assembly. *Adv. Mater.* **2006**, *18* (7), 829–840.

(161) Uğur, Ş. S.; Sariişik, M.; Aktaş, A. H.; Uçar, M. Ç.; Erden, E. Modifying of Cotton Fabric Surface with Nano-ZnO Multilayer Films by Layer-by-Layer Deposition Method. *Nanoscale Res. Lett.* **2010**, *5* (7), 1204–1210.

(162) Dubas, S. T.; Kumlangdudsana, P.; Potiyaraj, P. Layer-by-Layer Deposition of Antimicrobial Silver Nanoparticles on Textile Fibers. *Colloids Surfaces A Physicochem. Eng. Asp.* **2006**, *289* (1–3), 105–109.

(163) Kamra, T.; Xu, C.; Montelius, L.; Schnadt, J.; Wijesundera, S. A.; Yan, M.; Ye, L. Photoconjugation of Molecularly Imprinted Polymer Nanoparticles for Surface-Enhanced Raman Detection of Propranolol. *ACS Appl. Mater. Interfaces* **2015**, *7* (49), 27479–27485.

(164) Zhang, H.; Yi, Y.; Zhou, C.; Ying, G.; Zhou, X.; Fu, C.; Zhu, Y.; Shen, Y. SERS Detection of MicroRNA Biomarkers for Cancer Diagnosis Using Gold-Coated Paramagnetic Nanoparticles to Capture SERS-Active Gold Nanoparticles. *RSC Adv.* **2017**, *7* (83), 52782–52793.

(165) Xu, H.; Bjerneld, E. J.; Käll, M.; Börjesson, L. Spectroscopy of Single Hemoglobin Molecules by Surface Enhanced Raman Scattering. *Phys. Rev. Lett.* **1999**, *83* (21), 4357–4360.

(166) Sukhorukov, G. B.; Donath, E.; Lichtenfeld, H.; Knippel, E.; Knippel, M.; Budde, A.; M??hwald, H. Layer-by-Layer Self Assembly of Polyelectrolytes on Colloidal Particles. *Colloids Surfaces A Physicochem. Eng. Asp.* **1998**, *137* (1–3), 253–266.

(167) Shiratori, S. S.; Rubner, M. F. PH-Dependent Thickness Behavior of Sequentially

Adsorbed Layers of Weak Polyelectrolytes. *Macromolecules* **2000**, *33* (11), 4213–4219.

(168) Sukhishvili, S. A.; Granick, S. Layered, Erasable Polymer Multilayers Formed by Hydrogen-Bonded Sequential Self-Assembly. *Macromolecules* **2002**, *35* (1), 301–310.

(169) Turkevich, J.; Stevenson, P. C.; Hillier, J. A Study of the Nucleation and Growth Processes in the Synthesis of Colloidal Gold. *Discuss. Faraday Soc.* **1951**, *11* (c), 55–75.

(170) Hao, F.; Nehl, C. L.; Hafner, J. H.; Nordlander, P. Plasmon Resonances of a Gold Nanostar. *Nano Lett.* **2007**, *7* (3), 729–732.

(171) Guerrero-Martínez, A.; Barbosa, S.; Pastoriza-Santos, I.; Liz-Marzán, L. M. Nanostars Shine Bright for You. Colloidal Synthesis, Properties and Applications of Branched Metallic Nanoparticles. *Curr. Opin. Colloid Interface Sci.* **2011**, *16* (2), 118–127.

(172) Encai Hao; Ryan C. Bailey; George C. Schatz, *; Joseph T. Hupp, * and; Li, S. Synthesis and Optical Properties of "Branched" Gold Nanocrystals. **2004**.

(173) Rodríguez-Lorenzo, L.; Romo-Herrera, J. M.; Pérez-Juste, J.; Alvarez-Puebla, R. A.; Liz-Marzán, L. M. Reshaping and LSPR Tuning of Au Nanostars in the Presence of CTAB. *J. Mater. Chem.* **2011**, *21* (31), 11544.

(174) Xia, Y.; Xiong, Y.; Lim, B.; Skrabalak, S. E. Shape-Controlled Synthesis of Metal Nanocrystals: Simple Chemistry Meets Complex Physics? *Angew. Chemie Int. Ed.* **2009**, *48* (1), 60–103.

(175) Fales, A. M.; Yuan, H.; Vo-Dinh, T. Silica-Coated Gold Nanostars for Combined Surface-Enhanced Raman Scattering (SERS) Detection and Singlet-Oxygen Generation: A Potential Nanoplatform for Theranostics. *Langmuir* **2011**, *27* (19), 12186–12190.

(176) Senthil Kumar, P.; Pastoriza-Santos, I.; Rodríguez-González, B.; Javier García de Abajo, F.; Liz-Marzán, L. M. High-Yield Synthesis and Optical Response of Gold Nanostars. *Nanotechnology* **2008**, *19* (1), 015606.

(177) Yuan, H.; Fales, A. M.; Khoury, C. G.; Liu, J.; Vo-Dinh, T. Spectral Characterization and Intracellular Detection of Surface-Enhanced Raman Scattering (SERS)-Encoded Plasmonic Gold Nanostars. *J. Raman Spectrosc.* **2013**, *44* (2), 234–239.

(178) Gopalakrishnan, A.; Chirumamilla, M.; De Angelis, F.; Toma, A.; Zaccaria, R. P.; Krahne, R. Bimetallic 3D Nanostar Dimers in Ring Cavities: Recyclable and Robust Surface-Enhanced Raman Scattering Substrates for Signal Detection from Few Molecules. *ACS Nano* **2014**, *8* (8), 7986–7994.

(179) Pieczonka, N. P. W.; Aroca, R. F. Single Molecule Analysis by Surfaced-Enhanced Raman Scattering. *Chem. Soc. Rev.* **2008**, *37* (5), 946.

(180) Jalani, G.; Cerruti, M. Nano Graphene Oxide-Wrapped Gold Nanostars as Ultrasensitive and Stable SERS Nanoprobes. *Nanoscale* **2015**, *7* (22), 9990–9997.

(181) Min, Y.; Akbulut, M.; Kristiansen, K.; Golan, Y.; Israelachvili, J. The Role of Interparticle and External Forces in Nanoparticle Assembly. *Nat. Mater.* **2008**, *7* (7), 527–538.

(182) Silvera Batista, C. A.; Larson, R. G.; Kotov, N. A. Nonadditivity of Nanoparticle Interactions. *Science (80-.).* **2015**, *350* (6257), 1242477–1242477.

(183) Boström, M.; Williams, D. R. M.; Ninham, B. W. Specific Ion Effects: Why DLVO Theory Fails for Biology and Colloid Systems. *Phys. Rev. Lett.* **2001**, *87* (16), 168103.

(184) Ma, C. D.; Wang, C.; Acevedo-Vélez, C.; Gellman, S. H.; Abbott, N. L. Modulation of Hydrophobic Interactions by Proximally Immobilized Ions. *Nature* **2015**, *517* (7534), 347–350.

(185) Kwaadgras, B. W.; Verdult, M. W. J.; Dijkstra, M.; van Roij, R. Can Nonadditive Dispersion Forces Explain Chain Formation of Nanoparticles? *J. Chem. Phys.* **2013**, *138* (10), 104308.

(186) Yang, M.; Chan, H.; Zhao, G.; Bahng, J. H.; Zhang, P.; Král, P.; Kotov, N. A. Self-Assembly of Nanoparticles into Biomimetic Capsid-like Nanoshells. *Nat. Chem.* **2017**, *9* (3).

(187) Hao, E.; Schatz, G. C. Electromagnetic Fields around Silver Nanoparticles and Dimers. *J. Chem. Phys.* **2004**, *120* (1), 357–366.

(188) Schuck, P. J.; Fromm, D. P.; Sundaramurthy, A.; Kino, G. S.; Moerner, W. E. Improving the Mismatch between Light and Nanoscale Objects with Gold Bowtie Nanoantennas. *Phys. Rev. Lett.* **2005**, *94* (1), 14–17.

(189) Sinha, G.; Depero, L. E.; Alessandri, I. Recyclable SERS Substrates Based on Au-Coated ZnO Nanorods. *ACS Appl. Mater. Interfaces* **2011**, *3* (7), 2557–2563.

(190) Vayssieres, L. Growth of Arrayed Nanorods and Nanowires of ZnO from Aqueous Solutions. *Adv. Mater.* **2003**, *15* (5), 464–466.

(191) Yuan, H.; Khoury, C. G.; Hwang, H.; Wilson, C. M.; Grant, G. A.; Vo-Dinh, T. Gold Nanostars: Surfactant-Free Synthesis, 3D Modelling, and Two-Photon Photoluminescence Imaging. *Nanotechnology* **2012**, *23* (7).

(192) Haiss, W.; Thanh, N. T. K.; Aveyard, J.; Fernig, D. G. Determination of Size and Concentration of Gold Nanoparticles from UV-Vis Spectra. *Anal. Chem.* **2007**, *79* (11), 4215–4221.

(193) Begum, G.; Singh, S.; Rangaraj, N.; Srinivas, G.; Rana, R. K. Cellular Permeation with Nuclear Infiltration Capability of Biomimetically Synthesised Fluorescent Monodisperse Mesoporous Silica Nanospheres in HeLa and Human Stem Cells. *J. Mater. Chem.* **2010**, *20* (39), 8563.

(194) McFarland, A. D.; Young, M. A.; Dieringer, J. A.; Van Duyne, R. P. Wavelength-Scanned Surface-Enhanced Raman Excitation Spectroscopy. *J. Phys. Chem. B* **2005**, *109* (22), 11279–11285.

(195) Félidj, N.; Aubard, J.; Lévi, G.; Krenn, J. R.; Salerno, M.; Schider, G.; Lamprecht, B.; Leitner, A.; Aussenegg, F. R. Controlling the Optical Response of Regular Arrays of Gold Particles for Surface-Enhanced Raman Scattering. *Phys. Rev. B - Condens. Matter Mater. Phys.* **2002**, *65* (7), 0754191–0754199.

(196) Hildebrandt, P.; Stockburger, M. Surface-Enhanced Resonance Raman Spectroscopy of Rhodamine 6G Adsorbed on Colloidal Silver. *J. Phys. Chem.* **1984**, *88* (24), 5935–5944.

(197) Le Ru, E. C.; Blackie, E.; Meyer, M.; Etchegoint, P. G. Surface Enhanced Raman Scattering Enhancement Factors: A Comprehensive Study. *J. Phys. Chem. C* **2007**, *111* (37), 13794–13803.

(198) Khoury, C.; Vo-Dinh, T. Gold Nanostars for Surface-Enhanced Raman Scattering: Synthesis, Characterization and Optimization. *J. Phys. Chem. C* **2008**, *112*, 18849–18859.

(199) Hamaker, H. C. The London-van Der Waals Attraction between Spherical Particles. *Physica* **1937**, *4* (10), 1058–1072.

(200) Parsegian, V. A.; Weiss, G. H. Spectroscopic Parameters for Computation of van Der Waals Forces. *J. Colloid Interface Sci.* **1981**, *81* (1), 285–289.

(201) Israelachvili, J. N.; Israelachvili, J. N. Chapter 14 – Electrostatic Forces between Surfaces in Liquids. In *Intermolecular and Surface Forces*; 2011; pp 291–340.

(202) van Oss, C. J.; Chaudhury, M. K.; Good, R. J. Interfacial Lifshitz—van Der Waals and Polar Interactions in Macroscopic Systems. *Chem. Rev.* **1988**, *88* (6), 927–941.

(203) Gregory, J. Interaction of Unequal Double Layers at Constant Charge. *J. Colloid Interface Sci.* **1975**, *51* (1), 44–51.

(204) Chang, H.-C.; Yossifon, G.; Demekhin, E. A. Nanoscale Electrokinetics and Microvortices: How Microhydrodynamics Affects Nanofluidic Ion Flux. *Annu. Rev. Fluid Mech.* **2012**, *44* (1), 401–426.

(205) *Handbook of Micro/Nano Tribology*; Bhusan, B., Ed.; 1998.

(206) Ramaswamy, N.; He, Q.; Abbott, D.; Bates, M. Electrocatalysis in Alkaline Electrolytes - Research Overview. **2011**.

(207) Shinagawa, T.; Takanabe, K. Electrolyte Engineering toward Efficient Hydrogen Production Electrocatalysis with Oxygen-Crossover Regulation under Densely Buffered Near-Neutral PH Conditions. *J. Phys. Chem. C* **2016**, *120* (3), 1785–1794.

(208) Goldkorn, T.; Schejter, A. Electrostatic Effects on the Kinetics of Oxidation-Reduction Reactions of c-Type Cytochromes. *J. Biol. Chem.* **1979**, *254* (24), 12562–12566.

(209) Colic, V.; Pohl, M. D.; Scieszka, D.; Bandarenka, A. S. Influence of the Electrolyte Composition on the Activity and Selectivity of Electrocatalytic Centers. *Catal. Today* **2016**, *262*, 24–35.

(210) Ma, S.; Kenis, P. J. A.; others. Electrochemical Conversion of CO 2 to Useful Chemicals: Current Status, Remaining Challenges, and Future Opportunities. *Curr. Opin. Chem. Eng.* **2013**, *2* (2), 191–199.

(211) Schmickler, W.; Santos, E. *Interfacial Eletrochemistry*; Springer: Berlin: London, 2010.

(212) Zhang, C.; Hutter, J.; Sprik, M. Coupling of Surface Chemistry and Electric Double Layer at TiO2 Electrochemical Interfaces. *J. Phys. Chem. Lett.* **2019**, *10* (14), 3871–3876.

(213) Kister, T.; Monego, D.; Mulvaney, P.; Widmer-Cooper, A.; Kraus, T. Colloidal Stability of Apolar Nanoparticles: The Role of Particle Size and Ligand Shell Structure. *ACS Nano* **2018**, *12* (6), 5969–5977.

(214) Li, D.; Wang, C.; Tripkovic, D.; Sun, S.; Markovic, N. M.; Stamenkovic, V. R. Surfactant Removal for Colloidal Nanoparticles from Solution Synthesis: The Effect on Catalytic Performance. *ACS Catal.* **2012**, *2* (7), 1358–1362.

(215) Montjoy, D. G. D. G.; Bahng, J. H. J. H.; Eskafi, A.; Hou, H.; Kotov, N. A. N. A. Omnidispersible Hedgehog Particles with Multilayer Coatings for Multiplexed Biosensing. *J. Am. Chem. Soc.* **2018**, *140* (25), 7835–7845.

(216) Deng, D.; Hao, C.; Sen, S.; Xu, C.; Král, P.; Kotov, N. A. N. A. Template-Free Hierarchical Self-Assembly of Iron Diselenide Nanoparticles into Mesoscale Hedgehogs. *J. Am. Chem. Soc.* **2017**, *139* (46), 16630–16639.

(217) Jiang, W.; Qu, Z.; Kumar, P.; Vecchio, D.; Wang, Y.; Ma, Y.; Bahng, J. H.; Bernardino, K.; Gomes, W. R.; Colombari, F. M.; et al. Emergence of Complexity in Hierarchically Organized Chiral Particles. *Science (80-.).* **2020**, *eaaz7949* (DOI: 10.1126/science.aaz7949).

(218) Reynolds, D. C.; Look, D. C.; Jogai, B.; Hoelscher, J. E.; Sherriff, R. E.; Harris, M. T.; Callahan, M. J. Time-Resolved Photoluminescence Lifetime Measurements of the Γ[Sub 5] and Γ[Sub 6] Free Excitons in ZnO. *J. Appl. Phys.* **2000**, *88* (4), 2152.

(219) Özgür, Ü.; Alivov, Y. I.; Liu, C.; Teke, a.; Reshchikov, M. a.; Doğan, S.; Avrutin, V.; Cho, S. J.; Morkoç, H. A Comprehensive Review of ZnO Materials and Devices. *J. Appl. Phys.* **2005**, *98* (4), 1–103.

(220) Schmidt-Mende, L.; MacManus-Driscoll, J. L. ZnO - Nanostructures, Defects, and Devices. *Mater. Today* **2007**, *10* (5), 40–48.

(221) Schmitt, M. Synthesis and Testing of ZnO Nanoparticles for Photo-Initiation: Experimental Observation of Two Different Non-Migration Initiators for Bulk Polymerization. *Nanoscale* **2015**, 9532–9544.

(222) Wu, X.-F.; Neumann, H. Zinc-Catalyzed Organic Synthesis: C□C, C□N, C□O Bond Formation Reactions. *Adv. Synth. Catal.* **2012**, *354* (17), 3141–3160.

(223) Kandavelu, V.; Kastien, H.; Ravindranathan Thampi, K. Photocatalytic Degradation of Isothiazolin-3-Ones in Water and Emulsion Paints Containing Nanocrystalline TiO2 and ZnO Catalysts. *Appl. Catal. B Environ.* **2004**, *48* (2), 101–111.

(224) Zakzeski, J.; Bruijnincx, P. C. A.; Jongerius, A. L.; Weckhuysen, B. M. The Catalytic Valorization of Lignin for the Production of Renewable Chemicals. *Chem. Rev.* **2010**, *110* (6), 3552–3599.

(225) Behling, R.; Valange, S.; Chatel, G. Heterogeneous Catalytic Oxidation for Lignin Valorization into Valuable Chemicals: What Results? What Limitations? What Trends? *Green Chem.* **2016**, *18* (7), 1839–1854.

(226) Crossley, S.; Faria, J.; Shen, M.; Resasco, D. E. Solid Nanoparticles That Catalyze Biofuel

Upgrade Reactions at the Water/Oil Interface. *Science (80-.).* **2010**, *327* (5961), 68–72.

(227) Lin, L.; Xu, F.; Ge, X.; Li, Y. *Biological Treatment of Organic Materials for Energy and Nutrients Production—Anaerobic Digestion and Composting*, 1st ed.; Elsevier Inc., 2019; Vol. 4.

(228) Yu, B.; Cong, H.; Xue, L.; Tian, C.; Xu, X.; Peng, Q.; Yang, S. Synthesis and Modification of Monodisperse Silica Microspheres for UPLC Separation of C60 and C70. *Anal. Methods* **2016**, *8* (4), 919–924.

(229) Nishizawa, M.; Menon, V. P.; Martin, C. R. Metal Nanotubule Membranes with Electrochemically Switchable Ion-Transport Selectivity. *Science (80-.).* **1995**, *268* (5211), 700 LP – 702.

(230) Bruno, G.; Di Trani, N.; Hood, R. L.; Zabre, E.; Filgueira, C. S.; Canavese, G.; Jain, P.; Smith, Z.; Demarchi, D.; Hosali, S.; et al. Unexpected Behaviors in Molecular Transport through Size-Controlled Nanochannels down to the Ultra-Nanoscale. *Nat. Commun.* **2018**, *9* (1), 1682.

(231) Guillard, C.; Puzenat, E.; Lachheb, H.; Houas, A.; Herrmann, J. M. Why Inorganic Salts Decrease the TiO2 Photocatalytic Efficiency. *Int. J. Photoenergy* **2005**, *7* (1), 1–9.

(232) Guillard, C.; Lachheb, H.; Houas, A.; Ksibi, M.; Elaloui, E.; Herrmann, J. M. Influence of Chemical Structure of Dyes, of PH and of Inorganic Salts on Their Photocatalytic Degradation by TiO2 Comparison of the Efficiency of Powder and Supported TiO2. *J. Photochem. Photobiol. A Chem.* **2003**, *158* (1), 27–36.

(233) Hitkari, G.; Singh, S.; Pandey, G. Structural, Optical and Photocatalytic Study of ZnO and ZnO–ZnS Synthesized by Chemical Method. *Nano-Structures and Nano-Objects* **2017**, *12*, 1–9.

(234) Nipane, S. V.; Korake, P. V.; Gokavi, G. S. Graphene-Zinc Oxide Nanorod Nanocomposite as Photocatalyst for Enhanced Degradation of Dyes under UV Light Irradiation. *Ceramics International*. 2015, pp 4549–4557.

(235) Adeleke, J. T.; Theivasanthi, T.; Thiruppathi, M.; Swaminathan, M.; Akomolafe, T.; Alabi, A. B. Photocatalytic Degradation of Methylene Blue by ZnO_NiFe2O4 Nanoparticles. *Appl. Surf. Sci.* **2018**, *455*, 195–200.

(236) Wu, X.; Fan, X.; Xie, S.; Lin, J.; Cheng, J.; Zhang, Q.; Chen, L.; Wang, Y. Solar Energy-Driven Lignin-First Approach to Full Utilization of Lignocellulosic Biomass under Mild Conditions. *Nat. Catal.* **2018**, *1* (10), 772–780.

(237) Kjellander R. Intricate Coupling between Ion-Ion and Ion-Surface Correlations in Double Layers as Illustrated by Charge Inversion-Combined Effects of Strong Coulomb Correlations and Excluded Volume. *J. Phys. Condens. Matter* **2009**, *21*, 424101.

(238) Benselfelt, T.; Nordenström, M.; Hamedi, M. M.; Wågberg, L. Ion-Induced Assemblies of Highly Anisotropic Nanoparticles Are Governed by Ion–Ion Correlation and Specific Ion Effects. *Nanoscale* **2019**, *11* (8), 3514–3520.

(239) Smith, A. M.; Lee, A. A.; Perkin, S. The Electrostatic Screening Length in Concentrated

Electrolytes Increases with Concentration. *J. Phys. Chem. Lett.* **2016**, *7* (12), 2157–2163.

(240) Kent, P.; Saunders, B. R. The Role of Added Electrolyte in the Stabilization of Inverse Emulsions. *Journal of Colloid and Interface Science*. 2001, pp 437–442.

(241) Márquez, A. L.; Medrano, A.; Panizzolo, L. A.; Wagner, J. R. Effect of Calcium Salts and Surfactant Concentration on the Stability of Water-in-Oil (w/o) Emulsions Prepared with Polyglycerol Polyricinoleate. *Journal of Colloid and Interface Science*. 2010, pp 101–108.

(242) Augugliaro, V.; Bellardita, M.; Loddo, V.; Palmisano, G.; Palmisano, L.; Yurdakal, S. Overview on Oxidation Mechanisms of Organic Compounds by TiO2 in Heterogeneous Photocatalysis. *J. Photochem. Photobiol. C Photochem. Rev.* **2012**, *13* (3), 224–245.

(243) De, S.; Dutta, S.; Saha, B. Critical Design of Heterogeneous Catalysts for Biomass Valorization: Current Thrust and Emerging Prospects. *Catal. Sci. Technol.* **2016**, *6* (20), 7364–7385.

(244) Luo, N.; Wang, M.; Li, H.; Zhang, J.; Hou, T.; Chen, H.; Zhang, X.; Lu, J.; Wang, F. Visible-Light-Driven Self-Hydrogen Transfer Hydrogenolysis of Lignin Models and Extracts into Phenolic Products. *ACS Catal.* **2017**, *7* (7), 4571–4580.

(245) Ohshima, H.; Healy, T. W.; White, L. R. Accurate Analytic Expressions for the Surface Charge Density/Surface Potential Relationship and Double-Layer Potential Distribution for a Spherical Colloidal Particle. *J. Colloid Interface Sci.* **1982**, *90* (1), 17–26.

(246) Makino, K.; Ohshima, H. Electrophoretic Mobility of a Colloidal Particle with Constant Surface Charge Density. *Langmuir* **2010**, *26* (23), 18016–18019.

(247) Gagliardi, L. G.; Castells, C. B.; Ràfols, C.; Rosés, M.; Bosch, E. Static Dielectric Constants of Acetonitrile/Water Mixtures at Different Temperatures and Debye-Hückel A and A0B Parameters for Activity Coefficients. *J. Chem. Eng. Data* **2007**, *52* (3), 1103–1107.

(248) Jia, G. Z.; Liu, S.; Liu, F. H.; Liu, J. C. Ion–Water Cooperative Interactions in Aqueous Solutions of MgCl2 by Dielectric Spectroscopy. *J. Dispers. Sci. Technol.* **2016**, *37* (1), 1–5.

(249) Buchner, R.; Hefter, G. T.; May, P. M. Dielectric Relaxation of Aqueous NaCl Solutions. *J. Phys. Chem. A* **1999**, *103* (1), 8–9.

(250) Harknees, A. C.; Daggett, H. M. THE ELECTRICAL CONDUCTIVITIES OF SOME TETRA-n-ALKYLAMMONIUM SALTS IN ACETONITRILE. *Can. J. Chem.* **1965**, *43*, 1215–1221.

(251) Tsierkezos, N. G.; Philippopoulos, A. I. Studies of Ion Solvation and Ion Association of N-Tetrabutylammonium Hexafluorophosphate and n-Tetrabutylammonium Tetraphenylborate in Various Solvents. *Fluid Phase Equilib.* **2009**, *277* (1), 20–28.

(252) Stöber, W.; Fink, A.; Bohn, E. Controlled Growth of Monodisperse Silica Spheres in the Micron Size Range. *J. Colloid Interface Sci.* **1968**, *26* (1), 62–69.

(253) Landon, P. B.; Mo, A. H.; Zhang, C.; Emerson, C. D.; Printz, A. D.; Gomez, A. F.;

Delatorre, C. J.; Colburn, D. A. M.; Anzenberg, P.; Eliceiri, M.; et al. Designing Hollow Nano Gold Golf Balls. *ACS Appl. Mater. Interfaces* **2014**, *6* (13), 9937–9941.

(254) Caruso, F.; Shi, X.; Caruso, R. a.; Susha, a. Hollow Titania Spheres from Layered Prcursor Deposition on Sacrficial Colloidal Core Particles. *Adv. Mater.* **2001**, *13* (10), 740–745.

(255) Palmisano, G.; Addamo, M.; Augugliaro, V.; Caronna, T.; García-López, E.; Loddo, V.; Palmisano, L. Influence of the Substituent on Selective Photocatalytic Oxidation of Aromatic Compounds in Aqueous TiO2 Suspensions. *Chem. Commun. (Camb).* **2006**, No. 9, 1012–1014.

(256) Hadjiivanov, K. I.; Klissurski, D. G. Surface Chemistry of Titania (Anatase) and Titania-Supported Catalysts. *Chem. Soc. Rev.* **1996**, *25* (1), 61.

(257) Oldenburg, S. .; Averitt, R. .; Westcott, S. .; Halas, N. . Nanoengineering of Optical Resonances. *Chem. Phys. Lett.* **1998**, *288* (2–4), 243–247.

(258) Linic, S.; Christopher, P.; Ingram, D. B. Plasmonic-Metal Nanostructures for Efficient Conversion of Solar to Chemical Energy. *Nat. Mater.* **2011**, *10* (12), 911–921.

(259) Brown, A. M.; Sundararaman, R.; Narang, P.; Goddard, W. A.; Atwater, H. A. Nonradiative Plasmon Decay and Hot Carrier Dynamics: Effects of Phonons, Surfaces, and Geometry. *ACS Nano* **2016**, *10* (1), 957–966.

(260) Ashley, J. C.; Williams, M. W. Electron Mean Free Paths in Solid Organic Insulators Author (s): J . C . Ashley and M . W . Williams Published by : Radiation Research Society Stable URL : Https://Www.Jstor.Org/Stable/3575195 Electron Mean Free Paths in Solid Organic Insulators1 ’ 2. *Radiat. Res.* **1980**, *81* (3), 364–373.

(261) Boerigter, C.; Aslam, U.; Linic, S. Mechanism of Charge Transfer from Plasmonic Nanostructures to Chemically Attached Materials. *ACS Nano* **2016**, *10* (6), 6108–6115.

(262) Aslam, U.; Rao, V. G.; Chavez, S.; Linic, S. Catalytic Conversion of Solar to Chemical Energy on Plasmonic Metal Nanostructures. *Nat. Catal.* **2018**, *1* (9), 656–665.

(263) Nicewicz, D. A.; Macmillan, D. W. C. Organocatalysis : The Direct. **2008**, *105* (2005).

(264) Narayanam, J. M. R.; Stephenson, C. R. J. Visible Light Photoredox Catalysis: Applications in Organic Synthesis. *Chem. Soc. Rev.* **2011**, *40* (1), 102–113.

(265) Prier, C. K.; Rankic, D. a.; MacMillan, D. W. C. Visible Light Photoredox Catalysis with Transition Metal Complexes: Applications in Organic Synthesis. *Chem. Rev.* **2013**, *113* (7), 5322–5363.

(266) Maldotti, a.; Bartocci, C.; Varani, G.; Molinari, a.; Battioni, P.; Mansuy, D. Oxidation of Cyclohexane by Molecular Oxygen Photoassisted by Meso-Tetraarylporphyrin Iron(III)-Hydroxo Complexes. *Inorg. Chem.* **1996**, *35* (5), 1126–1131.

(267) Boarini, P.; Carassiti, V.; Maldotti, A.; Amadelli, R. Photocatalytic Oxygenation of Cyclohexane on Titanium Dioxide Suspensions : Effect of the Solvent and of Oxygen. **1998**, *7463* (c), 2080–2085.

(268) Almquist, C. B.; Biswas, P. The Photo-Oxidation of Cyclohexane on Titanium Dioxide: An Investigation of Competitive Adsorption and Its Effects on Product Formation and Selectivity. *Appl. Catal. A Gen.* **2001**, *214* (2), 259–271.

(269) Lu, G.; Gao, H.; Suo, J.; Li, S. Catalytic Oxidation of Cyclohexane into Cyclohexanol and Cyclohexanone over a TiO2/TS-1 System by Dioxygen under UV Irradiation. *J. Chem. Soc. Chem. Commun.* **1994**, No. 21, 2423.

(270) Zhang, Z.; Hossain, M. F.; Takahashi, T. Self-Assembled Hematite (α-Fe2O3) Nanotube Arrays for Photoelectrocatalytic Degradation of Azo Dye under Simulated Solar Light Irradiation. *Appl. Catal. B Environ.* **2010**, *95* (3–4), 423–429.

(271) Hsu, Y.-K.; Chen, Y.-C.; Lin, Y.-G. Novel ZnO/Fe $_2$ O $_3$ Core–Shell Nanowires for Photoelectrochemical Water Splitting. *ACS Appl. Mater. Interfaces* **2015**, *7* (25), 14157–14162.

(272) Xiong, S.; Xu, J.; Chen, D.; Wang, R.; Hu, X.; Shen, G.; Wang, Z. L. Controlled Synthesis of Monodispersed Hematite Microcubes and Their Properties. *CrystEngComm* **2011**, *13* (23), 7114.

(273) Lou, X. W.; Archer, L. A. A General Route to Nonspherical Anatase TiO2 Hollow Colloids and Magnetic Multifunctional Particles. *Adv. Mater.* **2008**, *20* (10), 1853–1858.

(274) Weiss, B.; Sturn, J.; Voglsam, S.; Strobl, S.; Mali, H.; Winter, F.; Schenk, J. Structural and Morphological Changes during Reduction of Hematite to Magnetite and Wustite in Hydrogen Rich Reduction Gases under Fluidised Bed Conditions. *Ironmak. Steelmak.* **2011**, *38* (1), 65–73.

(275) Liu, S.; Yu, J.; Jaroniec, M. Tunable Photocatalytic Selectivity of Hollow TiO 2 Microspheres Composed of Anatase Polyhedra with Exposed 001 Facets. *Communications* **2010**, *132* (34), 11914–11916.

(276) Yang, H. G.; Zeng, H. C. Preparation of Hollow Anatase TiO 2 Nanospheres via Ostwald Ripening. *J. Phys. Chem. B* **2004**, *108* (010), 3492–3495.

(277) Duff, D. G.; Baiker, A.; Edwards, P. P. A New Hydrosol of Gold Clusters. 1. Formation and Particle Size Variation. *Langmuir* **1993**, *9* (9), 2301–2309.

(278) Zhou, J. K.; Lv, L.; Yu, J.; Li, H. L.; Guo, P. Z.; Sun, H.; Zhao, X. S. Synthesis of Self-Organized Polycrystalline F-Doped TiO2 Hollow Microspheres and Their Photocatalytic Activity under Visible Light. *J. Phys. Chem. C* **2008**, *112* (14), 5316–5321.

(279) Liu, H.; Li, W.; Shen, D.; Zhao, D.; Wang, G. Graphitic Carbon Conformal Coating of Mesoporous TiO2 Hollow Spheres for High-Performance Lithium Ion Battery Anodes. *J. Am. Chem. Soc.* **2015**, *137* (40), 13161–13166.

(280) Xu, C.; Shin, P. H.; Cao, L.; Wu, J.; Gao, D. Ordered TiO 2 Nanotube Arrays on Transparent Conductive Oxide for Dye-Sensitized Solar Cells. **2010**, No. 4, 143–148.

(281) Deki, S.; Aoi, Y.; Hiroi, O.; Kajinami, a. Titanium(IV) Oxide Thin Films Prepared from Aqueous Solution. *Chemistry Letters*. 1996, pp 433–434.

(282) Macak, J. M.; Zlamal, M.; Krysa, J.; Schmuki, P. Self-Organized TiO2 Nanotube Layers as Highly Efficient Photocatalysts. *Small* **2007**, *3* (2), 300–304.

(283) Maki, H.; Okumura, Y.; Ikuta, H.; Mizuhata, M. Ionic Equilibria for Synthesis of TiO2 Thin Films by the Liquid-Phase Deposition. *J. Phys. Chem. C* **2014**, *118* (22), 11964–11974.

(284) Han, H.; Riboni, F.; Karlicky, F.; Kment, S.; Goswami, A.; Sudhagar, P.; Yoo, J.; Wang, L.; Tomanec, O.; Petr, M.; et al. α-Fe $_2$ O $_3$ /TiO $_2$ 3D Hierarchical Nanostructures for Enhanced Photoelectrochemical Water Splitting. *Nanoscale* **2017**, *9* (1), 134–142.

(285) Kirchner, S. R.; Su, M.-N. M. N.; Bahng, J. H.; Montjoy, D. G. D. G.; Chang, W.-S. W. S.; Kotov, N. A. N. A.; Link, S. Scattering Properties of Individual Hedgehog Particles. *J. Phys. Chem. C* **2018**, *122* (22), 12015–12021.

(286) Kotov, N. A.; Bahng, J. H. Enhancement of Forward Scattering, Suppresion of Backscattering, and Spectral Tuning of Optical Hedgehog Particles. US20180149887A1, 2018.

(287) *Liquid Phase Aerobic Oxidation Catalysis Industrial Applications and Academic Perspectives*; Stahl, S. S., Alsters, P. L., Eds.; Wiley-VCH, 2016.

(288) Castellan, A.; Bart, J. C. J.; Cavallaro, S. Industrial Production and Use of Adipic Acid. *Catal. Today* **1991**, *9* (3), 237–254.

(289) Pillai, U. R.; Sahle-Demessie, E. A Highly Efficient Oxidation of Cyclohexane over VPO Catalysts Using Hydrogen Peroxide. *Chem. Commun.* **2002**, *2* (18), 2142–2143.

(290) Raja, R.; Ratnasamy, P. Oxidation of Cyclohexane over Copper Phthalocyanines Encapsulated in Zeolites. *Catal. Letters* **1997**, *48*, 1–10.

(291) Zhou, W. J.; Wischert, R.; Xue, K.; Zheng, Y. T.; Albela, B.; Bonneviot, L.; Clacens, J. M.; De Campo, F.; Pera-Titus, M.; Wu, P. Highly Selective Liquid-Phase Oxidation of Cyclohexane to KA Oil over Ti-MWW Catalyst: Evidence of Formation of Oxyl Radicals. *ACS Catal.* **2014**, *4* (1), 53–62.

(292) Giannotti, C.; Le Greneur, S.; Watts, O. Photo-Oxidation of Alkanes by Metal Oxide Semiconductors. *Tetrahedron Lett.* **1983**, *24* (46), 5071–5072.

(293) Du, P.; Moulijn, J. A.; Mul, G. Selective Photo(Catalytic)-Oxidation of Cyclohexane: Effect of Wavelength and TiO2structure on Product Yields. *J. Catal.* **2006**, *238* (2), 342–352.

(294) Sato, K.; Aoki, M.; Noyori, R. A " Green " Route to Adipic Acid : Direct Oxidation of Cyclohexenes with 30 Percent Hydrogen Peroxide Onset of Catalytic Activity of Gold Clusters on Titania with the Appearance of Nonmetallic Properties. *Science (80-.).* **1998**, *281* (September), 1646–1648.

(295) Mizuno, N.; Yamaguchi, K.; Kamata, K. Epoxidation of Olefins with Hydrogen Peroxide Catalyzed by Polyoxometalates. *Coord. Chem. Rev.* **2005**, *249* (17-18 SPEC. ISS.), 1944–1956.

(296) Boudjema, S.; Rabah, H.; Choukchou-Braham, A. Oxidation of Cyclohexene with H2O2 Catalyzed by Vanadium Based Polyoxometalates Doped Modified Clays as Green Catalysts. *Acta Phys. Pol. A* **2017**, *132* (3), 469–472.

(297) Abu-Abdoun, I. I. Cationic Polymerization of Cyclohexene Oxide by Pentamethoxytrityl Salts. *Polym. Sci. - Ser. B* **2008**, *50* (9–10), 243–248.

(298) Woragamon, K.; Jongpatiwut, S.; Sreethawong, T. Liquid-Phase Cyclohexene Epoxidation with H2O2 over RuO2-Loaded Mesoporous-Assembled TiO2 Nanocrystals: Catalyst Preparation and Recyclability. *Catal. Letters* **2010**, *136* (3–4), 249–259.

(299) Binks, B. P.; Clint, J. H.; Mackenzie, G.; Simcock, C.; Whitby, C. P. Naturally Occurring Spore Particles at Planar Fluid Interfaces and in Emulsions. *Langmuir* **2005**, *21* (18), 8161–8167.

(300) Garcia-Bosch, I.; Siegler, M. A. Copper-Catalyzed Oxidation of Alkanes with H2O2under a Fenton-like Regime. *Angew. Chemie - Int. Ed.* **2016**, *55* (41), 12873–12876.

(301) Jin, M.; Cheng, Z. M. Oxidative Dehydrogenation of Cyclohexane to Cyclohexene over Mg-V-O Catalysts. *Catal. Letters* **2009**, *131* (1–2), 266–278.

(302) Coperet, C.; Adolfsson, H.; Sharpless, K. B. A Simple and Efficient Method for Epoxidation of Terminal Alkenes The Use of a Catalytic Amount of 3-Cyanopyridine in the Methyltrioxorhenium Catalysed Epoxidation of Terminal Alkenes with Aqueous Hydrogen Peroxide Speeds Turnover , Epoxides in High Yield. *Chem. Commun.* **1997**, 1565–1566.

(303) Ji, D.; Zhu, W.; Wang, Z.; Wang, G. Dehydrogenation of Cyclohexanol on Cu-ZnO/SiO2 Catalysts: The Role of Copper Species. *Catal. Commun.* **2007**, *8* (12), 1891–1895.

(304) Hereijgers, B. P. C.; Parton, R. F.; Weckhuysen, B. M. Mechanistic Insights in the Olefin Epoxidation with Cyclohexyl Hydroperoxide. *Catal. Sci. Technol.* **2012**, *2* (5), 951–960.

(305) Hereijgers, B. P. C.; Parton, R. F.; Weckhuysen, B. M. Cyclohexene Epoxidation with Cyclohexyl Hydroperoxide: A Catalytic Route to Largely Increase Oxygenate Yield from Cyclohexane Oxidation. *ACS Catal.* **2011**, *1* (10), 1183–1192.

(306) Shi, W.; Sahoo, Y.; Swihart, M. T.; Prasad, P. N. Gold Nanoshells on Polystyrene Cores for Control of Surface Plasmon Resonance. *Langmuir* **2005**, *21* (4), 1610–1617.

(307) Shul'pin, G. B. Metal-Catalyzed Hydrocarbon Oxygenations in Solutions: The Dramatic Role of Additives: A Review. *J. Mol. Catal. A Chem.* **2002**, *189* (1), 39–66.

(308) Kotov, N. A.; Dékány, I.; Fendler, J. H. Ultrathin Graphite Oxide-Polyelectrolyte Composites Prepared by Self-Assembly: Transition between Conductive and Non-Conductive States. *Adv. Mater.* **1996**, *8* (8), 637–641.

(309) Sukhorukov, G. B.; Donath, E.; Davis, S.; Lichtenfeld, H.; Caruso, F.; Popov, V. I.; Möhwald, H. Stepwise Polyelectrolyte Assembly on Particle Surfaces: A Novel Approach to Colloid Design. *Polym. Adv. Technol.* **1998**, *9* (10–11), 759–767.

(310) Lvov, Y.; Yamada, S.; Kunitake, T. Non-Linear Optical Effects in Layer-by-Layer

Alternate Films of Polycations and an Azobenzene-Containing Polyanion. *Thin Solid Films* **1997**, *300* (1–2), 107–112.

(311) Xie, X.; Melosh, N. A. Fabrication of Sub-Cell Size "Spiky" Nanoparticles and Their Interfaces with Biological Cells. *J. Mater. Chem. B* **2015**, *3* (26), 5155–5160.

(312) Qin, Y.; Zhou, Y.; Li, J.; Ma, J.; Shi, D.; Chen, J.; Yang, J. Fabrication of Hierarchical Core-Shell Au@ZnO Heteroarchitectures Initiated by Heteroseed Assembly for Photocatalytic Applications. *J. Colloid Interface Sci.* **2014**, *418*, 171–177.

(313) Wang, J.; Chen, H. J.; Hang, T.; Yu, Y.; Liu, G.; He, G.; Xiao, S.; Yang, B. ru; Yang, C.; Liu, F.; et al. Physical Activation of Innate Immunity by Spiky Particles. *Nat. Nanotechnol.* **2018**, *13* (11), 1078–1086.

(314) Qiao, L.; Zhao, W.; Qin, Y.; Swihart, M. T. Controlled Growth of a Hierarchical Nickel Carbide "Dandelion" Nanostructure. *Angew. Chemie* **2016**, *128* (28), 8155–8158.

(315) Sakr, O. S.; Borchard, G. Encapsulation of Enzymes in Layer-by-Layer (LbL) Structures: Latest Advances and Applications. *Biomacromolecules* **2013**, *14* (7), 2117–2135.

(316) Caruso, F. Nanoengineering of Particle Surfaces. *Adv. Mater.* **2001**, *13* (1), 11–22.

(317) Bunyakan, C.; Hunkeler, D. Precipitation Polymerization of Acrylic Acid in Toluene . I : Synthesis , Characterization and Kinetics. **1999**, *40*, 6213–6224.

(318) Barbosa, O.; Ortiz, C.; Berenguer-Murcia, Á.; Torres, R.; Rodrigues, R. C.; Fernandez-Lafuente, R. Glutaraldehyde in Bio-Catalysts Design: A Useful Crosslinker and a Versatile Tool in Enzyme Immobilization. *RSC Adv.* **2014**, *4* (4), 1583–1600.

(319) Wang, F.; Bazan, G. C. Aggregation-Mediated Optical Properties of PH-Responsive Anionic Conjugated Polyelectrolytes. *J. Am. Chem. Soc.* **2006**, *128* (49), 15786–15792.

(320) Shao, L.; Lutkenhaus, J. L. Thermochemical Properties of Free-Standing Electrostatic Layer-by-Layer Assemblies Containing Poly(Allylamine Hydrochloride) and Poly(Acrylic Acid). *Soft Matter* **2010**, *6* (14), 3363–3369.

(321) Sukhorukov, G. B.; Antipov, A. A.; Voigt, A.; Donath, E.; M̈hwald, H. PH-Controlled Macromolecule Encapsulation in and Release from Polyelectrolyte Multilayer Nanocapsules. *Macromol. Rapid Commun.* **2001**, *22* (1), 44–46.

(322) Shchukin, D. G.; Lamaka, S. V.; Yasakau, K. A.; Zheludkevich, M. L.; Ferreira, M. G. S.; Möhwald, H. Active Anticorrosion Coatings with Halloysite Nanocontainers. *J. Phys. Chem. C* **2008**, *112* (4), 958–964.

(323) Szarpak, A.; Cui, D.; Dubreuil, F.; De Geest, B. G.; De Cock, L. J.; Picart, C.; Auzély-Velty, R. Designing Hyaluronic Acid-Based Layer-by-Layer Capsules as a Carrier for Intracellular Drug Delivery. *Biomacromolecules* **2010**, *11* (3), 713–720.

(324) J. E., C.; M., Y. Y.; T., A.; Y., S.; T., O.; Chung, J. E.; Yokoyama, M.; Yamato, M.; Aoyagi, T.; Sakurai, Y.; et al. Thermo-Responsive Drug Delivery from Polymeric Micelles Constructed Using Block Copolymers of Poly(N-Isopropylacrylamide) and Poly(Butylmethacrylate). *J. Control. Release* **1999**, *62*, 115–127.

(325) Schild, H. G. Poly(N-Isopropylacrylamide): Experiment, Theory and Application. *Prog. Polym. Sci.* **1992**, *17* (2), 163–249.

(326) Min, Y.; Hammond, P. T. Catechol-Modified Polyions in Layer-by-Layer Assembly to Enhance Stability and Sustain Release of Biomolecules: A Bioinspired Approach. *Chem. Mater.* **2011**, *23* (24), 5349–5357.

(327) Xia, L. W.; Xie, R.; Ju, X. J.; Wang, W.; Chen, Q.; Chu, L. Y. Nano-Structured Smart Hydrogels with Rapid Response and High Elasticity. *Nat. Commun.* **2013**, *4*, 1–11.

(328) Kim, S. K.; Chang, H.; Cho, K.; Kil, D. S.; Cho, S. W.; Jang, H. D.; Choi, J. W.; Choi, J. Enhanced Photocatalytic Property of Nanoporous TiO2/SiO 2 Micro-Particles Prepared by Aerosol Assisted Co-Assembly of Nanoparticles. *Mater. Lett.* **2011**, *65* (21–22), 3330–3332.

(329) Lee, H.; Scherer, N. F.; Messersmith, P. B. Single-Molecule Mechanics of Mussel Adhesion. *Proc. Natl. Acad. Sci.* **2006**, *103* (35), 12999–13003.

(330) Yu, A.; Wang, Y.; Barlow, E.; Caruso, F. Mesoporous Silica Particles as Templates for Preparing Enzyme-Loaded Biocompatible Microcapsules. *Adv. Mater.* **2005**, *17* (14), 1737–1741.

(331) Chen, Z.; Hsu, P.-C.; Lopez, J.; Li, Y.; To, J. W. F.; Liu, N.; Wang, C.; Andrews, S. C.; Liu, J.; Cui, Y.; et al. Fast and Reversible Thermoresponsive Polymer Switching Materials for Safer Batteries. *Nat. Energy* **2016**, *1* (January), 15009.

(332) Mori, K.; Yamashita, H.; Anpo, M. Photocatalytic Reduction of CO2 with H2O on Various Titanium Oxide Photocatalysts. *RSC Adv.* **2012**, *2*, 3165.